Taking past temperatures with a grain of salt

Niels Brall

N°d'ordre NNT :
2022LYSE1087

THESE de DOCTORAT DE L'UNIVERSITE DE LYON

opérée au sein de:

l'Université Claude Bernard Lyon 1

Ecole Doctorale: 52

Spécialité de doctorat: Géologie

soutenue publiquement le 10/06/2022 par

Niels Sean Brall

TAKING PAST TEMPERATURES WITH A GRAIN OF SALT

Sous la direction de: **Véronique Gardien**
en co-direction avec **Frédéric Caupin**

Devant le jury composé de:

Giovanni Aloisi	Institut de Physique du Globe de Paris	**Rapporteur**
Marco Roveri	Université de Parma	**Rapporteur**
Emmanuela Mattioli	Université Lyon 1	**Présidente**
Kathryn Fitzsimmons	Université de Tübingen	**Examinatrice**
Véronique Gardien	Université Lyon 1	**Directrice**
Frédéric Caupin	Université Lyon 1	**Directeur**

DECLARATION

I here by declare that the thesis entitled "Taking past temperatures with a grain of salt" submitted by me, for the award of the degree of *Doctor of Philosophy* to University Lyon is a record of genuine work carried out by me under the supervision of Dr. Véronique Gardien, Laboratoire de Géologie de Lyon: Terre, Planètes, Environnement, Université Claude Bernard Lyon 1, France.

I further declare that the work reported in this thesis has not been submitted and will not be submitted, either in part or in full, for the award of any other degree or diploma in this institute or any other institute or university.

Lyon, France

Date: 03/05/2022 **Signature of the Candidate**

ABSTRACT

Evaporites such as salt and gypsum are common minerals in, for example, oceans, sabkhas, caves, desertic regions and lakes. Evaporite sequences can be useful climate archives: physical and chemical conditions of formation of the host mineral can be retrieved from water droplets (fluid inclusions; FIs) trapped in the crystal during its growth. Recently, a novel method has been developed to measure sound velocity in FIs and to determine their entrapment temperatures in host halite crystals. It is based on Brillouin Spectroscopy (BS), which measures small frequency shifts in inelastically scattered light. Can BS be used to generate high-resolution temporal reconstructions of climate for regions and time intervals with evaporite deposition? To address this question, we applied BS on halite sections from the Dead Sea Basin (DSB). The DSB is a unique study site, because halite layers were deposited annually (varves) during drier and warmer interglacial periods (Marine Isotope Stages; MIS 7c and MIS 5e).

BS measurements on halite FIs reveal maximum temperature differences of 4 °C between bottom and uppermost intervals of individual layers during both interglacial intervals. Palaeotemperatures from the oldest halite section (ca 215 ka; MIS 7c) further highlight a decadal warming of the lake bottom waters during summer (+3 °C) and winter (+4 °C) periods along the core section. These results also show annual winter lake temperature fluctuations throughout all layers, whereas summer lake temperatures remained constant for six years, followed by annual variations until the end of halite deposition. A possible connection between varve thicknesses and summer water temperatures is also discussed. These results have major implications for future studies on layered halite sequences at larger geographical and temporal scales.

The question remains to which extent BS can be applied to other minerals, such as the evaporitic sulphate mineral gypsum. Experiments were carried out using BS analysis on capillary solutions with various NaCl concentrations as well as on synthetic gypsum. This method was also applied to natural gypsum samples from (high) saline environments (e.g., Tunisian sabkha, Aral Sea) and from outcrop dating back to the Messinian Salinity Crisis in the Mediterranean realm.

Gypsum entrapment temperatures scarcely reproduce the expected values for synthetical samples of known water temperatures. Experiments carried out with natural gypsum samples, on the other hand, provide a larger quantity of T data from FIs, suggesting that natural gypsum samples might serve for temperature studies using BS. Further work is needed to confirm this.

Developing the methodology on gypsum is further motivated by the sensitivity of sound velocity on salinity, as observed in capillary solution experiments and in biphasic FIs in natural gypsum. Thus, sound velocity can be used as a high throughput salinity proxy in evaporites making Brillouin spectroscopy a promising tool for future palaeosalinity reconstructions.

Keywords: *Brillouin Spectroscopy*, *Evaporites*, *Gypsum*, *Dead Sea*, *Sound Velocity*, *Palaeoclimate reconstructions*.

RESUMÉ

Le sel ou le gypse sont des minéraux courants des séries évaporitiques se formant dans des contextes variés comme les océans, les sebkhas, les grottes, les régions désertiques et les lacs. Lors de leur croissance ces minéraux piègent des micro-gouttelettes d'un fluide (inclusions fluides : IFs) ayant préservé les conditions physiques et chimiques à partir desquels les cristaux ont poussé. De fait, ses séquences d'évaporites sont des archives climatiques potentielles. Récemment, une nouvelle méthode a été développée pour mesurer la vitesse du son dans les inclusions fluides d'halite afin de déterminer leur température de piégeage. Cette méthode, la spectroscopie Brillouin (BS) mesure les petits décalages de fréquence (le shift Brillouin) de la lumière diffusée inélastiquement.

La question majeure que je me suis posé au cours de cette thèse est de savoir si la BS peut être utilisée pour reconstruire à haute résolution l'évolution de la température dans des régions et pour des intervalles de temps où se forme un dépôt d'évaporite ? Pour répondre à cette question, nous avons choisi d'étudier un site unique, le bassin de la mer Morte où des dépôts d'halite se sont déposés en couches annuelles (varves) pendant les périodes interglaciaires (stades isotopiques marins ; MIS 7 et MIS 5e). Un forage ICDP effectué en 2011 au centre de la Mer Morte a permis d'avoir accès à cette séquence sédimentaire qui couvre les 200 derniers ka. Pour les deux intervalles interglaciaires, les mesures de BS sur les FI d'halite révèlent une différence de température maximales de 4 °C entre la base et le sommet de chaque varve. Les paléotempératures de la section d'halite la plus ancienne (environ 200 ka ; MIS 7) soulignent en outre un réchauffement décennal des eaux du fond du lac pendant les périodes estivales (+3 °C) et hivernales (+4 °C). De plus, pour tous les dépôts d'halite nous observons des fluctuations annuelles de la température du lac en hiver. Pour les dépôts estivales les températures sont restées constantes pendant 6 ans suivies de variations annuelles jusqu'à la fin du dépôt d'halite. Nous montrons qu'il existe un lien possible entre l'épaisseur des varves et les températures estivales de l'eau. **Ces résultats majeurs ont des implications sur les futures études des séquences halitiques à des échelles de temps et d'espace plus grandes.**

La question subsidiaire à laquelle j'ai tenté de répondre au cours de ma thèse est de savoir si la BS peut être appliquée à d'autres minéraux présents dans les séquences évaporitiques, comme le gypse. Des expériences ont été menées en utilisant l'analyse BS sur des solutions capillaires avec différentes concentrations de NaCl ainsi que sur du gypse synthétique. Cette méthode a également été appliquée à des échantillons de gypse naturel provenant d'environnements hyper salins tels qu'une sebkha tunisienne, la mer d'Aral et des dépôts Messiniens dans le domaine méditerranéen. Si les températures de piégeage du gypse synthétique obtenus avec la BS reproduisent à peine les valeurs attendues en revanche les données sur des échantillons de naturels sont encourageant et suggèrent que le gypse naturel est un bon candidat pour les reconstructions de paleotempératures à l'aide de la BS.

Le développement méthodologique sur le gypse à permit de mettre en évidence la sensibilité de la vitesse du son par rapport à la salinité de la solution, faisant de la spectroscopie Brillouin un outil prometteur pour les futures reconstructions de paléosalinité.

Mots clés: *Spectroscopie Brillouin*, *Évaporites*, *Gypse*, *Mer morte*, *Vitesse du son Reconstructions paléoclimatiques*

ACKNOWLEDGEMENT

I am grateful to be part of the Make Our Planet Great Again program by Campus France, and for the financial support for more than three years. Furthermore, I wish to express my sincere thanks to the University of Lyon 1, the Institute of Light and Matter, the Doctoral School, and to our team 'Liquides et Interfaces' for all pandemic-related extensions obtained (especially Emmanuel Martelat for his approval to extend the contract once again, and all other team members).

I would like to thank all the jury members for their willingness to review and evaluate this work.

I express my sincere thanks to my two supervisors Véronique Gardien and Frédéric Caupin for their support in difficult times, for their patience, for their time spent on administrative and experimental issues, as well for all the nice moments we shared together apart the institute. Not a month went by without a problem to solve, but we handled it pretty well collectively as a group. I am proud to have worked with you!

I have appreciated the great help in private and professional matters by Daniel Ariztegui and Philippe Sorrel, who provided me with moral support and encouragement whenever required, for providing samples from Lake Petén Itzá and the Aral Sea, and for their scientific advice to publish my first article. This project could not have been realized without Hedi Oberhänsli, Peter Zavialov, Francesco Dela Pierre and Marcello Natalicchio, and Markus Schwab, who provided valuable sampling material to be studied during the last three years. Thank you very much to all of you!

Furthermore, I thank Giovanni Aloisi and all members of SaltGiant, as well as the colleagues from Palermo for organising and inviting me for the amazing field trip to Sicily in 2019.

Furthermore, I thank Thierry Alboussière for his help, time, and patience with tax issues, and Jean Colombani for providing the gypsum powder, without which much

of this work could not have been realised. Special thanks to Emanuel Guillerm for the intensive training phase on the instruments, his constant assistance and help to deal with scientific problems, and for introducing me to the Dead Sea subject.

Thanks to Olivier for the blind trust in the beginning and the exciting time in Craponne (greetings to Julien, Maxime and Misca). Thanks to Marie, with whom I spent most of my time with a wide variety of (quirky) personalities, and who showed me many beautiful places in France.

The time in Lyon was also marked by short but intense encounters (greetings to Amanda, Cecilia and Massimo, Marion, and all former flatmates), as well as beautiful moments among fellow countrymen (Theo, Johannes and especially Anne, our visits to the pub together were always great, and thanks for showing me the good taste of IPA beers). I thank Chenglong Ge for exciting Mölki games and for showing me chicken paws and delicious Chinese 'wine'. A shout out goes to Wiem, my fellow sufferer in the lab, our lunch breaks and Wizard games were always a great distraction to me.

I couldn't have completed this work without my great friends from the office who provided many bright spots away from university. Thanks to Team Mont Blanc for numerous video game nights, mineral exhibitions, hikes, football sessions, etc (Antoine and Raphaël), and to Laëtitia who became my closest friend here. You were there for me all the time, in funny and bad moments, which was immensely important to me. I will miss you, our funny conversations in the office, and our activities around Lyon.

I thank my parents Sabine and Peter, Stefan, Gerda, Kerstin, and Luca, for their mental and financial support when things got tight; Max, Nils, Alek and Jan for their their constant encouragement and moral support. Love you guys!

Lyon

Date: 25/04/2022 **Niels Brall**

Contents

List of Figures

List of Tables

LIST OF TERMS AND ABBREVIATIONS

b Molality (mol/kg)

BS Brillouin spectroscopy

CI Confidence interval to estimate the range of values that likely include the unknown mean of a sample population; here always referred to 95% with Z = ±1.96; thus the margin of error is 1.96 times the standard error of the mean

CO Coarse coarse halite; grain sizes typically >1000 µm

CU Cumulate coarse halite; grain sizes typically <500 µm

$CaSO_4$*2H_2O Chemical formula of the sulfate mineral gypsum

Δd_{abs} Absolute thickness of coarse or cumulate halite layers (cm)

Δf_B Frequency shift between incoming and scattered laser beam by using Brillouin spectroscopy

$\Delta T_{cooling}$ Difference in T_x between CO-TOP and overlying CO-BOT samples, representing the seasonal transition from summer to winter

ΔT_P Constant accounting for hydrostatic pressure on fluid inclusions; applied on T_x values when estimates are available for the palaeo water depth

$\Delta T_{warming}$ Difference in T_x between CO-BOT and overlying CO-TOP samples, representing the seasonal transition from winter to summer

ΔV_i Thickness of relative varves along coarse-cumulate halite layers by using the documented core section depth (cm) with i = top or bot

DS Dead Sea

DSB Dead Sea basin

DSDDP Dead Sea Deep Drilling Program

FI(s) Fluid inclusion(s)

FI_{ref} Reference fluid inclusion, measured every two hours while using BS. It is used to correct for the daily instrumental drift

FIA Fluid inclusion assemblage

FIB Fluid inclusion band

I_{low} Lowermost interval in core section 176-2 from 445.695 to 445.423 m blf (CO13-BOT to CO8-TOP); based on constantly low T_x values

I_{cen} Central interval in core section 176-2 from 445.37 to 445.255 m blf (CO7-BOT to CO4-BOT); based on the onset of stable seasonality

I_{upp} Uppermost interval in core section 176-2 from 445.09 to 445.24 m blf (CO1-TOP until CO4-TOP; based on maximum T_x values

IRF Instrumental resolution function; used as a constant parameter of the Brillouin spectroscope

ka / kyr Kilo years; or 1,000 years

Lmax Local temperature maxima along coarse halite layers in core section 176-2

Lmin Local temperature minima along coarse halite layers in core section 176-2

M Molar mass (g/mol)

Ma Million years; or 1,000,000 years

MIS 5e Marine Isotope Stage 5e (ca 130,000 - 116,000 years ago); last interglacial

MIS 7c Marine Isotope Stage 7c (ca 220,000 - 190,000 years ago); interglacial

MSC Messinian Salinity Crisis

m blf Sediment core depth (meters below lake floor)

N Number of analysed fluid inclusions or (sub)-samples

N.A. Not determined

NaCl Chemical formula of the salt mineral halite

S Salinity (weight % NaCl)

SD Standard deviation calculated for a sample population

SE Standard error of the mean calculated from the standard deviation

SLVE / LVE Solid-liquid-vapor-equilibrium; term to describe data derived from biphasic FIs

T Temperature (°C)

$\mathbf{T}_e$ Eutectic temperature; first melting point of ice crystals in a FI (°C)

$\mathbf{T}_h$ Homogenisation temperature of FIs: disappearance of vapor bubble (°C)

$\mathbf{T}_x$ Initial crossing temperature of single FIs by isochore and LVE (°C)

$\mathbf{T}_x$ **mean** Average of analysed FIs which are trapped in a sub-sample (°C)

$\mathbf{T}_f$ Pressure-corrected entrapment temperature of FIs by adapting a constant on T_x (°C)

$\mathbf{T}_{ice}$ Ice melting temperature; last point of melting of ice crystals in a FI (°C)

w Sound velocity (m/s)

Chapter 1

Introduction

1.1 Historical background of palaeoclimate research

Our modern understanding of complex interrelationships in the atmospheric Earth system is fundamentally shaped by multidisciplinary methods in geosciences. From the first insights into the four principles of stratigraphy and the detection of crystallographic structures in minerals by Nicolaus Steno in 1669, it took more than three centuries to develop climate models of the past and future. The study of past climate conditions on Earth's surface is one of the major keys to understand modern and anticipate future global climate conditions, as illustrated by the essential sentence "the present is the key to the past". It is related to the first findings of modern geology in the 18th and 19th century by James Hutton and 42 years later by Charles Lyell (Lyell and Deshayes, 1830). Hutton was one of the major drivers of modern geology in the 18th century, because he hypothesised that sediments at the Earth surface must be much older than previously thought. Further, he developed the pioneering concept of "uniformitarianism" that assumes quite the same natural laws and principles prevailing today and in the past, thus, being responsible for the formation of geological units (Hutton, 1788; Hutton, 1795). After Hutton's death in 1797, it was Charles Lyell who published three volumes of "Principles of Geology" (1830-1833) in which he defined for the first time the Tertiary period, and more importantly, his ideas about the origin of glaciers and moraines (Lyell, 1837). Around at the same time, similar observations were made by Louis Agassiz with the outcome of his glaciation theory (Agassiz, 1840; Flint, 1968), which convinced also the famous geologist William Buckland who had already described glacial traces in Scotland many years before (Buckland, 1824).
It was Svante Arrhenius, a physical chemist from Sweden, who mathematically calculated the effect of atmospheric carbon dioxide (CO_2) concentrations on global temperatures in 1896. Based on his calculations, he pointed out that the global climate should rather move towards decreasing global temperatures to end up in a new ice age (Arrhenius, 1896). Afterwards, the presence of periodic orbital variations was described mathematically in terms of the rotation of the earth axis ("precession"; 23,000 years), the degree of the Earth's spin axis ("obliquity"; 41,000 years), and the Earth's distance to the sun ("eccentricity"; 120,000 years) by Milankovitch, 1930. This had led to the hypothesis that the Earth's climate varied over time in the past, controlled by the amount of incoming solar radiation. The discovery of stable isotopes (Thomson, 1912) with the development of the first mass spectrometer by Aston (1920) opened a new world in particular for geoscientists later.
Another pioneering work was done by Giaque and Johnston who measured different masses of oxygen atoms apart from the known mass of 16 which was the discovery

of oxygen isotopes ^{17}O and ^{18}O (Giauque and Johnston, 1929a; Giauque and Johnston, 1929b). Oxygen isotopic analysis (δ^{18}O) of minerals is still by far the most widely used proxy in palaeoenvironmental studies. Probably as important as oxygen was the discovery of the heavy isotope hydrogen 'deuterium' with ^{2}H (Urey and Teal, 1935). After WWII, the techniques developed for previously military purposes were widely released for civilian and scientific use. For example, Harold Urey, being involved in the Manhattan Project to participate in building the nuclear bomb, focused during the post-war period on the extension of oxygen isotopes to geological studies. He reported the mass-dependent fractionation processes of isotopes and particularly between carbonates and water (Urey, 1947), further he provided the first evidence for a temperature-dependency of δ^{18}O based on Cretaceous calcareous fossils (Urey, 1948; Urey et al., 1951). At the same time, the first linear palaeotemperature scale for inorganic carbonates has been proposed by McCrea (1950), including both the temperature T in °C and the oxygen composition Δ^{18}O in ‰:

$$T = 18 - 5.4 * \Delta^{18}O \tag{1.1}$$

Two years later, a palaeothermometer for marine organic carbonates was published based on both, laboratory-grown (lab-grown) organically precipitated carbonate species and collected marine calcareous shells, with the isotopic composition reported in δ^{18}O (Epstein et al., 1951):

$$T = 11.88 - 5.91 * \delta^{18}O \tag{1.2}$$

Two years later, this equation had to be revised because organic matter from shells has influenced the previous isotopic analyses (Epstein et al., 1953):

$$T = 16.5 - 4.3 * \delta^{18}O + 0.14 * \delta^{18}O \tag{1.3}$$

Furthermore, there were indications of a weak linear relationship between the salinity (ranging from 33 to 38 ‰) and the abundance of the heavier oxygen isotope ^{18}O in water samples (Epstein et al., 1951).
These fundamental works have led Cesare Emiliani, an Italian micropalaeontologist working in Urey's geochemistry lab' in Chicago, to analyse benthic foraminifera (single-celled marine organisms with calcareous shells). First, material obtained from pacific bore cores was used to determine the oxygen isotopic composition to reconstruct ocean bottom water temperatures in four samples from the Oligocene (Emiliani and Edwards, 1953), continued by a long-term Pleistocene reconstruction covering the last 290 ka with the definition of isotope stages and the observation of fluctuating marine temperatures using 1.3 (Emiliani, 1955; Emiliani, 1961; Emiliani,

1970). Emiliani should became one of the pioneer of modern palaeooceanography, especially in view of his results, showing cyclical variations during the Pleistocene similar to the mathematical predictions by Milankovitch in 1930. It is worth noting that, once again, the outcome of scientific cooperation among interdisciplinary fields ('crosscutting concept') enabled the geological importance of Emiliani's work (among others), by the discovery of the radiocarbon dating method (^{14}C) (Libby et al., 1949). However, ^{14}C dating is limited in geological timescales to ca 50 ka due to its short half-life of ^{14}C (5730 $\pm$40 years; Godwin, 1962).

Therefore, and due to the immense technological advances, various 'absolute' dating methods have been developed (e.g., U-Th, U-U, U-Pb, Rb-Sr, K-Ar, etc.) besides 'relative' dating methods (biostratigraphy, Marine Isotope Stages, tephrochronology, palaeomagmatism, etc.). For instance, palaeoclimatic events during the last five million years could be assigned to magnetic reversals based on palaeomagnetism which had also broad implications for the community and the understanding of Earth's climate (Hays and Opdyke, 1967; A. Cox et al., 1964). Shortly afterwards, Shackleton, 1969 revisited the findings of Emiliani, 1961 for the last interglacial warming period (ca 130 - 80 ka) and introduced isotopic sub-stages for Marine Isotope Stage 5 (MIS; a, b, c, d, e). However, the exact cause of Earth's temperature variations during MIS 5 remained ambiguous because the observed temperature rises/drops in the records were asymmetric (Shackleton, 1969).

Finally, a study dealing with marine cores in the Southern Hemisphere impressively proved the connection between orbital variations, as predicted by Milankovitch, and the occurrence of global ice ages in the geological record (Hays et al., 1976). Another major outcome of this study was a model predicting a long-term Northern Hemispheric glaciation over the next several thousand years **without anthropogenic effects** (Hays et al., 1976).

After the first discovery of related increased atmospheric CO_2 concentrations and rising global temperatures in the late 1930's (Callendar, 1938), the 1980's then were marked by a rapid global temperature rise, and further studies pointed out the dramatic impact of atmospheric CO_2 concentrations on global temperatures and rising sea-levels due to polar ice melting (e.g., Hansen et al., 1981; Gornitz et al., 1982). A study reported variations in atmospheric CO_2 concentrations from the Vostok ice core, Antarctica, for the past 160 ka (Barnola et al., 1987). Although it showed that such variations are linked to interglacial-glacial climate states, it also revealed that atmospheric CO_2 concentrations have never been such high than in the 1980's (338-350 ppm from 1980-1989). In 1989, the Intergovernmental Panel on Climate Change (IPCC) was founded to get a scientific-based global state of the Earth' climate by combining numerous scientific disciplines. Since then

six assessment reports have been published in 1990, 1995, 2001, 2007, 2014, and 2022, all of them generally have increased the warnings towards drastic changes not only in climate and extinction of species, but also on inhabitable regions for humans. Modern climate change is also termed 'global warming' because it takes into account the mean global atmospheric temperature rise relative to the pre-industrial period (1850), but in fact this temperature rise does not affect all regions equally (IPCC, 2022). The latest report by IPCC (2022) has once again revelead that future mean temperatures will rise more at higher latitudes at the poles than at lower latitudes, but that regions at lower latitudes are not equally affected due to non-linear responses of complex oceanic/atmospheric circulation patterns. Moreover, reconstructed CO_2 over the past three million years suggested that 'by 2024/2025 levels of atmospheric CO2 will be higher than any point in the last 3.3 million years' (De La Vega et al., 2020).

Therefore, palaeoclimate studies by using geological records and proxy methods are still essential to provide detailed data sets from remote regions where monitoring data are missing. Although an extensive database is already available, there is still a substantial need for additional proxy methods to better investigate specific climate archives. This in turn supports climate models to predict future changes of important climatic parameters such as temperature or salinity.

The main limitation of terrestrial palaeoclimate research is, however, the lack of accessible, suitable, continuous, and/or datable climate archives and proxies. Nevertheless, the most powerful method is to combine data sets obtained from multiple proxy methods for models (Lelieveld et al., 2012). Evaporitic minerals, for example, are commonly present in arid environmental regions where other climate archives are absent, which makes them a potential gap filler for specific dry periods of the Earth history.

1.2 Climate archives: Evaporites

Commonly, chemical salty minerals that form (sub)aqueously in arid or semi-arid climate settings under solar-driven evaporation processes from a water body are defined as "evaporites" and make up a group of 60 major minerals (Warren, 2016). Evaporites form in marine, continental (including lakes, caves), and coastal environments. The (sea)water chemistry (i.e., ion composition) controls which evaporitic mineral forms with respect to the prevailing supersaturation state of each mineral (Warren, 2016). The composition of seawater is fairly homogeneous worldwide, with small anomalies (e.g., in the eastern Mediterranean), affecting the order of mineral precipitation due to solubility in **marine environments**:

- 1. Carbonates
- 2. Gypsum
- 3. Halite
- 4. Potash minerals

The chemical composition of water bodies in continental regions depends mainly on regional geology, water balance, or even microbacterial activity, which makes it mostly very different from seawater. This also changes the order of the first forming minerals in **nonmarine environments**:

- 1. Carbonates
- 2. Gypsum
- 3. $NaSO_4$, $NaCO_3$, $MgSO_4$
- 4. $MgCl_2$, $CaCl_2$
- 5. NaCl

Both lists represent the most common evaporitic sequences from the sediment record and modern observations (Warren, 2016), but it might differ in hyperarid regions with unique water chemistries (e.g., Dead Sea).
Main groups of evaporites are constituted by the major cations on Earth's surface, e.g., Ca^{2+}, Mg^{2+}, K^{+}, Na^{+}, $Fe^{2}+$ or $Sr^{2}+$, forming molecules by mainly covalent or ionic bounds with anion-complexes, e.g., ${CO_3}^{2-}$ (carbonate group), ${SO_4}^{2-}$ (sulfate group), or Cl^{-} (chloride group) (Holser, 1979). Therefore, evaporites are quite diverse by incorporating either two (e.g., NaCl, "halite"), three (e.g., $CaSO_4$, "anhydrite"), four (e.g., $Mg_3B_7O_{13} \cdot Cl$, "boracite") or even five elements (e.g.,

$NaCaB_5O_9 \cdot 5\,H_2O$, "proberite"). However, despite the diversity, the dominating minerals are carbonates, sulphates, and salts. In most cases, their timing of formation depends on the degree of supersaturation with respect to a particular salty mineral (Warren, 2016). The supersaturation depends on the solubility of an individual mineral and thus the nucleation starts for each mineral differently according to the amount of evaporated water molecules of a water body. For example, the solubility of NaCl in 1 L of water is 360 g at 25 °C (Haynes et al., 2017), so that the first NaCl crystal precipitates at a concentration >360 g/L. On the contrary, the sulphate mineral gypsum ($CaSO_4 \cdot 2\,H_2O$) has an extremely low solubility of 2.4 g/L at 25 °C (International Labour Organization, n.d.), defining a narrow range of possible amounts of dissolved/precipitated gypsum of a brine. With an increase in (elemental) concentration of any solution, brine, or water body, the heat capacity decreases whereas the density increases (Warren, 2016).
Other processes than solar-driven evaporation to precipitate evaporites can involve biological processes or temperatures close to negative. For example, cryogenic salts like mirabilite (Nelson and Thompson, 1954), hydrohalite (Drebushchak et al., 2019), antarcticite (Kimura and Kai, 1984), and epsomite form at temperatures close to or below the freezing point of the liquid phase (Warren, 2016).
Both the temporal and spatial local distribution of evaporites are neither limited to space nor time in Earth history. The oldest evaporitic sequences have been reported from the Onega Basia, Russia, and dated to the Paleoproterozoic Era, that is, 2 billion years ago (Blättler et al., 2018). Further studies confirmed the occurrence of evaporites during the Proterozoic (Spear et al., 2014; Lindsay, 1987; Kah et al., 2001). Besides the marine realm being a major accommodation space for carbonates, sulphates, and salts, they also form in caves, in saline pans, coastal environments, sabkhas, deserts, and in lakes.
Therefore, non-altered evaporites are potentially excellent climate archives that can be used for specific geological periods.

1.2.1 Halite

Being part of the chlorides group, the mineral 'halite' (or 'rock salt') is composed of sodium chloride (NaCl) and is assigned to the isometric crystal system, thus, NaCl crystals are cube-shaped (a = 5.64 Å, $\alpha = 90°$) (Figure 1.1). Commonly halite formation is associated with evaporitic environments in dry and/or semi-arid to arid climate zones in which solar radiation enriches a saline brine in its Na^+ and Cl^- concentrations by removal of H_2O. However, an alternative NaCl nucleation pathway has been recently proposed based on serpentinization processes (Debure et al., 2019. Further, NaCl solubility in water increases with temperature, so that NaCl nucleation takes place even by local cooling of the parent water body (Pinho

and Macedo, 1996).

NaCl is globally distributed over time and space, and its suitability for palaeoclimate studies has been already reported for several locations (e.g., Lowenstein et al., 1999; Kiro et al., 2016; Schubel and Lowenstein, 1997; Hardie and Lowenstein, 2004). Another benefit for experimental work is its high solubility (360 g/L), which allows to produce a vast amount of material in a day or two with a sufficiently amount of trapped fluid inclusions (Figure 1.1 B) (Rigaudier et al., 2012). Further it was shown that the composition of stable isotopes of both oxygen and hydrogen of extracted FIs can be used as a proxy for isotopic trajectories of water evaporation, and to estimate temperature and wind velocity (Rigaudier et al., 2011). As pointed out later in this work in more detail, this early work on salty inclusions in NaCl has paved the way for extended palaeoclimatic applications of salt. Data obtained from material from the Dead Sea basin provided evidence for accurate temperature reconstructions using Brillouin Spectroscopy for progressive studies (Guillerm, 2019; Guillerm et al., 2020; Brall et al., 2022).

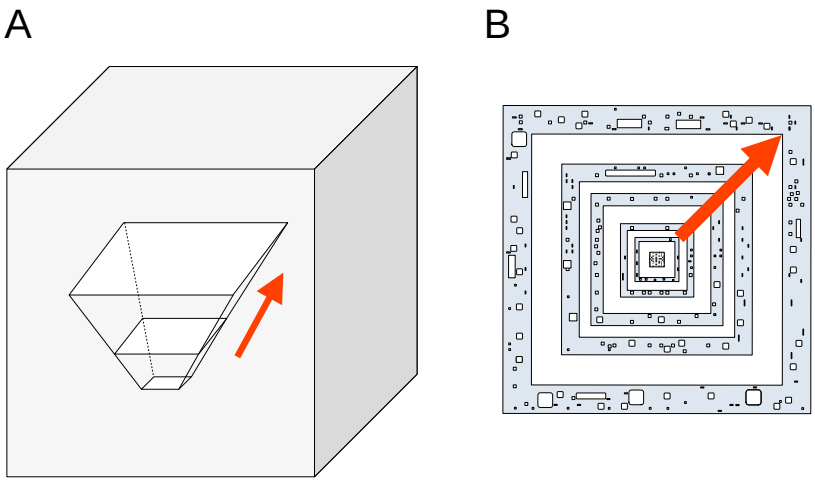

Figure 1.1 A) 3D Sketch showing the principal growth of halite. A centered nucleus serves as starting point, followed by planar and diagonal growth along the edges. B) Top view on halite growth zones with trapped fluid inclusions. Red arrow marks the highest growth rates along the edges. Not to scale.

1.2.2 Gypsum

The mineral gypsum is a member of the calcium sulfate group ($CaSO_4$) which holds in its crystal lattice up to 20% H_2O as molecular water ('crystal water'). The crystal system is monoclinic (a = 5.67 Å, b = 15.15 Å, c = 6.28 Å, and $\beta = 113°50'$; Aronson et al., 1983). Gypsum is the most abundant sulfate mineral on Earth's surface and an important industrial product. The stability of gypsum is limited to less than 42 °C, a threshold above which it starts slowly to dehydrate to the hemihydrate form ('bassanite'). However, as time is relative, the actual transformation takes place at higher temperatures of >70-90 °C. After complete dehydration it transforms further into anhydrite with a change into the orthorhombic crystal system (Figure 1.2). However, the inverse is possible by re-hydrating anhydrite, and to re-transform back into the stable gypsum phase. Hence, natural geological gypsum records that have been exposed on Earth's surface could have suffered from several transformation processes after deposition.

The abiotic growth mechanisms of gypsum minerals have long been undetermined due to the complexity of incorporated ions into the molecular crystal structure. Based on in-situ observations in nucleation experiments of calcium sulfate crystals (e.g., He et al., 2018; Van Driessche et al., 2012), a more complex and non-universal nucleation pathway has been stated (Van Driessche et al., 2019).

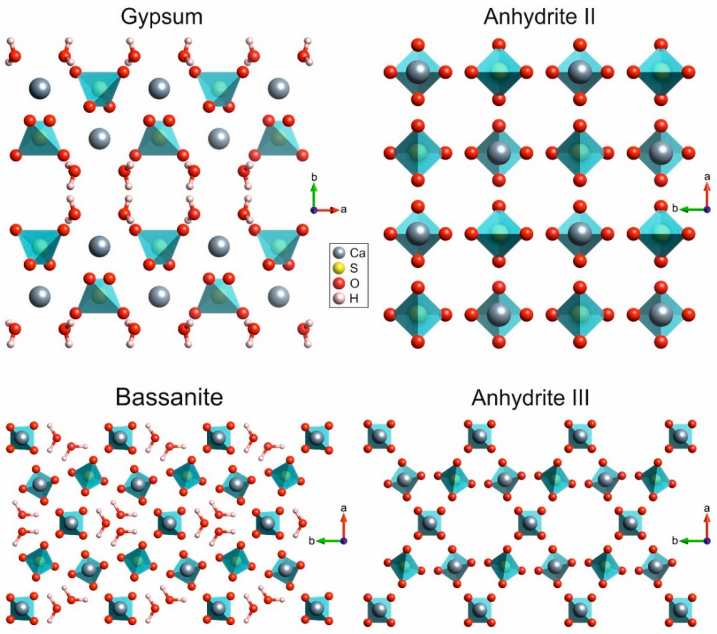

Figure 1.2 Calcium sulfate minerals, in monoclinic crystal system and molecular water (reduced water) in gypsum (bassanite), and in the orthorhombic system after dehydration (anhydrite II, III) (from Schmid et al., 2020).

1.3 Fluid inclusions

While a crystal nucleates from a supersaturated brine, solution, or fluid, crystal defects in the lattice are filled by the surrounding supersaturated liquid or gas, leading to local cavities. The occurrence of local cavities in solid crystals is known for approximately 230 years since the first observation of petroleum-filled cavities in quartz (Dolomieu, 1792). The first detailed description of such inclusions ("fluid inclusions"; FIs), has been published for a variety of minerals with the important suggestion that probably all crystals contain liquid cavities (Brewster, 1823). Further, it was then Sorby, 1858 who expanded the scientific knowledge about fluid inclusions, e.g. by categorising quantitatively their sizes that can be still seen as valid today: calculated from his sizes in inches, his scale ranged from <2.5 µm (very small), ≤25.4 µm (moderately small), ≤254 µm (moderately large), to more than 254 µm (very large). During this thesis, the relative fluid inclusion size categories will be defined as very small (<2 µm), small (2-5 µm), intermediate (5-15 µm), and large (>15 µm).

Trapped fluid inclusions are often mimicking the crystal system of its host mineral by negative shapes. For example, FIs in a cubic NaCl crystal are themselves cubic-shaped (Figure 1.3 A, although other forms can also occur, e.g. as rectangular-elongated forms (Figure 1.3 B). FIs that have been trapped during crystal growth in a specific layer at similar depth, aligned along crystal growth zones, are termed 'Fluid inclusions assemblages' (FIA) (Roedder, 1984). Due to the large complexity of numerous varieties of FIs in minerals at the Earth's surface, in the crust or mantle, this thesis will be only focussing on NaCl ('halite') and $CaSO_4 \cdot 2\,H_2O$ ('gypsum') minerals. For detailed information about analysis, studies, occurrences, or pitfalls, the reader is referred to Roedder (1984), Samson et al. (2003), or Fall and Bodnar (2018).

Pristine or primary FIs (non-altered) are trapped as monophasic liquids at the Earth subsurface at ambient pressure (e.g., minerals forming in arid sabkhas, salt pans, or in the upper water layer in lakes) or at higher pressure (e.g., in metamorphic zones, or deeper water layer in lakes). Owing to major improvements in analytical techniques in the 20th century, studies of minerals containing FIs have been widely extended since the 1960's (e.g., Roedder, 1962; Roedder, 1963). The main benefit to study FIs is their phase behaviour with changing pressure and temperature, which allows to determine the relative elemental compositions (Roedder, 1972). Moreover, the usage of microthermometry to determine maximum homogenisation temperatures (T_h), at which the vapor bubble of a two phase FI (liquid+vapor) vanishes, has been considered as a reliable tool to identify crystal formation temperatures in halite (Lowenstein et al., 1999. Fall and Bodnar (2018) defined a

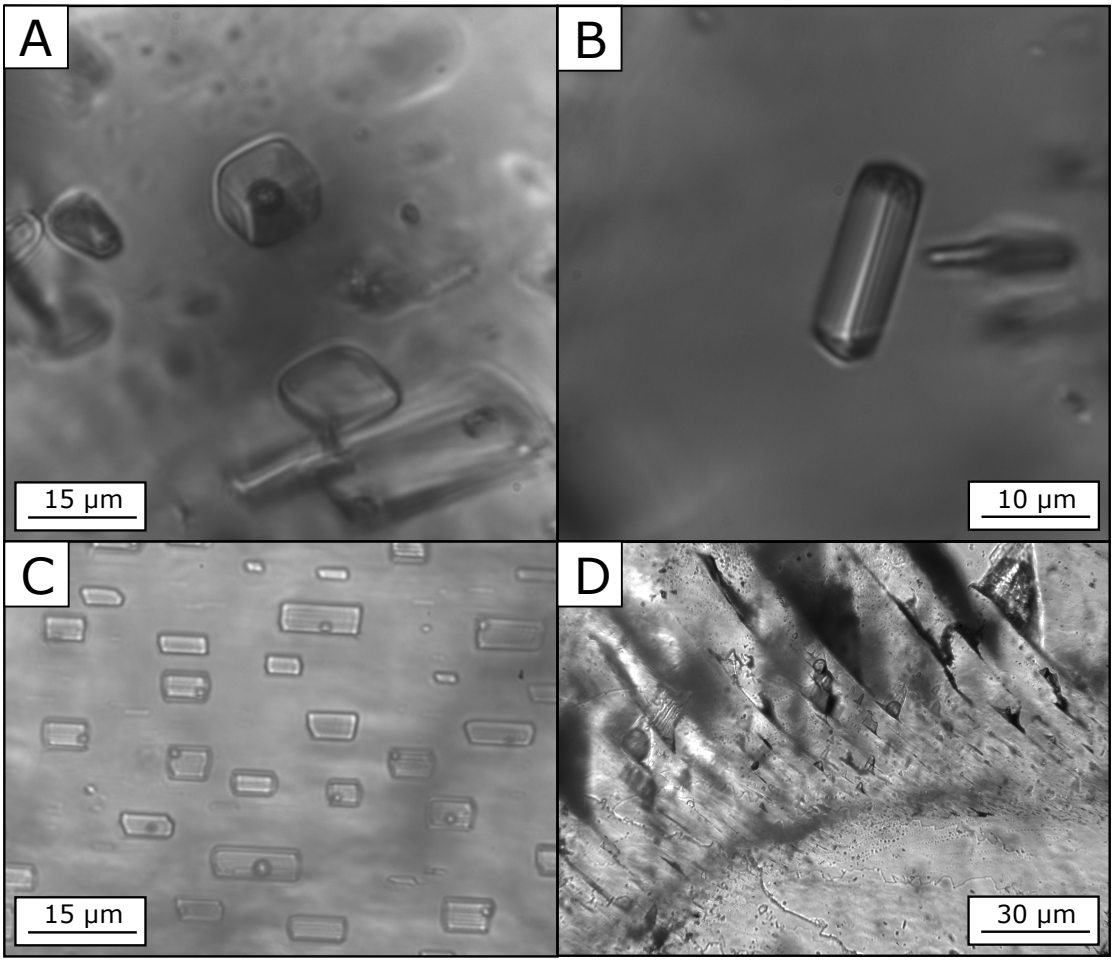

Figure 1.3 Common shapes of fluid inclusions in minerals of halite (A, B) and gypsum (C, D). Note that three-dimensional images of FIs as in A-B images are scarce. Top-view as C) with monoclinic negative crystal shapes are usual. FIs can even be trapped along growth bands, as shown in gypsum from Sicily (D; Sample provided by M. Natalicchio). Many thanks to W. Ben Aissa for providing the images in A-B.

range combined with median T_h data to precisely describe palaeotemperatures in minerals from different environments.

Further studies applied FIs as a palaeoenvironmental archive to diverse geological records, e.g., the occurrence of living halobacteria in FIs (Norton and Grant, 1988), crystal formation temperatures (Lowenstein et al., 1999; Guillerm, 2019), hydrothermal ore deposits (Wilkinson, 2001), the composition of FIs (Burke, 2001), DNA extraction from FIs that showed long-living cycles of halophilic archaea and bacteria in Dead Sea sediments (Thomas and Ariztegui, 2019), or δ^{18}O variations in speleothem FIs (Griffiths et al., 2010).

1.4 Temperature proxy in this work

Despite decades of research in the field of geosciences (including palaeoclimate research), fundamental misconceptions about climate archives and climate proxies can still be found in many media and publications. A climate archive serves as material with physical, chemical, or biological properties which can be both quantitatively and qualitatively analyzed and measured by instruments, and thus providing information about past environmental conditions of a sample specimen (Jones and Mann, 2004). A climate proxy is both measurable and calibrated against an instrumental standard. Climate archives are solids (minerals, rocks, or layers) and are comparable to a computer hardware: tree rings, speleothems, ice cores, ocean sediments, lake sediments, and in more detail, (a)biogenic carbonates, quartz veins, or evaporites. On the other hand, climate proxies are like the "software" of a solid system by describing (and explaining) the nature of the solid, and by defining its environmental formation conditions. Hence, fluid inclusions are here defined as the 'internal' climate archive, whereas the host mineral would be the 'external' archive. The derived property of FIs, here the temperature, is thus the climate proxy.

Analytical capabilities in the natural sciences have expanded rapidly since the technological advances of the 20th century, allowing a range of global climate archives to be studied. Hence, marine climate archives have been increasingly used to reconstruct paleoclimate. Although such oceanic bore cores are costly, they are available virtually everywhere, and they also cover the climate history of several million years. However, since continental archives are also important for understanding complex atmospheric processes and are both far less expensive and easier to sample, various temperature proxies, among others, have been developed. A frequent problem in continental archives such as caves, tree rings, lakes, fluvial sediments, cores, or outcrops, are among others erosion, limited temporal resolution, or the lack of directly measurable temperature proxies.

Huge advances during the past two decades have been reported for carbonates in temperature reconstructions using clumped isotope thermometry. This method, an extension of the classical isotope mass spectrometry, benefits from the "clumping" effect of relatively heavier isotopes ^{13}C and ^{18}O when $CaCO_3$ precipitates in (sub)aquatic solutions (Eiler, 2007; Eiler, 2011). The formation of heavier isotope bounding is directly related to temperature, and most important, not dependent on the oxygen isotope composition of the parent water. Hence, this technique circumvents the long-term issue of unknown palaeo-seawater oxygen compositions when applying the classical stable isotope method ($\delta^{13}C$; δ^{18}). The applicability of clumped isotopes has been shown on various carbonate species from nearly all

environments, e.g., caves (Affek et al., 2008), travertines and tufa (Kele et al., 2015), or soils (Kelson et al., 2020).

However, even such a seemingly impeccable technique has its limitations, because continental carbonates do not form everywhere and at all times, for example in lakes only under certain conditions with low sedimentation rates. Evaporites, on the other hand, fill this gap, at least in saline lakes, so that distinct periods could be reconstructed paleoclimatically for specific regions such as the Dead Sea or arid sabkhas.

A common tool to reconstruct palaeotemperatures in evaporites has long been the microthermometry method that is based on the observation of the timing when a vapor bubble disappears ('homogenizes'). It can be used to determine the salinity of samples, and thus is a well-established technique to obtain important information about the parent brine of the respective host mineral. It has been used in many geological domains, e.g., for pyrite (Kouzmanov et al., 2002), sulfides (Zaw et al., 2003), petroleum inclusions (Grimmer et al., 2003), pegmatites (Beurlen et al., 2001) and salts (Lowenstein et al., 1999).

However, there are few limitations towards low-temperature minerals that commonly form at the Earth's surface at low-pressure. Recent experiments in synthetically-produced halite FIs have shown a significant offset (ca 5 °C) to the known crystal growth temperatures (Guillerm, 2019; Lowenstein et al., 1999). Contrary to that, results obtained from a previously developed palaeothermometer (Brillouin spectroscopy, BS) gave evidence to overcome the relative large uncertainty by studies on pure water FIs in quartz (Mekki-Azouzi et al., 2015). The BS method has further been adapted in detail for natural NaCl samples, and offered insights into lake-level variations in the Dead Sea basin (Guillerm, 2019). However, there are potentially further studies dealing with sedimentary records from the Dead Sea possible, since the halite successions form an analogue to modern-day seasonal halite formation in the Dead Sea (Ben Dor et al., 2019; Sirota et al., 2017). Moreover, BS has never been tested on gypsum FIs in particular, which leaves a question unanswered if such abundant subsurface minerals might serve as an accurate climate archive when in combination with BS.

The major important advance of BS is the direct measurement of crossing temperatures derived from both monophasic and biphasic fluid inclusions along a controlled temperature-pressure path in the laboratory. It was shown that a small amount (ca 20 FIs per sample) suffices to measure accurately halite samples within a short period of time (Guillerm et al., 2020). Therefore, this approach has been extended to another evaporitic mineral, gypsum, and to seasonal halite layers from the Dead Sea basin. Since gypsum is not only a mineral but also a

common marine/ continental climate archive, the BS technique might help to reveal palaeoenvironmental conditions such as temperature for geological records.

1.5 History of salinity definitions

The term "salinity" aims to describe the "saltiness" of a water body or solution, and thus refers generally to the amount of dissolved ions in water. It has undergone various definitions throughout the past since its first definition (Forchhammer, 1865). Around two decades later, Dittmar et al. (1884) published first his findings of mainly constant seawater salt concentrations on a global scale. From 1900 on, "chlorinity" has been used as Primary Standard of seawater describe the salinity of a solution which has been defined "as the weight in grams of chlorides obtained in 1 kg of sea water" in parts per thousand (Cl‰), being proportional to the mass fraction of chlorine (Knudsen, 1901; Forch et al., 1902; Barnes, 1954). Knudsen (1901) defined empirically the relation between chlorinity and salinity S:

$$S‰ = 0.03 + 1.805 * Cl‰ \tag{1.4}$$

However, it is not possible to measure the salinity S of a sample analytically and directly, whereas this can be achieved for density and/or chlorinity (Millero et al., 2008). Decades after the first definition and calibration of the chlorinity standard, a new "Primary Standard" was established in 1937 due to a depletion of the former (Jacobsen and Knudsen, 1940; Culkin and Smed, 1979). This chlorinity standard has been calibrated against silver and was distributed in ampoules for laboratories (Culkin and Smed, 1979). Afterwards, additional salinity definitions have been introduced to express the amount of dissolved salts in seawater while assuming a nearly constant chemical composition of the oceans (Knudsen, 1903). For example, the electrical conductivity of seawater has been frequently used since the 1950s to account for both, chlorinity and salinity because a proportional relation of conductivity to chlorinity was found (R. Cox et al., 1967). It was defined as the conductivity ratio R_{15} of the measured electrical conductivity of a water sample to that of water with a salinity of exactly 35 ‰ (Wooster et al., 1969). It was calibrated by both chlorinity and R_{15} measurements on 135 natural seawater samples, converted into S by equation 1.4 and then fitted by a polynomial function (Wooster et al., 1969):

$$\begin{aligned} S‰ = &-0.08996 + 28.29720 * R_{15} + 12.80832 * R_{15}^2 \\ &-10.67869 * R_{15}^3 + 5.98624 * R_{15}^4 - 1.32311 * R_{15}^5 \end{aligned} \tag{1.5}$$

followed by the Practical Salinity Scale of 1978 (S_P; PSS-78) (UNESCO, 1981; Tyler et al., 2017) that soon after was integrated in the Equation of State for Seawater (EOS-80; Fofonoff, 1985).
The definition of S_P is based on "the conductivity ratio K_{15} which is the electrical conductivity of the sample at temperature t_{68} = 15 °C and pressure equal to one standard atmosphere (p = 0 dbar and Absolute Pressure P equal to 101 325 Pa), "divided by the conductivity of a standard potassium chloride (KCl) solution at the same temperature and pressure" (IOC, 2010). Importantly, and sometimes ignored, the Practical Salinity is unit-less, with $S_P = 35$ at $K_{15} = 1$ (IOC, 2010). A new standard has been proposed called "Reference Salinity S_R" that "represents accurately the Absolute Salinity S_A of an artificial seawater solution" (Millero et al., 2008). It is related to Practical Salinity S and can be seen "as an SI-based extension of Practical Salinity, as a reference for natural seawater composition anomalies", and as the currently best estimate for Absolute Salinity of IAPSO Standard Seawater (Millero et al., 2008). The conversion between S and Chlorinity Cl is $S = 1.80655{*}Cl$ [g/kg] for $2 < S < 42$ (Millero et al., 2008). Further, the authors found for S_R the relations to both S and Cl to be:

- $S_R \approx$ (35.16504/35) g/kg x S, and
- $S_R \approx$ (35.16504/35) x 1.80655 x $Cl \approx$ 1.815069 x Cl

Common pitfalls occurring in both, older and recent literature, by expressing non-uniformly the term "salinity". This is due to the various definitions described above, and the applied method to analyse water samples. For example, soil salinity results in the southern Aral Sea region have been reported consistently in dS/cm because the electrical conductivity was measured (Devkota et al., 2022). On the contrary, Aral Sea water samples were reported in g/kg and parts per thousand (ppt) in the same paper (Zavialov et al., 2009), and in g/L in an older study (Létolle and Chesterikoff, 1999). Another method is to analyse a water sample for its total dissolved solids (TDS; commonly in mg/L), a widespread salinity term that has been used to categorise the saltiness of large lakes of the world (Herdendorf, 1990): fresh (<2000 mg/L), brackish (2000-20000 mg/L), saline (20000-40000 mg/L), and hypersaline (>40000 mg/L). An other classical salinity unit is ppt, but also units in mol/kg, g/L or in weight percentage of NaCl (wt.% NaCl, or wt.‰NaCl) can still be found. Further, it is essential to pay attention to what the concentration of dissolved salts refers to:

- uniquely the volume of solvent in L or mL
- mass volume of the total solvent (solutes includes) in g or kg

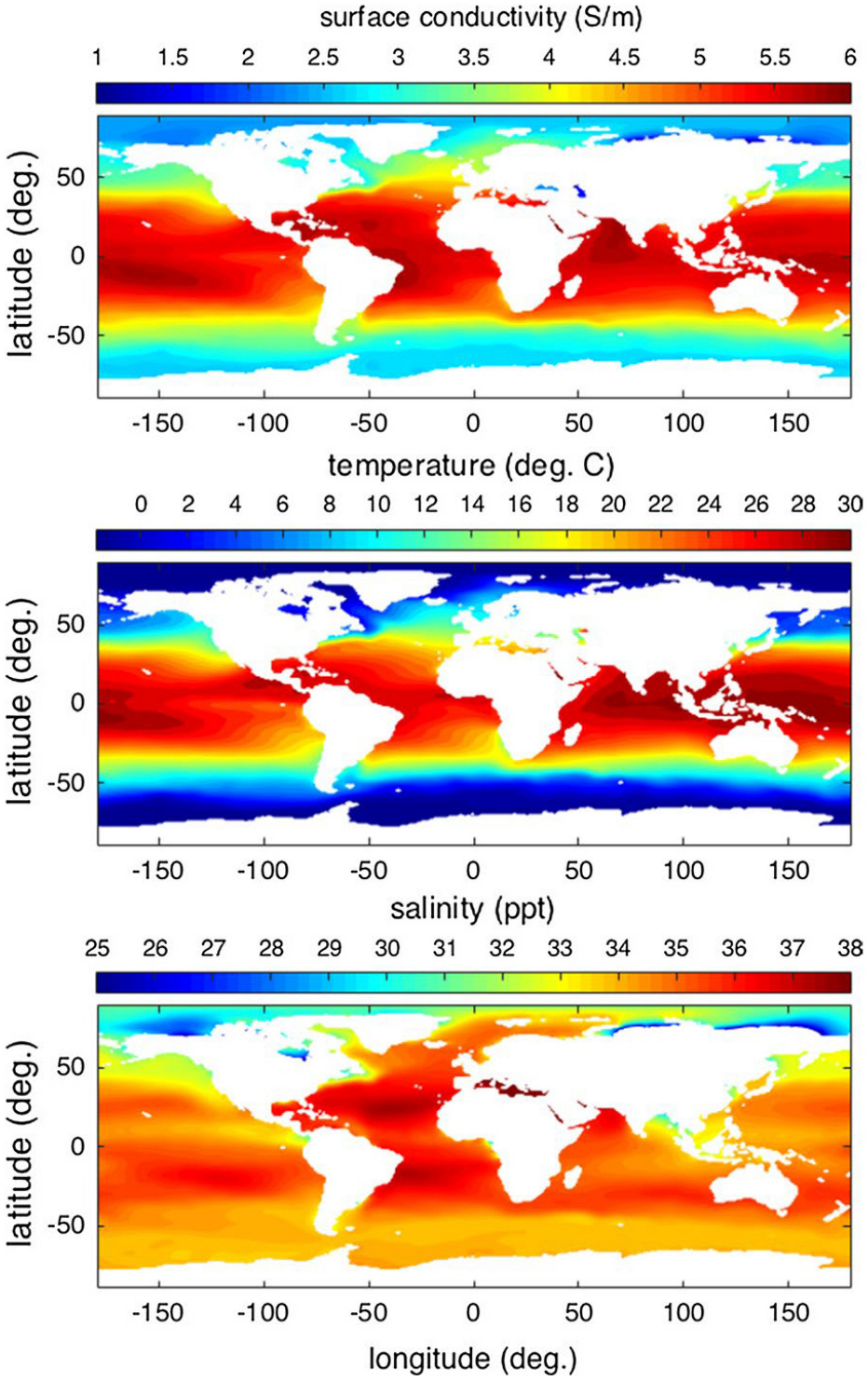

Figure 1.4 Relation between conductivity, temperature, and salinity in global ocean surfaces (from Tyler et al., 2017).

For example, if NaCl with a solubility of maximal 360 g/L is dissolved in 1 L of H_2O, it has a volume percentage of 36%, but a mass percentage of 360 g/(1000 g_{H_2O} + 360 g) x 100 = 26.47 weight % NaCl. Therefore, in fluid inclusions studies of geological interest, the traditional expression of salinity is reported in weight % NaCl (Bodnar, 1993). To present fluid inclusions data, the % scale can also be converted into the ‰ scale to increase the informative value of data (Bigi et al., 2022). It is important to note that the 'weight % NaCl' definition refers to the concentration of the ternary system Na-Cl-H_2O, while it does not refer to seawater salinity scales that had been adapted for complex solutions containing multiple ions.

This section aimed to introduce to the various salinity definitions that exist in the literature. The physical-chemical properties of conductivity, temperature, and salinity are strongly linked with each other, and might be used independently to get rough estimates about the two other properties (Figure 1.4). Therefore, the close relation between temperature and salinity, e.g. in oceans, provides the framework for using two proxy methods of geological records.

As previously mentioned, reported salinity values of water bodies and fluid inclusions are not on the same scale, and should always be treated with caution. The relative relationship between individual data in a sample or between sub-samples appears more important here than presenting absolute or exact values that would represent the exact concentration of TDS or Cl. Hence, the use of the same method during a geological salinity study would not affect the data validity in terms of relative salinity changes along a geological profile, a core section, a bedded interval or a single crystal.

1.6 Aim of the thesis

The last decades have shown a growing interest in past climate reconstructions within the scientific community, politicians and stakeholders. As a result, these reconstructions are now integrated in international initiatives such as the Intergovernmental Panel on Climate Change (IPCC) that is the United Nations body for assessing the science related to climate change. Marine and lake sediments, tree-rings, ice cores and speleothems, among others, are the most used archives for these reconstructions depending on their temporal and geographical settings. The integration of past data with modern instrumental data allows to better evaluate ongoing and eventually forecast future changes in climate. Attaining these ambitious goals, however, imply the development of suitable proxies that permit not only to identify but also to quantify the impact of climate in different geological archives. A climate proxy is a physical and/or chemical property that can be measured using various analytical techniques and approaches, surely responding to changes in environmental conditions. The measurement of sound velocity and entrapment temperatures in fluid inclusions from evaporitic minerals, such as halite and gypsum, using Brillouin Spectroscopy (BS) is a fine example of this approach and the highlight of this thesis. These data are further used as primary proxies to generate more robust and accurate climate reconstructions.

The first case study of this thesis focusses on halite fluid inclusions from the Dead Sea testing the use of BS to resolve seasonal temperature variations. The formation temperature of FIs in halite layers throughout annual depositional cycles were measured and used to reconstruct palaeo-seasonal changes. Samples from ICDP (International Continental Drilling Program)-retrieved sedimentary cores encompassing two Pleistocene interglacial periods have been successfully used to further establish BS results as a quantitative climate proxy with the highest temporal resolution.

To extend the use of this novel proxy to other evaporitic minerals, BS experimental work was conducted on laboratory-grown gypsum, aiming to calibrate the proxy prior to its application to natural samples. The comparison of the temperatures obtained by measuring FIs in synthetically generated samples with respect to their well-known formation temperatures is providing the grounds to establish the use of BS in gypsum as a palaeo-temperature proxy.

Based on the previous data, the method is applied to natural gypsum samples from diverse environmental settings reflecting arid to semi-arid conditions, either due to anthropogenic influence or to natural climate variations throughout time.

Finally, possible correlations between sound velocity and salinity relationship are investigated and combined with ice melting temperatures of FIs. The experimental work in capillaries with different NaCl concentrations serve as the basis for this approach and is investigated as a possible reference for synthetic and natural gypsum samples.

Bibliography

Affek, H. P., Bar-Matthews, M., Ayalon, A., Matthews, A., and Eiler, J. M. (2008). Glacial/interglacial temperature variations in Soreq cave speleothems as recorded by 'clumped isotope' thermometry. *Geochimica et Cosmochimica Acta*, *72*(22), 5351–5360. https://doi.org/10.1016/j.gca.2008.06.031

Agassiz, L. (1840). Glaciers, and the evidence of their having once existed in Scotland, Ireland, and England. *Proceedings of The Geological Society of London*, *3*(72), 327–332.

Aronson, J. R., Emslie, A. G., Miseo, E. V., Smith, E. M., and Strong, P. F. (1983). Optical constants of monoclinic anisotropic crystals: Gypsum. *Applied Optics*, *22*(24), 4093. https://doi.org/10.1364/ao.22.004093

Arrhenius, S. (1896). On the influence of carbonic acid in the air upon the temperature of the ground. *The London, Edinburgh, and Dublin Philosophical Magazine and Journal of Science*, *41*(251), 237–276. https://doi.org/10.1080/14786449608620846

Aston, F. (1920). The mass-spectra of chemical elements. *The London, Edinburgh, and Dublin Philosophical Magazine and Journal of Science*, *39*(233), 611–625. https://doi.org/10.1080/14786440508636074

Barnes, H. (1954). Some tables for the ionic composition of sea water. *Journal of experimental biology*, *31*(4), 582–588.

Barnola, J.-M., Raynaud, D., Korotkevich, Y. S., and Lorius, C. (1987). Vostok ice core provides 160,000-year record of atmospheric CO2. *Nature*, *329*(6138), 408–414.

Ben Dor, Y., Neugebauer, I., Enzel, Y., Schwab, M. J., Tjallingii, R., Erel, Y., and Brauer, A. (2019). Varves of the Dead Sea sedimentary record. *Quaternary Science Reviews*, *215*, 173–184. https://doi.org/10.1016/j.quascirev.2019.04.011

Beurlen, H., da Silva, M. R., and de Castro, C. (2001). Fluid inclusion microthermometry in Be-Ta-(Li-Sn)-bearing pegmatites from the Borborema Province, northeast Brazil. *Chemical Geology*, *173*(1-3), 107–123.

Bigi, D., Lugli, S., Manzi, V., and Roveri, M. (2022). Are fluid inclusions in gypsum reliable paleoenvironmental indicators? An assessment of the evidence from the Messinian evaporites. *Geology*.

Blättler, C. L., Claire, M. W., Prave, A. R., Kirsimäe, K., Higgins, J. A., Medvedev, P. V., Romashkin, A. E., Rychanchik, D. V., Zerkle, A. L., Paiste, K., Kreitsmann, T., Millar, I. L., Hayles, J. A., Bao, H., Turchyn, A. V., Warke, M. R., and Lepland, A. (2018). Two-billion-year-old evaporites capture Earth's great oxidation. *Science*, *360*(6386), 320–323. https://doi.org/10.1126/science.aar2687

Bodnar, R. J. (1993). Revised equation and table for determining the freezing point depression of H2O-NaCl solutions. *Geochimica et Cosmochimica acta*, *57*, 683–684.

Brall, N. S., Gardien, V., Ariztegui, D., Sorrel, P., Guillerm, E., and Caupin, F. (2022). Reconstructing lake bottom water temperatures and their seasonal variability in the Dead Sea Basin during MIS 5e. *The Depositional Record*. https://doi.org/10.1002/dep2.185

Brewster, D. (1823). On the existence of two new fluids in the cavities of minerals which are immiscible and possess remarkable physical properties. *Transactions of the Royal Society of Edinburgh*, *10*, 94–107.

Buckland, W. (1824). *Reliquiae diluvianae; or, observations on the organic remains contained in caves, fissures and diluvial gravel, and on other geological phenomena, attesting the action of an universal deluge*. John Murray; Albemarle-Street.

Burke, E. A. (2001). Raman microspectrometry of fluid inclusions. *Lithos*, *55*(1-4), 139–158.

Callendar, G. S. (1938). The artificial production of carbon dioxide and its influence on temperature. *Quarterly Journal of the Royal Meteorological Society*, *64*(275), 223–240.

Cox, A., Doell, R., and Dalrymple, G. (1964). Reversals of the Earth's Magnetic Field. *Science*, *144*(3626), 1537–1543. https://doi.org/10.1126/science.144.3626.1537

Cox, R., Culkin, F., and Riley, J. (1967). The electrical conductivity/chlorinity relationship in natural sea water. *Deep Sea Research and Oceanographic Abstracts*, *14*(2), 203–220.

Culkin, F., and Smed, J. (1979). History of standard seawater. *Oceanologica Acta*, *2*(3), 355–364.

De La Vega, E., Chalk, T. B., Wilson, P. A., Bysani, R. P., and Foster, G. L. (2020). Atmospheric CO2 during the Mid-Piacenzian Warm Period and the M2 glaciation. *Scientific reports*, *10*(1), 1–8.

Debure, M., Lassin, A., Marty, N. C., Claret, F., Virgone, A., Calassou, S., and Gaucher, E. C. (2019). Thermodynamic evidence of giant salt deposit formation

by serpentinization: An alternative mechanism to solar evaporation. *Scientific reports*, *9*(1), 1–11.

Devkota, K. P., Devkota, M., Rezaei, M., and Oosterbaan, R. (2022). Managing salinity for sustainable agricultural production in salt-affected soils of irrigated drylands. *Agricultural Systems*, *198*, 103390.

Dittmar, W. et al. (1884). Report on researches into the composition of ocean-water collected by HMS Challenger during the years 1873-76. *Physics and Chemistry*, *1*, 1–251.

Dolomieu, D. G. (1792). Sur de l'huile de pétrole dans le cristal de roche and les fluides élastiques tirés du quartz (Lettre à Monsieur Delamétherie). *Journal de Physique*, *40*, 318–319.

Drebushchak, V., Drebushchak, T., Ogienko, A., and Yunoshev, A. (2019). Crystallization of sodium chloride dihydrate (hydrohalite). *Journal of Crystal Growth*, *517*, 17–23. https://doi.org/10.1016/j.jcrysgro.2019.04.009

Eiler, J. M. (2007). "Clumped-isotope" geochemistry—The study of naturally-occurring, multiply-substituted isotopologues. *Earth and Planetary Science Letters*, *262*(3-4), 309–327. https://doi.org/10.1016/j.epsl.2007.08.020

Eiler, J. M. (2011). Paleoclimate reconstruction using carbonate clumped isotope thermometry. *Quaternary Science Reviews*, *30*(25-26), 3575–3588. https://doi.org/10.1016/j.quascirev.2011.09.001

Emiliani, C. (1955). Pleistocene Temperatures. *The Journal of Geology*, *63*(6), 538–578. https://doi.org/10.1086/626295

Emiliani, C. (1970). Pleistocene Paleotemperatures. *Science*, *168*(3933), 822–825. https://doi.org/10.1126/science.168.3933.822

Emiliani, C., and Edwards, G. (1953). Tertiary Ocean Bottom Temperatures. *Nature*, *171*(4359), 887–888. https://doi.org/10.1038/171887c0

Emiliani, C. (1961). Cenozoic climatic changes as indicated by the stratigraphy and chronology of deep sea cores of Globigerina ooze facies. *Annals of the New York Academy of Sciences*, *95*(1), 521–536. https://doi.org/10.1111/j.1749-6632.1961.tb50057.x

Epstein, S., Buchsbaum, R., Lowenstam, H., and Urey, H. C. (1951). Carbonate-water isotopic temperature scale. *Geological Society of America Bulletin*, *62*(4), 417. https://doi.org/10.1130/0016-7606(1951)62[417:cits]2.0.co;2

Epstein, S., Buchsbaum, R., Lowenstam, H. A., and Urey, H. C. (1953). Revised carbonate-water isotopic temperature scale. *Geological Society of America Bulletin*, *64*(11), 1315. https://doi.org/10.1130/0016-7606(1953)64[1315:rcits]2.0.co;2

Fall, A., and Bodnar, R. J. (2018). How Precisely Can the Temperature of a Fluid Event be Constrained Using Fluid Inclusions? *Economic Geology*, *113*(8), 1817–1843. https://doi.org/10.5382/econgeo.2018.4614

Flint, R. F. (1968). The Idea of an Ice Age: Studies on Glaciers. Preceded by the Discourse of Neuchâtel. Louis Agassiz. Translated from the French and edited by Albert V. Carozzi. Hafner, New York, 1967. lxxii 213 pp., illus. 27.50. *Science*, *159*(3814), 520–520. https://doi.org/10.1126/science.159.3814.520.a

Fofonoff, N. (1985). Physical properties of seawater: A new salinity scale and equation of state for seawater. *Journal of Geophysical Research: Oceans*, *90*(C2), 3332–3342.

Forch, C., Knudsen, M., and Sørensen, S. (1902). Berichte uber die Konstantenbestimmungen zur Aufstellung der Hydrographischen Tabellen. *Kongekie Danske Videnskabernes Selskabs Skrifter, 61 Raekke naturvidensk. og mathem*, *1*, 1–151.

Forchhammer, G. (1865). Iv. on the composition of sea-water in the different parts of the ocean. *Philosophical Transactions of the Royal Society of London*, (155), 203–262.

Giauque, W. F., and Johnston, H. L. (1929a). An isotope of oxygen, mass 17, in the Earth atmosphere. *Journal of the American Chemical Society*, *51*(12), 3528–3534. https://doi.org/10.1021/ja01387a004

Giauque, W. F., and Johnston, H. L. (1929b). An Isotope of Oxygen, Mass 18. *Nature*, *123*(3096), 318–318. https://doi.org/10.1038/123318c0

Godwin, H. (1962). Half-life of Radiocarbon. *Nature*, *195*(4845), 984–984. https://doi.org/10.1038/195984a0

Gornitz, V., Lebedeff, S., and Hansen, J. (1982). Global sea level trend in the past century. *Science*, *215*(4540), 1611–1614.

Griffiths, M. L., Drysdale, R. N., Vonhof, H. B., Gagan, M. K., Zhao, J.-x., Ayliffe, L. K., Hantoro, W. S., Hellstrom, J. C., Cartwright, I., Frisia, S., et al. (2010). Younger Dryas–Holocene temperature and rainfall history of southern Indonesia from δ18O in speleothem calcite and fluid inclusions. *Earth and Planetary Science Letters*, *295*(1-2), 30–36.

Grimmer, J. O., Pironon, J., Teinturier, S., and Mutterer, J. (2003). Recognition and differentiation of gas condensates and other oil types using microthermometry of petroleum inclusions. *Journal of Geochemical Exploration*, *78*, 367–371.

Guillerm, E. (2019). *Turning halite fluid inclusions into accurate paleothermometers with Brillouin spectroscopy: development of a new method and application to the Last Interglacial in the Dead Sea.*

Guillerm, E., Gardien, V., Ariztegui, D., and Caupin, F. (2020). Restoring Halite Fluid Inclusions as an Accurate Palaeothermometer: Brillouin Thermometry

Versus Microthermometry. *Geostandards and Geoanalytical Research*, *44*, 243–264. https://doi.org/10.1111/ggr.12312

Hansen, J., Johnson, D., Lacis, A., Lebedeff, S., Lee, P., Rind, D., and Russell, G. (1981). Climate impact of increasing atmospheric carbon dioxide. *Science*, *213*(4511), 957–966.

Hardie, L. A., and Lowenstein, T. K. (2004). Did the Mediterranean Sea dry out during the Miocene? A reassessment of the evaporite evidence from DSDP Legs 13 and 42A cores. *Journal of Sedimentary Research*, *74*(4), 453–461.

Haynes, W. M., Lide, D. R., and Bruno, T. J. (2017). *Crc handbook of chemistry and physics. 97th edition*. Boca Raton, Florida: CRC Press/Taylor and Francis.

Hays, J. D., Imbrie, J., and Shackleton, N. J. (1976). Variations in the Earth's Orbit: Pacemaker of the Ice Ages. *Science*, *194*(4270), 1121–1132. https://doi.org/10.1126/science.194.4270.1121

Hays, J. D., and Opdyke, N. D. (1967). Antarctic Radiolaria, Magnetic Reversals, and Climatic Change. *Science*, *158*(3804), 1001–1011. https://doi.org/10.1126/science.158.3804.1001

He, K., Nie, A., Yuan, Y., Ghodsi, S. M., Song, B., Firlar, E., Lu, J., Lu, Y.-p., Shokuhfar, T., Megaridis, C. M., et al. (2018). In situ transmission electron microscopy explores a new nanoscale pathway for direct gypsum formation in aqueous solution. *ACS Applied Nano Materials*, *1*(10), 5430–5440.

Herdendorf, C. E. (1990). Distribution of the world's large lakes. *Large lakes* (pp. 3–38). Springer.

Holser, W. T. (1979). Mineralogy of evaporites. *Marine Minerals* (pp. 211–294). De Gruyter. https://doi.org/10.1515/9781501508646-012

Hutton, J. (1795). Theory of the Earth.

Hutton, J. (1788). Theory of the Earth, or an Investigation of the Laws observable in the Composition, Dissolution, and Restoration of Land upon the Globe. *Transactions of the Royal Society of Edinburgh*, *1*(2), 209–304. https://doi.org/10.1017/s0080456800029227

International Labour Organization. (n.d.). International Chemical Safety Cards ICSC [Accessed: 2022-01-15]. http://www.ilo.org/dyn/icsc/showcard.home

IOC. (2010). The Practical Salinity Scale 1978 and the International Equation of State of Seawater 1980. *Unesco Technical Papers in Marine Science 36*, 196. https://unesdoc.unesco.org/ark:/48223/pf0000188170

IPCC. (2022). *Climate Change 2022: Impacts, Adaptation, and Vulnerability. Contribution of Working Group II to the Sixth Assessment Report of the Intergovernmental Panel on Climate Change* (H.-O. Pörtner and D.C. Roberts and M. Tignor and E.S. Poloczanska and K. Mintenbeck and A. Alegría and M. Craig

and S. Langsdorf, S. Löschke and V. Möller and A. Okem and B. Rama, Ed.) [In Press.]. Cambridge University Press.

Jacobsen, J., and Knudsen, M. (1940). Urnormal 1937 or primary standard sea water 1937. publ. sci. *Ass. Océanogr. phy*, (7).

Jones, P. D., and Mann, M. E. (2004). Climate over past millennia. *Reviews of Geophysics*, *42*(2).

Kah, L. C., Lyons, T. W., and Chesley, J. T. (2001). Geochemistry of a 1.2 Ga carbonate-evaporite succession, northern Baffin and Bylot Islands: implications for Mesoproterozoic marine evolution. *Precambrian Research*, *111*(1-4), 203–234. https://doi.org/10.1016/s0301-9268(01)00161-9

Kele, S., Breitenbach, S. F., Capezzuoli, E., Meckler, A. N., Ziegler, M., Millan, I. M., Kluge, T., Deák, J., Hanselmann, K., John, C. M., Yan, H., Liu, Z., and Bernasconi, S. M. (2015). Temperature dependence of oxygen- and clumped isotope fractionation in carbonates: A study of travertines and tufas in the 6–95°C temperature range. *Geochimica et Cosmochimica Acta*, *168*, 172–192. https://doi.org/10.1016/j.gca.2015.06.032

Kelson, J. R., Huntington, K. W., Breecker, D. O., Burgener, L. K., Gallagher, T. M., Hoke, G. D., and Petersen, S. V. (2020). A proxy for all seasons? A synthesis of clumped isotope data from Holocene soil carbonates. *Quaternary Science Reviews*, *234*, 106259. https://doi.org/10.1016/j.quascirev.2020.106259

Kimura, H., and Kai, J. (1984). Phase change stability of CaCl2x6H2O. *Solar Energy*, *33*(6), 557–563. https://doi.org/10.1016/0038-092x(84)90011-2

Kiro, Y., Goldstein, S. L., Lazar, B., and Stein, M. (2016). Environmental implications of salt facies in the Dead Sea. *Geological Society of America Bulletin*, *128*, 824–841. https://doi.org/10.1130/b31357.1

Knudsen, M. (1903). On the standard-water used in the hydrographical research until July 1903. *ICES Journal of Marine Science*, *1*(2), 3–9.

Kouzmanov, K., Bailly, L., Ramboz, C., Rouer, O., and Beny, J.-M. (2002). Morphology, origin and infrared microthermometry of fluid inclusions in pyrite from the Radka epithermal copper deposit, Srednogorie zone, Bulgaria. *Mineralium deposita*, *37*(6), 599–613.

Lelieveld, J., Hadjinicolaou, P., Kostopoulou, E., Chenoweth, J., Maayar, M. E., Giannakopoulos, C., Hannides, C., Lange, M. A., Tanarhte, M., Tyrlis, E., and Xoplaki, E. (2012). Climate change and impacts in the Eastern Mediterranean and the Middle East. *Climatic Change*, *114*(3-4), 667–687. https://doi.org/10.1007/s10584-012-0418-4

Létolle, R., and Chesterikoff, A. (1999). Salinity of surface waters in the Aral sea region. *International Journal of Salt Lake Research*, *8*(4), 293–306. https://doi.org/10.1007/bf02442116

Libby, W. F., Anderson, E. C., and Arnold, J. R. (1949). Age Determination by Radiocarbon Content: World-Wide Assay of Natural Radiocarbon. *Science*, *109*(2827), 227–228. https://doi.org/10.1126/science.109.2827.227

Lindsay, J. F. (1987). Upper Proterozoic evaporites in the Amadeus basin, central Australia, and their role in basin tectonics. *Geological Society of America Bulletin*, *99*(6), 852. https://doi.org/10.1130/0016-7606(1987)99<852:upeita>2.0.co;2

Lowenstein, T. K., Li, J., Brown, C., Roberts, S. M., Ku, T.-L., Luo, S., and Yang, W. (1999). 200 ky paleoclimate record from Death Valley salt core. *Geology*, *27*(1), 3–6.

Lyell, C. (1837). *Principles of Geology: Being an Inquiry how Far the Former Changes of the Earth's Surface are Referable to Causes Now in Operation*. J. Kay, jun. and brother. https://books.google.de/books?id=4BlDAAAAIAAJ

Lyell, C., and Deshayes, G. P. (1830). *Principles of geology: Being an attempt to explain the former changes of the earth's surface, by reference to causes now in operation* (Vol. 1). J. Murray.

McCrea, J. M. (1950). On the Isotopic Chemistry of Carbonates and a Paleotemperature Scale. *The Journal of Chemical Physics*, *18*(6), 849–857. https://doi.org/10.1063/1.1747785

Mekki-Azouzi, M. E., Tripathi, C. S. P., Pallares, G., Gardien, V., and Caupin, F. (2015). Brillouin spectroscopy of fluid inclusions proposed as a paleothermometer for subsurface rocks. *Scientific Reports*, *5*. https://doi.org/10.1038/srep13168

Milankovitch, M. (1930). Mathematische Klimalehre und astronomische Theorie der Klimaschwankungen. In W. Köppen and R. Geiger (Eds.), *Handbuch der Klimatologie. Band 1: Allgemeine Klimalehre*. Borntraeger, Berlin 1930.

Millero, F. J., Feistel, R., Wright, D. G., and McDougall, T. J. (2008). The composition of Standard Seawater and the definition of the Reference-Composition Salinity Scale. *Deep Sea Research Part I: Oceanographic Research Papers*, *55*(1), 50–72.

Nelson, K. H., and Thompson, T. G. (1954). Concentration of brines and deposition of salts from sea water under frigid conditions. *American Journal of Science*, *254*, 227–238.

Norton, C. F., and Grant, W. D. (1988). Survival of halobacteria within fluid inclusions in salt crystals. *Microbiology*, *134*(5), 1365–1373.

Pinho, S. P., and Macedo, E. A. (1996). Representation of salt solubility in mixed solvents: A comparison of thermodynamic models. *Fluid Phase Equilibria*, *116*(1-2), 209–216.

Rigaudier, T., Gardien, V., Martineau, F., Reverdy, G., and Lécuyer, C. (2012). Hydrogen and Oxygen Isotope Reference Materials for the Analysis of Water Inclusions in Halite. *Geostandards and Geoanalytical Research*, *36*(1), 51–59. https://doi.org/10.1111/j.1751-908x.2011.00139.x

Rigaudier, T., Lécuyer, C., Gardien, V., Suc, J.-P., and Martineau, F. (2011). The record of temperature, wind velocity and air humidity in the δD and δ18O of water inclusions in synthetic and Messinian halites. *Geochimica et Cosmochimica Acta*, *75*(16), 4637–4652. https://doi.org/10.1016/j.gca.2011.05.034

Roedder, E. (1963). Studies of fluid inclusions;[Part] 2, Freezing data and their interpretation. *Economic geology*, *58*(2), 167–211.

Roedder, E. (1972). *Composition of Fluid Inclusions: Reviews of World Literature*. US Government Printing Office.

Roedder, E. (1984). Volume 12: Fluid inclusions. *Reviews in mineralogy*, *12*.

Roedder, E. (1962). Studies of fluid inclusions; Part 1, Low temperature application of a dual-purpose freezing and heating stage. *Economic Geology*, *57*(7), 1045–1061.

Samson, I., Anderson, A., and Marshall, D. D. (2003). *Fluid inclusions: Analysis and interpretation* (Vol. 32). Mineralogical Association of Canada.

Schmid, T., Jungnickel, R., and Dariz, P. (2020). Insights into the CaSO4–H2O System: A Raman-Spectroscopic Study. *Minerals*, *10*(2), 115. https://doi.org/10.3390/min10020115

Schubel, K. A., and Lowenstein, T. K. (1997). Criteria for the recognition of shallow-perennial-saline-lake halites based on recent sediments from the Qaidam Basin, western China. *Journal of Sedimentary Research*, *67*(1), 74–87.

Shackleton, N. J. (1969). The last interglacial in the marine and terrestrial records. *Proceedings of the Royal Society of London. Series B. Biological Sciences*, *174*(1034), 135–154. https://doi.org/10.1098/rspb.1969.0085

Sirota, I., Enzel, Y., and Lensky, N. G. (2017). Temperature seasonality control on modern halite layers in the Dead Sea: In situ observations. *Bulletin*, *129*, 1181–1194.

Sorby, H. C. (1858). On the Microscopical, Structure of Crystals, indicating the Origin of Minerals and Rocks. *Quarterly Journal of the Geological Society*, *14*(1-2), 453–500. https://doi.org/10.1144/gsl.jgs.1858.014.01-02.44

Spear, N., Holland, H., Garcia-Veígas, J., Lowenstein, T., Giegengack, R., and Peters, H. (2014). Analyses of fluid inclusions in Neoproterozoic marine halite provide oldest measurement of seawater chemistry. *Geology*, *42*(2), 103–106. https://doi.org/10.1130/g34913.1

Thomas, C., and Ariztegui, D. (2019). Fluid inclusions from the deep Dead Sea sediment provide new insights on Holocene extreme microbial life. *Quaternary Science Reviews*, *212*, 18–27.

Thomson, J. (1912). Further experiments on positive rays. *The London, Edinburgh, and Dublin Philosophical Magazine and Journal of Science*, *24*(140), 209–253. https://doi.org/10.1080/14786440808637325

Tyler, R. H., Boyer, T. P., Minami, T., Zweng, M. M., and Reagan, J. R. (2017). Electrical conductivity of the global ocean. *Earth, Planets and Space*, *69*(1), 1–10.

Urey, H. C. (1947). The thermodynamic properties of isotopic substances. *Journal of the Chemical Society (Resumed)*, 562. https://doi.org/10.1039/jr9470000562

Urey, H. C., Lowenstam, H. A., Epstein, S., and McKinney, C. R. (1951). Measurement of paleotemperatures and temperatures of the upper Cretaceous of England, Denmark, and the Southeastern United States. *Geological Society of America Bulletin*, *62*(4), 399. https://doi.org/10.1130/0016-7606(1951)62[399:mopato]2.0.co;2

Urey, H. C. (1948). Oxygen Isotopes in Nature and in the Laboratory. *Science*, *108*(2810), 489–496. https://doi.org/10.1126/science.108.2810.489

Urey, H. C., and Teal, G. K. (1935). The Hydrogen Isotope of Atomic Weight Two. *Reviews of Modern Physics*, *7*(1), 34–94. https://doi.org/10.1103/revmodphys.7.34

Van Driessche, A., Benning, L. G., Rodriguez-Blanco, J., Ossorio, M., Bots, P., and García-Ruiz, J. (2012). The role and implications of bassanite as a stable precursor phase to gypsum precipitation. *Science*, *336*(6077), 69–72.

Van Driessche, A., Stawski, T., and Kellermeier, M. (2019). Calcium sulfate precipitation pathways in natural and engineered environments. *Chemical Geology*, *530*, 119274.

Warren, J. K. (2016). *Evaporites*. Springer International Publishing. https://doi.org/10.1007/978-3-319-13512-0

Wilkinson, J. (2001). Fluid inclusions in hydrothermal ore deposits. *Lithos*, *55*(1-4), 229–272.

Wooster, W., Lee, A., and Dietrich, G. (1969). Redefinition of salinity. *Z. Geophys*, *35*, 611–613.

Zavialov, P., Ni, A., Kudyshkin, T., Kurbaniyazov, A., and Dikarev, S. (2009). Five years of field hydrographic research in the Large Aral Sea (2002–2006). *Journal of Marine Systems*, *76*(3), 263–271.

Zaw, K., Hunns, S., Large, R., Gemmell, J., Ryan, C., and Mernagh, T. (2003). Microthermometry and chemical composition of fluid inclusions from the Mt Chalmers volcanic-hosted massive sulfide deposits, central Queensland, Australia: implications for ore genesis. *Chemical Geology*, *194*(1-3), 225–244.

Chapter 2

Sampling locations

2.1 Introduction

Five locations from different environmental settings have played a role during this PhD thesis. The actual PhD project was approved by Campus France in the course of the national science program 'Make Our Planet Great Again', and was assigned to work on Holocene lake sediments solely, i.e. Lake Petén Itzá (Guatemala), and the Aral Sea (Kazakhstan, Uzbekistan). However, during the first months after the start of the project, it became apparent that the sample material was less suitable for the realization of the pursued goals (see chapter 7.1). Therefore, the project was slightly modified, resulting in other localities in Europe and the Levante region (Figure 2.1). The additional localities vary in both spatial and temporal extent, from marine to coastal Miocene gypsum (Piedmont, NW Italy; Caltanisetta basin, Sicily), lacustrine Pleistocene salt deposits (Dead Sea, Israel), to Holocene gypsum from an arid sabkha pan (Tunisia).

Figure 2.1 Sampling locations, marked by white rectangles, of material used for the PhD thesis. 1 = Banengo outcrop, Piedmont basin, Italy (Miocene; Messinian); 2 = Diverse outcrops on Sicily, Italy (Miocene; Messinian); 3 = Sabkha shoreline, Sebkha El Melah, Tunisia (Holocene); 4 = Bore core from the Dead Sea basin, Israel (Holocene-Pleistocene); 5 = Aral Sea shoreline, Kazakhstan (Holocene).

2.2 Terrestrial climate archives

2.2.1 Dead Sea

The modern-day Dead Sea (DS) is an endorheic (or, terminal) hypersaline lake in the Jordan Rift Valley, a result of the Dead Sea transform fault, located between Israel and Jordan (central part: 31° 30' 0" N, 35° 30' 0" E). The regional climate is influenced by the Mediterranean Sea, causing mild winters and hot summers. The Dead Sea basin has been occupied by three lakes in its younger history during the Pleistocene and the current Holocene (Lake Amora, Lake Lisan, Dead Sea) (Stein, 2003; Stein, 2014). Since the DS is a terminal lake and only has the Jordan river as its major freshwater supply, the water balance between inflow vs. evaporation/water loss is the dominating factor in terms of the lake-level. The DS is well-known for its rapid lake-level drop since the 1960's due to an intensified industrial usage of its water resources and stronger surface water evaporation rates, which have caused a drop of around 30 m from -390 to currently (2020) -435 m below mean sea level with an annual mean lake-level drop of 1 m/year. Therefore, the salinity increased dramatically to ca 34.2 % and former uniform lake has been separated into two basins: the ca 320 m deep northern basin (area ca 45x16 km), and a smaller one in the southern part where salt works are actively precipitating potash for industrial purposes.

The limnological system is sensitive to climate changes and varied over time, e.g. lake-levels declined during warmer periods of Heinrich stadials or increased summer insolation, whereas lake-level rose during colder periods like the Last Glacial Maximum (Stein et al., 2010; Torfstein et al., 2013). However, the lake-level has (probably) never been as low as today, and there are serious concerns about the future water budget that will supply the unstable region with water. However, models showed that the DS will not completely desiccate because a steady state might be reached in a century or later (Yechieli et al., 1998).

Annual winter period lasts from October to March, the summer period from April-September. Modern-day air temperatures over the Dead Sea are seasonal-controlled and vary accordingly to winter (lowest) and summer (highest), ranging between 18.3 °C (average January) to 32.9 °C (average August) during 1992-2002 (Gertman and Hecht, 2002). Sea-surface temperatures are slightly higher, but follow the same seasonal-controlled pattern with lowest averaged temperatures in January (21.6 °C), and highest in August (33.7 °C). Further, diurnal changes (daily minimum vs. maximum) in air temperatures were monitored during 1992-2002 and reported to vary in winter by 2.7 °C and by 5.2 °C in summer (Gertman and Hecht, 2002). A suitable feature of the Dead Sea basin for palaeoclimate research is a well-preserved

Figure 2.2 (A) Map showing the arid climate regions of North Africa and Western Asia. (B) Dead Sea location with northern and southern basins.

sedimentary record of the last 220 ka, documented by characteristic lithologies of aragonite, gypsum, mud, halite and detrital material (Neugebauer et al., 2014). Hence, specific periods in its younger history (Holocene-Upper Pleistocene) can be investigated by different analytical methods and sedimentological analyses since elevated terraces around the lake's shoreline also bear witness of past climate conditions (Lowenstein et al., 2021; Ghazleh and Kempe, 2021; Lazar et al., 2014). Furthermore, modern-day observations of in situ halite precipitation revealed a seasonal mechanism that drives coarse halite bottom-growth during summer, and cumulate halite nucleation in the free water body during winter due to a high supersaturation with respect to NaCl, leading to the formation of evaporitic varves (Sirota et al., 2017; Ben Dor et al., 2019). These findings might be an analogue for ancient halite deposits that were described in a long sedimentary record covering several glacial-interglacial periods up to 220 ka ago (Goldstein et al., 2020; see Chapter 5).

2.2.2 Aral Sea

The Aral Sea region was a former endorheic large lake, located in Central Asia between Uzbekistan and Kazakhstan (Figure 2.1). It is a further example of anthropogenic exploitation of natural ecosystems and the environmental consequences: The lake volume has decreased steadily by ca 1000 km^3 since 1960 at varying average rates between 1960-2001 (22.92 km^3/a), a maximum in 1974–1975 (47.59 km^3/a) and a lowered average rate of 2 km^3 in 2009-2018 (Yang et al., 2020). Hence, the lake area has decreased as well by ca 60156 km^2, which has caused a separation into two basins in 1988 (Yang et al., 2020; Zavialov et al., 2009) (Figure 2.3 D). Since then, the basins were termed 'Small Sea' and 'Large Sea'. The Large Sea has been further reduced in its area until the onset of two sub-basins ('Western basin'; 'Eastern basin'), connected by a small channel ('Strait'). The Western basin is much deeper (maximum: 43.5 m vs. 7 m), but the salinity increases during the past decades are similar for both basins from 10 to 92 g/kg and 10 to 110 g/kg for the Western and Eastern basin, respectively (Zavialov et al., 2009). For comparison, the lake was brackish with a salinity $\leq$12 g/kg before 1960 (Zavialov et al., 2009).

The Aral Sea region resembles the Levante region (including the Dead Sea) in terms of regional aridity, terminal lake state, and rapid decline of lake-level, triggered in both cases by excessive consumption of water resources for industrial and agricultural purposes. Like in the Dead Sea, the negative water balance of the Aral Sea region is accompanied by increasing salinity of the surface and bottom waters (Létolle and Chesterikoff, 1999; Zavialov et al., 2009). This caused an intensive salinization of soils and a highly salinity increase of the two main rivers (Amu Darya, Syr Darya) that have been supplied the lake with freshwater from the Central Asian mountain belt (Létolle and Chesterikoff, 1999). Not even the glacier melt in the mountain belts due to climate change could equalize the negative water balance of the Aral Sea region (Yang et al., 2020).

The state of the Aral Sea region as a climate archive has been reported in several studies dealing with Holocene lithological units (Oberhänsli et al., 2011; Sorrel et al., 2007; Sorrel et al., 2006). The main key to interpret different lithologies was found in past lake levels, varying in time according to the amount of water inflow from the main rivers. A high water inflow was related with higher runoff of detrital material into the lake, leading to fine laminated sediments of clay and salt which hindered the deposition of gypsum and carbonates (Oberhänsli et al., 2011). A reduced water inflow, in contrast, triggered the precipitation of gypsum and carbonates. The lack of salt units was due to the low salinity and a relatively high $SO_4{}^{2-}$ content (Zavialov et al., 2009).

Nonetheless, a high-resolution palaeotemperature study is lacking, which provided the framework to investigate Holocene gypsum material by using Brillouin spectroscopy.

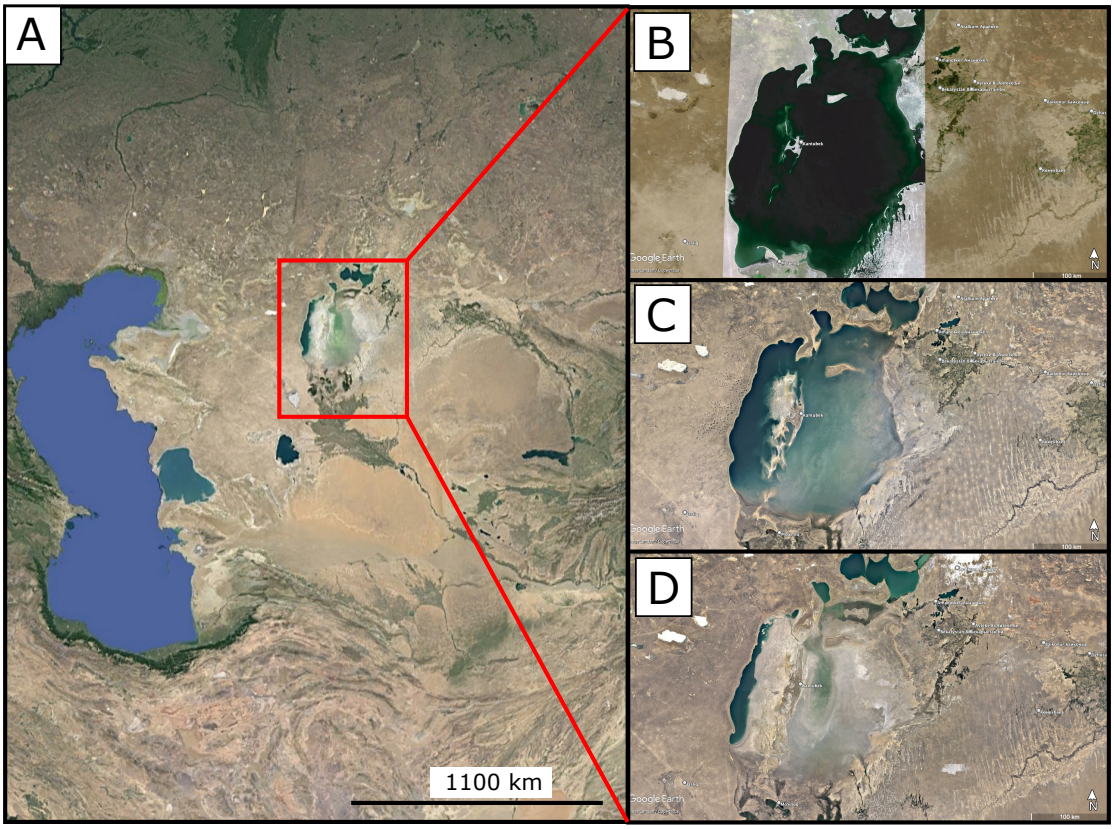

Figure 2.3 Overview on the remains of the Aral Sea (Red rectangle). Caspian Sea to the West. (B-D) Aral Sea satellite images showing the excessive water loss from 1973 (B), 1988 (C), and 2020 (D). Sources: Google Earth.

2.2.3 Sabkha El Melah

The chosen study site is located in the sabkha 'El Melah' (SE Tunisia) which is a large depression at the northern edge of the 'Jeffara coastal plain' with an area of ca 150 km^2 (Perthuisot et al., 1990; Ben Ameur et al., 2022). The sedimentary record of the sabkha covers the last 5300 years (Fontes and Perthuisot, 1973). The lithology consists mainly of lacustrine and continental deposits, oolithic/biogenic sands, gypsum, huntite, and salt (Davaud et al., 1996; Perthuisot et al., 1990) (Figure 2.5). The local climate is dominated by arid to semi-arid conditions with a mean annual temperature of 20 °C with maximum values of 40 °C occurring in August, with an annual rainfall of ≤200 mm (Ben Ameur et al., 2022).

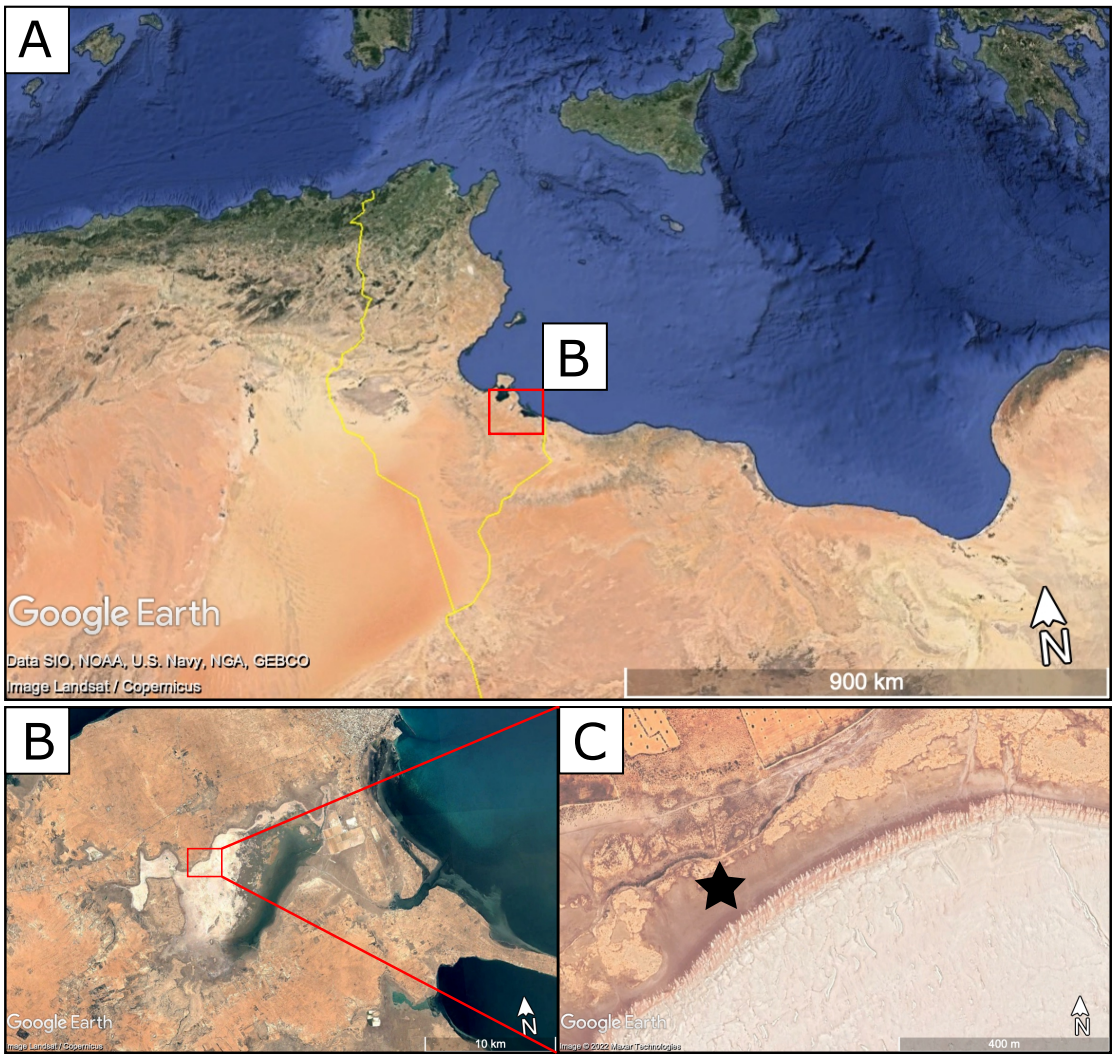

Figure 2.4 A) Study site of Sabkha El Melah in Tunisia. B) Modern-day evaporitic pan with halite nucleation (white colours). Note the proximity to the Mediterranean Sea. C) Sampling sites of gypsum material MG1.

Gypsum crystals were observed along the shoreline as second evaporitic mineral after carbonates and prior or concurrently mixed with halite. Common gypsum shapes are characterised by needles, flat crystals, or lenses, with displacement features within the coastal sediments. Further, larger swallow-tail crystals form 'gypsum beaches' (Davaud et al., 1996).

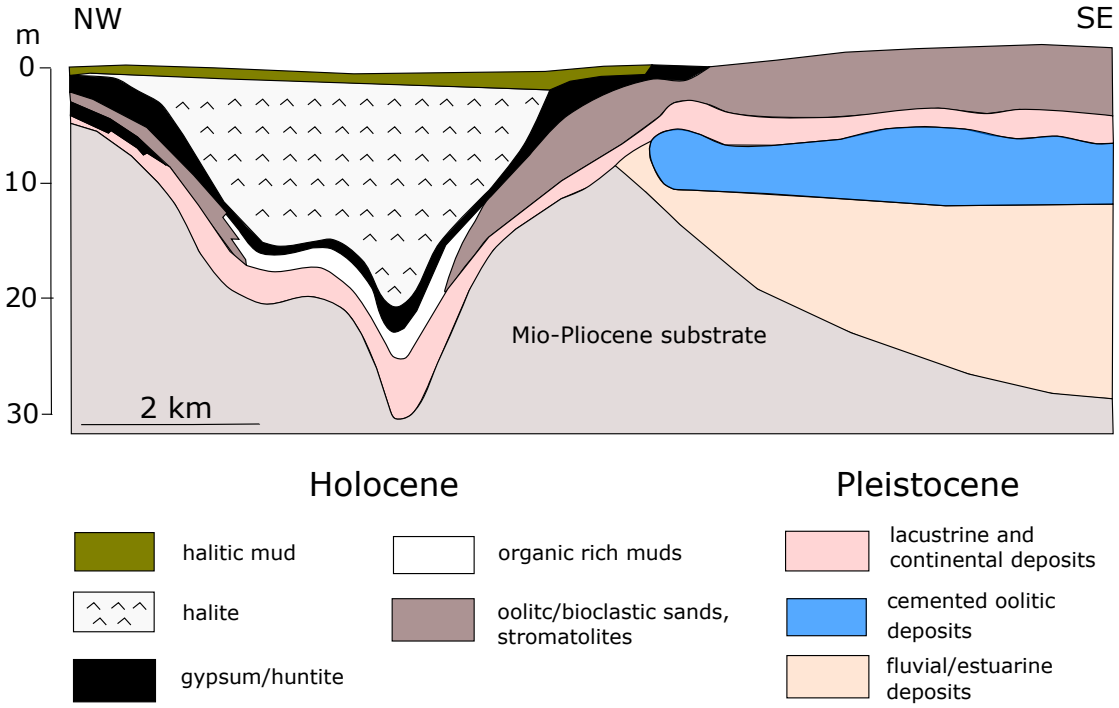

Figure 2.5 Principal geological units of the sabkha El Melah, Tunisia. Modified after Davaud et al., 1996.

2.3 Archives from the Mediterranean

The accommodation of huge salt and gypsum units in the Mediterranean realm over a short time period (ca 640 ka) occurred during the Miocene and is referred to the 'Messinian Salinity Crisis' (MSC) (Decima and Wezel, 1971; Hsu et al., 1973; Krijgsman et al., 1999). The first theories that might have caused the rapid evaporitic deposition over a large area were attributed to a desiccated Mediterranean Sea after the closure of the Strait of Gibraltar that interrupted the Atlantic seawater inflow into the Mediterranean (Hsu et al., 1973).
However, during the last two decades, the MSC has been subject to various studies and debates about key aspects, e.g., the spatial-temporal chronology between locations, the timing of drawdown phases, the water depth formation of evaporites, and models that were designed to link different onshore and offshore sites from Sorbas to Sicily to the Eastern Mediterranean (Rouchy and Caruso, 2006; Roveri, Flecker, et al., 2014). A general consensus was found for the onset of the MSC (currently: 5.97 Ma, based on gypsum cycles in the Sorbas basin, Spain (Manzi et al., 2013)), the division into three internal stages, termed as 'Primary Lower Gypsum' (1. stage), 'Resedimented Lower Gypsum' (2. stage), and 'Upper Gypsum' (3. stage) (Roveri et al., 2008; Manzi et al., 2012), and that the lithological units are related to precessional-controlled cycles of 21 ka (Hilgen et al., 1993; Hilgen et al., 1995).
Furthermore, seasonal-derived signatures were discovered in halite and gypsum units in the 2. stage which has been referred to lunar and solar periodicities (Manzi et al., 2012). The end of the Messinian stage is defined by the Zanclean 'Global Boundary Stratotype Section and Point' (GSSP) at 'Eraclea Minoa' section, Sicily, which is also related to the flooding of the Mediterranean realm, 5.33 Ma ago (Van Couvering et al., 2000).
The current idea about the formation of the various evaporitic units is mainly based on a model with regional sub-basins in the Mediterranean, each one characterised by differences in water depth, freshwater support, and timing of evaporite deposits (Rouchy and Caruso, 2006; Rigaudier et al., 2011) (Figure 2.6 A-1). There are also approaches that take into account tectonic uplifting in combination with precessional cycles to explain non-marine deposits in a non-desiccated basin (Roveri and Manzi, 2006), and 'a deep-water deep-basin model' that hypothesised the flow of dense saline waters towards deeper water depths to be possible causes for super-saturated bottom brines for the formation of evaporites (Roveri, Manzi, et al., 2014).

Specifically the widely distributed gypsum units, both onshore and offshore, have led to studies about the initial environmental conditions during gypsum formation such as salinity, the water depth, and the source of ions by using fluid inclusions, petrographical, geochemical and sedimentological analyses (Natalicchio et al., 2014; Natalicchio et al., 2021; Bigi et al., 2022).

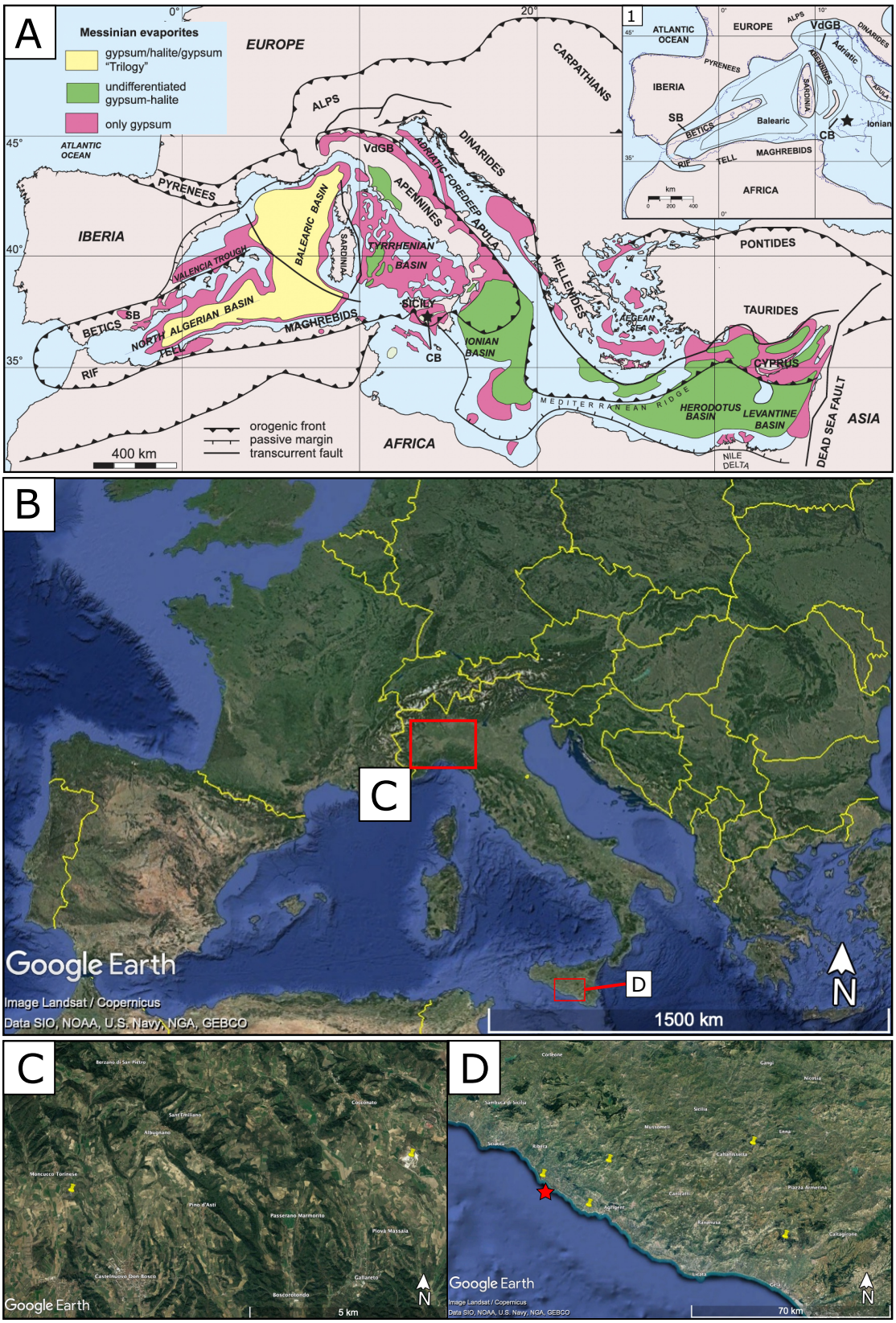

Figure 2.6 A) Messinian evaporites in the Mediterranean. A-1) Map of proposed sub-basins. CB, Caltanissetta basin; SB, Sorbas basin; VdGB, Vena del Gesso basin (Slightly modified from Manzi et al., 2012, published first in Rouchy and Caruso, 2006). B) Overview on locations with Messinian deposits which were relevant for this work. C) Piedmont Basin. D) Outcrops on Sicily in the CB. Red star marks the location of a seawater sample.

Bibliography

Ben Ameur, M., Masmoudi, S., Omar, H., Ouameni, I., Medhioub, M., and Yaich, C. (2022). Middle to late Holocene sedimentary filling history of the Sebkha el Melah in the south-eastern Tunisia. *Sedimentology*. https://doi.org/10.1111/sed.12995

Ben Dor, Y., Neugebauer, I., Enzel, Y., Schwab, M. J., Tjallingii, R., Erel, Y., and Brauer, A. (2019). Varves of the Dead Sea sedimentary record. *Quaternary Science Reviews*, *215*, 173–184. https://doi.org/10.1016/j.quascirev.2019.04.011

Bigi, D., Lugli, S., Manzi, V., and Roveri, M. (2022). Are fluid inclusions in gypsum reliable paleoenvironmental indicators? An assessment of the evidence from the Messinian evaporites. *Geology*.

Davaud, E. J., Jedoui, Y., and Strasser, A. (1996). Holocene peritidal and evaporitic sedimentation in Southern Tunisia. *17th Regional African European Meeting of Sedimentology: field trips guide book*, 1–13.

Decima, A., and Wezel, F. (1971). Osservazioni sulle evaporiti messiniane della Sicilia centro-meridionale. *Rivista Mineraria Siciliana*, *130–134*, 172–187.

Fontes, J. C., and Perthuisot, J. (1973). Climatic recorder for past 50,000 yr in Tunisia. *Nature-Physical Science*, *244*(135), 74–75.

Gertman, I., and Hecht, A. (2002). *The Dead Sea hydrography from 1992 to 2000*. www.elsevier.com/locate/jmarsys

Ghazleh, S. A., and Kempe, S. (2021). Discovery of high-level terraces of Last Glacial Lake Lisan (Dead Sea) and Eastern Mediterranean paleoclimatic implications. *Quaternary International*, *604*, 38–50.

Goldstein, S. L., Kiro, Y., Torfstein, A., Kitagawa, H., Tierney, J., and Stein, M. (2020). Revised chronology of the ICDP Dead Sea deep drill core relates drier-wetter-drier climate cycles to insolation over the past 220 kyr. *Quaternary Science Reviews*, *244*. https://doi.org/10.1016/j.quascirev.2020.106460

Hilgen, F., Krijgsman, W., Langereis, C., Lourens, L., Santarelli, A., and Zachariasse, W. (1995). Extending the astronomical (polarity) time scale into the Miocene. *Earth and Planetary Science Letters*, *136*(3-4), 495–510.

Hilgen, F., Lourens, L., Berger, A., and Loutre, M.-F. (1993). Evaluation of the astronomically calibrated time scale for the late Pliocene and earliest Pleistocene. *Paleoceanography*, *8*(5), 549–565.

Hsu, K., Cita, M., and Ryan, W. (1973). The origin of the Mediterranean evaporites: Initial Reports of Deep Sea Drilling Project, v. 13.

Krijgsman, W., Hilgen, F., Raffi, I., Sierro, F., and Wilson, D. (1999). Chronology, causes and progression of the Messinian salinity crisis. *Nature*, *400*(6745), 652–655.

Lazar, B., Sivan, O., Yechieli, Y., Levy, E., Antler, G., Gavrieli, I., and Stein, M. (2014). Long-term freshening of the Dead Sea brine revealed by porewater Cl- and $\delta^1$8O in ICDP Dead Sea deep-drill. *Earth and Planetary Science Letters*, *400*, 94–101.

Létolle, R., and Chesterikoff, A. (1999). Salinity of surface waters in the Aral sea region. *International Journal of Salt Lake Research*, *8*(4), 293–306. https://doi.org/10.1007/bf02442116

Lowenstein, T. K., Weldeghebriel, M. F., Sirota, I., Eyal, H., Mor, Z., and Lensky, N. G. (2021). Criteria for the recognition of clastic halite: The modern Dead Sea shoreline. *Sedimentology*, *68*(6), 2253–2269.

Manzi, V., Gennari, R., Hilgen, F., Krijgsman, W., Lugli, S., Roveri, M., and Sierro, F. J. (2013). Age refinement of the Messinian salinity crisis onset in the Mediterranean. *Terra Nova*, *25*(4), 315–322.

Manzi, V., Gennari, R., Lugli, S., Roveri, M., Scafetta, N., and Schreiber, B. C. (2012). High-frequency cyclicity in the Mediterranean Messinian evaporites: evidence for solar–lunar climate forcing. *Journal of Sedimentary Research*, *82*(12), 991–1005.

Natalicchio, M., Dela Pierre, F., Lugli, S., Lowenstein, T. K., Feiner, S. J., Ferrando, S., Manzi, V., Roveri, M., and Clari, P. (2014). Did Late Miocene (Messinian) gypsum precipitate from evaporated marine brines? Insights from the Piedmont Basin (Italy). *Geology*, *42*(3), 179–182.

Natalicchio, M., Pellegrino, L., Clari, P., Pastero, L., and Pierre, F. D. (2021). Gypsum lithofacies and stratigraphic architecture of a Messinian marginal basin (Piedmont Basin, NW Italy). *Sedimentary Geology*, *425*, 106009.

Neugebauer, I., Brauer, A., Schwab, M. J., Waldmann, N. D., Enzel, Y., Kitagawa, H., Torfstein, A., Frank, U., Dulski, P., Agnon, A., Ariztegui, D., Ben-Avraham, Z., Goldstein, S. L., and Stein, M. (2014). Lithology of the long sediment record recovered by the ICDP Dead Sea Deep Drilling Project (DSDDP). *Quaternary Science Reviews*, *102*, 149–165. https://doi.org/10.1016/j.quascirev.2014.08.013

Oberhänsli, H., Novotná, K., Píšková, A., Chabrillat, S., Nourgaliev, D. K., Kurbaniyazov, A. K., and Grygar, T. M. (2011). Variability in precipitation, temperature and river runoff in W Central Asia during the past ~2000yrs. *Global and Planetary Change*, *76*(1-2), 95–104. https://doi.org/10.1016/j.gloplacha.2010.12.008

Perthuisot, J.-P., Castanier, S., and Maurin, A. (1990). La huntite (CaMg 3 (CO 3) 4) de la Sebkha el Melah (Zarzis, Tunisie); un exemple de microbiodiagenese carbonatogene. *Bulletin de la Société géologique de France*, *6*(4), 657–666.

Rigaudier, T., Lécuyer, C., Gardien, V., Suc, J.-P., and Martineau, F. (2011). The record of temperature, wind velocity and air humidity in the δD and δ18O of water inclusions in synthetic and Messinian halites. *Geochimica et Cosmochimica Acta*, *75*(16), 4637–4652. https://doi.org/10.1016/j.gca.2011.05.034

Rouchy, J. M., and Caruso, A. (2006). The Messinian salinity crisis in the Mediterranean basin: a reassessment of the data and an integrated scenario. *Sedimentary Geology*, *188*, 35–67.

Roveri, M., and Manzi, V. (2006). The Messinian salinity crisis: looking for a new paradigm? *Palaeogeography, Palaeoclimatology, Palaeoecology*, *238*(1-4), 386–398.

Roveri, M., Manzi, V., Bergamasco, A., Falcieri, F., Gennari, R., Lugli, S., and Schreiber, B. (2014). Dense shelf water cascading and Messinian canyons: a new scenario for the Mediterranean salinity crisis. *American Journal of Science*, *314*(3), 751–784.

Roveri, M., Flecker, R., Krijgsman, W., Lofi, J., Lugli, S., Manzi, V., Sierro, F. J., Bertini, A., Camerlenghi, A., De Lange, G., et al. (2014). The Messinian Salinity Crisis: past and future of a great challenge for marine sciences. *Marine Geology*, *352*, 25–58.

Roveri, M., Lugli, S., Manzi, V., and Schreiber, B. C. (2008). The Messinian Sicilian stratigraphy revisited: new insights for the Messinian salinity crisis. *Terra Nova*, *20*(6), 483–488.

Sirota, I., Enzel, Y., and Lensky, N. G. (2017). Temperature seasonality control on modern halite layers in the Dead Sea: In situ observations. *Bulletin*, *129*, 1181–1194.

Sorrel, P., Popescu, S.-M., Head, M., Suc, J., Klotz, S., and Oberhänsli, H. (2006). Hydrographic development of the Aral Sea during the last 2000 years based on a quantitative analysis of dinoflagellate cysts. *Palaeogeography, Palaeoclimatology, Palaeoecology*, *234*(2-4), 304–327. https://doi.org/10.1016/j.palaeo.2005.10.012

Sorrel, P., Popescu, S.-M., Klotz, S., Suc, J.-P., and Oberhänsli, H. (2007). Climate variability in the Aral Sea basin (Central Asia) during the late Holocene based on vegetation changes. *Quaternary Research*, *67*(3), 357–370. https://doi.org/10.1016/j.yqres.2006.11.006

Stein, M. (2003). The limnological history of late Pleistocene-Holocene water bodies in the Dead Sea basin.

Stein, M. (2014). The evolution of Neogene-Quaternary water-bodies in the Dead Sea rift valley. *Dead Sea Transform fault system: reviews* (pp. 279–316). Springer.

Stein, M., Torfstein, A., Gavrieli, I., and Yechieli, Y. (2010). Abrupt aridities and salt deposition in the post-glacial Dead Sea and their North Atlantic connection. *Quaternary Science Reviews*, *29*(3-4), 567–575.

Torfstein, A., Goldstein, S. L., Stein, M., and Enzel, Y. (2013). Impacts of abrupt climate changes in the Levant from Last Glacial Dead Sea levels. *Quaternary Science Reviews*, *69*, 1–7. https://doi.org/10.1016/j.quascirev.2013.02.015

Van Couvering, J. A., Castradori, D., Cita, M. B., Hilgen, F. J., and Rio, D. (2000). The base of the Zanclean Stage and of the Pliocene Series. *Episodes*, *23*(3), 179–187.

Yang, X., Wang, N., He, J., Hua, T., Qie, Y., et al. (2020). Changes in area and water volume of the Aral Sea in the arid Central Asia over the period of 1960–2018 and their causes. *Catena*, *191*, 104566.

Yechieli, Y., Gavrieli, I., Berkowitz, B., and Ronen, D. (1998). Will the Dead Sea die? *Geology*, *26*(8), 755–758.

Zavialov, P., Ni, A., Kudyshkin, T., Kurbaniyazov, A., and Dikarev, S. (2009). Five years of field hydrographic research in the Large Aral Sea (2002–2006). *Journal of Marine Systems*, *76*(3), 263–271.

Chapter 3

Material

3.1 Halite (Dead Sea basin)

Experimental results obtained during a preceding thesis have shown that both laboratory-grown and natural halite samples could be used for accurate temperature measurements of the host crystal by combining fluid inclusions and Brillouin spectroscopy (Guillerm, 2019). In addition to the finding that it can be used to accurately reconstruct aquatic conditions in halite-bearing terrestrial climate archives, it was further observed that both lake level and volume of the Dead Sea basin (DSB) could be approximately calculated using both, the speed of sound in fluid inclusions and the modeled composition of the lake water body at time of halite accumulation (Guillerm, 2019).

Based to these great findings, a major part of the present dissertation was devoted to the extended practical application of BS on halite layers from the sediment core 5017-1 from the DSB. The sediment core 5017-1 has the advantage of having a full record of the climate conditions covering the last 250 ka (Neugebauer et al., 2014; Torfstein et al., 2015; see chapter 2.2.1). Halite layers from the DSB have been interpreted as annual records of drier and/or lower lake levels (Kiro et al., 2016; Ben Dor et al., 2019), thus providing the unique opportunity to reveal palaeotemperatures on annual scales using BS. Hence, two core sections were selected to measure entrapment temperatures of fluid inclusions, and to reconstruct the annual evolution during two interglacial periods, the MIS 5e (chapter 5), and the MIS 7c (chapter 6). While halite intervals from core section 5017-1-A-122-2 (MIS 5e) cover a short period of 4-5 years, samples from core section 5017-1-A-176-2 were deposited during more than one decade as successive halite layers on annual scales during MIS 7c.

The aim to study extensively such halite layers is related to recent findings of modern halite depositional mechanisms in the Dead Sea, which showed that seasonal-driven temperature changes have a major control on the formation of two

halite types (Sirota et al., 2017):

- cumulate halite (grain size 50-150 µm)
- coarse halite (grain size 400-1000 µm)

It has been observed that cumulate halite precipitates in the mixed water column during winter due to an increased supersaturation of NaCl, while coarse halite forms predominantly during summer when the lake returns to stratified conditions (Sirota et al., 2017). These modern observations are thus an unique opportunity to test qualitatively if such seasonal-driven temperatures changes could be found in the sediment record, and to evaluate if modern observations might act as an analogue for paleohydrological mechanisms in the DSB.

3.2 Laboratory-grown gypsum

Laboratory experimental work was required initially to test the applicability of Brillouin spectroscopy on natural gypsum minerals from geological records. Thus, laboratory-grown ('lab-grown') gypsum crystals were produced from aqueous solutions under varying conditions (temperature, concentrations, degree of saturation, salinity, and wind velocities) to determine the most effective crystallization pathway for bulk crystals, by means of maximum crystal sizes with a maximum amount of entrapped FIs.

All experiments implied a full evaporation of the aqueous solutions until the last solid crystals precipitated. The first evaporitic experiments were conducted by dissolving pure $CaSO_4 \cdot 2\,H_2O$ powder (Sigma Aldrich, ReagentPlus ®, $\geq 99\%$) in beakers (volumes = 50, 100, 500, 1000 ml) with pure H2O (Milli-Q ®, 18.2 M Ω cm). The solubility of $CaSO_4 \cdot 2\,H_2O$ in 1 L H_2O is 2.2 g at 25 °C which is very low compared to NaCl (360 g/L).

The first solution has been prepared to investigate the synthetical process of crystal shapes, sizes, and entrapment of fluid inclusion in solution of 1 L with 2.2 g dissolved $CaSO_4 \cdot 2\,H_2O$ powder. Gypsum nucleation started after evaporation of ca 220 mL H_2O and continued until full evaporation as seen by fine layers on the beaker glass walls (Figure 3.1 A). After ca 10 days of evaporation at constantly 21 °C, very tiny (<20 µm) gypsum crystals with non-detectable thicknesses remained at the beaker bottom (Figure 3.1 B).

The second solution ("Solution II") was prepared by dissolving 0.88 g $CaSO_4 \cdot 2\,H_2O$ in 0.4 L H_2O, thus the solution was saturated by 96.1%. The powder was dissolved after 24 hours and the stock solution of 0.4 L further divided into smaller experimental solutions to test gypsum crystal growth at different temperature conditions. Solution II-A (volume = 0.1 L) evaporated for 1 week in a 1 L glass beaker using a

thermal bath set to 26.5 °C. The actual beaker water temperature was constantly 25 ±0.4 °C. After complete evaporation of 0.1 L solution, the resulting gypsum crystals were fine-grained (<50 µm) with fibrous-needle shapes forming abundant circular assemblages. Solution II-B (volume = 0.187 L) was evaporated in a 0.2 L beaker contemporaneously on a stirring hotplate (Cat Scientific MCS 66) with a temperature set to 60 °C. The beaker water temperature reached a constant value of 42 °C after 6 hours. First gypsum crystals were observed to appear at the water-air interface as small nucleates after 47% of H_2O evaporation loss. The final solids were collected after 1 week.

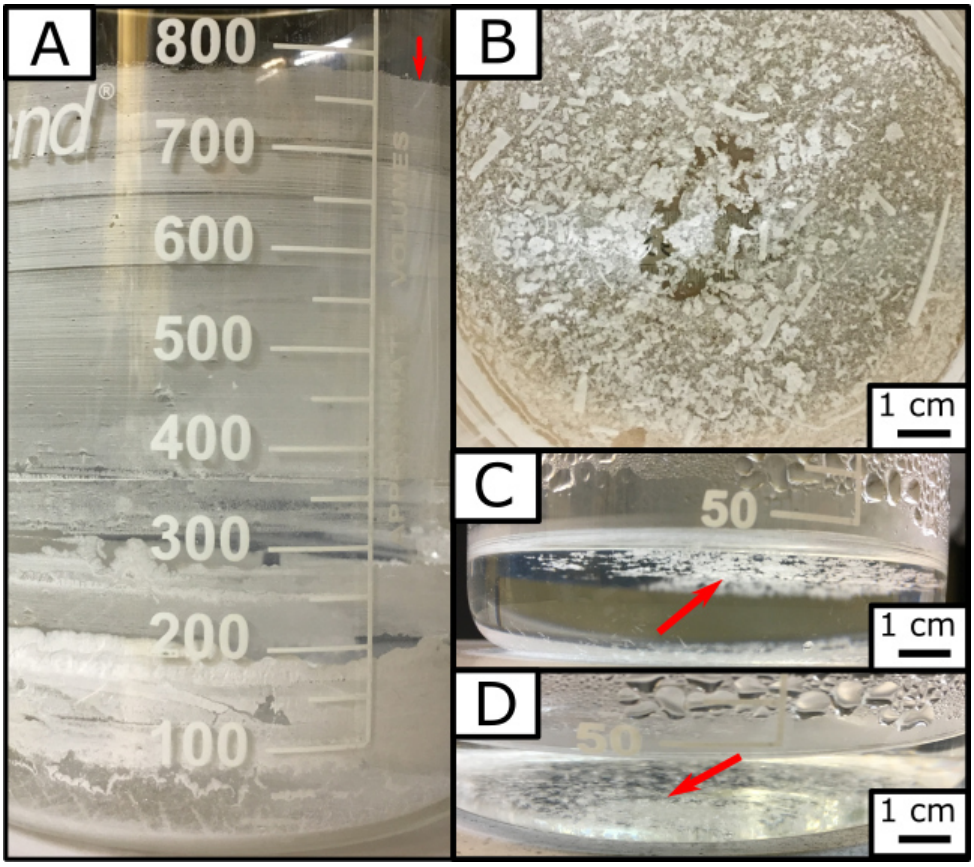

Figure 3.1 Lab-grown gypsum material of purely dissolved $CaSO_4 \cdot 2\,H_2O$ in water. A) nucleation steps of gypsum during evaporation of water, forming thin layers. B) Top view of (A) with tiny (<40 µm) crystals. C) Gypsum nucleation takes places at the air-solution interface (red arrow), and D) sinks then to the beaker's bottom (red arrow).

Growth experiments of purely dissolved $CaSO_4 \cdot 2\,H_2O$ in pure water resulted in very fine-grained (10 - 50 µm) single gypsum crystals with thin elongated shapes with crystal widths of 10 - 30 µm) (3.1 B). Another common feature is the formation of larger, rounded assemblages of small crystals with sizes of up to 2000 µm (3.2 A). A third group of precipitated gypsum crystals contains either single tabular forms with broader sizes (up to 150 µm) or crystal twinning (3.2 B-C). Synthetic gypsum

samples from growth experiments with solutions containing dissolved solutes of both NaCl and $CaSO_4 \cdot 2\,H_2O$ are generally larger in individual crystal sizes with very abundant crystal twinning (3.2 C). Further, entrapped fluid inclusions are more abundant than in samples from pure $CaSO_4 \cdot 2\,H_2O$ evaporated solutions. Small halite nucleates (1-10 µm) were observed as solid inclusions entrapped in bulk gypsum crystals or being attained on the surfaces of bulk gypsum crystals. Lenticular crystal shapes, naturally common in lake sediments or arid sabkha environments (Al-Youssef, 2014), have been observed irregularly in synthetic bulk gypsum samples.

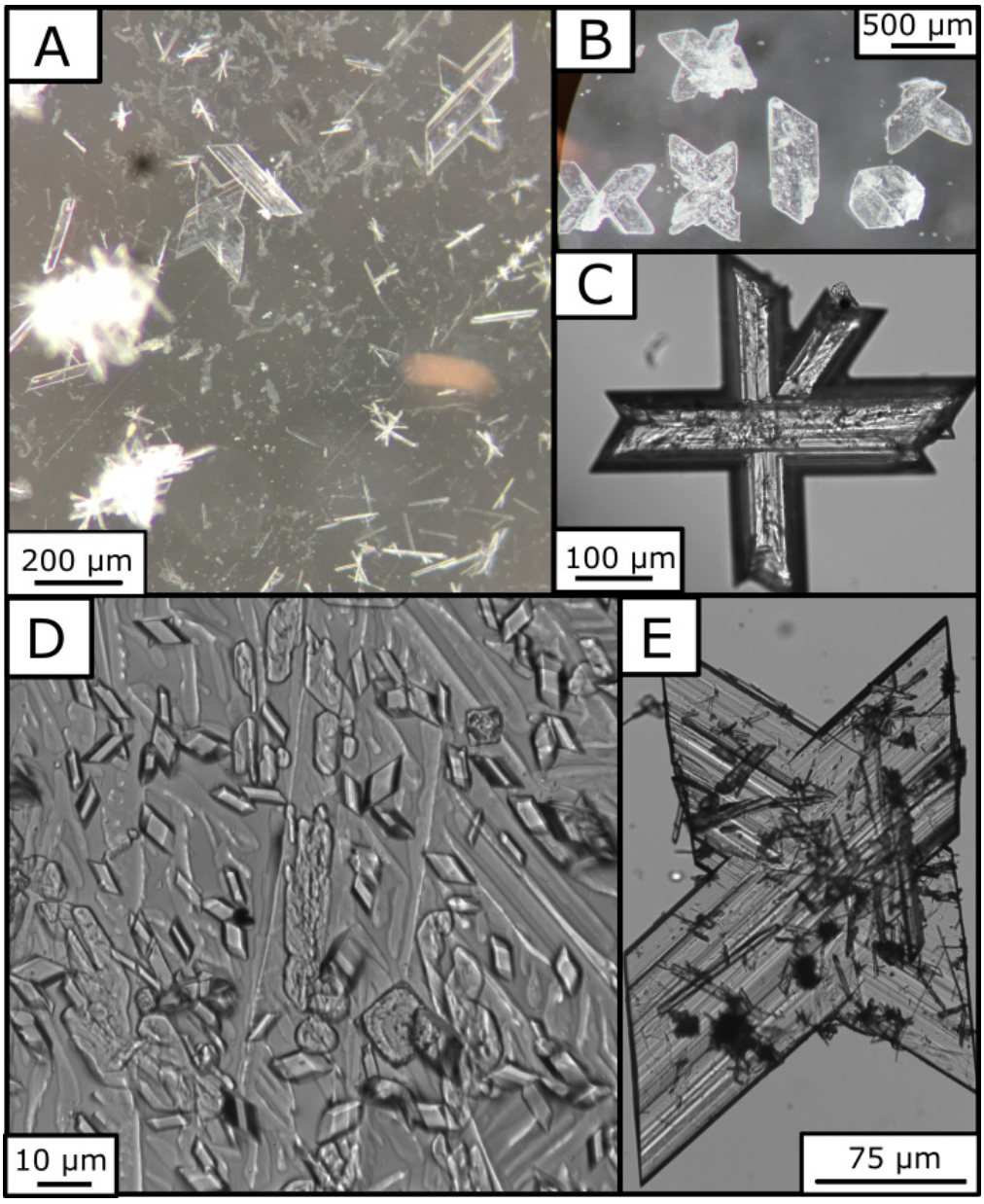

Figure 3.2 Microscopic view on synthetically-produced gypsum samples. A, C, D) precipitates from bulk solutions with dissolved CaSO4*2H2O in pure water. B, E) Crystals from bulk solutions containing small amounts of NaCl. Note the difference in crystal sizes between salty bulk solutions and pure water.

3.3 Natural gypsum samples

3.3.1 Aral Sea

As described in Section 2.2.2, today's Aral Lake is located in a highly saline drying area with strongly reduced water volume. As a consequence, regression features characterise the modern shoreline with abundant formations of large-sized gypsum crystals. During two field campaigns in December 2018 and May 2019 by Hedi Oberhänsli and a team led by Peter Zavialov, several samples were collected at various sites along the shorelines. The gypsum samples are up to 10 cm long and contain very thin (ca <50 µm) individual layers (ca 1 cm thick) that form larger monocrystals (Figure 3.3 A). The direction of crystal growth is mainly indicated in the reversed direction of dihedral (V-shaped) forms that contain macroscopic-visible whitish fluid inclusion bands. Some fluid inclusions have sizes big enough to be observed under a binocular or even with the naked eye. Samples were cut along the {010}, cleavage plane and broken into small pieces of ca 1.5 cm length for microscopy. Characteristic features of all samples are abundant fluid inclusion assemblages with varying sizes, both of primary and secondary origin with elongated to monoclinic shapes. In some pieces, very large FIs were observed (>500 µm) with irregular shapes, and some of them suggested to contain other fluid or gases than just H_2O.

A short core from the Western basin revealed one distinct gypsum layer with lenticular gypsum crystals with size ranges between 50-300 µm (Figure 3.3 B). Each crystal needs to be cut 2-3 times during preparation due to the angular form. They neither contain FIA nor abundant FI bands, only in rare cases single elongated small (<5 µm) FIs were observed. Samples from this core were no further used during the work, but it is worth to know that both types were found along the

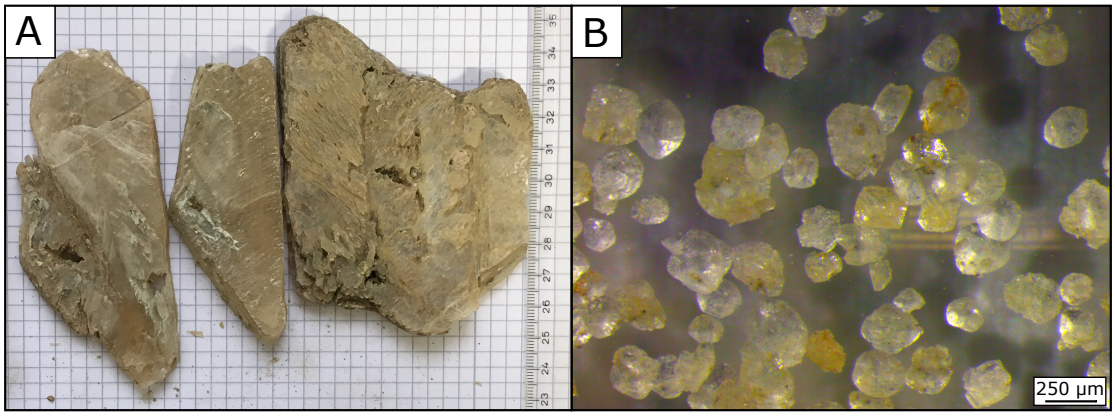

Figure 3.3 Natural gypsum samples used for experiments. A) Selenite-type growth of Holocene soil gypsum (not dated). B) Typical lenticular gypsum crystals from a short core drilled in the Western basin (Sorrel, 2006).

Western basin shoreline.

Four water samples could be collected from the Western basin, two of them from small surface ponds fed by upwelling groundwater flows (Figure 3.4). Salt crusts around the bottles were observed when the samples arrived in Lyon, and indeed the water differed in its optical appearance from pure water. Both samples were used for sound velocity measurements and labelled as AS11 and AS13. Further, two samples from the Large lake were collected at the surface and at the bottom of ca 20 m depth. Conductivity measurements in 2002 showed that salinity varied from the surface (82 g/kg) to the 25 m lake bottom (110 g/kg) (Friedrich and Oberhänsli, 2004). Hence, a relatively apparent difference in sound velocity can be hypothesised for both water body samples.

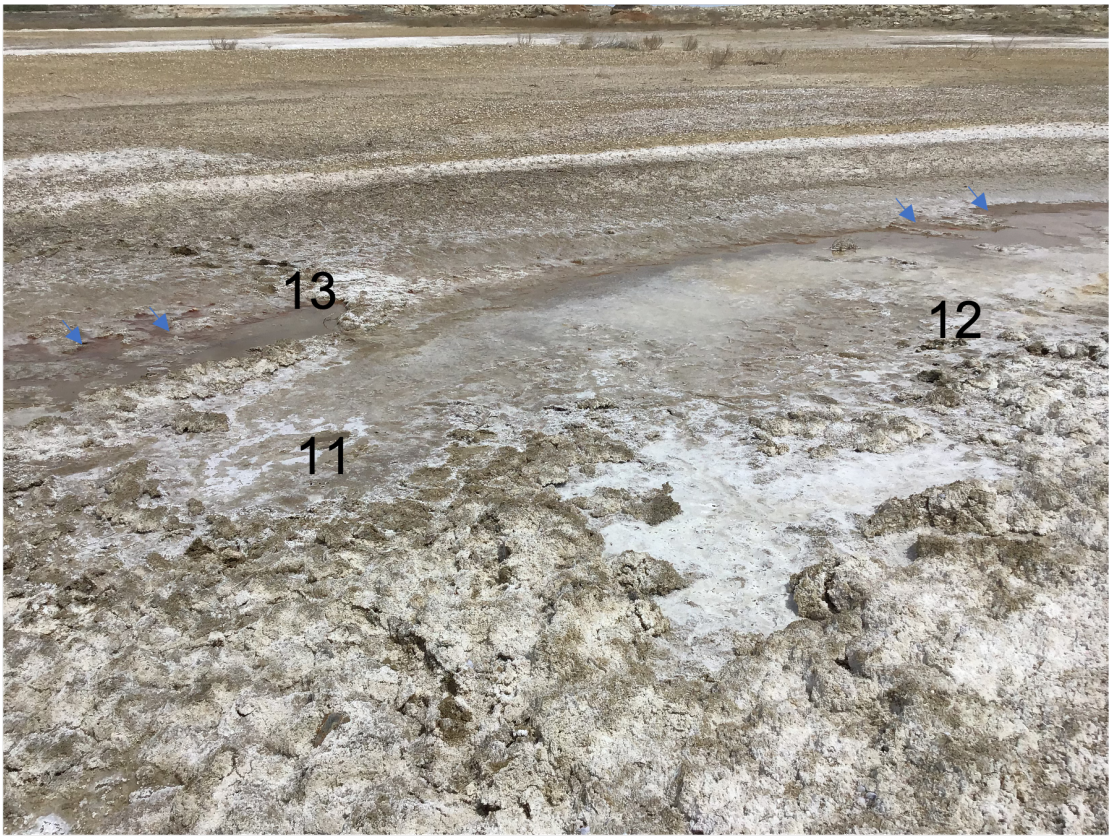

Figure 3.4 Water samples used in this work for sound velocity measurements (11 = AS11, 13 = AS13). See chapter 8.2.3 for results.

3.3.2 Sabkha El Melah

A large (6 cm size) swallowtail gypsum crystal from the Holocene sabkha El Melah was used for detailed studies on trapped fluid inclusions using microthermometry and Brillouin spectroscopy to measure final ice melting points of biphasic FIs and sound velocities of both mono- and biphasic FIs. Its depositional origin has been attributed to the desiccated shoreline of the sabkha in which sulphate-rich waters form bottom-grown gypsum (selenite type).
The growth direction runs in direction to the dihedral form, so that the flat crystal bottom (uppermost part in Figure 3.5) is the relatively youngest part, and the pyramidal-shaped part the relatively oldest part (lowermost part in Figure 3.5. Three sub-samples were cut out of the crystal along the { 010} cleavage plane by using a razor blade with labels 05 (youngest part), 09 (intermediate part), and 07 (oldest part). Each sub-sample contains three types of FIs: growth bands with aligned primary FIs having flat bases and triangular-like shapes to the top (Figure 3.6 A), randomly distributed elongated fields with abundant occurrences of probably secondary FIs, and fields of secondary FIs with smaller but broader irregular shapes (Figure 3.6 B).

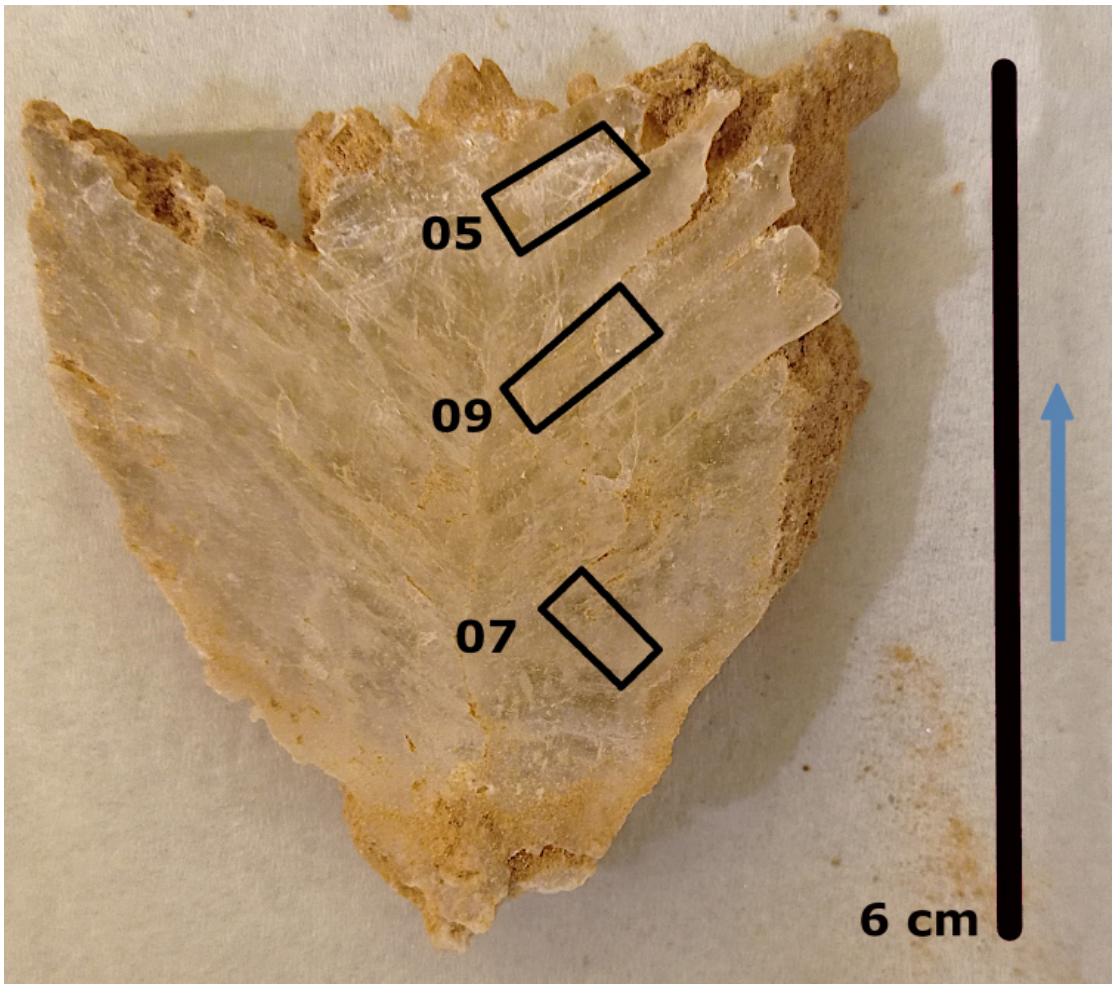

Figure 3.5 Selenite gypsum sample MG1 from the El Melah sabkha environment. Blue arrow indicates the direction of growth.

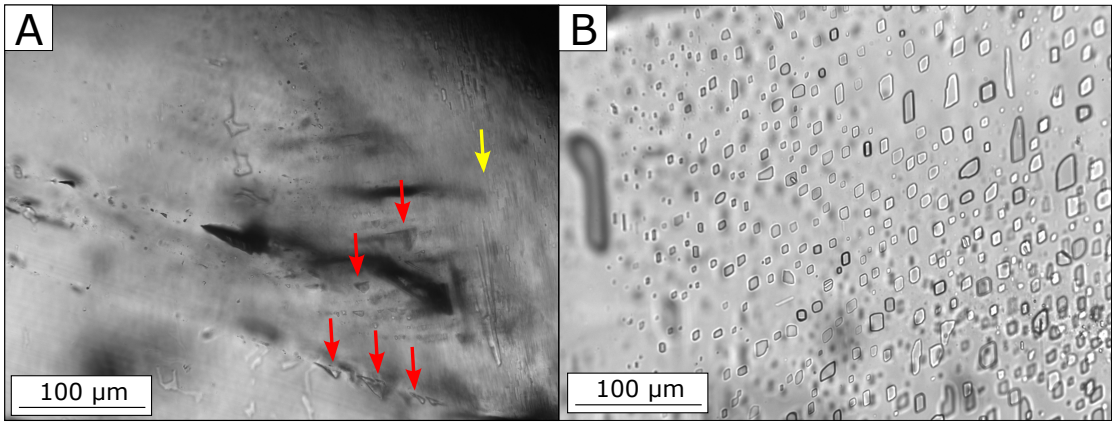

Figure 3.6 Fluid inclusions in gypsum sample MG1. A) Primary FIs (red arrows) aligned on growth bands indicating the crystals' growth direction. Yellow arrow points to an adjacent secondary elongated FIA. B) Secondary FIs in the same crystal as A), but ca 2 mm apart towards a younger part of this interval.

3.3.3 Gypsum formed during the MSC

A field trip to Sicily in May 2019 offered the unique opportunity to collect gypsum samples from various locations. The trip was organised by SaltGiant, an European funded multi-project related to the formation of the Mediterranean Salt Giant (MSG). For this thesis, material was used for potential Brillouin spectroscopy analyses from mainly two outcrops located at the Western shoreline (Eraclea Minoa) and in the interior part close to Santa Elisabetta. The swallowtail gypsum (selenite) forms large crystals that are strongly bound by fine-grained detrital material (Figure 3.7).

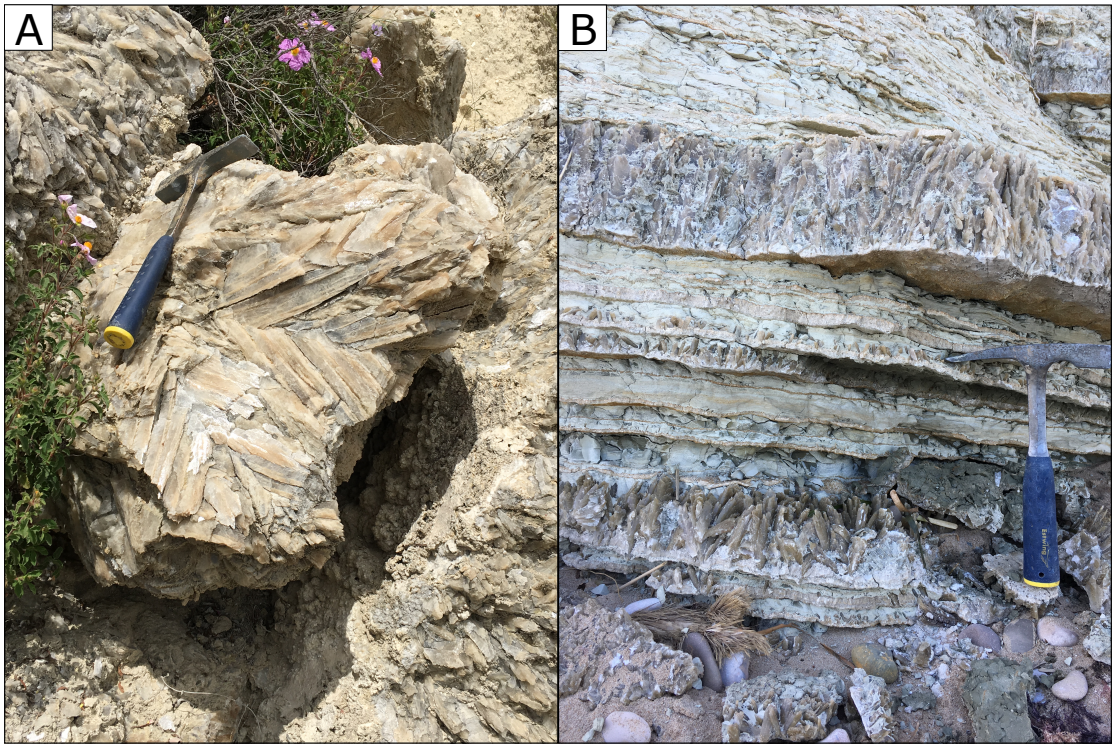

Figure 3.7 Messinian gypsum samples from Sicily. A) Selenite close to Santa Elisabetta. B) Eraclea Minoa GSSP locality with bedded selenite gypsum units intercalated by fine mud and silt layers.

Growth bands with aligned primary FIs are lacking in all studied sub-samples, however, elongated to pentagonal shapes could be observed in each case. This indicates alteration of the material, likely due to its long exposure to solar radiation.

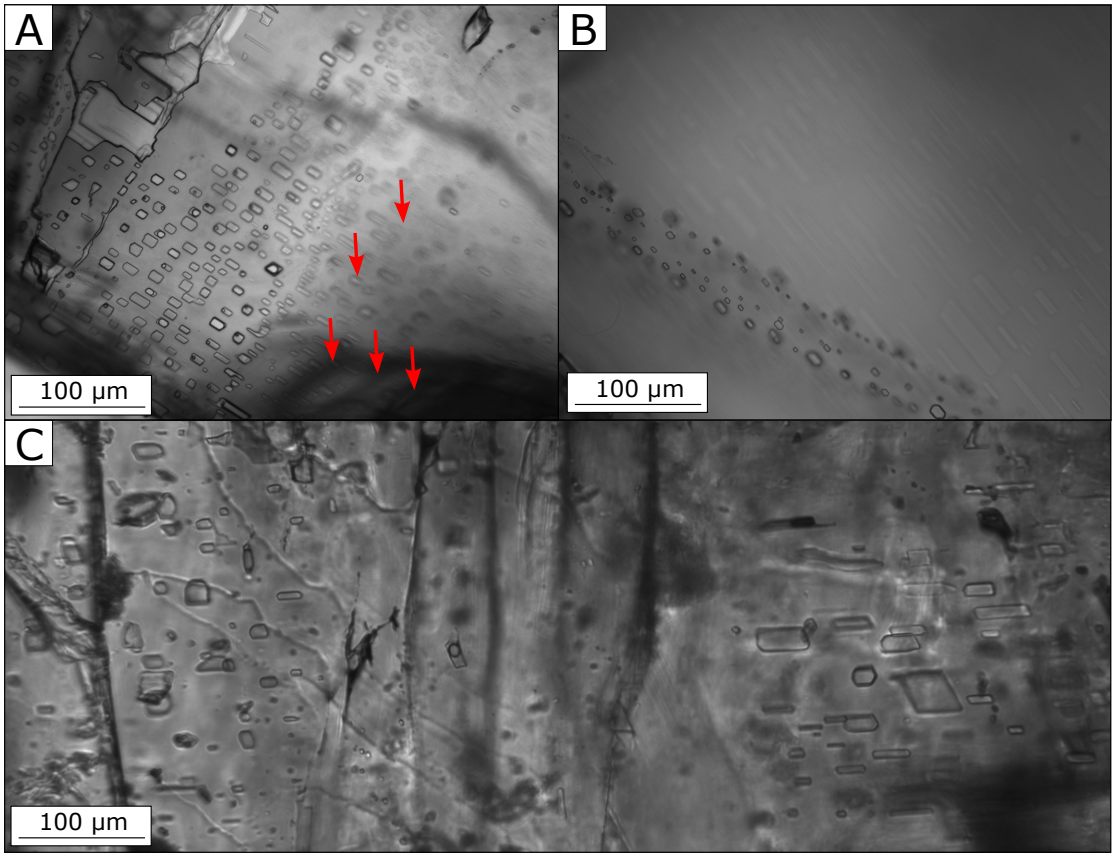

Figure 3.8 Messinian gypsum samples from both NW Italy and Sicily. A) FIs in a sample from Banengo, Piedmont Basin (provided by M. Natalicchio). B) Healed crack filled with FIs (from Eraclea Minoa, Sicily). C) Two fields showing the large variations in FI shapes (from Eraclea Minoa, Sicily).

Bibliography

Al-Youssef, M. (2014). Gypsum Crystals Formation and Habits, Umm Said Sabkha, Qatar. *Sabkha ecosystems* (pp. 23–54). Springer.

Ben Dor, Y., Neugebauer, I., Enzel, Y., Schwab, M. J., Tjallingii, R., Erel, Y., and Brauer, A. (2019). Varves of the Dead Sea sedimentary record. *Quaternary Science Reviews*, *215*, 173–184. https://doi.org/10.1016/j.quascirev.2019.04.011

Friedrich, J., and Oberhänsli, H. (2004). Hydrochemical properties of the Aral Sea water in summer 2002. *Journal of Marine Systems*, *47*(1-4), 77–88.

Guillerm, E. (2019). *Turning halite fluid inclusions into accurate paleothermometers with Brillouin spectroscopy: development of a new method and application to the Last Interglacial in the Dead Sea.*

Kiro, Y., Goldstein, S. L., Lazar, B., and Stein, M. (2016). Environmental implications of salt facies in the Dead Sea. *Geological Society of America Bulletin*, *128*, 824–841. https://doi.org/10.1130/b31357.1

Neugebauer, I., Brauer, A., Schwab, M. J., Waldmann, N. D., Enzel, Y., Kitagawa, H., Torfstein, A., Frank, U., Dulski, P., Agnon, A., Ariztegui, D., Ben-Avraham, Z., Goldstein, S. L., and Stein, M. (2014). Lithology of the long sediment record recovered by the ICDP Dead Sea Deep Drilling Project (DSDDP). *Quaternary Science Reviews*, *102*, 149–165. https://doi.org/10.1016/j.quascirev.2014.08.013

Sirota, I., Enzel, Y., and Lensky, N. G. (2017). Temperature seasonality control on modern halite layers in the Dead Sea: In situ observations. *Bulletin*, *129*, 1181–1194.

Sorrel, P. (2006). *The Aral Sea: a palaeoclimate archive.* University of Potsdam, Germany.

Torfstein, A., Goldstein, S. L., Kushnir, Y., Enzel, Y., Haug, G., and Stein, M. (2015). Dead Sea drawdown and monsoonal impacts in the Levant during the last interglacial. *Earth and Planetary Science Letters*, *412*, 235–244. https://doi.org/10.1016/j.epsl.2014.12.013

Chapter 4

Methods

Experiments performed during this PhD thesis have been related largely to Brillouin spectroscopy (BS) and included a variety of sample types, technical parameters, analytical approaches, and scientific objectives. Therefore, this chapter aims to provide any necessary information about the experiments, however, all subsequent sub-chapters dealing with BS refer to the methodology described in 4.1.

This chapter outlines several approaches to finally measure:
(1-A) single sound velocity (w) of fluid inclusions (FIs) in natural gypsum (4.2) and
(1-B) the salinity of FIs using microthermometry (4.7),
(2) multiple w to calculate entrapment temperatures (T_x) of gypsum and halite (4.3), and
(3) single w of capillary solutions to build a salinity proxy based on BS (4.6).

4.1 Brillouin spectroscopy

This section provides technical information about the basic principles of Brillouin spectroscopy and the instrumental set-up using aligned optics in the laboratory. For information about the practical procedure during measurements of fluid inclusions, the reader is referred to chapters 5.3 and 5.7.

4.1.1 Principles

The Brillouin spectroscopy method (BS) is named after the French physicist Léon Brillouin (1889 - 1969) who predicted theoretically for the first time how x-rays would propagate through crystals by inelastic scattering of light (Brillouin, 1922). The method is based on scattering effect due to an inelastic interaction of an incoming monochromatic light and thermodynamic fluctuations of any substance. Travelling light is characterised with a frequency f and corresponding to photons of energy:

$$E = h * f \tag{4.1}$$

with E the energy and h the Planck constant. The light-matter interaction can be either elastic (no energy change) or inelastic (energy increase or decrease). The principle of BS is the inelastic scattering of light, which induces a change in energy of the photons, associated to a frequency shift, the Brillouin frequency shift Δf_B). The main principle for BS measurements is the relationship between Δf_B and sound velocity w at a given laser wavelength λ and refractive index n, respectively:

$$\Delta f_B = 2 * \frac{\sin(\frac{\theta}{2}) * n * w}{\lambda} \tag{4.2}$$

where θ is the scattering angle. In our case, backscattering is used in the microscope objective, which corresponds to $\theta = 180°$.

4.1.2 Optical setup

The spectroscopy laboratory in Lyon (Institute of Light and Matter, Campus de la Doua) is equipped with a Verdi V-6 system (Coherent) that is a diode-pumped Nd:Vanadate (Nd:YVO_4) laser, working with green monochromatic light (532 nm). To cool the system, it is supplied externally by both an air-conditioning system and a chiller that is connected with water lines to the system. The common working laser beam power is set to 4 W. This high power is required to ensure longitudinal mono-mode (single frequency) operation of the laser, which is critical for Brillouin spectroscopy. Note that the beam intensity is later attenuated to reach $\leq$ 100 mW at the sample to avoid any thermal effects. A tandem multi-pass Fabry-Pérot interferometer (TFP-2) inside the Brillouin box (JRS Scientific

Instruments) focuses the scattered light finally into the multichannel analyser (MCA) that detects the photons (Figure 4.1). The detected intensity in number of counts is then transferred to a computer and subsequently fitted to compute the sound velocity (Figures 4.2 and 4.3; for more details see Mekki-Azouzi et al., 2015).

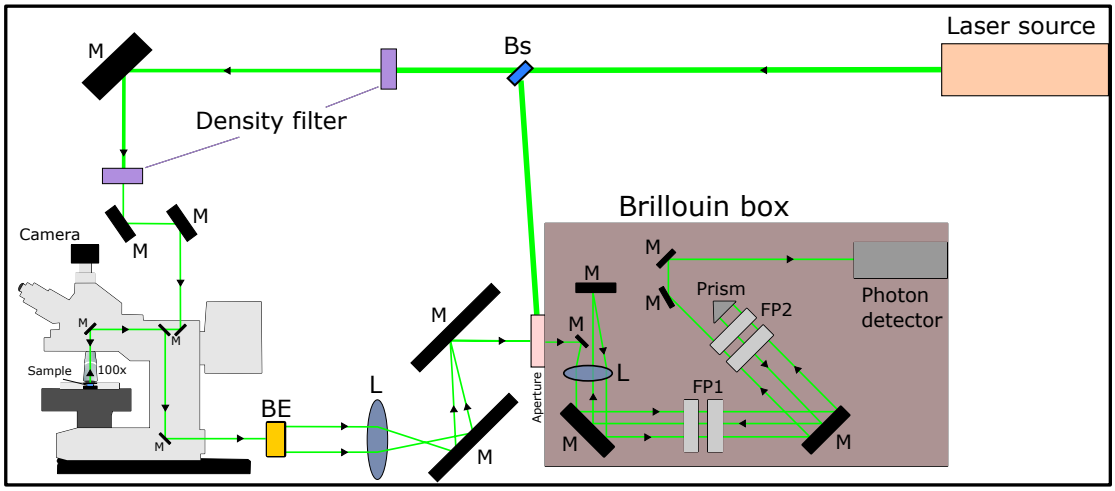

Figure 4.1 Sketch of the instrumental setup for BS. Green line represents the trajectory of the laser beam, black arrows indicate direction of travel. M = Mirror, L = Lens, Bs = Beamsplitter, FP = Fabry-Pérot interferometer. To outline the backscattering process, note that the microscope is shown in side view, while the other elements are drawn in top view. Not to scale.

Samples were studied with an upright optical microscope (Zeiss Axio Imager.Z2 Vario), equipped with a long-working distance x100 objective (Mitutoyo Plan-Apo, N.A. 0.7). The microscope is linked to a temperature-controlled stage (Linkam, THMS 600) with an uncertainty of ≤ 0.1 °C. Any thermal cycles (heating) necessary for any sample are controlled by a silver block on which the sample is placed, and cooling of the material is performed using liquid nitrogen.

4.1.3 Fitting procedure

Subsequently, each detected Brillouin peak is fitted by a viscoelastic model (see Boon and Yip, 1991 for more details). It includes a memory function with an exponential decay (Pallares et al., 2014):

$$m(Q,t) = (c_\infty^2 - c^2) * Q^2 * [\exp -(\frac{c}{c_\infty})^2 * \frac{t}{\tau}] \tag{4.3}$$

where Q is the wavevector probed by the scattering setup, c and c_∞ the sound velocity at zero and infinite frequency, respectively, and τ a structural relaxation time. Note that c_∞ is chosen to be a constant at 3000 m/s (Pallares et al., 2014).

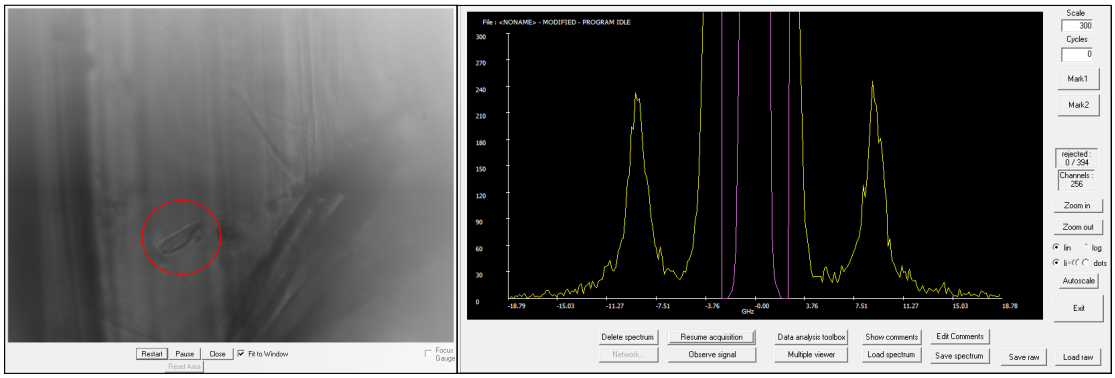

Figure 4.2 Brillouin spectra of a FI (red circle) in a lab-grown gypsum crystal. Left: Gypsum FI. Right: Recorded spectrum with reference line (violet) and inelastic (yellow) scattering from the FI.

Further, Q is given in backscattering geometry by:

$$Q = \frac{4 * \pi * n}{\lambda} \tag{4.4}$$

where n is the refractive index of the liquid. The full analysis includes further both the instrumental resolution function (IRF) and the dark count of the setup. The IRF was determined for each pinhole (entrance of Brillouin box in Figure 4.1 from the elastically scattered light from a suspension of 350 nm polystyrene spheres. The final IRF resulted finally in a Gaussian fit. To measure the dark count of the photodetector, spectra were taken with the spectrometer entrance closed (Pallares et al., 2014). After Pallares et al. (2014), the necessary steps to analyse Δf_B spectra are to get the functional form of the viscoelastic model 4.3, to perform a numerical convolution with the IRF, to add the known dark count of the photomultiplier, and to fit the resulting function on the raw spectra (Pallares et al., 2014). Three fitting parameters are used in each analysis: c, τ, and an overall intensity factor K. The merit function χ^2 is minimised by the sum of square errors and normalised by the error bars on the data points. The error bars are caused by the photon noise which is defined as the square root of the number of counts (Pallares et al., 2014).

4.2 Sound velocity measurements

An individual sound velocity measurement of FI_i follows a specific protocol that has to be respected with respect to its workflow, security standards, and data organisation (see Appendice A). Suitable locations of FIs were initially investigated using objectives x10, x20, x50 or x100.

Gypsum samples were mostly measured at seven to eight, partly even at more than eight temperature points. The first experiments were initially carried out at room temperatures because (1) the Linkam stage does not need to be cooled using liquid nitrogen (N_2), (2) the potential risk to nucleate a vapor bubble is prevented, and (3) potential damages during sample preparation can be detected by analysing the first batch of acquired spectra. Regardless of the FI phase, the most secure way was found to start at 22 °C $< T <$ 25 °C. Subsequently, the crystal (including all FIs) was cooled down gradually by maintaining a distinct temperature difference between each temperature step, e.g., a 8 °C difference would be respected between the starting measurement I (23 °C), the followed measurements II (15 °C) and III (7 °C), and the last measurement IV (31 °C). These thermal cycles can be adapted for each sample with varied temperature differences.

It is important to note that the lowest temperatures (III) should be well $<$ 10 °C since local thermal fluctuations in natural brines can occur. However, for natural samples from locations with warmer climates (e.g. sabkhas, deserts, thermal springs), the temperature ranges can be adapted towards higher values. As an example, FIs in gypsum samples from Tunisia with known brine temperatures well $>$ 20 °C were measured for Brillouin Spectroscopy at elevated temperatures between 15-50 °C to investigate their potential entrapment temperatures.

To analyse a dataset of $crystal_i$ with n sets of FI_is, a registered *.txt*-file after acquiring the frequency shift has to be analysed with a special analytical code using Wolfram Mathematica. This *.txt*-file contains all essential information about

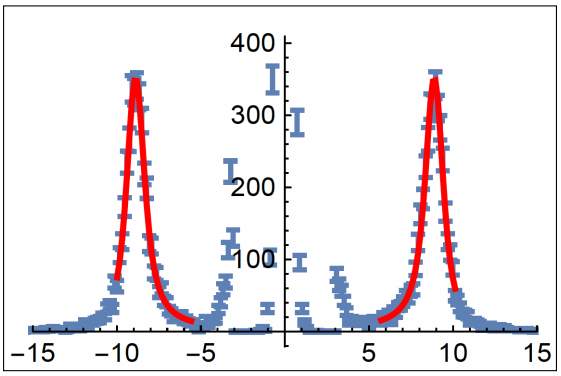

Figure 4.3 Fitted Brillouin spectra by using a specific code written in Wolfram Mathematica.

FI_i (e.g., size, crystal depth, scan number, temperature) which then can be read by the analytical code. It translates the frequency shift, that is the number of photon counts as a function of frequency in GHz, into both relative sound velocity values and relative ratios with respect to a NaCl reference FI_{ref}. The NaCl reference FI_{ref} is used to correct for the instrumental daily drifts of both, the optical alignment and the laser engine (e.g., it warms up during several hours of usage). The final files after spectra analysis contain besides the raw sound velocity values and the referenced ratio for FI_i also χ^2 values for each spectrum fit which indicates potential fitting issues. As a rule of thumb, χ^2 values should be < 2 to ensure a well fitted spectra, leading to relative precise raw sound velocity values, whereas χ^2 values > 2 might point to potential problems related to (1) the choice of FI_i, (2) the measurement itself, (3) not optimally set "Brillouin windows", or even (4) typing errors within the *.txt*-file.

4.3 Entrapment temperatures

The procedure for entrapment temperature measurements in FIs is slightly more advanced than for single w measurements : Although the main principle of acquiring Δf_B spectra does not change, it is based on six to eight runs per FI. E.g., for halite the most accurate way to produce a significant amount of FI data are eight single measurements (Guillerm, 2019; see chapter 5). The choice of intervals to be selected is left up to the sample type, the mineral, or the scientific objective, however, it should be well thought out before starting the work.
Entrapment temperatures (T_f) are defined as the intersecting point of fitted isochores and SLVE curves at ambient pressure. Hence, single w values obtained in 4.2 had to be sorted by descending temperature values and for each FI per crystal in separated files for isochores and SLVE data, allowing to find each intersection by calculating the crossing point (T_x) between a line (isochore) and a polynomial (SLVE). The calculation of T_x was carried out by using a program code in Wolfram Mathematica.

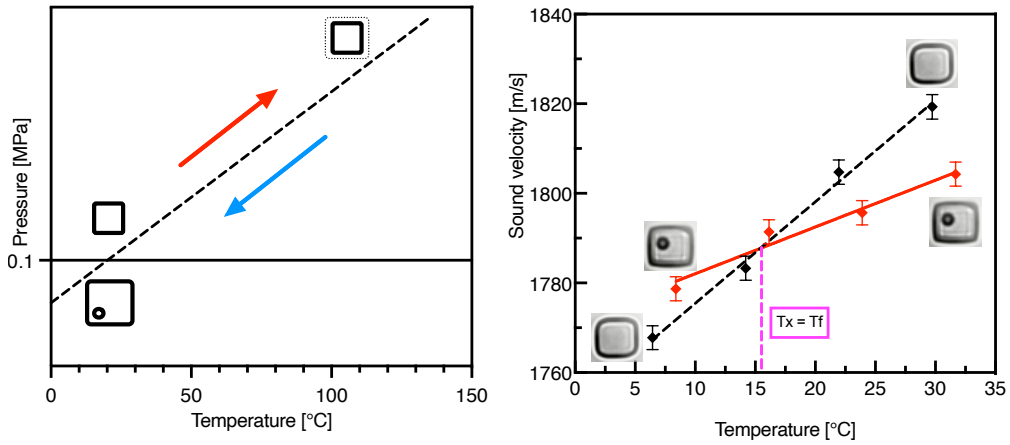

Figure 4.4 Left: Sketch of the cavitation process of a FI. A monophasic FI follows a quasi-isochore (dashed black line) upon heating (red arrow) with increasing internal pressure. During cooling (blue arrow) the internal pressure becomes negative. The FI stretches to to overcome the metastable phase (dashed black rectangles). Energy release forces a vapor to nucleate to re-enter the stable phase. By theory, the thermal path of a biphasic FI follows SLVE that represents ambient pressure conditions. Right: Sound velocity measurement in monophasic (black dashed line; isochore) and biphasic (red solid line; SLVE) phases by at four temperature steps. The intersection of both lines (T_x) gives the entrapment temperature (T_f) if the sample has precipitated at ambient pressure. In most geological cases, a pressure-correction is needed.

4.4 Thermal cycles of fluid inclusions

The analysis of entrapment temperatures in FIs of any kind of mineral requires two thermodynamic phases as shown in Section 4.1. The measurement of monophasic FIs is carried out simply by varying the temperature in the Linkam Stage. For a moderate temperature interval (e.g., between 5-40 °C), the resulting pseudo-isochoric curves for w(T) are linear. In general, w(T) along the solid-vapor-equilibrium (SLVE) is not linear, and we use a polynomial fitting to describe the SLVE. An issue is that it is not always straightforward to nucleate a bubble in a monophasic FI to make it biphasic. A usual method is to sufficiently cool the sample in order to induce a tension in the liquid high enough to trigger cavitation. Unfortunately, this does not happen systematically. Experiments carried out on both synthetical and natural halite (NaCl) samples showed that salt-rich FIs cavitated rapidly (within seconds to minutes) after thermal heating-cooling cycles from ambient temperatures up to 130 °C and back within 2-4 minutes (Guillerm, 2019). Heating results in permanent plastic deformation of the FI, with a volume increase that makes the tension higher when cooling back to ambient temperature, leading to cavitation. This procedure was found to transform FIs reliably from monophasic into biphasic phases in most cases, enabling to perform measurements

of both phases within the same day of experiments (Guillerm, 2019).
However, thermal-heating cycles might be limited for the four phases of the $CaSO_4-H_2O$-system with gypsum $CaSO_4 \cdot 2\,H_2O$, hemihydrate $CaSO_4 \cdot \frac{1}{2}\,H_2O$, y-$CaSO_4$ and anhydrite (van't Hoff, 1912). This is due to the low dehydration temperature at atmospheric pressure that starts slowly above 42 °C, with a metastable field between 42-97 °C (Posnjak, 1938). Other studies showed that dehydration to hemi-hydrate starts >80 °C and further >115 °C to transform into the anhydrous phase, depending on the external partial pressure of water vapor (Ball and Norwood, 1969). Nevertheless, two kinds of thermal cycles have been tested to find the best cavitation procedure for gypsum samples: (1) heating-cooling cycles (hcc) and (2) cooling-heating cycles (chc) at several temperature steps, temperature ranges and heating or cooling rates. The stepwise heating during hcc should test if gypsum FIs cavitated faster and more often compared to a direct heating from room temperature to +130 °C. During chc, more negative temperature steps were tested (e.g., -20, -40, -60, -80, -100 °C) with varying duration. Temperature ranges of hcc (chc) did not extend beyond 130 °C (-130 °C). The rates of heating or cooling were either set to be slow (e.g., 2-10 °C/min) or fast (e.g., 10-30 °C/min) to study the control on gypsum FI cavitation processes with respect to the thermal rates.

4.5 Salinity

As introduced in chapter 1.5, The term "salinity" refers to a variety of used definitions and units. For this work, both published data and derived equations for NaCl solutions were used for interpreting the measured sound velocity data (see Chapter 8.1, 4.1). This allowed to compare and evaluate directly the data from the literature with measured sound velocity values of pure water and NaCl solutions. Following this, other solutions containing natural brines from the Mediterranean Sea, the Aral Sea and the Dead Sea were used to estimate the salinity values.
A crucial point in interpreting sound velocity data from Brillouin spectroscopy is the correction factor for the capillaries because the refraction of light at interfaces affects the detected final w value. The correction factor is determined by measuring the raw value of w in a capillary filled with pure water. The average ratio of the tabulated values for w to the raw values is 0.9741 ±0.002 (8.1).
The temperature to account for the correction factor evaluation was set to $T =$ 25 °C because it turned out to be the most practical value during BS-salinity measurements (see chapter results and discussion). The relative NaCl w values

from Chen and Millero, 1986 are converted into absolute ones, using 4.5:

$$w^0_{H2O} = 1402.388 + 5.03711T - 5.80852 * 10^{-2}T^2 + 3.342 * 10^{-4}T^3 \\ -1.478 * 10^{-6}T^4 + 3.1464 * 10^{-9}T^5 \quad (4.5)$$

with T the temperature in °C. After 4.5, $w^0_{H2O}(25\ °C) = 1496.7$ m/s, which is used as constant summand for absolute NaCl w values. Both the relative and absolute NaCl w values from Chen and Millero, 1986 are listed in Table 4.1. The derived equation from the cubic fit is:

$$w^0_{NaCl} = 0.031m^3 - 2.3728m^2 + 61.82m + 1497.2 \quad (4.6)$$

with m the concentration (molar ionic strength) in mol/kg or mol/L. The known concentrations of NaCl-bearing capillaries have been inserted into 4.6 and compared to data from the literature (Table 4.1).

The observed final ice melting points (in °C; see 4.7) were used to calculate the salinity S, expressed here as "weight % NaCl equivalent" (wt. % NaCl eq.). The salinity of each FI was calculated after Bodnar, 1993:

$$S = -1.78 * T_{ice} * (-1) - 0.0442 * T^2{}_{ice} + 0.0005572 * T^3{}_{ice} * (-1) \quad (4.7)$$

with T_{ice} the final ice melting temperature (in °C) of each FI. The resulting nonlinear fit is shown in Figure 4.5). Since the exact chemical compositions of the individual gypsum FIs could not be determined elsewhere, those FIs were first also analysed whose eutectic points were ≠ -21.2 °C.

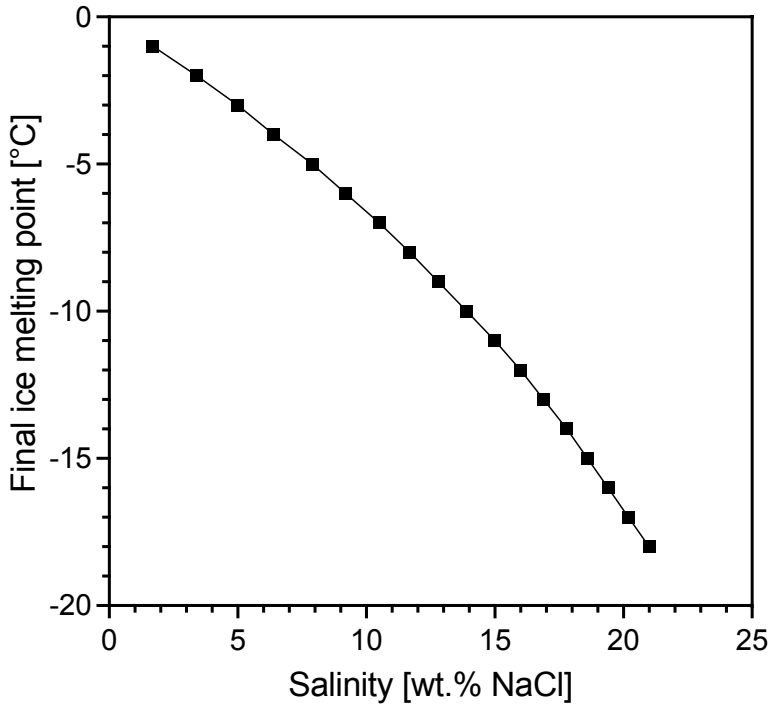

Figure 4.5 Final ice melting temperatures as a function of salinity in salty aqueous solutions after Bodnar (1993).

4.6 Saline aqueous solutions

First, the mass of NaCl to be weighed in x mass water (m_{H_2O}) for a certain desired salinity S_i (in wt %) was calculated by:

$$m_{NaCl} = -\frac{m_{H_2O} * S_i}{S_i - 100} \tag{4.8}$$

with m_{NaCl} in g, m_{H_2O} in g, and S_i in %. For a molar mass M of NaCl of 58.44 g/mol, the molality b (in mol/kg) was calculated using:

$$b = \frac{m_{NaCl} * 1000}{M * m_{H_2O}} \tag{4.9}$$

Under air-conditioning controlled conditions at 21 °C, the masses of NaCl (UMR Chemicals NORMAPUR, 100% NaCl) of S_i were first weighted dry into 100 mL beakers using a balance (Sartorius CPA225D, ±0.01 mg), and then filled up to 50 g with pure H_2O (Milli-Q® 18.2 MΩ-cm at 25 °C). The sample was then placed on a magnetic stirrer (Cat MCS66) and homogenised using a magnetic stirrer bar until the salt was completely dissolved (ca 30 minutes of stirring). For each sample, a rectangular borosilicate capillary (Vitrotubes^{TM}; 0.05 x 0.5 mm) was dipped into the solution within seconds until it was about three quarters filled. Placed on a

borosilicate coverslip (Menzel, ø 16 mm) immediately afterwards, both openings were sealed with a slightly heated blue wax. The same procedure was applied on other solutions with different ionic compositions (pure H_2O, $CaSO_4$ + pure H_2O, $CaSO_4$ + NaCl + pure H_2O).

After sealing, speed of sound measurements were started without delay at 5 °C until maximal 65 °C. A typical Brillouin spectra needs to reach at least 300 counts during its acquisition so that the frequency shift can be analysed precisely finally. Samples were acquired three times at each temperature step ($\approx$ 5 seconds per acquisition). The Brillouin spectra were analyzed by fitting the acquired frequency shifts in the same package of Wolfram Mathematica as used for FIs.

A list of all NaCl mass solutes, molalities, and salinities is given in Table 4.2.

4.7 Final ice melting temperatures

The essential step to derive the salinity of a sample using microthermometry on fluid inclusions, was to freeze the sample and to cavitate a vapor bubble to avoid metastable conditions (Roedder, 1984; see chapter 4.5). Then, the temperature of the Linkam stage was slowly increased from negative low temperatures, and the point, at which the last ice crystal within a FI melts, was documented and labelled the final ice melting point of the studied FI.
A natural gypsum sample from a sabkha, Tunisia, was prepared using a razor blade to cut small pieces (ca 1.5 cm) along the 010 plane. The pieces were placed in a temperature-controlled stage (Linkam THMS 600) with 0.1 °C resolution (Figure 3.5). To find out whether both sound velocity and final ice melting temperatures differ significantly between two more distant parts of the same parent sample, >30 growth bands with primary FIs were selected for BS analysis (Figure 3.6 A). Petrographic observations of FIs were carried out using reflected light with an objective of magnification x100 of the same microscope as described in chapter 4.1. The selected FIs were documented with a camera attached to the microscope. Post-depositional processes affecting the pristine signal of FIs (e.g. by external forcing such as burial, exposure, dissolution-(re)precipitation, necking down, etc.) have been ruled out by selecting only primary monophasic FIs that are aligned along straight growth bands.
The samples were cooled from room temperature at a rate of ca 20 °C/min to -96 °C for 3-5 minutes to ensure a completely freezing of all investigated FIs. Subsequently, the sample was heated again at ca 10 °C/min. The rates were reduced to 1 °C/min when phase changes from liquid+vapor to solid+liquid+vapor were expected to occur. To determine if the chemical system of the FIs would be H2O-NaCl, the eutectic point was documented when FIs started to melt. For H2O-NaCl the eutectic point was determined to be at -21.2 ± 0.1 °C (Sterner and Bodnar, 1984). Above this mark (i.e. > -21.2 °C), the rate was reduced to about 0.5 °C/min to be able to document the final ice melting point. Care was always taken to ensure the presence of a gas bubble, as otherwise the exact determination of salinity cannot be guaranteed (Roedder, 1967). He observed ice-liquid equilibrium in pure water at 6.5 °C, because of tension. The observed data were then grouped by sub-sample and growth band and plotted against sound velocity (see Section 4.2).

Table 4.1 Published sound velocity values for increasing NaCl concentrations at 25 °C (from Chen and Millero, 1986).

Molality b [mol/kg]	Weight % NaCl [m/s]	$w^0_{NaCl,relative}$ [m/s]	$w^0_{NaCl,absolute}$
0.2519	1.5	15.88	1513
0.4906	2.8	30.14	1527
0.7541	4.2	46	1543
1.0399	5.7	62.14	1559
1.5935	8.5	93.46	1590
2.3418	12.0	132.14	1629
3.3723	16.5	183.24	1680
3.8718	18.5	206.17	1703
4.5985	21.2	237.96	1735
4.8797	22.2	249.32	1746
5.0751	22.9	256.98	1754
5.4347	24.1	271.04	1768
6.1469	26.4	298.17	1795

Table 4.2 Properties of prepared NaCl capillary samples. S = Salinity, m = Mass.

Mass volume H_2O [g]	S [wt.% NaCl]	m NaCl [g]	Moles of solute [mol]	Molality b [mol/kg]
50	0.5	0.2492	0.0043	0.086
50	2.5	1.2793	0.0214	0.439
50	5	2.6299	0.0428	0.901
50	10	5.5604	0.0856	1.901
50	15	8.8198	0.1283	3.020
50	20	12.5004	0.1711	4.278
50	25	16.6710	0.2139	5.704
50	26.4	17.9291	0.2267	6.167

Bibliography

Ball, M., and Norwood, L. (1969). Studies in the system calcium sulphate–water. part i. kinetics of dehydration of calcium sulphate dihydrate. *Journal of the Chemical Society A: Inorganic, Physical, Theoretical*, 1633–1637.

Bodnar, R. J. (1993). Revised equation and table for determining the freezing point depression of H2O-NaCl solutions. *Geochimica et Cosmochimica acta*, *57*, 683–684.

Boon, J. P., and Yip, S. (1991). *Molecular hydrodynamics*. Courier Corporation.

Chen, C.-T., and Millero, F. J. (1986). Thermodynamic properties for natural waters covering only the limnological range 1. *Limnology and Oceanography*, *31*(3), 657–662.

Guillerm, E. (2019). *Turning halite fluid inclusions into accurate paleothermometers with Brillouin spectroscopy: development of a new method and application to the Last Interglacial in the Dead Sea*.

Mekki-Azouzi, M. E., Tripathi, C. S. P., Pallares, G., Gardien, V., and Caupin, F. (2015). Brillouin spectroscopy of fluid inclusions proposed as a paleothermometer for subsurface rocks. *Scientific Reports*, *5*. https://doi.org/10.1038/srep13168

Pallares, G., Azouzi, M. E. M., González, M. A., Aragones, J. L., Abascal, J. L., Valeriani, C., and Caupin, F. (2014). Anomalies in bulk supercooled water at negative pressure. *Proceedings of the National Academy of Sciences*, *111*(22), 7936–7941.

Posnjak, E. (1938). The system caso4-h20. *Am. J. Sci.*, *35A*, 247–272.

Roedder, E. (1984). Volume 12: Fluid inclusions. *Reviews in mineralogy*, *12*.

Roedder, E. (1967). Metastable Superheated Ice in Liquid-Water Inclusions under High Negative Pressure. *Science*, *155*(3768), 1413–1417. https://doi.org/10.1126/science.155.3768.1413

Sterner, S., and Bodnar, R. (1984). Synthetic fluid inclusions in natural quartz I. Compositional types synthesized and applications to experimental geochemistry. *Geochimica et Cosmochimica Acta*, *48*(12), 2659–2668. https://doi.org/10.1016/0016-7037(84)90314-4

van't Hoff, J. (1912). Untersuchungen über die bildungsverhältnisse der ozeanischen salzablagerungen.

Chapter 5

Reconstructing lake bottom water temperatures and their seasonal variability in the Dead Sea Basin during MIS 5e

This chapter was published in the journal 'The Depositional Record' in February 2022. https://doi.org/10.1002/dep2.185

Authors: Brall, N., Gardien, V., Ariztegui, D., Sorrel, P., Guillerm, E. and Caupin, F.

Abstract

Interglacial periods are characterised by thick accumulations of halite units in the Dead Sea Basin. During these intervals, small water droplets (fluid inclusions) were entrapped in the halite crystals which serve as windows to estimate the chemistry and physical properties of the primary lake water conditions. Brillouin spectroscopy is used here to reconstruct annual resolution temperatures from a halite core section in the Dead Sea Basin during the onset of Marine Isotope Stage 5e (ca 130 ka) of the Last Interglacial. Lake bottom temperatures can be inferred based on the occurrence of coarse/fine halite facies, as observed today with the formation of equivalent halite facies during winter/summer seasons in the Dead Sea. A recurring increase in lake bottom temperatures is found along the direction of coarse halite layers in three successive years. Moreover, low fluid inclusion entrapment temperatures were detected in layers of fine (cumulate) halite facies. These results imply a two-fold stronger seasonality in the Dead Sea Basin compared to today, with colder winters at the onset of Marine Isotope Stage 5e. The results therefore highlight the potential of using cyclic salt deposits to reconstruct seasonal temperature variability for numerous evaporitic environments in the geological record.

Keywords

Brillouin spectroscopy, Dead Sea Basin, fluid inclusions, marine isotope stage (MIS) 5e, palaeotemperature, seasonal halite facies

5.1 Introduction

Palaeoclimatic reconstructions often show that long-term global climate changes are largely induced through processes and feedbacks on seasonal timescales (Werner et al., 2000; Denton et al., 2005). A substantial impact of seasonality on various proxies has been proposed (Clemens and Prell, 2003; Huguet et al., 2006) at annual (Brocas et al., 2018; Felis et al., 2004), centennial (Bar-Matthews et al., 2000; Brauer and Dulski, 2009) or millennial-scale resolutions (Milner et al., 2012). Continental archives such as tree rings, laminated speleothems and varved lake sediments can provide seasonal records of different climate variables (Shi et al., 2010; Baldini et al., 2021; Ben Dor et al., 2019). For example, laminations in speleothems commonly accumulate more calcite in the cool season and less or none during the warm season (Riechelmann et al., 2020). Analogously, varved sediments have been extensively used for the last few decades, to reconstruct, e.g., seasonal rainfall intensity in temperate/periglacial lakes (Ariztegui et al., 2010), the long-term progressive lake-level decline in a hyper-arid region in northern Chad (Francus et al., 2013), both winter precipitation and temperatures in southern Finland (Ojala et al., 2013), flooding events in the Southern Alps (Wirth et al., 2013) as well as Holocene temperatures in China and Switzerland (Chu et al., 2005; Trachsel et al., 2012).

Calibration studies using the $\delta^{18}O$ composition of modern ostracods in turn provide temperature reconstructions that are in good agreement with the observed range of seasonal changes in lake water temperature (Labuhn et al., 2021), based on "palaeotemperature" equations for equilibrium carbonate precipitation and the estimated mean $\delta^{18}O$ of lake water. However, the high intra-species carbonate $\delta^{18}O$ variability of samples leads to a large scatter in the reconstructed temperatures often compromising palaeotemperature reconstructions. Recent progress in reconstructing palaeotemperatures has been made by using biomarkers (i.e., leaf wax n-alkanes, bacterial branched glycerol dialkyl glycerol tetraethers (brGDGTs)), however, these geochemical proxies include certain limitations as well (Wang et al., 2018; Liu and An, 2020). Thus, most palaeoclimate proxies provide relative changes in climate variables while a direct and precise reconstruction of such variables is still lacking. Therefore, there is a crucial need for resolving seasonal temperature variations using continental archives to improve long-term palaeoclimate reconstructions.

In this study, halite (NaCl) samples from the Dead Sea Basin (DSB) are used to reconstruct seasonal temperature variability during Marine Isotope Stage 5e (MIS 5e). Today, halite precipitates on the deep hypolimnion lake floor of the DSB as alternating layers responding to a seasonal frequency (Sirota et al., 2021; Kiro et al.,

2016). During their formation, NaCl crystals may trap droplets of the surrounding lake water from which they precipitate, called fluid inclusions (FIs). Recently, a new palaeothermometer based on Brillouin spectroscopy (BS) was elaborated on FIs in natural quartz (Mekki-Azouzi et al., 2015) and laboratory-grown NaCl crystals (Guillerm et al., 2020), and used on a sedimentary core from the DSB to reconstruct temperature and lake-level changes of the Dead Sea over the Last Interglacial (LIG, 130–115 ka; Guillerm, 2019). In the present contribution, the focus is on a shorter time interval encompassing three closely spaced samples, to reconstruct palaeotemperature variability of the lake waters at an unprecedented (i.e., seasonal) resolution.

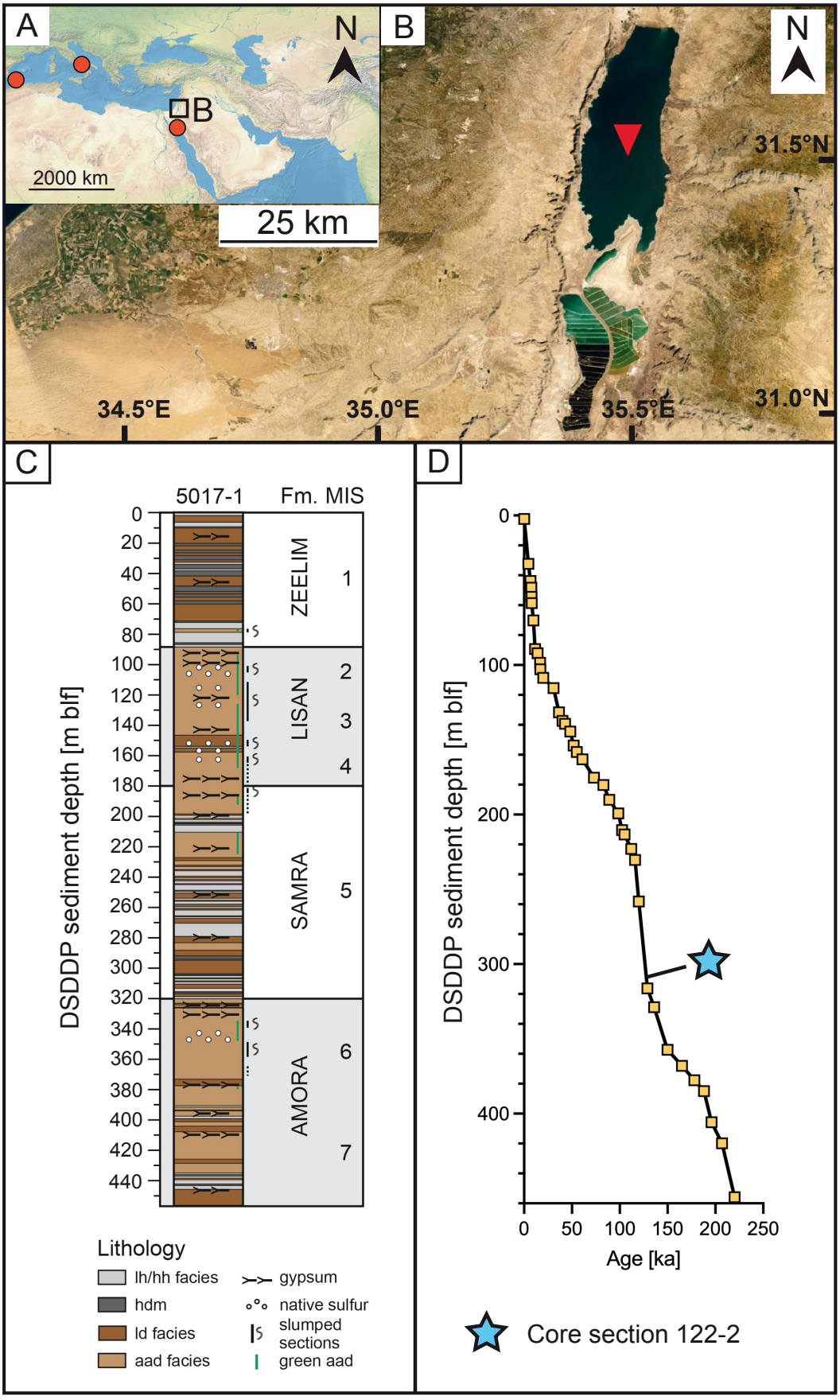

Figure 5.1 (Caption next page.)

Figure 5.1 (A and B) Location of Dead Sea, middle East, with DSDDP site (red triangle) and study sites referred to in the discussion (red circles). (C) Lithological profile of DSDDP core 5017-1-A with related formations (Fm.) and Marine Isotope Stages (MIS) (from Ben Dor et al., 2019; modified after Neugebauer et al., 2014). Facies types indicated by lh/hh (layered/homogeneous halite), hdm (halite and detrital marl), ld (laminated detritus), and aad (alternating aragonite and detritus). (D) Revised age model for DSDDP core 5017-1-A after Goldstein et al., 2020, sampled core section indicated by blue star.

5.2 Geological Setting and Material

The modern Dead Sea is a hypersaline terminal lake occupying a pull-apart basin along the DSB (Smit et al., 2008) (Figure 5.1 A). With a current water surface at 434 m below mean sea level (m bsl) receding at a rate of 1 m/year, it is nowadays the lowest exposed continental point on Earth. Located at the Levantine land bridge connecting Africa with Asia, the region is influenced by both Mediterranean climate and tropical storms surging from the Saharo-Arabian desert belt (Neugebauer et al., 2014 and references therein).

The hydrographic lake regime has been switching between meromictic (stable stratification without mixing during a year) and holomictic (lake mixing once a year) periods since 1978 (Gertman and Hecht, 2002; Anati et al., 1987). The long-term meromictic regime of the modern Dead Sea was interrupted for just two months with an overturn of the water body in winter 1978–1979 (Steinhorn, 1985), associated with the onset of halite precipitation on the surface in February 1979 (Steinhorn, 1983). After several switches between both regimes (meromictic phases from 1979–1982 and 1991–1995; holomictic phase from 1983–1991), perpetual holomictic conditions have prevailed since 1996 coevally with the precipitation of halite (Gertman and Hecht, 2002; Anati et al., 1987; Anati and Stiller, 1991). Moreover, seasonal-driven variations in solar radiation, temperature, quasi-salinity and the degree of halite supersaturation have been both observed and extensively studied (Arnon et al., 2016; Gertman and Hecht, 2002; Sirota et al., 2017). The main seasonal feature is a well-mixed water body from surface to bottom during the winter season between late November to early March (Gertman and Hecht, 2002), and a thermal stratification from early spring to late fall (Gertman and Hecht, 2002). Modern halite precipitation is characterised by (1) bottom-grown coarse halite (mainly spring–late summer) and (2) floating fine cumulate halite that nucleates in the whole water column excessively during winter due to a high supersaturation of halite, and to a minor extent during summer below the thermocline (Sirota et al., 2017).

The DSB has been successively occupied by several lakes and water bodies since the first marine incursion from the Mediterranean Sea during the Miocene (Neev and Emery, 1967; Stein, 2001). The current study focusses on the sediments from Lake Samra, which was the last interglacial (ca 129–116 ka) precursor of the Dead Sea (Waldmann et al., 2009). The first long sedimentary core covering this time interval was retrieved within the framework of an International Continental Drilling Program (ICDP)-sponsored initiative (5017-1-A) (Neugebauer et al., 2014; Stein et al., 2011) (Figure 5.1 C). In this core, a layered halite facies ('lh') accounts for around 20% of the sedimentary sequence and is composed of alternating grey marl

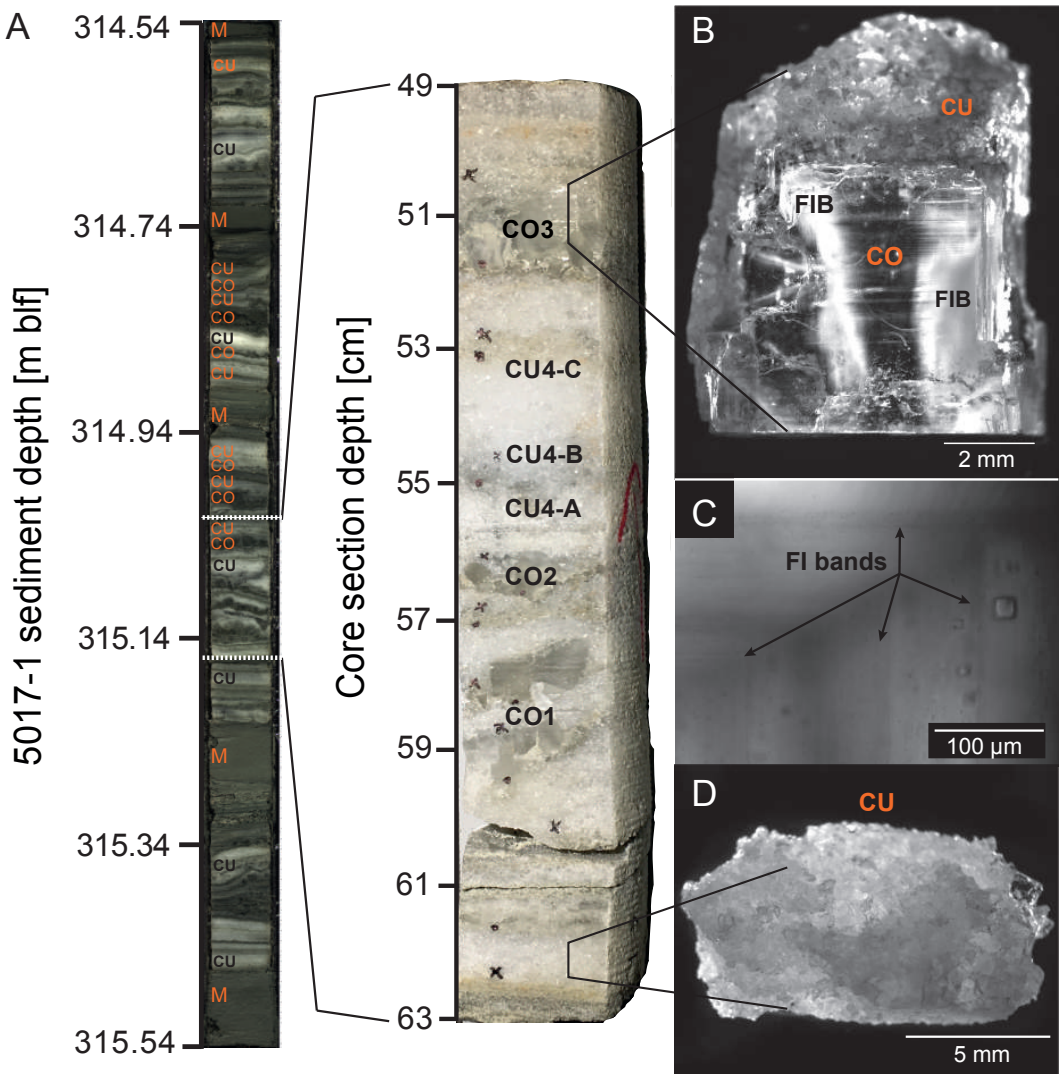

Figure 5.2 (A) Left, image of core section 122-2 with alternations of mud (M), cumulate (CU) and coarse (CO) facies. Right, image of coarse-cumulate depositional cycles. (B) CO and CU crystals, separated by a sharp transition that indicates a change in hydrological lake conditions. Peculiar cloudy fluid inclusion bands (FIB) in CO. (C) Common primary FIB from sample CO2-BOT. (D) CU assemblages bounded by countless single CU crystals.

laminae (<1 mm), fine cumulate halite (0.2–4 cm; termed 'CU') and coarse halite (1–10 mm; termed 'CO') Kiro et al., 2016 (Neugebauer et al., 2014). Core section interval 5017-1-A-122-A-2 (315.17 to 315.03 m below lake floor, (m blf)) yields four continuous segments of such cumulate-coarse halite alternations, enclosed by ca 4–10 cm thick mud intervals (Figure 5.2 A). Three of these halite alternations were investigated in the present study (Figure 5.2 A). Further, the whitish cumulate halite layers are characterised by assemblages of single NaCl grains ca 150–400 µm in size containing dense fluid inclusions bands (FIB) around a central FI-free zone (Figure 5.2 D). Conversely, dark-grey coarse layers encompass cubic single NaCl crystals with grain sizes of ca 5 mm (Figure 5.2 B). Milky/cloudy FIB in coarse samples represent primary FIs that have been entrapped during crystal growth (Figure 5.2B) with sizes varying from 1 to 40 µm (Figure 5.2 C).
A recently improved age model for core 5017-1-A (Figure 5.1 D) includes a new tie point at 129 ka ± 1 ka at 316.24 m blf (i.e., close to the bottom core section at 315.17 m blf), which therefore corresponds to the onset of MIS 5e during the last interglacial period (Goldstein et al., 2020).

5.3 Methods

Sampling of core section 5017-1-A-122-A-2 was carried out at GFZ Potsdam (Germany). Selected pieces of halite crystals were placed on their flat side on a microscope cover slip in a temperature-controlled stage (Linkam THMS 600) with 0.1 °C resolution. Samples were studied with an upright optical microscope (Zeiss Axio Imager.Z2 Vario), equipped with a long-working distance x100 objective (Mitutoyo Plan-Apo, N.A. 0.7). To select suitable FIs for analysis, published criteria for accurate Brillouin analysis on halite crystals (Guillerm et al., 2020) was followed. For palaeothermometry, the previously described full set-up and detailed physical principles of BS were used (Mekki-Azouzi et al., 2015).
The method is based on the measurement of sound velocity (w) in a liquid which depends on the composition, temperature (T) and pressure of the liquid. When heated or cooled, a monophasic FI (only liquid) follows an isochore at constant volume, along which w varies with T. In a biphasic FI (liquid + vapour), w of the liquid is measured as a function of T at the solid-liquid-vapour equilibrium (SLVE). Hence, a transformation (cavitation) from a monophasic phase into a biphasic phase is required for each FI and achieved by a short-term thermal cycle (Figure 5.5). By definition, for a FI trapped near ambient pressure (0.1 MPa), the crossing temperature T_x equals the entrapment temperature T_f at which both w curves intersect (along both the isochore and SLVE; S1 and S2).
A value for one fluid inclusion (FI) consists of eight single measurements conducted

at different temperatures to establish both an isochore (monophasic FI) and a solid-liquid-vapour equilibrium (SLVE; biphasic FI) curve (Figure 5.5). The intersection of both curves is defined as T_x (Figure 5.6). To obtain biphasic FIs, large temperature excursions are necessary by means of an increase from room temperature to +130 °C, then back to room temperature. This causes plastic deformation of the salt host crystal with an increase in volume, forcing cavitation of a vapour bubble in the FIs. At this point, the FIs enters the stability field and represents ambient pressure conditions (Figure 5.5). During the cavitation process, the chemical composition of an individual fluid inclusion does not change. Data are presented here as mean T_x values for each sub-section (i.e., uppermost samples in coarse layers, labelled "CO-TOP" and lowermost samples in coarse layers labelled "CO-BOT").
Each mean T_x value is calculated by the mean of all measured FIs:

$$T_{x,mean} = \frac{\sum x_i}{N} \tag{5.1}$$

with x_i the T_x value for FI_i and N the number of all FIs. Mean T_x values are analysed statistically by means of their standard deviation (SD), derived from equation (2):

$$SD = \sqrt{\frac{\sum (x_i - T_{x,mean})^2}{(N-1)}} \tag{5.2}$$

The standard error of the mean (SE), used as error bars in each figure, is calculated by equation (3):

$$SE = \frac{SD}{\sqrt{N}} \tag{5.3}$$

To rule out post-entrapment processes in the samples, histograms were used to check for statistical distributions that are close to Gaussian distributions (Figure 5.7).

A correction term was applied on measured T_x data according to the pressure of the water column above where crystals form ($T_f = T_x + \Delta T_P$, with $\Delta T_P = 4.8$ °C for crystals precipitated at lake bottom). Here, a water column height of 539 m was calculated based on a pressure of 6.45 MPa and a lake-level of -250 m above sea level (Guillerm, 2019). Such a reconstructed lake-level value, based on speed of sound measurements in biphasic FIs (Guillerm, 2019), is similar to that of a recently published synthetic lake-level for the beginning of the Last Interglacial (Torfstein et al., 2013). It is noteworthy to mention that, as the coarse halite layers

studied here were deposited during a short time interval, the pressure correction is virtually equal for all of them. Therefore, any difference between uncorrected T_x can be directly converted into a difference between T_f values. Conversely, as cumulate halite crystals form in the water column between the surface and the bottom of the lake the unknown T correction for formation depth is less or equal to the T correction for coarse halite crystals. Therefore, in view of the T_x values, the T_f of cumulate halite layers must be less than the T_f for the surrounding coarse halite layers.

5.4 Results

Individual T_x of FIs were measured in three successive CO halite layers (CO1, CO2, CO3) (Figure 5.3 A) with increasing core depths (from 315.138 to 315.052 m blf, Table 5.1). Additionally, the T_x of FIs were measured in one fine CU layer (CU4) that deposited prior to the youngest CO3 halite layer (CO3-BOT) (Figure 5.3 A). Here the pressure-corrected temperature (T_f), with reported uncertainties as standard error of the mean (SE), is reported for each interval. The deepest and oldest layer CO1 has been divided into three sub-sections (total number of measured FIs n = 103) with T_f values of 18.4 ± 0.5 °C, 21.7 ± 0.4 °C and 21.4 ± 0.4 °C for CO1-BOT, CO1-MID and CO1-TOP, respectively. The second CO layer CO2 is divided into three sub-sections (n = 90). T_f values vary from 18.3 ± 0.5 °C, 19.9 ± 0.4 °C and 22.9 ± 0.6 °C for CO2-BOT, CO2-MID and CO2-TOP, respectively (Figure 5.3 B).

The uppermost and relatively youngest CO layer CO3, divided into two sub-sections, base and top (n = 48), provides T_f values of 21.6 ± 0.5 °C and 23.1 ± 0.7 °C for CO3-BOT and CO3-TOP, respectively (Table 5.1, Figure 5.3 B). This dataset shows that mean T_f values in each CO layer increase with increasing layer thickness from base to top. A clear difference in T_f values is therefore observed by separating the dataset into groups of only coarse-bottom and coarse-top values, which reveals that lowest temperatures correspond to samples from the coarse-bottom layers, while highest temperatures are found only in coarse-top layers (Figure 5.4). Three CU sub-samples provide uncorrected T_x values of 16.1 ± 1.4 °C (n = 14), 16.5 ± 0.7 °C (n = 26) and 15.9 ± 1.0 °C (n = 15) for CU4-A, CU4-B and CU4-C, respectively (Table 5.1, Figure 5.3 B). Hence, those temperatures are lower than both surrounding uncorrected T_x values of CO layers with 16.8 °C and 18.1 °C for CO3-BOT and CO2-TOP, respectively (Figure 5.8). As cumulate crystals form in the water column between the surface and the bottom of the lake, the unknown temperature correction is less or equal to the temperature correction for coarse crystals. Therefore, the T_f of these cumulate crystals must be less than the T_f for

Table 5.1 Measured entrapment temperatures in halite fluid inclusions. Columns provide the sediment core depth in metres below lake floor (m blf), the number of fluid inclusions per sample (N), the averaged entrapment temperature per sample (Mean T_x), the standard deviation of a sample population (SD), and the standard error of the mean (SE). Both lower and upper boundaries of 95% confidence intervals of each sample mean calculated with student's t-test. Coarse sampled were corrected for hydrostatic pressure (Mean T_f) (see Methods). Mean T_f values were not determined for cumulate halite samples (N.A.).

Sample name	Halite facies	Depth in core 5017-1 (m blf)	Section depth (cm)	N	Mean T_x (°C)	SD (°C)	SE (°C)	Lower 95% CI (°C)	Upper 95% CI (°C)	Mean T_f (°C)	Lower 95% CI (°C)	Upper 95% CI (°C)
CO3-TOP	coarse	315.052	2.2	31	18.3	3.9	0.7	16.9	19.7	23.1	21.7	24.5
CO3-BOT	coarse	315.055	2.5	17	16.8	2.1	0.5	15.7	17.9	21.6	20.5	22.7
CU4-C	cumulate	315.074	4.4	15	15.9	3.9	1	13.7	18.1	N.A.	N.A.	N.A.
CU4-B	cumulate	315.09	6	26	16.5	3.4	0.7	15.1	17.9	N.A.	N.A.	N.A.
CU4-A	cumulate	315.095	6.5	14	16.1	5.2	1.4	13	19.1	N.A.	N.A.	N.A.
CO2-TOP	coarse	315.103	7.3	21	18.1	2.6	0.6	16.9	19.3	22.9	21.7	24.1
CO2-MID	coarse	315.105	7.5	35	15.1	2.4	0.4	14.3	15.9	19.9	19.1	20.7
CO2-BOT	coarse	315.109	7.9	34	13.5	3	0.5	12.4	14.5	18.3	17.2	19.3
CO1-TOP	coarse	315.12	9	37	16.6	2.1	0.4	16	17.4	21.4	20.8	22.2
CO1-MID	coarse	315.124	9.4	40	16.9	2.6	0.4	16	17.7	21.7	20.8	22.5
CO1-BOT	coarse	315.138	10.8	26	13.6	2.5	0.5	12.6	14.6	18.4	17.4	19.4

the surrounding coarse halite layers.

5.5 Discussion

The studied section of cumulate-coarse alternations provides insights into a short depositional period (ca 3 years) during which Lake Samra was most likely holomictic with a seasonal precipitation mechanism (Kiro et al., 2016). Another type (white, brown and black laminae with fine detritus and/or gypsum) of the layered 'lh' facies in core 5017-1-A has already been related to annual deposition cycles with periodicities of ca 11, 7–8, and 4–5 years (Palchan et al., 2017). However, the sampled section in this study lacks clear detrital layers and only consists of cumulate-coarse alternations. The fact that alternating detrital layers are missing indicates rather dry depositional conditions without flood events or increased runoff into Lake Samra during cumulate-coarse halite deposition (Ben Dor et al., 2019). However, the 'lh' facies type described by Palchan et al., 2017 is observed below and above the studied section in core 5017-1-A-122-2 (Figure 5.2 B), indicating a full annually deposited sequence with changing hydrological parameters that drove halite precipitation and clastic deposition. Further, the studied section can be considered a seasonal record of winter (cumulate halite) and summer (coarse halite) as previously observed in the modern Dead Sea (Sirota et al., 2016). Only a few climate archives in the Levantine region (or in Europe)

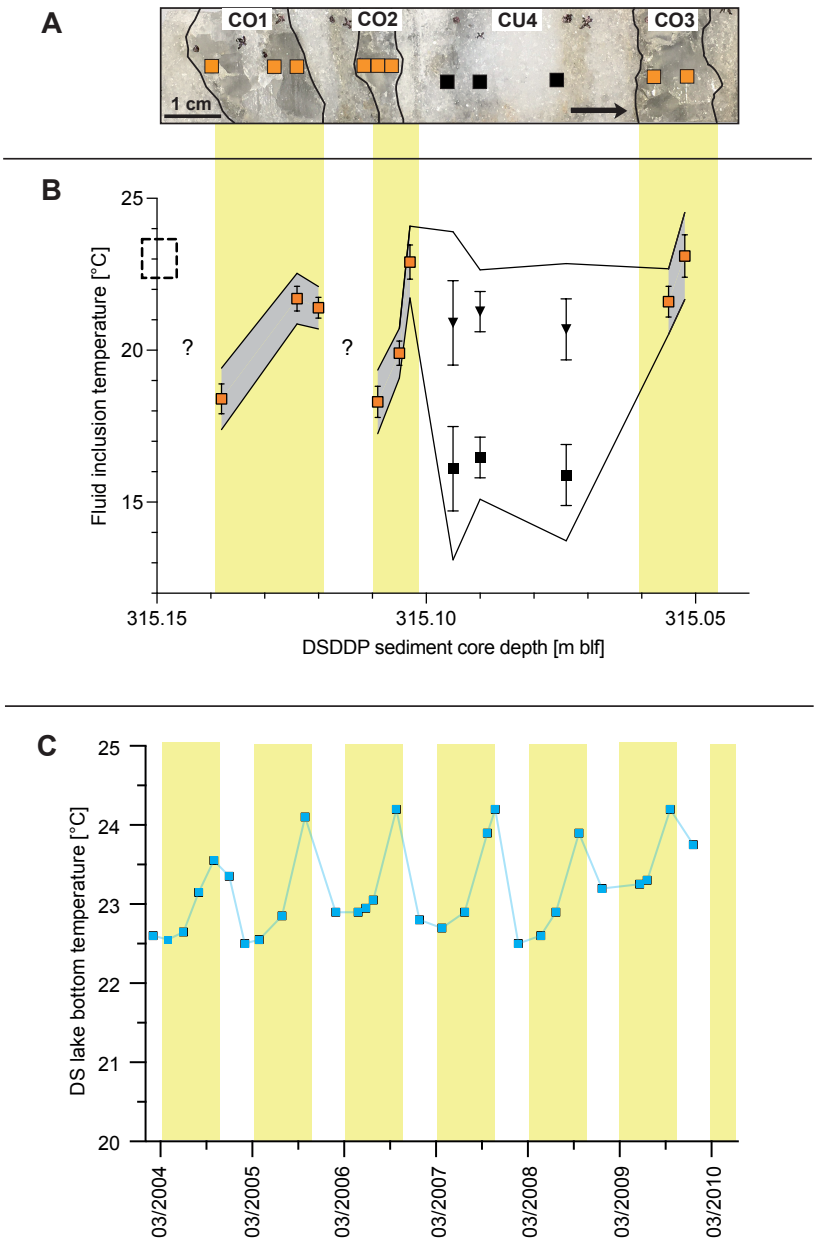

Figure 5.3 (A) Halite layers in core section 5017-1-A-122-2. Black lines mark facies boundaries between layers of coarse halite (CO) and cumulate halite (CU). Sampling locations of CO (orange) and CU (black) indicatedby squares. Black arrow = growth direction. (B) Corrected coarse T_f data (orange squares), uncorrected cumulate T_x data (black squares). Corrected cumulate T_f data (triangles) show the uncertainty of BS for cumulate halite. Dashed black box marks monitored deep lake temperatures in the Dead Sea for the period 1996–2010 (from Gertman and Hecht, 2002; Gertman et al., 2010). The uncertainties are reported as both, standard error of the mean (SE; error bars), and 95% confidence intervals (black lines). CO layers highlighted by vertical bands. (C) Monthly monitored deep lake temperatures between 2004–2010 (blue squares; from Gertman et al., 2010). The vertical bands illustrate the approximate period during which CO halite crystals grow on the deep lake floor.

have revealed annual to seasonal temperature variability during MIS 5e. The $\delta^{18}O$ values and Sr/Ca ratios in corals from the Red Sea reported sea surface temperatures (SST) with a seasonal amplitude of 8.4 °C at 122 ka (Felis et al., 2004), whereas pollen records enabled the reconstruction of seasonal temperature and moisture changes for the last 150 kyr (Chen and Litt, 2018). Based on their definition of pollen assemblage zones (PAZ) for core 5017-1-A, the sampled section at 315.15 m blf falls into the end of PAZ IV2 (340.6 - 313.7 m blf). This period marks the start of a transition from humid to dry conditions in the Levantine region by a progressive aridification, which is in line with the onset of the first halite deposition at the beginning of MIS 5e (Chen and Litt, 2018). Further, the authors report an initial warming starting in PAZ IV1 (313.7–290.2 m blf) judging by the significant pistachio pollen increase at this time. Since the sampled section is slightly older, it is suggested that the obtained lake water temperatures of cumulate/coarse halite layers might still reflect relatively colder conditions under an increasing drying trend in the region.
Sedimentary records in Europe covering the MIS 5e interval are more abundant. For instance, reconstructed mean temperatures of the coldest and warmest months in South-West Europe (Alboran Sea) allowed definition of the SST seasonality to 6 to 7.5 °C on millennial timescales during the MIS 5e, coevally with an increase in precipitation and highly evaporative summer conditions (Martrat et al., 2004). In southern Italy, a carbonate varved section of Lago Grande di Monticchio (127.20 ka; associated with the onset of MIS 5e) exhibits a rapid increase in Quercus pollen (128.85 ka) and abundant pollen of Mediterranean woody taxa (Brauer et al., 2007). This has been interpreted as intervals of hot summers, seasonal moisture deficiency and high fire frequency, associated with peak summer insolation (Brauer et al., 2007). Alternatively, speleothems from the Soreq Cave reported an increase in annual rainfall on centennial scales at the onset of the MIS 5e, associated with frost-free winters and drought-free summers in the Levantine region (Bar-Matthews et al., 2000). Most of these records, however, are missing a precise quantification of the interpreted palaeoseasonality.

Annually grown halite layers in the Dead Sea can be used to overcome such limitations by considering modern halite deposits as an analogue for the abundant halite layers in DSDDP core 5017-1-A (Figure 5.2 A). The onset of modern CO halite growth coincides with a seasonal transition, when lake bottom temperatures are comparatively colder during winter (Sirota et al., 2017). A subsequent hypolimnetic warming during the summer has been shown in recent works, with maximum values attained each year during late summer and a seasonal difference of around 1 °C

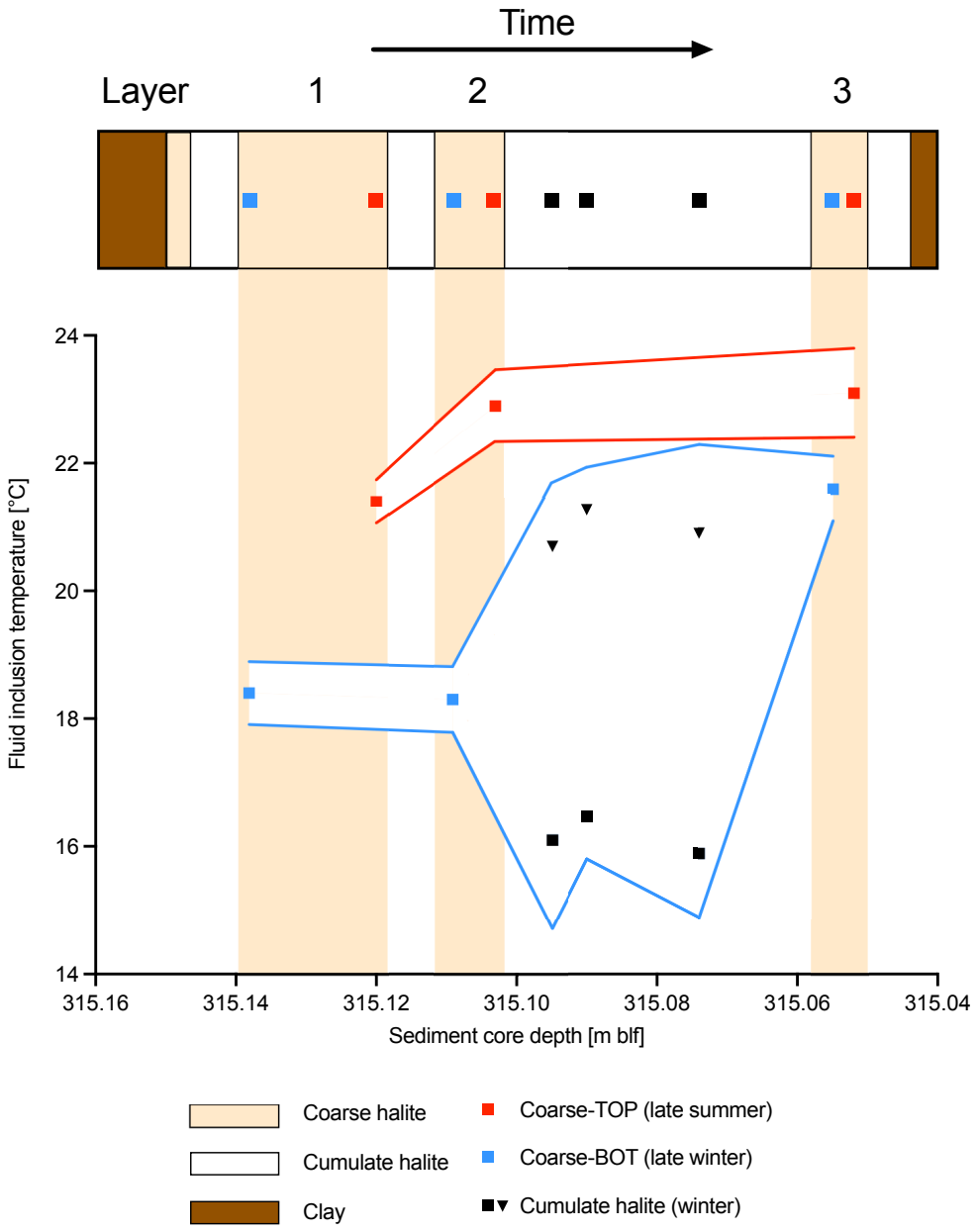

Figure 5.4 (Above) Sketch illustrating the annual depositional cycles in sediment core section 5017-1-A-122-2 with sub-sample locations. (Below) Temperature offset between grouped data in terms of the interpreted growth period: deep winter cumulate halite (uncorrected T_x, black squares; corrected T_f, triangles), late winter/early spring coarse halite (blue squares), and late summer coarse halite (red squares). Note that the corrected cumulate data reflect maximal potential palaeo lake temperatures, and thus should be considered with caution (see text for more details). Coloured (red and blue) envelopes are presented as the standard error of the mean. Vertical bands indicate growth season of coarse halite crystals on the deep lake floor.

between early and late summer lake bottom temperatures (Gertman et al., 2010; Arnon et al., 2016; Sirota et al., 2016). The results of this study follow this pattern with increasing hypolimnetic temperatures from the base to the top of CO halite layers in DSDDP core 5017-1-A-122-2 (with an increase of 3.0, 4.6 and 1.5 °C for CO1, CO2 and CO3, respectively; Figure 5.3 B). Hence, CO top samples can be interpreted as palaeo-summer halite precipitates. Accordingly, CO bottom samples (i.e., CO1-BOT, CO2-BOT, CO3-BOT) most probably recorded cold (late winter and early spring) hypolimnetic temperatures. The results thus highlight that holomictic periods in Lake Samra must have been associated with coarse halite precipitation in summer and seasonal temperature variations in the hypolimnion. Further support for large seasonal water temperature differences can be found in cumulate halite samples and their modern analogues: the Dead Sea starts mixing in late November–early December today, with both a cooling of the brine and a (nearly coeval) increase in NaCl saturation which drives nucleation of cumulate halite in the homogeneous water column (Sirota et al., 2017). Thus, the lower T_x values obtained in cumulate halite FIs can be considered as seasonal winter records in this study. This is further in line with higher palaeotemperatures in both surrounding coarse halite samples CO2-TOP and CO3-BOT, which reflect the end and the onset of two successive summer seasons, respectively (Figures 5.3 B; 5.4). However, it is important to note that the uncorrected cumulate T_x values do not picture the factual palaeoseasonal temperature variations with respect to the surrounding coarse layers. Since the initial (absolute) water depth of cumulate halite nucleation remains unknown, only the lower (= T_x; ca 16 °C) and upper boundary (= T_x + 4.8 °C; ca 20.8 °C) can be estimated for the studied cumulate layer. Hence, the palaeoseasonality would range between ca 2–7 °C which prevents the absolute temperature differences from being assessed quantitatively, e.g., between early spring/deep winter or late summer/deep winter. The focus, therefore, will be on entrapment temperatures obtained from coarse halite samples.

In accordance with this, the averaged T_f of coarse-bottom samples (19.4 ± 1.1 °C), which reflects late winter water/early spring lake bottom temperatures, is lower than the present-day lake bottom temperature in winter of ca 23 °C. On the contrary, the averaged T_f of coarse-top samples (22.5 ± 1.1 °C) is close to present-day mean summer maxima (23.8 °C for the period 1996-2010; Figure 5.3 B). The offset between palaeo-late winter and present-day winter values of ca 4 °C could be explained by an enhanced seasonality during MIS 5e. A lower winter insolation (200 W/m^2 versus present day 220 W/m^2) and enhanced summer insolation at both 30° and 35° North at that time may have driven the regional climate towards colder winters over the south and central Levant (Kiro et al., 2017; Torfstein et al.,

2015). This is in line with climate simulations that showed a southward shift of winter storm track rains in the Mediterranean Basin and the Levant, linked with a strengthened Siberian anticyclone that pushed colder air farther south in Europe (Kutzbach et al., 2020). Further, the climate model indicated slightly wetter winters and no change or even drier conditions at times of precession-caused high seasonality (ca 125 ka) in summertime (Kutzbach et al., 2020). Interestingly, a stronger palaeoseasonality was also reported in Red Sea corals during the peak of MIS 5e based on increased sea surface temperatures (with seasonal cycles of 8.4 °C at 122 ka), compared to a modern seasonal amplitude ranging between 4.5 and 5.6 °C (Felis et al., 2004). The weaker modern seasonality in the Levant and eastern Mediterranean Sea region has been associated with enhanced winter insolation and lower summer insolation in the Northern Hemisphere during the Holocene (Kiro et al., 2017).

The modern amplitude of seasonality, measured as the difference between winter and summer lake bottom water temperatures, exhibits a nearly constant value of 1.5 °C for the period 1996-2010 (Figure 5.3 C). This modern seasonal thermal amplitude is thus at least half lower than the reconstructed seasonal amplitude from coarse halite data for the MIS 5e (Figures 5.3; 5.4). The results therefore suggest a stronger palaeoseasonality during MIS 5e, with distinct differences in entrapment temperatures between the bottom and the top of each coarse halite layer (Figure 5.4).

5.6 Conclusions

Using the speed of sound in halite fluid inclusions from the Dead Sea basin, this study reconstructs lake-bottom temperatures of Lake Samra during Marine Isotope Stage (MIS) 5e. As demonstrated by three successive coarse halite layers, palaeotemperatures increased between the bottom (late winter/spring) and the uppermost (late summer) sampling interval of each coarse layer. Conversely, three sub-samples of a fine cumulate halite layer yield stable and lower (deep winter) temperature values, highlighting that the alternation of coarse and cumulate halite layers in core 5017-1 reflect seasonal contrasts of lake-bottom waters under holomictic conditions during MIS 5e. Our data further imply that the reconstructed seasonal amplitude of lake-bottom water temperatures at the onset of MIS 5e in Lake Samra was at least twice as high as the modern amplitude of seasonality.

Hence, this study clearly highlights the potential of using BS to investigate primary FIs in annual salt layers and reconstruct palaeotemperature variations in lacustrine sediment cores, at a seasonal resolution. Moreover, using BS on base-top

halite crystals from multiple halite layers does not require any preparation of thin sections, is easily applied on small FIs, and can provide a reasonable quantity of T_x measurements. Thus, future studies dealing with (palaeo) Dead Sea-like hydroclimates should focus on coarse salt layers to reconstruct the seasonal variability of lake temperatures on decadal to millennial scales.

ACKNOWLEDGEMENTS

We thank M. Schwab and A. Brauer from GFZ Potsdam (Germany) and the Dead Sea Deep Drilling Project members for providing core material of sediment core DSDDP-5017-1-A. We appreciate the constructive feedbacks of two anonymous reviewers who largely improved the manuscript. This study is part of the PhD thesis of NB and was funded by Campus France during the national research program MOPGA.

Author Contributions

NSB, EG, VG and FC developed the concept of the study. EG sampled the bulk core material. NSB sampled the core section and prepared the samples. NSB conducted the measurements and produced the entrapment temperature data. FC, EG and NSB analysed the data. NSB created the figures. All authors contributed to the main text, interpretations of data and finalised the manuscript.

Competing Interests statement

The authors declare no competing interests.

5.7 Supporting information

This part contains supporting figures (S1 - S4) with legends related to the described analytical procedure in the methods.

Figure S1: (Upper panel) Example of a typical thermal path of both monophasic (black dashed line; isochore) and biphasic (red solid line; $SLVE$) FIs by measuring the sound velocity at four temperature steps. The intersection of both lines (T_x) gives the entrapment temperature (T_f) if the sample has precipitated at ambient pressure. In most geological cases, a pressure-correction is needed. (Lower panel) Sketch illustrating the basic concept of Brillouin spectroscopy by using fluid inclusions (FIs). A monophasic FI follows a quasi-isochore (dashed black line) upon heating (red arrow) with increasing internal pressure. During cooling (blue arrow) the internal pressure becomes at some point negative, causing the FI to stretch to overcome the metastable phase (dashed black rectangles). By releasing energy during the nucleation of a vapor bubble, the biphasic FI becomes stable again. By theory, the thermal path of a biphasic FI follows the solid-liquid-vapor equilibrium ($SLVE$) that represents ambient pressure conditions.

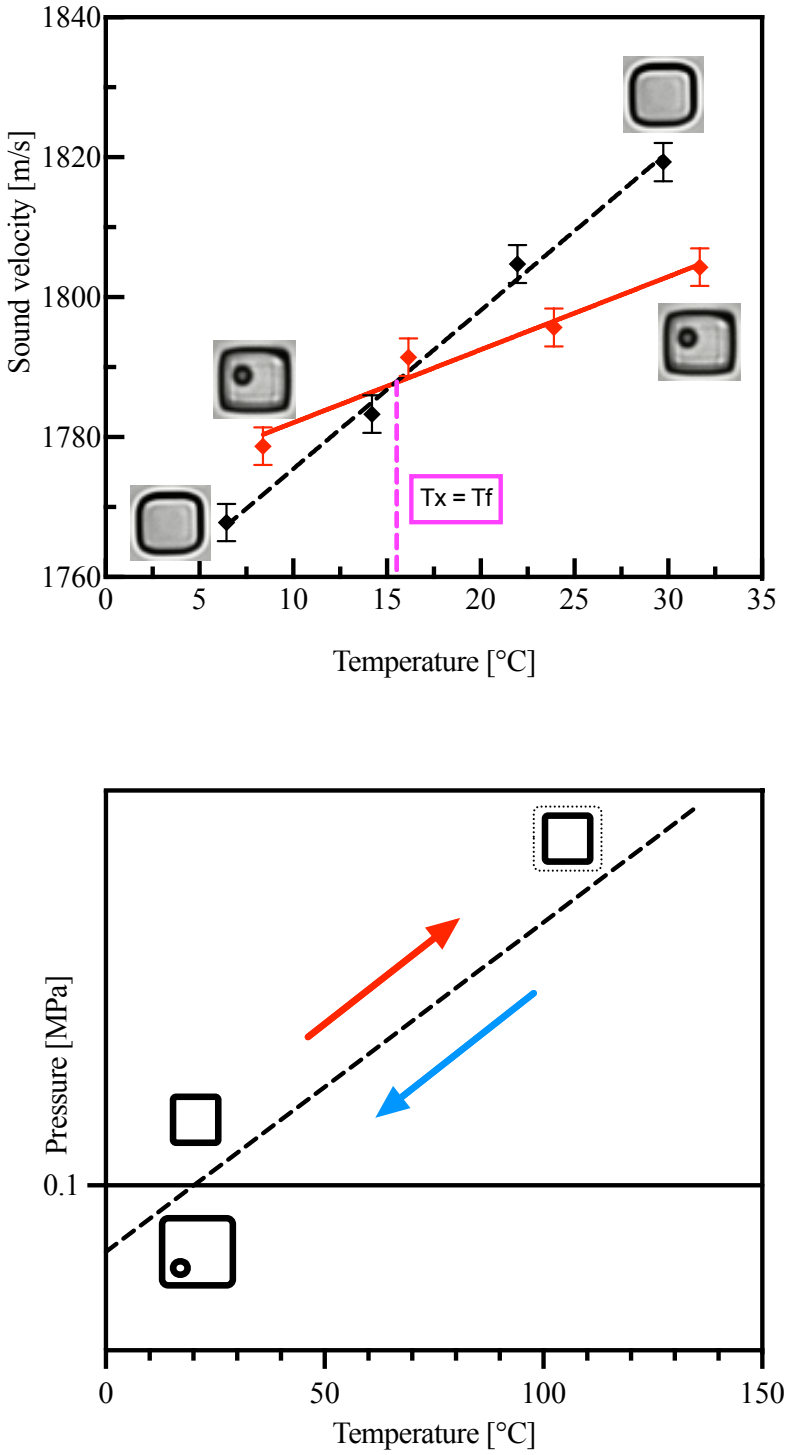
1840
1820
1800
1780
1760
Sound velocity [m/s]
0
5
10
15
20
25
30
35
Temperature [°C]
Tx = Tf
Pressure [MPa]
0.1
0
50
100
150
Temperature [°C]

Figure 5.5 S1

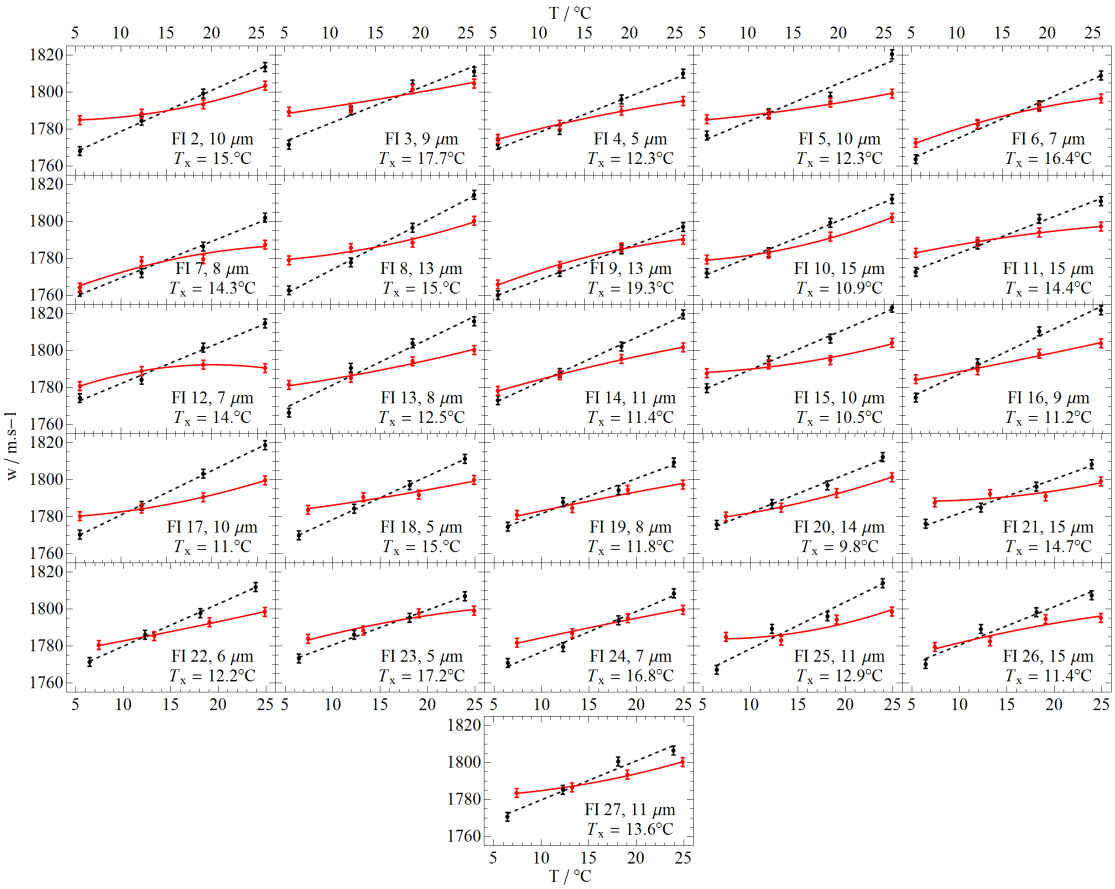

Figure 5.6 Example of a whole set of individual T_x values in 26 fluid inclusions (FIs) in coarse-grained sample section CO1-BOT at 5017-1-A core depth of 315.138 m blf. The T_x values are obtained from the intersection of isochores in monophasic FIs (black dashed lines) and parabolic fits of $SLVE$ in biphasic FIs (red solid curves).

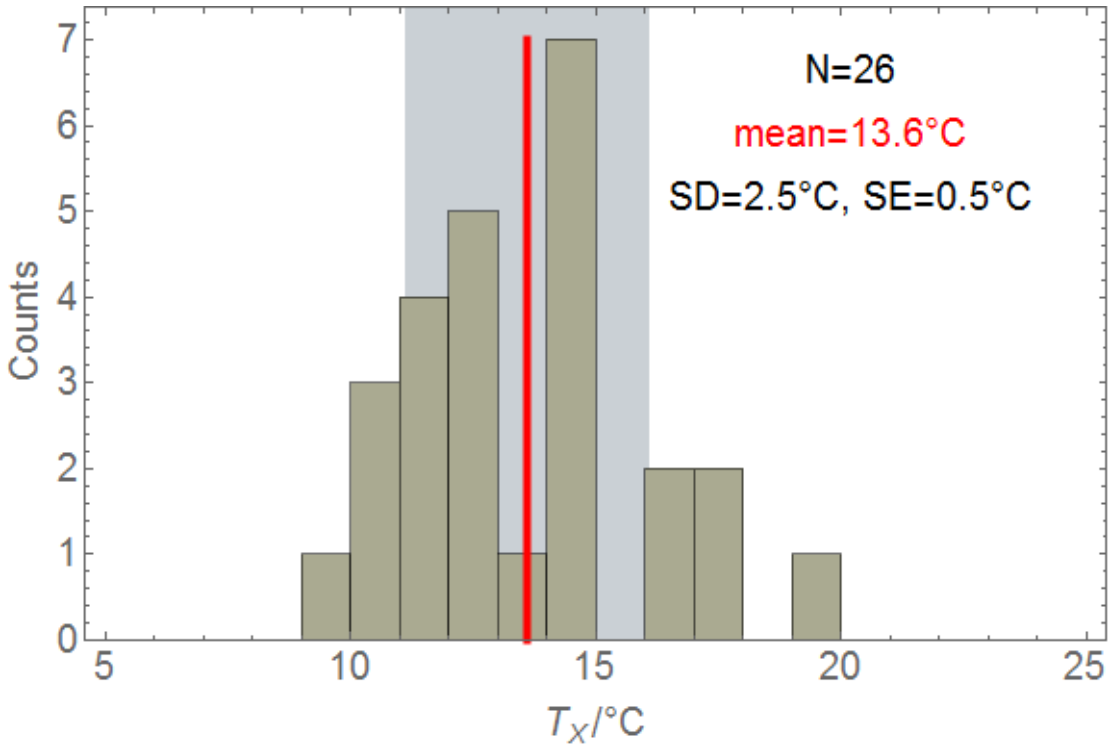

Figure 5.7 Corresponding histogram to displayed single T_x intersections in Supplementary Fig. 2. Bold red line marks the mean of T_x values (number of measured FIs in section = 26), gray shaded area shows the standard deviation interval (SD).

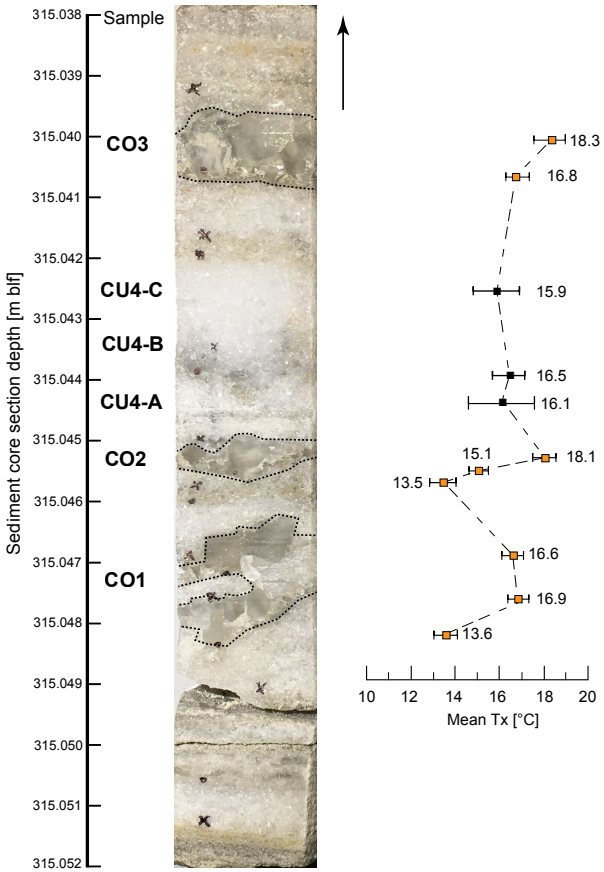

Figure 5.8 (Left) Sampled core section (315.052 – 315.038 m below lake floor) with coarse-grained halite layers (CO1-CO3, orange squares) and one sampled fine-grained cumulate layer (CU4, black squares). Black arrow indicates direction of halite growth. (Right) Mean T_x values derived from 5.1 for each sub-layer. Error bars calculated with 5.3.

Bibliography

Anati, D. A., and Stiller, M. (1991). The post-1979 thermohaline structure of the Dead Sea and the role of double-diffusive mixing. *Limnology and Oceanography*, *36*, 342–353. https://doi.org/10.4319/lo.1991.36.2.0342

Anati, D. A., Stiller, M., Shasha, S., and Gat, J. R. (1987). Changes in the thermohaline structure of the Dead Sea: 1979-1984. *Earth and Planetary Science Letters*, *84*, 109–121.

Ariztegui, D., Anselmetti, F. S., Robbiani, J. M., Bernasconi, S. M., Brati, E., Gilli, A., and Lehmann, M. F. (2010). Natural and human-induced environmental change in southern Albania for the last 300 years - Constraints from the Lake Butrint sedimentary record. *Global and Planetary Change*, *71*, 183–192. https://doi.org/10.1016/j.gloplacha.2009.11.016

Arnon, A., Selker, J. S., and Lensky, N. G. (2016). Thermohaline stratification and double diffusion diapycnal fluxes in the hypersaline Dead Sea. *Limnology and Oceanography*, *61*, 1214–1231. https://doi.org/10.1002/lno.10285

Baldini, J. U., Lechleitner, F. A., Breitenbach, S. F., van Hunen, J., Baldini, L. M., Wynn, P. M., Jamieson, R. A., Ridley, H. E., Baker, A. J., Walczak, I. W., and Fohlmeister, J. (2021). Detecting and quantifying palaeoseasonality in stalagmites using geochemical and modelling approaches. *Quaternary Science Reviews*, *254*. https://doi.org/10.1016/j.quascirev.2020.106784

Bar-Matthews, M., Ayalon, A., and Kaufman, A. (2000). *Timing and hydrological conditions of sapropel events in the eastern mediterranean, as evident from speleothems, soreq cave, israel*. www.elsevier.comrlocaterchemgeo

Ben Dor, Y., Neugebauer, I., Enzel, Y., Schwab, M. J., Tjallingii, R., Erel, Y., and Brauer, A. (2019). Varves of the Dead Sea sedimentary record. *Quaternary Science Reviews*, *215*, 173–184. https://doi.org/10.1016/j.quascirev.2019.04.011

Brauer, A., Allen, J. R. M., Mingram, J., Dulski, P., Wulf, S., and Huntley, B. (2007). *Evidence for last interglacial chronology and environmental change from Southern Europe*. www.pnas.orgcgidoi10.1073pnas.0603321104

Brauer, A., and Dulski, P. (2009). *The potential of varves in high-resolution paleolimnological studies*.

Brocas, W. M., Felis, T., Gierz, P., Lohmann, G., Werner, M., Obert, J. C., Scholz, D., Kölling, M., and Scheffers, S. R. (2018). Last Interglacial Hydroclimate Seasonality Reconstructed From Tropical Atlantic Corals. *Paleoceanography and Paleoclimatology*, *33*, 198–213. https://doi.org/10.1002/2017PA003216

Chen, C., and Litt, T. (2018). Dead Sea pollen provides new insights into the paleoenvironment of the southern Levant during MIS 6–5. *Quaternary Science Reviews*, *188*, 15–27. https://doi.org/10.1016/j.quascirev.2018.03.029

Chu, G., Liu, J., Schettler, G., Li, J., Sun, Q., Gu, Z., Lu, H., Liu, Q., and Liu, T. (2005). Sediment fluxes and varve formation in Sihailongwan, a maar lake from northeastern China. *Journal of Paleolimnology*, *34*, 311–324. https://doi.org/10.1007/s10933-005-4694-0

Clemens, S. C., and Prell, W. L. (2003). A 350,000 year summer-monsoon multi-proxy stack from the Owen Ridge, Northern Arabian Sea. *Marine Geology*, *201*, 35–51. https://doi.org/10.1016/S0025-3227(03)00207-X

Denton, G. H., Alley, R. B., Comer, G. C., and Broecker, W. S. (2005). The role of seasonality in abrupt climate change. *Quaternary Science Reviews*, *24*, 1159–1182. https://doi.org/10.1016/j.quascirev.2004.12.002

Felis, T., Lohmann, G., Kuhnert, H., Lorenz, S. J., Scholz, D., Pätzold, J., Al-Rousan, S. A., and Al-Moghrabi, S. M. (2004). Increased seasonality in Middle East temperatures during the last interglacial period. *Nature*, *429*, 164–168. https://doi.org/10.1038/nature02493

Francus, P., von Suchodoletz, H., Dietze, M., Donner, R. V., Bouchard, F., Roy, A. J., Fagot, M., Verschuren, D., and Kröpelin, S. (2013). Varved sediments of Lake Yoa (Ounianga Kebir, Chad) reveal progressive drying of the Sahara during the last 6100 years. *Sedimentology*, *60*, 911–934. https://doi.org/10.1111/j.1365-3091.2012.01370.x

Gertman, I., and Hecht, A. (2002). *The Dead Sea hydrography from 1992 to 2000.* www.elsevier.com/locate/jmarsys

Gertman, I., Kress, N., Katsenelson, B., Zavialov, P., and Shirshov, P. P. (2010). *Final Report. Equations of state for the Dead Sea and Aral Sea: Searching for common approaches.*

Goldstein, S. L., Kiro, Y., Torfstein, A., Kitagawa, H., Tierney, J., and Stein, M. (2020). Revised chronology of the ICDP Dead Sea deep drill core relates drier-wetter-drier climate cycles to insolation over the past 220 kyr. *Quaternary Science Reviews*, *244*. https://doi.org/10.1016/j.quascirev.2020.106460

Guillerm, E. (2019). *Turning halite fluid inclusions into accurate paleothermometers with Brillouin spectroscopy: development of a new method and application to the Last Interglacial in the Dead Sea.*

Guillerm, E., Gardien, V., Ariztegui, D., and Caupin, F. (2020). Restoring Halite Fluid Inclusions as an Accurate Palaeothermometer: Brillouin Thermometry Versus Microthermometry. *Geostandards and Geoanalytical Research*, *44*, 243–264. https://doi.org/10.1111/ggr.12312

Huguet, C., Kim, J. H., Damsté, J. S., and Schouten, S. (2006). Reconstruction of sea surface temperature variations in the Arabian Sea over the last 23 kyr using organic proxies (TEX86 and U 37K′). *Paleoceanography*, *21*(3). https://doi.org/10.1029/2005PA001215

Kiro, Y., Goldstein, S. L., Garcia-Veigas, J., Levy, E., Kushnir, Y., Stein, M., and Lazar, B. (2017). Relationships between lake-level changes and water and salt budgets in the Dead Sea during extreme aridities in the Eastern Mediterranean. *Earth and Planetary Science Letters*, *464*, 211–226. https://doi.org/10.1016/j.epsl.2017.01.043

Kiro, Y., Goldstein, S. L., Lazar, B., and Stein, M. (2016). Environmental implications of salt facies in the Dead Sea. *Geological Society of America Bulletin*, *128*, 824–841. https://doi.org/10.1130/b31357.1

Kutzbach, J. E., Guan, J., He, F., Cohen, A. S., Orland, I. J., and Chen, G. (2020). African climate response to orbital and glacial forcing in 140,000-y simulation with implications for early modern human environments. *PNAS*, *117*. https://doi.org/10.1073/pnas.1917673117/-/DCSupplemental

Labuhn, I., Tell, F., Grafenstein, U. V., Hammarlund, D., Kuhnert, H., and Minster, B. (2021). A modern snapshot of the isotopic composition of lacustrine biogenic carbonates: Records of seasonal water temperature variability. https://doi.org/10.5194/egusphere-egu21-13178

Liu, J., and An, Z. (2020). Leaf wax n-alkane carbon isotope values vary among major terrestrial plant groups: Different responses to precipitation amount and temperature, and implications for paleoenvironmental reconstruction. *Earth-Science Reviews*, *202*. https://doi.org/10.1016/j.earscirev.2020.103081

Martrat, B., Grimalt, J. O., Lopez-Martinez, C., Cacho, I., Sierro, F. J., Flores, J. A., Zahn, R., Canals, M., Curtis, J. H., and Hodell, D. A. (2004). Abrupt temperature changes in the Western Mediterranean over the past 250,000 years. *Science*, *306*, 1762–1765. https://doi.org/10.1126/science.1101706

Mekki-Azouzi, M. E., Tripathi, C. S. P., Pallares, G., Gardien, V., and Caupin, F. (2015). Brillouin spectroscopy of fluid inclusions proposed as a paleothermometer for subsurface rocks. *Scientific Reports*, *5*. https://doi.org/10.1038/srep13168

Milner, A. M., Collier, R. E., Roucoux, K. H., Müller, U. C., Pross, J., Kalaitzidis, S., Christanis, K., and Tzedakis, P. C. (2012). Enhanced seasonality of precipitation

in the Mediterranean during the early part of the Last Interglacial. *Geology*, *40*, 919–922. https://doi.org/10.1130/G33204.1

Neev, D., and Emery, K. O. (1967). The Dead Sea: depositional processes and environments of evaporites. *Geol. Surv. Israel Bull.*, *41*, p. 167.

Neugebauer, I., Brauer, A., Schwab, M. J., Waldmann, N. D., Enzel, Y., Kitagawa, H., Torfstein, A., Frank, U., Dulski, P., Agnon, A., Ariztegui, D., Ben-Avraham, Z., Goldstein, S. L., and Stein, M. (2014). Lithology of the long sediment record recovered by the ICDP Dead Sea Deep Drilling Project (DSDDP). *Quaternary Science Reviews*, *102*, 149–165. https://doi.org/10.1016/j.quascirev.2014.08.013

Ojala, A. E., Kosonen, E., Weckström, J., Korkonen, S., and Korhola, A. (2013). Seasonal formation of clastic-biogenic varves: The potential for palaeoenvironmental interpretations. *GFF*, *135*, 237–247. https://doi.org/10.1080/11035897.2013.801925

Palchan, D., Neugebauer, I., Amitai, Y., Waldmann, N. D., Schwab, M. J., Dulski, P., Brauer, A., Stein, M., Y., E., and Enzel, Y. (2017). North Atlantic controlled depositional cycles in MIS 5e layered sediments from the deep Dead Sea basin. *Quaternary Research*, *87*, 168–179.

Riechelmann, D. F., Riechelmann, S., Wassenburg, J. A., Fohlmeister, J., Schöne, B. R., Jochum, K. P., Richter, D. K., and Scholz, D. (2020). High-Resolution Proxy Records From Two Simultaneously Grown Stalagmites From Zoolithen-cave (Southeastern Germany) and their Potential for Palaeoclimate Reconstruction. *Geochemistry, Geophysics, Geosystems*, *21*. https://doi.org/10.1029/2019GC008755

Shi, J., Cook, E. R., Lu, H., Li, J., Wright, W. E., and Li, S. (2010). Tree-ring based winter temperature reconstruction for the lower reaches of the yangtze river in southeast China. *Climate Research*, *41*, 169–175. https://doi.org/10.3354/cr00851

Sirota, I., Arnon, A., and Lensky, N. G. (2016). Seasonal variations of halite saturation in the Dead Sea. *Water Resources Research*, *52*, 7151–7162.

Sirota, I., Enzel, Y., and Lensky, N. G. (2017). Temperature seasonality control on modern halite layers in the Dead Sea: In situ observations. *Bulletin*, *129*, 1181–1194.

Sirota, I., Enzel, Y., Mor, Z., Moshe, L. B., Eyal, H., Lowenstein, T. K., and Lensky, N. G. (2021). Sedimentology and stratigraphy of a modern halite sequence formed under Dead Sea level fall. *Sedimentology*, *68*, 1069–1090. https://doi.org/10.1111/sed.12814

Smit, J., Brun, J. P., Fort, X., Cloetingh, S., and Ben-Avraham, Z. (2008). Salt tectonics in pull-apart basins with application to the Dead Sea Basin. *Tectonophysics*, *449*, 1–16. https://doi.org/10.1016/j.tecto.2007.12.004

Stein, M. (2001). *The sedimentary and geochemical record of Neogene-Quaternary water bodies in the Dead Sea Basin-inferences for the regional paleoclimatic history.*

Stein, M., Ben-Avraham, Z., Goldstein, S., Agnon, A., Ariztegui, D., Brauer, A., Haug, G., Ito, E., and Yasuda, Y. (2011). Deep Drilling at the Dead Sea. *Scientific Drilling*. https://doi.org/10.2204/iodp.sd.11.04.2011

Steinhorn, I. (1983). In situ salt precipitation at the Dead Sea. *Limnology and oceanography*, *28*, 580–583.

Steinhorn, I. (1985). The disappearance of the long term meromictic stratification of the Dead Sea. *Limnology and Oceanography*, *30*, 451–472. https://doi.org/10.4319/lo.1985.30.3.0451

Torfstein, A., Goldstein, S. L., Kushnir, Y., Enzel, Y., Haug, G., and Stein, M. (2015). Dead Sea drawdown and monsoonal impacts in the Levant during the last interglacial. *Earth and Planetary Science Letters*, *412*, 235–244. https://doi.org/10.1016/j.epsl.2014.12.013

Torfstein, A., Goldstein, S. L., Stein, M., and Enzel, Y. (2013). Impacts of abrupt climate changes in the Levant from Last Glacial Dead Sea levels. *Quaternary Science Reviews*, *69*, 1–7. https://doi.org/10.1016/j.quascirev.2013.02.015

Trachsel, M., Kamenik, C., Grosjean, M., McCarroll, D., Moberg, A., Brázdil, R., Büntgen, U., Dobrovolný, P., Esper, J., Frank, D. C., Friedrich, M., Glaser, R., Larocque-Tobler, I., Nicolussi, K., and Riemann, D. (2012). Multi-archive summer temperature reconstruction for the European Alps, AD 1053-1996. *Quaternary Science Reviews*, *46*, 66–79. https://doi.org/10.1016/j.quascirev.2012.04.021

Waldmann, N., Stein, M., Ariztegui, D., and Starinsky, A. (2009). Stratigraphy, depositional environments and level reconstruction of the last interglacial Lake Samra in the Dead Sea basin. *Quaternary Research*, *72*, 1–15. https://doi.org/10.1016/j.yqres.2009.03.005

Wang, M., Zong, Y., Zheng, Z., Man, M., Hu, J., and Tian, L. (2018). Utility of brGDGTs as temperature and precipitation proxies in subtropical China. *Scientific Reports*, *8*. https://doi.org/10.1038/s41598-017-17964-0

Werner, M., Mikolajewicz, U., Heimann, M., and Hoffmann, G. (2000). Borehole versus isotope temperatures on Greenland: Seasonality does matter. *Geophysical Research Letters*, *27*, 723–726. https://doi.org/10.1029/1999GL006075

Wirth, S. B., Gilli, A., Simonneau, A., Ariztegui, D., Vannière, B., Glur, L., Chapron, E., Magny, M., and Anselmetti, F. S. (2013). A 2000 year long seasonal record of floods in the southern European Alps. *Geophysical Research Letters*, *40*, 4025–4029. https://doi.org/10.1002/grl.50741

Chapter 6

Sharp increase of lake temperatures over one decade during interglacial MIS 7c: Insights from the Dead Sea basin

6.1 Introduction

A pioneering step of our understanding in global Earth's climate processes has been made by identifying variations of stable isotope compositions derived from Pleistocene-Holocene climate archives (Martinson et al., 1987; Petit et al., 1999). Such variations were recognised by isotopic excursions and have led to the definition of Marine Isotope Stages (MIS) that correspond to glacial (cold) and interglacial (warm) periods, with synchronous trends in continental ice volumes, and both atmospheric CO_2 concentrations and temperatures (Figure 6.1). Each period is characterised by the presence (glacial) or absence (interglacial) of major continental ice sheets that thus have a major control on global sea-level.

The general MIS numbering is based on marine fossil foraminifera and has provided a detailed palaeoclimatic record of the past 5 million years on millennial to centennial resolution (Lisiecki and Raymo, 2005). For example, MIS 7 is divided into five sub-stages (labelled from a to e), while MIS 7e is the oldest at the boundary to Termination III (ca 246 ka ago), marked by a rapid shift from glacial to interglacial conditions (Tzedakis et al., 2004) (Figure 6.1).

However, terrestrial climate archives are often affected by stratigraphic gaps (hiatus) due to erosion or deposition shortages (omission). Therefore, well-resolved climate records are scarce and not uniformly distributed for all regions of interest. Nevertheless, ice core and terrestrial-derived pollen records have helped to resolve palaeoclimatic periods during Early-Middle Pleistocene MIS sub-stages in, e.g., Antarctica (Petit et al., 1999), Britain (Candy and Schreve, 2007), Portugal (Tzedakis et al., 2004), or Greece (Tzedakis et al., 2003).

The Vostok ice core revealed four prominent peaks in atmospheric CO_2 concentrations during MIS 11.3, 9.3, 7.5 (=MIS 7e), and 5.5 (=MIS 5e) (Petit et al., 1999). Further, records have marked the MIS 7 period as an interesting study interval that might be an analogue to present-day global warming, with similar global sea-levels during 7c and 7e compared to present-day (Tzedakis et al., 2004). It is further characterised by three warm shorter sub-stages (7e, 7c, 7a) which revealed short periods of strong atmospheric warming in Antarctica which coincides with increased CO_2 concentrations, decreased ice volume, and more negative $\delta^{18}O$ signatures (Figure 6.1; Watanabe et al., 2003). The site Dome Fuji (E Antarctica) provided a millennial-scale record showing an increase by 8 °C around 220 ka ago during the MIS 7d-7c transition (Watanabe et al., 2003). Support for such an abrupt warming 220 ka ago comes also from marine sediment records retrieved 100 km offshore of NW Spain (42°N), where reconstructed sea-surface temperatures from planktic foraminifera increased by ca 10 °C (summer) and 8 °C (winter) (Desprat et al., 2006).

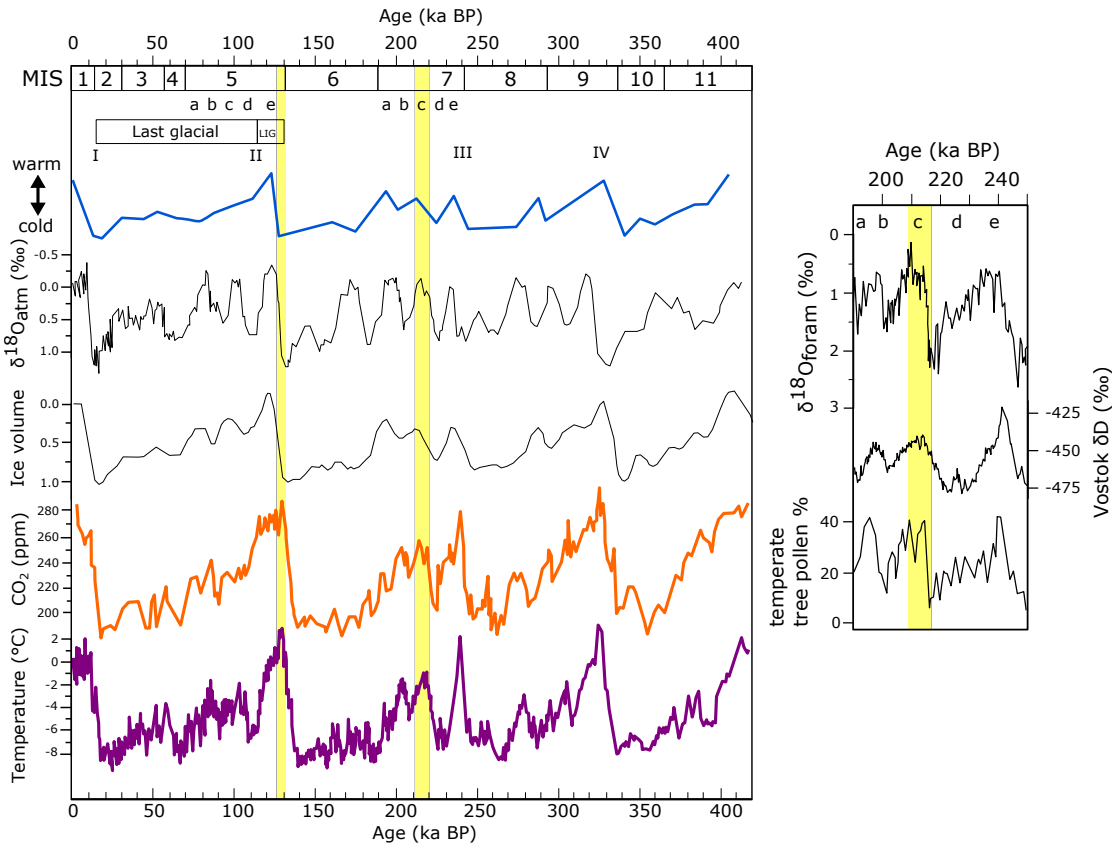

Figure 6.1 Overview of global climate conditions during the past 400 ka. Left: Defined MIS stages plotted together with atmospheric oxygen isotope composition (Sowers et al., 1993; Jouzel et al., 1996; Malaizé et al., 1999), ice volume changes, atmospheric CO_2 variations, and Antarctic temperatures reconstructed from oxygen isotopes (Petit et al., 1999). Glacial-interglacial sub-stages of MIS 5 and 7 indicated by a to e, climatic transitions marked by Terminations I-IV. LIG: Last interglacial. Right: MIS 7 with three short-term warming sub-stages (a, c, e) and two glacial intervals (b, d), reconstructed by planktonic foraminiferal oxygen isotopes and tree pollen abundances (Tzedakis et al., 2004), and deuterium isotopes from the Vostok ice core (Petit et al., 1999). Yellow vertical bands in both plots show the halite units studied in this thesis (MIS 7c = 5017-1-A-176-2; MIS 5e = 5017-1-A-122-2).

The Climatic Optimum of MIS 7 has been reported for the Bay of Biscay (North Atlantic; 46°N) between 220-210 ka based on benthic foraminiferal species yielding an oxygen isotope excursion, coinciding with a strong increase in dinocyst species at maximum July insolation at 65°N (Penaud et al., 2008).

However, none of these climate records could achieve a temporal resolution better than centennial scales, hence terrestrial palaeoclimate studies are often temporarily limited. Although orbital processes had the major control on ancient climatic cycles, the present-day warming takes place on decadal scales which needs to be interrupted immediately to maintain warming by maximal 1.5 °C (IPCC, 2022).

Thus, it is important to understand which short-term conditions (e.g., temperatures) might have prevailed at terrestrial study sites in the past.

The Levant region, located in an arid climatic zone between the south-eastern edge of Europe, western Asia and north-eastern Africa, is an interesting area of study due to its climate sensitivity and archaeological findings indicating an early influence of our ancestors on the region in the last 300 ka (Slon et al., 2014). It was also probably the main corridor for migration to Asia and Europe (Hershkovitz et al., 2018).

The DSDDP core 5017-1-A retrieved from the Dead Sea basin (DSB) yields a full sedimentary record of the past 250 ka, thus, including several glacial-interglacial periods that are represented by specific lithological units during wetter (detrital material) and drier (autochthonous gypsum, aragonite, salt) regional climate conditions. Halite units accumulated during lake mixing periods (monomixis) and respond to seasonal shifts of summer-winter in the present-day Dead Sea, which makes it attractive for short-term climate studies. Furthermore, previous studies have shown that fluid inclusions trapped in salt (halite, NaCl) serve as accurate palaeothermometer using Brillouin spectroscopy (Guillerm et al., 2020; Brall et al., 2022).

The work performed in this chapter deals with annually-deposited halite layers from a sediment core section that corresponds to the interglacial MIS 7c. Trapped fluid inclusions in coarse halite layers are used to determine their entrapment temperatures on decadal scales. The temperature difference of sub-samples in each layer will be used to calculate palaeoseasonal variations, and averaged annual temperatures will be compared to present-day temperatures as well as to the interglacial MIS 5e period.

6.2 Material

In this work, the oldest halite-bearing core section has been studied of core 5017-1-A. Core 5017-1-A has been drilled in December 2010 in the central basin of the Dead Sea (Levantine region, Israel) during the 'Dead Sea Deep Drilling Project' (DSDDP; Stein et al., 2011). The overall drill length was 1087.2 m, the cored length 922.4 m of which 78.2% could be recovered (that is, a core length of 721.2 m). For a general overview about the geological setting in the Levantine region including the DSB, the reader is referred to Chapter 5. Basically, core 5017-1 comprises two lithological groups (marl and halite facies, respectively) with main sub-facies of gypsum detritus (gd), alternating aragonite and silty detritus (aad), laminated detritus (ld), layered halite (lh) often accompanied with homogeneous halite (hh), and halite and detrital marl (hdm). Further, slumped deposits of mass transported deposits (mtd), halite transported deposits (htd), and coarse clastic detritus (ccd) have been defined (Neugebauer et al., 2014; Figure 6.2 A).
Core section 5017-1-A-176-2 belongs to the Amora formation and has been deposited during Marine Isotope Stage 7 (MIS 7), located between 445.03 meters below lake floor (m blf) to 446.50 m blf (Figure 6.2 A). The lithology of section 176-2 is dominated by detrital dark clay layers (144.5 to 82 cm, 78.5 to 67 cm, and 6 to 0 cm of core section depth), an ochre-colored aragonite part of 3.5 cm total thickness (82 to 78.5 cm), and salt alternations (67 to 6 cm) (Figure 6.3 A, B). Thus, based on a core section length of 144.5 cm, the total fraction is largest for clay (55.4%), followed by salt (42.2%), and aragonite (2.4%). The closest dated tie point of 176-2 was published at 455.89 m blf with an age of 220 ± 2.0 ka (Goldstein et al., 2020). Another tie point, of the same study, was defined at 419.83 m blf with 207 ± 2.0 ka. Thus, both tie points lie 10.06 m below and 27.34 m above the lowest salt layer, respectively (Figure 6.2 B).
clay intervals are considered to represent meromictic lake regimes (no mixing throughout a year) due to modern observations in the Dead Sea (Gertman and Hecht, 2002). On the contrary, salt crystals have been reported to nucleate/deposit uniquely during holomictic periods when the water body mixes at least once a year (Gertman and Hecht, 2002).

Successional halite layers of the lh facies reveal two types that are defined in mineralogical aspects by their grain sizes, and in sedimentological aspects by their limnological nucleation environment. Coarse halite layers are characterised by centimeter-sized opaque crystals with clear cubic shapes, while cumulate (CU) halite forms layered assemblages of fine-grained crystals (50-400 µm) with frequent cementation of the grain boundaries by detrital material (Figure 6.3 B). Modern observations have shown that halite formation in the Dead Sea is dependent on the

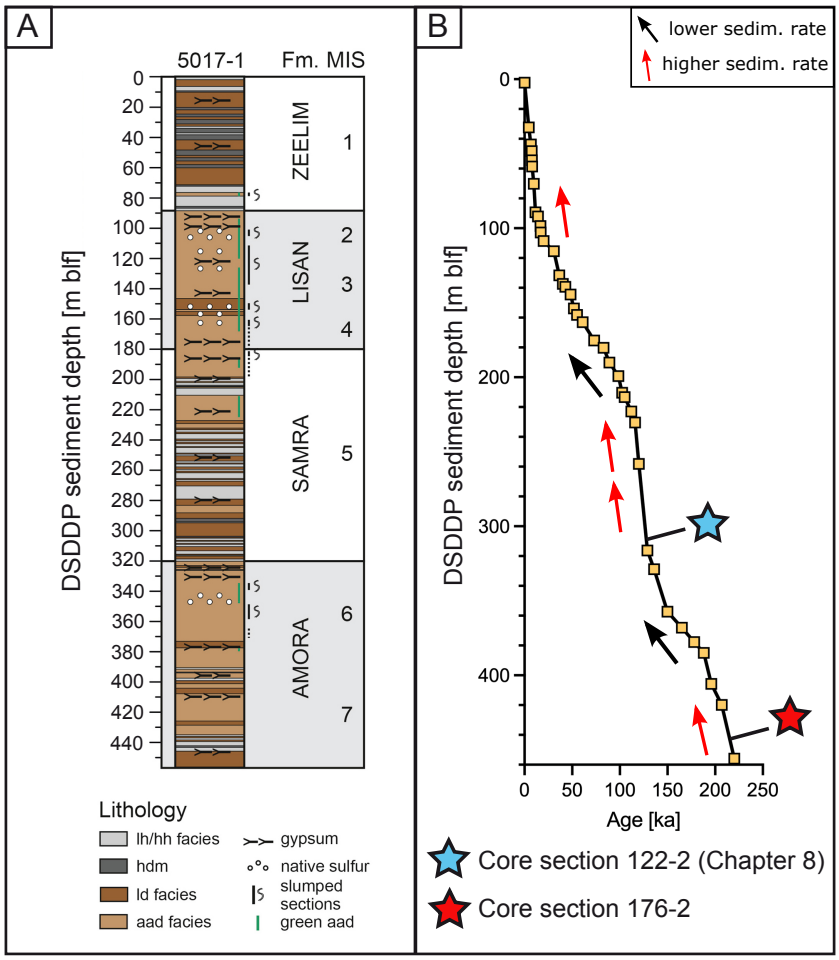

Figure 6.2 (A) Lithology of core 5017-1 (from Ben Dor et al., 2019; modified after Neugebauer et al., 2014). (B) Age model with both core sections studied during this PhD thesis (after Goldstein et al., 2020).

degree of supersaturation with respect to NaCl (Sirota et al., 2017). CO crystals nucleate from the brine below the thermocline in the deeper lake environment (hypolimnion) during the summer season, while dissolution takes place at the shallow lake floor (epilimnion) (Sirota et al., 2017). During winter when the water body is mixed, cumulate crystals precipate uniformly in the epi- and hypolimnion by settling on the previously formed CO layers.

Core section 176-2 encloses 13 coarse and 12 cumulate layers of such halite types (Figure 6.3 A). Above CO layers the grain size boundaries show frequently sharp changes in both color and grain size, pointing to a rapid accommodation of settled CU crystals that form smooth surfaces (e.g., CO9-TOP -> CU in Figure 6.3 B-3; Kiro et al., 2016; Sirota et al., 2017). The transition of CU to CO types show in most cases also a sharp boundary (e.g., CU -> CO10-BOT in Figure 6.3 B-3). However, the exact position where CO crystals started to nucleate on the underlying CU layer is sometimes not easy to detect due to transitions zones of unconsolidated CU surfaces (e.g., CU -> CO2-BOT in Figure 6.3 B-1).

Typical pristine (non-altered) halite crystals contain normally growth-zonations with entrapped assemblages of FIs which appear macroscopically as visible cloudy bands (see Figure 1.1). Cumulate crystals contain also growth bands of FIs on a smaller scale with a FI-free central part that probably served as crystal nucleus. FIs in CU layers are much smaller compared to CO layers, typically not exceeding sizes of 5 µm. Moreover, the FIs clouds are very dense in terms of the amount of FIs which complicates the temperature measurement with BS due to larger uncertaintes of the resulting T_x data (see also Chapter 5).

Therefore, only coarse halite FIs have been studied for palaeothermometry. The selected FIs are located along dark-to-bright alternated growth bands (Figure 6.3 C-1). Nonetheless, it is important to note that not every single CO crystal has such growth zonations, so that some areas can be free of FIs.

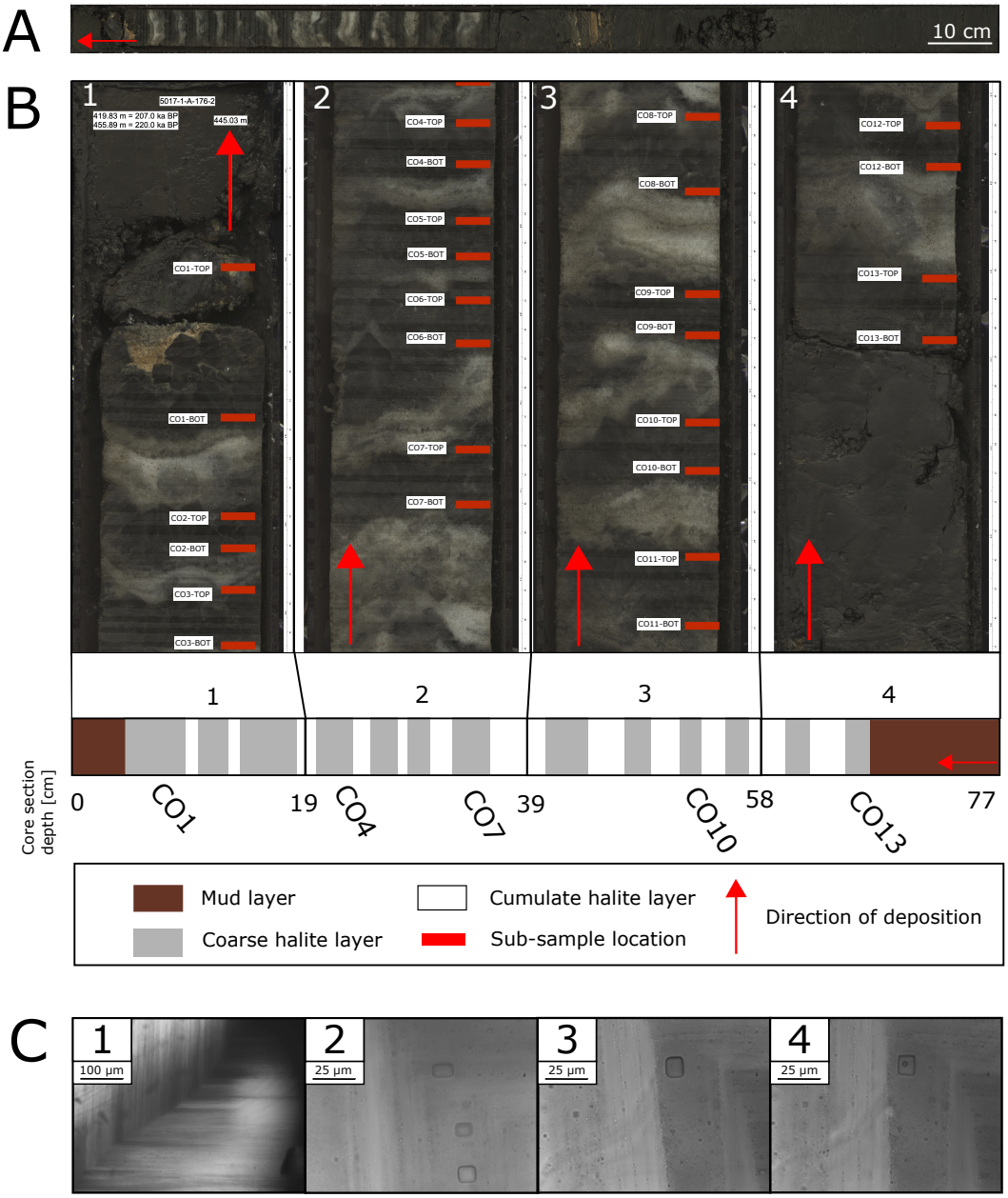

Figure 6.3 (A) Lithology of core section 176-2. Direction of deposition marked by red arrow. (B) Four segments (1-4) showing coarse-cumulate halite layering. All sub-samples are labelled next to their location (red bars). Illustrated lithology below for each segment with core section depths and numbered coarse layers. (C) Examples of CO halite growth zonations (1), three adjacent FIs within the same growth band, and a FI in monophasic (3) and biphasic (4) state.

6.3 Methods

6.3.1 Sampling strategy

Bulk sampling of core section 5017-1-A-176-2 was carried out at GFZ Potsdam, Germany, in August 2021, and afterwards transported in isothermal bags to University Lyon. All further steps were done at the Brillouin laboratory at the Institute of Light and Matter, Campus de la Doua, Villeurbanne. The sub-sampling strategy was slightly modified to that described in Chapter 5.3 because (1) no cumulate layers were sampled, and (2) only the uppermost (= CO-TOP) and lowermost (= CO-BOT) coarse halite layers were sampled. The sampling has been conducted in stratigraphic order from youngest to oldest, thus, from top (= 6 cm, CO1) to the bottom (= 67 cm, CO13) of the core section. Sub-samples were taken apart from the exact grain boundary because the previous study in core 5017-1-A-122-2 indicated that both minimum and maximum entrapment temperatures may be reached prior to the seasonal transition that is accompanied with a change in the dominating halite type in the sediment record (Chapter 5). The reader is referred to Chapter 5.3 for detailed information about the equipment used and the basic principles of Brillouin spectroscopy. Data are presented here as mean T_x values for each sub-section (i.e., uppermost samples in coarse layers labelled "CO-TOP", and lowermost samples in coarse layers labelled "CO-BOT", respectively). The depth of the water column at time of halite deposition must be taken into account because the pressure affects the water density at the lake floor (Guillerm, 2019). Due to the lack of a lake-level model, no correction term could be applied on measured T_x for this study so far. Therefore, the presented results show only the evolution of the relative lake bottom temperatures within 13 years of coarse halite deposition. An additional modelling study is in work to reconstruct the prevailing lake-level during MIS 7 by using the obtained solid-liquid-vapor-equilibrium (SLVE) sound velocity values (Guillerm et al., work in progress). Still, we note that, in view of the reduced time interval, the lake level and composition was virtually constant during deposition of the studied samples. Therefore, the correction is the same for all data, and differences between values can be directly discussed without knowing the correction.

6.4 Results

6.4.1 Entrapment temperatures

The total number of T_x measurements per sample (n_{sample}) depends on the amount of trapped FIs that are in agreement with certain criteria (see Guillerm et al., 2020). Thus, n_{sample} varies along the core section 176-2 because some selected sub-samples did not always contain suitable FIs in size, shape, or abundance.
A total of 13 coarse layers was studied, each one separated by fine cumulate layers with varying thicknesses. Here, the T_x data are reported as mean values of each studied sub-sample, with uncertainties reported as standard error of the mean (SE). The whole data set can be found in Table 6.1, results of both, CO-TOP sections are presented in Table 6.3 and of CO-BOT in Table 6.4, respectively. In addition, the results of CO-TOP sub-intervals have been split into two parts with respect to the core section, including data from both, 6-32 cm (upper part) and 39-63 cm (lower part), respectively (Table 6.6).
The coarse-TOP temperature is always very close to or higher than the BOT one, consistent with the expected seasonal warming (Table 6.1; Figure 6.4). There is an excursion in layer 8 with an anomalous increase in coarse-BOT temperature; however the two values of layer 8 have marginally overlapping error bands, which leaves the possibility for the two values to be nearly equal. The coarse-TOP temperatures are first nearly constant and then increase, while the BOT temperatures show a 3-year cycling of relatively lowest temperatures (Figure 6.5).
Exclusively all sub-samples stratigraphically above CO8-TOP show a rise in T_x along the growth direction of coarse layers (Figure 6.4 A), further, all remaining CO-TOP data are significantly elevated compared to sub-samples from CO13-TOP to CO8-TOP with a mean of 19.0 °C vs. 17.0 °C for the uppermost 26 cm and the lowermost 24.2 cm, respectively (Tables 6.5, 6.6). Hence, the interval from CO13-BOT to CO8-TOP is defined as lowermost interval I_{low} (445.695 to 445.423 m blf; 27.3 cm length).

Table 6.1 Measured uppermost (TOP) and lowermost (BOT) sub-intervals in coarse halite layers in core 5017-1-A-176-2.

Sample name	Section depth [cm]	5017-1 depth [m blf]	T_x mean [°C]	N[1]	SD[2] [°C]	SE[3] [°C]	CI[4] 95% [°C]	-z*[5] [°C]	+z*[6] [°C]
CO1-TOP	6	445.09	19.8	31	2.9	0.5	1.02	18.8	20.8
CO1-BOT	11.8	445.148	18.7	25	2.9	0.6	1.14	17.6	19.8
CO2-TOP	14.4	445.174	20.2	28	2.9	0.5	1.07	19.1	21.3
CO2-BOT	15.7	445.187	20	14	2.5	0.7	1.31	18.7	21.3
CO3-TOP	18.2	445.212	18.7	22	2.6	0.6	1.09	17.6	19.8
CO3-BOT	20	445.23	17.5	26	3	0.6	1.15	16.3	18.7
CO4-TOP	21	445.24	18.5	29	3	0.6	1.09	17.4	19.6
CO4-BOT	22.5	445.255	16.2	16	2.3	0.6	1.13	15.1	17.3
CO5-TOP	24.5	445.275	17.8	22	2.8	0.6	1.17	16.6	19.0
CO5-BOT	25.5	445.285	16.5	21	2.4	0.5	1.03	15.5	17.5
CO6-TOP	27	445.3	18.8	22	2.4	0.5	1.00	17.8	19.8
CO6-BOT	28.5	445.315	17.6	16	3	0.7	1.47	16.1	19.1
CO7-TOP	32	445.35	19.4	20	1.6	0.4	0.70	18.7	20.1
CO7-BOT	34	445.37	16.2	21	2.5	0.5	1.07	15.1	17.3
CO8-TOP	39.3	445.423	16.8	15	2.7	0.7	1.37	15.4	18.2
CO8-BOT	42	445.45	18.2	19	2.5	0.6	1.12	17.1	19.3
CO9-TOP	45.5	445.485	16.9	24	2.7	0.6	1.08	15.8	18.0
CO9-BOT	47	445.5	16	17	2.4	0.6	1.14	14.9	17.1
CO10-TOP	50	445.53	17.5	17	1.8	0.4	0.86	16.6	18.4
CO10-BOT	51.5	445.545	15.5	14	2	0.6	1.05	14.5	16.5
CO11-TOP	54.5	445.575	17	25	2.5	0.5	0.98	16.0	18.0
CO11-BOT	57	445.6	17.1	13	1.4	0.4	0.76	16.3	17.9
CO12-TOP	59	445.62	16.8	19	2.7	0.6	1.21	15.6	18.0
CO12-BOT	60	445.63	17.4	16	2.2	0.5	1.08	16.3	18.5
CO13-TOP	63.5	445.665	17.5	18	2.6	0.6	1.20	16.3	18.7
CO13-BOT	66.5	445.695	14.8	15	2.8	0.7	1.42	13.4	16.2
Total	**60.5**[7]	**0.605**[7]	**17.6**[8]	**525**	**2.5**[8]	**0.6**[8]	**1.10**[8]	**16.5**[8]	**18.7**[8]

[1] number of measured fluid inclusions per sample and in total
[2] standard deviation of a sample population
[3] standard error of the mean
[4] confidence interval
[5] T_x mean - CI 95%

The central interval I_{cen} describes the layers from CO7-BOT to CO4-BOT (445.37 to 445.255 m blf; 11.5 cm length). The maximum of Δ $T_{warming}$ along the whole core (+3.2 °C) is observed in layer CO7 by a sharp warming along the 2-cm thick coarse layer. This peak is followed by a stepwise two-year decline in both CO-BOT and CO-TOP (by maintaining Δ $T_{warming} > 0$ °C) until a local minimum at CO4-BOT is reached with 16.2 ± 0.6 °C. Regarding only the youngest bottom coarse sub-samples above CO4-BOT, a strong increase is found by +1.3, +3.8, and 2.5 °C for CO3-BOT, CO2-BOT, and CO1-BOT, respectively. Note that the maximum bottom T_x (20.0 ± 0.7 °C) is reported for CO2-BOT, a difference to the oldest bottom coarse sub-sample CO13-BOT of 5.2 °C (Table 6.4). Based on these

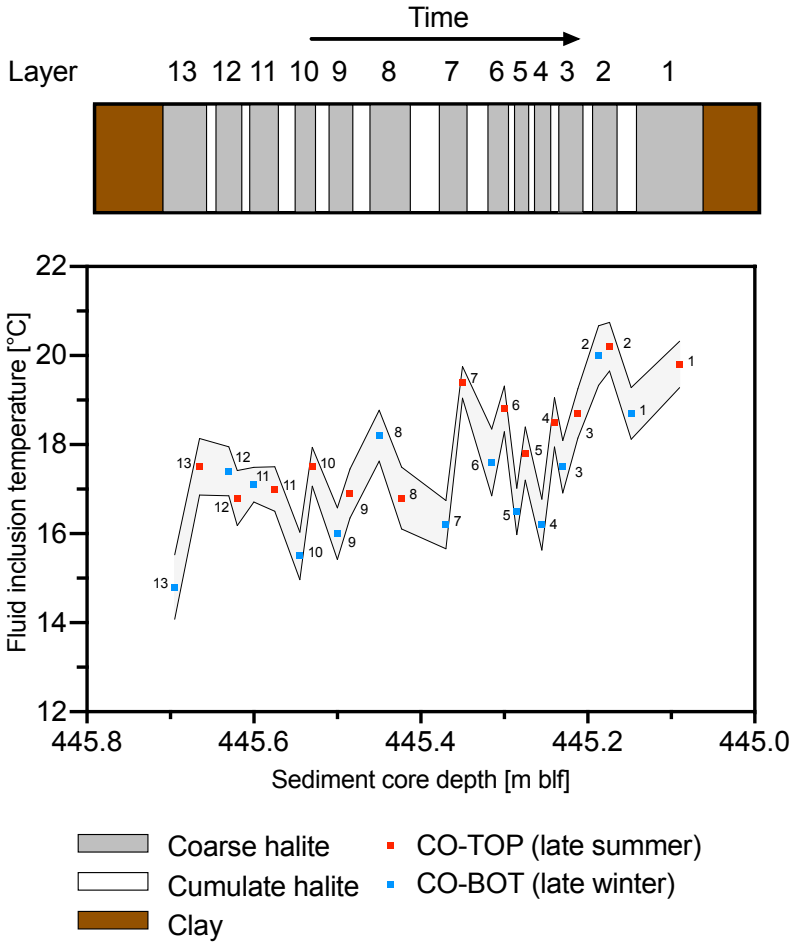

Figure 6.4 Palaeotemperatures from core section 176-2 (MIS 7c). Blue / red points labelled with respective layer numer (see sketch above). Blue points were sampled in the lowermost parts which correspond in the upper panel to the left-handed part of each grey bar. The inverse accounts for red points. The SE of each data points is presented by the grey band.

[6] T_x mean + CI 95%
[7] length of sampling interval in core section
[8] mean

findings of maximum T_x, this part is defined as the uppermost interval of core section 176-2 (I_{upp}) from 445.09 to 445.24 m blf (= CO1-TOP until CO4-TOP; 15 cm length). CO4-TOP was chosen here because this sub-sample marks the return to rising temperatures after the short-term local minimum when both CO-BOT and CO-TOP T_x declined. In addition, the sharp and continuous rise in CO-BOT T_x is characterising as well (Figure 6.5). Grouping the data set into bottom- and

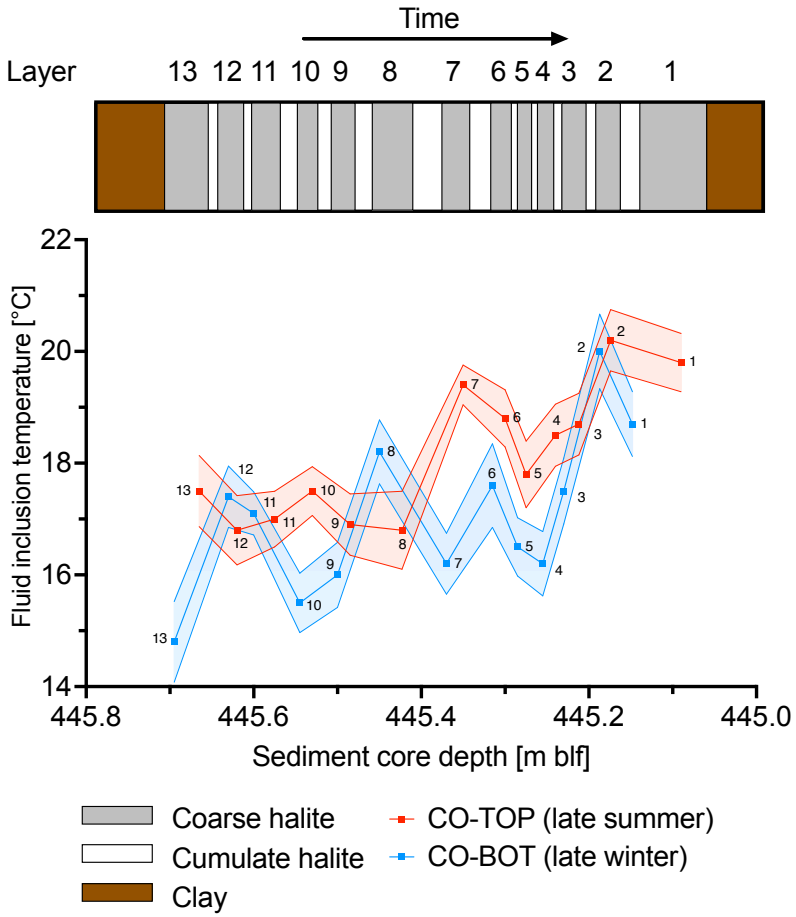

Figure 6.5 Evolution of winter (blue) and summer (red) palaeotemperatures during MIS 7c. The coloured bands yield the margin of error (SE).

top-related sub-samples reveals another interesting feature of core section 176-2. In I_{low} the CO-TOP sub-samples fluctuate constantly with local maxima (Lmax) during three-year cycles, including the transition to I_{cen} from halite layers 13 to 8 (Figure 6.4). However, CO-BOT sub-samples are characterised by local minima (Lmin) every three years throughout the studied core section, with CO-BOT being in anti-phase to CO-TOP along the layers CO13 to CO7. Although the anti-phase is just showing the (weak) seasonal signal that had been defined earlier, the CO-BOT oscillation pattern changes from anti-phase to a phase difference during I_{cen} to I_{upp} (Figure 6.5).

This "parallel-like" oscillation along the layers 7 to 1 is described by:

- an increase in both, CO-TOP and CO-BOT T_x values (CO7-TOP Lmax; CO6-BOT Lmax),
- a two-year decline in both, CO-TOP and CO-BOT T_x (CO5-TOP Lmin; CO4-BOT Lmin),
- by a successive rise in T_x within three years (CO2-TOP Lmax) and two years (CO2-BOT Lmax),
- and by a final decline in T_x in both CO-BOT and CO-TOP.

Total maximum T_x differences (absolute maximum minus absolute minimum of each sub-sample type) are 3.4 °C (CO-TOP) and 5.2 °C (CO-BOT). The temporal differences (uppermost T_x minus lowermost T_x for each sub-sample type) are 2.3 ± 0.6 °C (CO-TOP) and 3.9 ± 0.6 °C (CO-BOT), respectively. Finally, mean temperatures increased by 5.0 °C (CO1-TOP minus CO13-BOT) during more than one decade of halite deposition, with a combined uncertainty of ± 0.9 °C by taking into account the uncertainty (SE) of both sub-samples (± 0.5 °C for CO1-TOP, and ± 0.7 °C for CO13-BOT, respectively).

The major results observed are:

- in three layers, the coarse halite derived (bottom) temperature is nearly equal or larger than top temperature
- in the first half of the layers, the top temperature is initially rather constant, and shows an increasing trend by around 3 °C in the second half
- the bottom layer oscillates throughout the layers, but shows an overall increasing trend by around 3 °C too
- similar temperature trends (rising/declining) of both top and bottom coarse halite samples from layers 8 to 1

6.4.2 Halite layer thicknesses

The absolute thickness Δd_{abs} of halite layers differs from that of the calculated sub-sample locations (CO-TOP minus CO-BOT) because the samples have not been taken exactly at the grain size boundaries but rather a few millimeters above. Therefore, the following halite thicknesses are reported as Δd_{abs}.
The mean thickness of all coarse layers is 2.6 cm. The youngest coarse layer CO1 has the maximum thickness (3.5 cm), while the minimum thickness was measured in the second-youngest coarse layer CO2 (1.7 cm). The three defined intervals have mean thicknesses of 2.7 cm (I_{low}), 2.5 cm (I_{cen}), and 2.4 cm (I_{upp}), respectively.
Cumulate halite layers have a mean thickness of 2.1 cm with a minimum value of 0.6 cm between CO6-TOP and CO5-BOT, and a maximum thickness of 4.3 cm between CO8-TOP and CO7-BOT. The minimum cumulate layer is located within the sub-interval where both CO-BOT and CO-TOP data show a Lmin. Furthermore, note that the maximum cumulate thickness coincides with the sharp increase in T_x from CO7-BOT to CO7-TOP. Finally, each of the defined intervals yields a mean cumulate layer thickness of 2.4 cm (I_{low}), 2.2 cm (I_{cen}), and 1.6 cm (I_{upp}), respectively.

6.5 Discussion

6.5.1 Meromictic vs. holomictic periods in the DSB

clay deposits in the Dead Sea sedimentary record have been interpreted to reflect rather wetter climate conditions associated with colder temperatures and increased lake levels (Torfstein et al., 2015; Kiro et al., 2016). A possible cause might have been increased moisture in the DSB due to diverted southward storm tracks with more intense and frequent Eastern Mediterranean cyclones (Torfstein et al., 2015). The overlying clay layer in core section 176-2 indicates thus a temporal shift towards wetter climate conditions in the Levant, while elevated temperatures in the studied uppermost halite interval reflect the peak of a temporal dry period, which is in line with general interpretations of halite units in the Dead Sea basin (Neugebauer et al., 2014; Kiro et al., 2016).

The record of 176-2 provides a seasonal signature after the onset of halite deposition, with a calculated mean value of 2.7 °C (Figure 6.6 A). Mean annual deep lake temperatures in the modern DS increase slightly (<1 °C) in years 0-4 after the onset of the holomictic period (Figure 6.6 B) similar to mean annual values for the MIS 7c record (Figure 6.6 C). A particularly reversed mode of seasonal temperature variations, however, might have been prevailed due to the anti-phasic ΔT curves in Figure 6.6 C. Further, the summer-winter cooling seems to be slightly pronounced (layers 12-11), indicated by ΔT cooling values $\leq$ 0 °C.

As figured out, the first post-meromictic year 0 (= 1996 CE) is associated with a warming by +1 °C (ΔT warming: difference of maximal and minimal monitored deep lake water temperatures). A similar but less strong increase can be seen by ΔT cooling (<1 °C), thereby both parameters practically describe the annual seasonality. ΔT cooling never exceeds ΔT warming during the post-meromictic years in the modern DS until year 4 (= 2000 CE) (Figure 6.6 A). Interestingly, both curves of ΔT show parallel decreasing and increasing trends from years 2 to 4 (= 1998-2000 CE), respectively, and reach their highest rates when the late-summer lake temperature rises more pronounced by exceeding 24 °C. The derived estimates of T_f are in line with modern deep lake temperatures in the Dead Sea which ranged between 22-25 °C between 1996-2010 after the onset of holomictic conditions in 1996, coeval with the nucleation of halite (Gertman et al., 2010). The averaged increase in lake-bottom temperatures can be estimated to +0.38 °C per year which is more than the actual DS surface warming (+0.8 °C per decade) (Kishcha et al., 2021). Averaged temperature increases for each season specifically yield values of both +0.3 °C/year during late winter, and +0.18 °C/year for late-summer episodes, respectively.

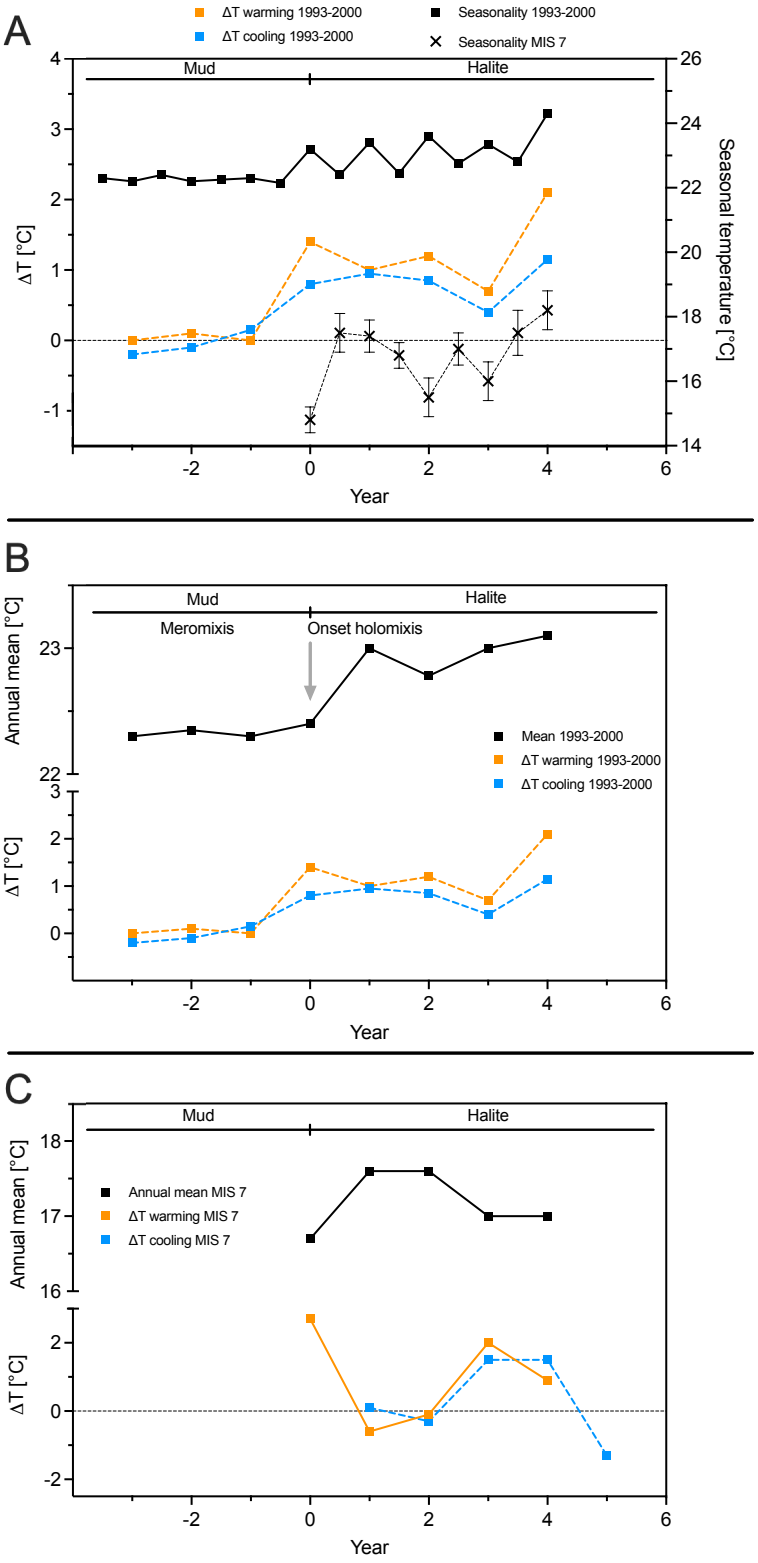

Figure 6.6 Evolution of bottom water temperatures after the onset of holomictic conditions. Note that the year of regime change from mero- to holomixis is called year zero here to co-image data of 176-2 simultaneously. A) present-day seasonality after onset of holomixis in 1996 compared to uncorrected T_x data from MIS 7c, B) annual temperatures increased slightly during the first holomictic years in the DS, C) similar increase of annual temperatures from MIS 7c in lowermost halite layers.

6.5.2 Temperature variability during interglacial MIS 7c

Continental areas are not affected in the same manner by modern global warming, i.e. at the same frequency or amplitude of occurring natural hazards, because the regional climate has often a major control on environmental processes (IPCC, 2022). However, it has already been reported that the Northern Hemisphere's seasons have shifted since 1952, and that summer days became longer and warmer while winters shortened but warmed too (Wang et al., 2021). Therefore, the interglacial period MIS 7c may help us to better understand on which time scales climate-sensitive continental regions underwent significant temperature changes or not. To identify potential seasonal changes over a decade and expecting a cooling (warming) during winter (summer), the temperature changes were calculated from data of both summer-to-winter and winter-to-summer intervals (see Figure 6.10):

$$\begin{aligned} \Delta T\,cooling &= T_x\,CO{-}TOP(n) - T_x\,CO{-}BOT(n{+}1) \\ \Delta T\,warming &= T_x\,CO{-}TOP(n) - T_x\,CO{-}BOT(n) \end{aligned} \tag{6.1}$$

Hence, typical winter seasons in the Levant would yield $\Delta T\,cooling$ values greater than 0 due to a drop in temperature (Gertman et al., 2010). Anomalies would be represented by $\Delta T\,cooling$ values less than 0 due to an increase in temperature during cumulate halite nucleation. Temperatures usually increase during spring to late summer when coarse halite crystal growth is dominating with $\Delta T\,warming$ values greater than 0. $\Delta T\,warming$ values less than 0 would rather imply a temperature anomaly.

Two cooling anomalies ($\Delta T\,cooling$ greater than 1 °C) were identified in layers 9/8 and 3/2 which is supported by one warming anomaly along the growth direction of the corresponding coarse summer layer 8 and $\Delta T\,warming$ close to 0 in layer 2 (Figure 6.7 D). To summarise, highest $\Delta T\,warming$ values appear on a 3-year cyclicity over one decade with a declining trend starting at the central part of the core section (layer 7).

The results imply that a similar seasonal shift like today could have occurred in MIS 7c when lake bottom waters became warmer in both, summers and winters. It is supported by slightly increased cumulate layer thicknesses (Figure 6.7 B), indicating higher degrees of supersaturation of salt like in the modern Dead Sea (Sirota et al., 2017). The timing of present-day lake mixing depends on the salt concentration in the upper water layer (epilimnion): at some point, the water density is high enough to induce 'double diffusion diapycnal fluxes' (DD flux) where salt is transferred to the deeper water layer (hypolimnion) (Arnon et al., 2016). Hence, the DD flux could have appeared earlier than usual (late November) in MIS 7c to account

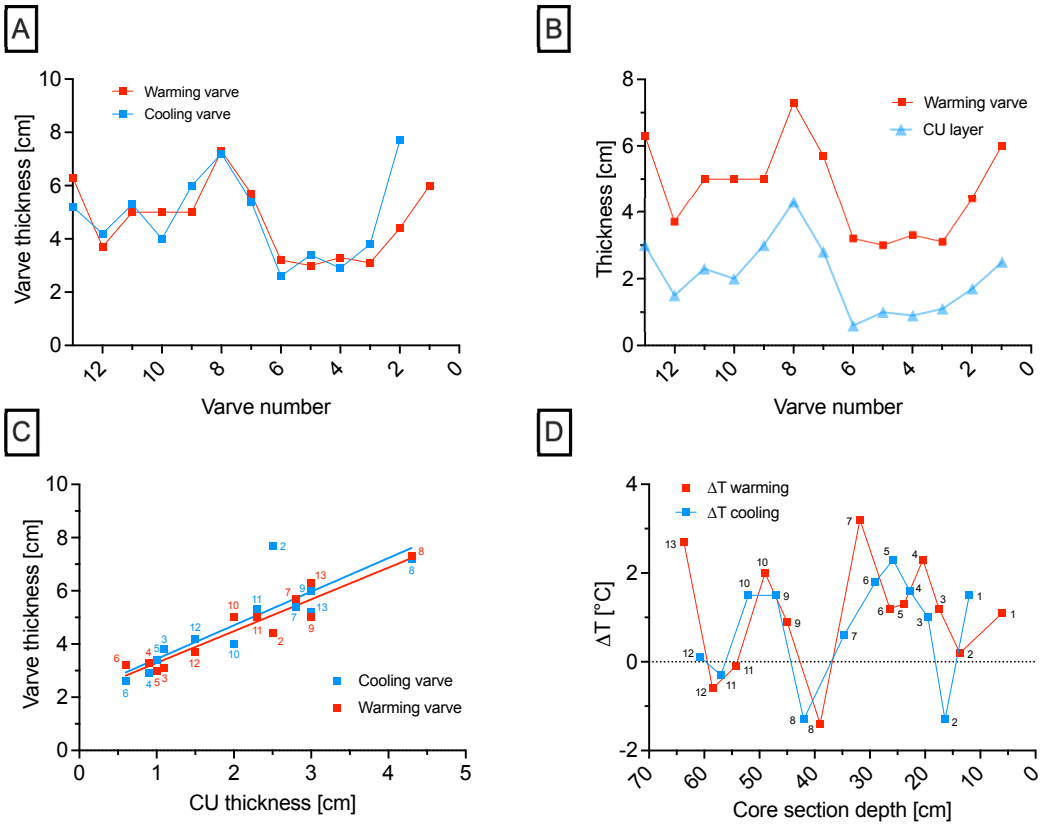

Figure 6.7 Characteristics of core section 176-2. A) Thickness of warming/cooling varves. B) Warming varve thickness vs. cumulate halite layer thickness. C) Cooling/warming varve thickness of each layer vs. cumulate halite layer thickness of each varve. D) Seasonality of summer-winter (blue) and winter-summer (red), respectively.

for a higher amount of nucleated cumulate crystals which form thicker layers at the lake floor. However, the results obtained here do not allow to claim if the summers became even longer and the winters shorter, as observed for the Northern Hemisphere during the last decades due to modern global warming (Wang et al., 2021). The total mean temperature difference between the oldest and youngest coarse halite layers is 5 °C ± 0.9 °C. However, since a strong seasonality lasting for multiple years has been established ca 6 years after the onset of the holomictic lake regime, it remains questionable if a comparison is reasonable between layers CO1-TOP and CO13-BOT because the seasonal temperature difference might likely be included. Therefore, it is recommended to compare only data that are related to summer or winter sub-samples.

6.5.3 Temperature shift for entrapment pressure

The analytical approach of measuring directly the entrapment temperatures of fluid inclusions using Brillouin spectroscopy is valid for (sub)surface minerals or rocks which formed close to ambient pressure. If this applies, then we write Tx = Tf. However, pristine evaporites can be found in even deeper environments in both oceans and lakes at higher water pressure. This pressure acts on the fluid inclusions during crystal growth, leading to a final temperature shift of both, "true" and measured temperatures. Hence, it is necessary to estimate either the water pressure at time of fluid entrapment (crystal growth), the water level (i.e., sea or lake level), or the water height (water level minus floor level). It follows:

$$C = Q * D * g * H \tag{6.2}$$

with C the temperature correction (°C), Q the quasi-isochore (°C/MPa), D the brine density (kg/m^3), g the gravitation acceleration at Dead Sea latitude (m/s2), and H the water height (m). For core section 176-2, the temperature correction equals (calculated by Guillerm et al., 2022, in review):

C (°C) = 0.74 °C/MPa * 1218.9 kg/m^3 * 9.795 m/s^2 * 318 ± 40 m
C (°C) = 2.9 ± 0.4 °C

Note that C is around 1.9 °C lower during MIS 7c than C during MIS 5e (chapter 5), despite similar lake levels (-306 ± 23 m vs. -311 ± 18 m, respectively). As an important factor to estimate the absolute water height, the subsidence rate of the DSB needs to be considered, and thus the floor elevation. The subsidence rate during the last 220 ka has been estimated to 2.00-2.45 mm/year with minor variations (Goldstein et al., 2020). Hence, the subsidence rate might have likely outpaced the sedimentation rate of the basin, leading to deeper basin floors during MIS 5e than MIS 7c. Therefore, both the water height and the pressure were higher as well, causing a higher temperature correction of 4.8 °C for MIS 5e samples (Guillerm, 2019; Guillerm et al., 2022, in review).
Final corrected fluid inclusions temperatures (in °C) using BS are calculated following:

$$T_f = T_x + C \tag{6.3}$$

on each T_x value from MIS 7c, and thus provides a straight comparison to other measured lake-bottom temperatures in the Dead Sea basin (Figure 6.8).

6.5.4 Palaeoclimate implications of fluid inclusion temperatures during MIS 7c

The applied pressure-related temperature shift on each T_x data point provides a better comparison with both modern and MIS 5e data of the Dead Sea basin. The resulting T_f data are in relatively good agreement (50 % of the data within the error bands) with the averaged temperatures obtained from core 122-2 dating back to MIS 5e (gray band in Figure 6.8; Table 6.2). The lowest temperature in sample CO13-BOT (17.7 °C at 445.695 m blf) is indicative for a change of the lake's hydroclimate which is associated with a lithological change from clay to salt deposition (Figure 6.3). This provides first evidence that such clay-dominated core sections may be associated with colder, wetter periods due to an increased runoff of fine detrital material into the lake, as it was interpreted in first studies of the environmental implications of the DSDDP sediment core 5017-1 (Kiro et al., 2016). However, temperature estimates of such interglacial periods were missing until now due to the lack of accurate palaeothermometry methods to be applied on DSDDP samples. Compared to mean temperatures of the modern DS (averaged over 1993-2010 for the hypolimnion), the obtained T_f data from MIS 7c are generally lower until the final increase during the years 12-13 after onset of salt deposition (Figure 6.8).

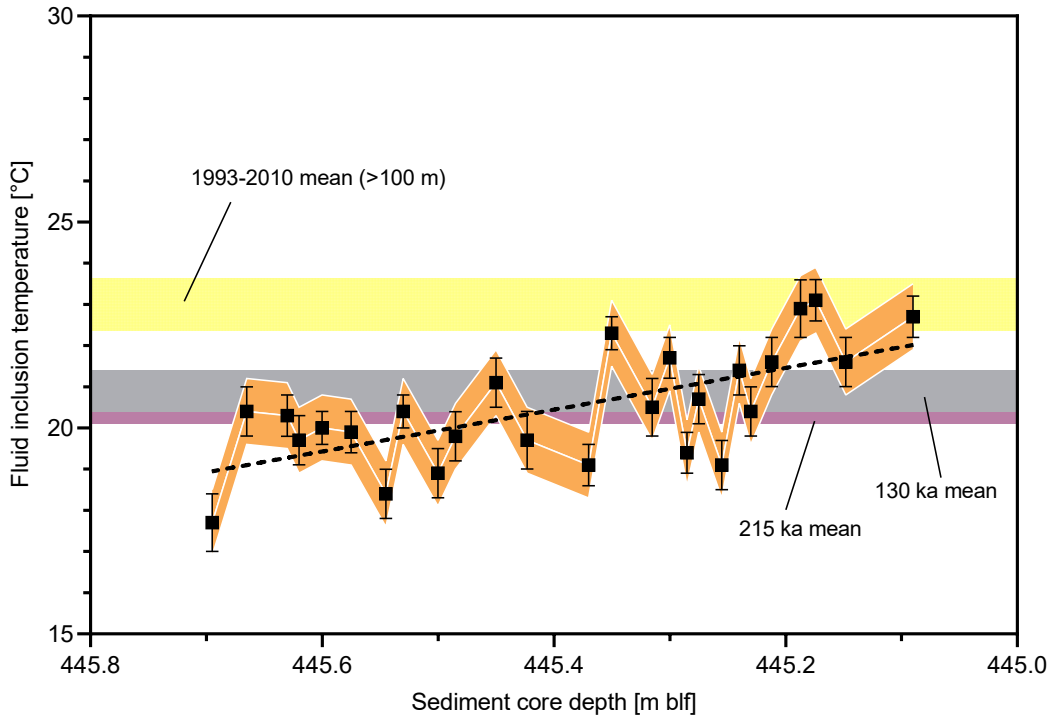

Figure 6.8 Corrected fluid inclusion temperatures in core 5017-1-A-176-2. The yellow band shows the present-day mean of DS deep waters (including an error margin of ± 0.6 °C). The blue band displays the mean of corrected fluid inclusion data from core 5017-1-A-122-2 (MIS 5e) (error margin of ± 0.5 °C), the purple band marks the mean of core section 176-2. Note that the error overlaps with the gray band due to almost identical values.

This finding is in good agreement with previous interpretations of salt facies in DSDDP core 5017-1: salt facies were interpreted as regional responses to periods of global climate warming with drier, hypersaline conditions in the Levant region, associated with major lake level drawdowns (Kiro et al., 2017; Torfstein et al., 2015). These arguments could also be used here to explain the maximum temperatures at the end of halite deposition in core section 176-2. However, recent results from analyzed fluid inclusion data (including the data set presented in this chapter), combined with reconstructed lake levels, subsidence rates, and the modeled NaCl inventory of the DSB (Guillerm, pers. comm.), suggest that lake levels were not primarily affected by global climate changes. The extent to which lake levels are correlated with (hypolimnion) temperatures remains an open question, which requires future studies using multiproxy approaches.

Nevertheless, the results suggest the great potential of analyzing halite section in the sediment record to estimate the thermometric evolution of the DS water body through time. Further, the method is a powerful tool to accomplish high-resolutional reconstructions of decadal palaeoseasonal variations in halite sections. In this study,

the estimated temperature increase over 13 years is about 2.3 °C, being a reasonable value compared to modern global warming in many continental regions (IPCC, 2022). This study suggests furthermore that continental water bodies such as the Dead Sea basin might experience decadal-to-centennial temperature fluctuations as seen by the relation between both, the onset (lowest T_f) and the end (highest T_f) of halite deposition during relatively drier interglacial periods.

Lake bottom temperatures are estimated to have increased by 3.9 ± 1.4 °C for winter intervals, and 2.3 ± 1.2 °C for summer intervals, respectively. This is in contrast to present-day model projections that have shown that the Eastern Mediterranean region (including the Levant) will be affected by a strong warming: Mean surface temperatures in winter seasons will increase by ca 2-3 °C between 2040-2070, and in summer seasons by ca 4-5 °C (Lelieveld et al., 2012)(Figure 6.9). Another model for the Levant region reconfirmed that global warming will result in a stronger warming of summers than of winters due to the westward expansion of a thermal low, which will increase the number of hot days per year, decrease the regional rainfall amount and lead to dry soils with less heat storage capacities (Lelieveld et al., 2016). The contradicting reversed decadal rise of both winter and summer lake temperatures could be explained by the onset of a global interglacial period (ca 220-210 ka; Martinson et al., 1987). Summer insolation was highest at that time during the past 400 ka (Berger, 1978), further evidence of a short-term (ca 16 ka; Tzedakis et al., 2004) global warming event comes from other proxy records, e.g., from the Antarctic Vostok ice core (Petit et al., 1999). However, the MIS 7c interglacial was not as pronounced as other strong interglacials because the peaks of both global mean temperatures and CO_2 concentrations were lower than MIS 11 or MIS 5e, although both variables increased in a short time (Figure 6.1; Petit et al., 1999). Hence, the lower CO_2 concentration during MIS 7c could have controlled the continental temperature effect like it does today, and explain why winters warmed stronger than summers in the Dead Sea Basin. Desprat et al. (2006) reported that Atlantic sea-surface temperatures increased by ca 8 °C in winter and ca 10 °C in summer, respectively, during the transition from MIS 7d to 7c.

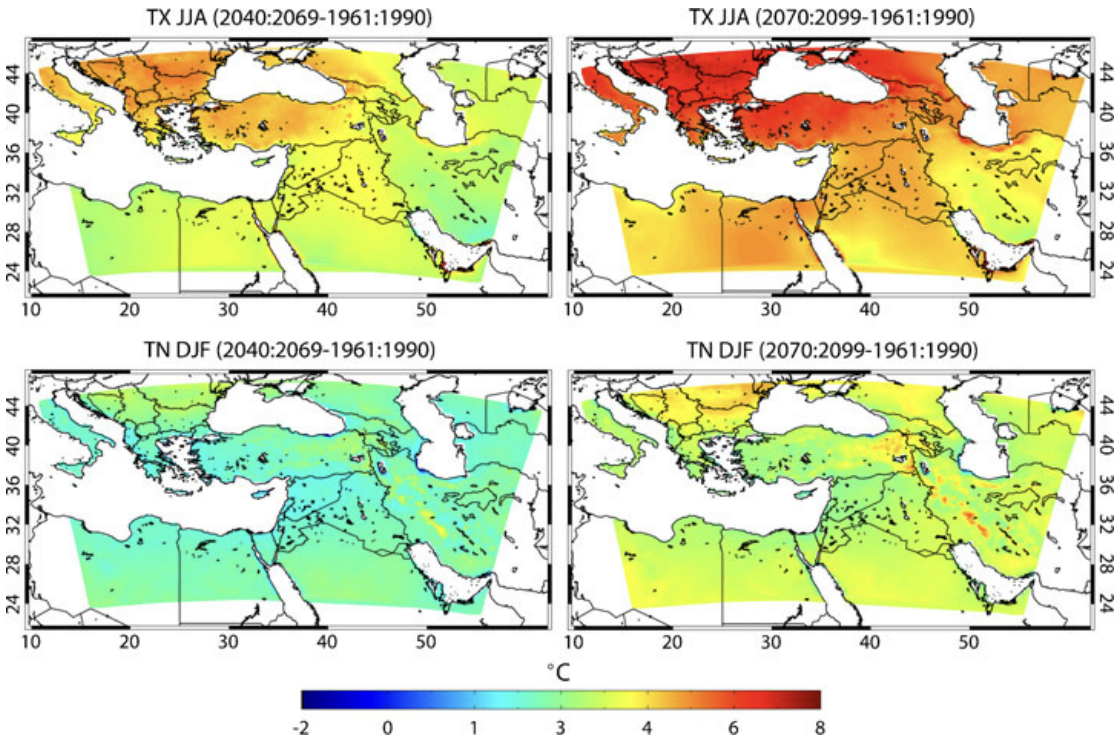

Figure 6.9 Modelled changes of mean summer maximum (July-August, JJA; TX) and mean winter minimum (December-February, DJF; TN) temperatures. Changes relative to a control period (1961-1990) for 2040–2069 (left) and 2070–2099 (right) (Lelieveld et al., 2012).

Tzedakis et al. (2004) showed positive isotopic excursions in both benthic and planktonic foraminifera from a marine core off SW Portugal. Unfortunately, terrestrial climate archives are scarce in the Levant region. Speleothems from the Soreq Cave have shown to be able to reconstruct the climatic history of the last 160 ka, covering MIS 6 (Matthews et al., 2021), and to decipher modern seasonal changes on monthly time scales (Orland et al., 2014). Therefore, the results obtained here from a halite section covering 13 years of lake history might encourage further palaeotemperature reconstructions by using Brillouin spectroscopy. To uncover additional seasonal patterns of other interglacial periods will improve our understanding of the Dead Sea Basin, and extend the database derived from palaeoclimate proxies.

6.6 Conclusions

A detailed palaeoclimate study covers an episode of dry conditions in Lake Amora (Dead Sea basin) during MIS 7c. The data set obtained in this study provides for the first time direct temperature measurements of the DSB over more than one decade. The record bears seasonal varying signatures along a halite unit that is comprised of 13 alternating coarse/cumulate layers. The presence of such halite layers between two thick clay units implies holomictic lake conditions at the time of deposition. Contrary to the onset of holomictic conditions in 1996 and a seasonality of 1 °C, the results presented here suggest a rather sluggish onset of annual seasonality (winter-summer) during MIS 7c. However, winter temperatures vary with a 2-3 year periodicity and rise steadily throughout more than one decade. A general decadal temperature rise of lake-bottom temperatures can be inferred from the data set, as seen by averaged increases of both, 3.9 ± 1.4 °C for winter intervals, and 2.3 ± 1.2 °C for summer intervals, respectively. The overall mean temperature increase can be estimated to 5 ± 0.9 °C. The rapid warming of both winter and summer seasons imply that the Dead Sea Basin has ever been a very sensitive hydrological system, with a strong response of the dominating lithological facies to intervals of global climate warming. The sharp increase of palaeo-lake temperatures also suggest that the present-day global warming might strongly effect the yet hypersaline Dead Sea and adjacent water resources, which could exacerbate the regional water supply for people, and increase the vulnerable situation of the Levant.

This study confirmed the power of halite layers as climate archives when combined with Brillouin spectroscopy to determine palaeotemperatures. Future studies could be thus performed on other halite units in DSDDP core 5017-1-A to investigate palaeoclimate lake conditions for any dry period of interest.

6.7 Appendices

6.7.1 Definition of varves

Formation temperatures of coarse halite samples have been used to compute the seasonal difference of individual layers by the offset between top T_x data and bottom T_x data (Δ $T_{warming}$) (see Chapter 5). It has been assumed that modern halite precipitation patterns might be valid for sedimentary records because the maximum palaeo-lake water temperatures were obtained for sub-samples from uppermost coarse intervals (CO-TOP). The modern Dead Sea is dominated by a holomictic lake regime with a mixing of the whole water body once a year (late November) due to salt fluxes from the lake's surface to the lake floor (Gertman and Hecht, 2002; Arnon et al., 2016). This process coincides with a change in the prevailing halite type from coarse to fine halite. Further, the depth in the water body, where halite nucleation takes place, turns from the lake floor (coarse halite) into the whole water column (including the brine-air interface). Although other suggestions were made to define lacustrine palaeoseasonality (Kwiecien et al., 2022), the approach using Δ $T_{warming}$ may be most suitable in the case of annually-deposited halite layers in the DSB.

Two approaches to define evaporitic varves have been used in this work to test the correlation between varve thickness and palaeotemperature data (Figure 6.10). Initially, the thickness of individual halite layers has been determined for both types from the bottom to the top of the core section, by measuring the distance between the first clear occurrence of a halite type to the occurrence of the overlying other type (Figure 6.10 B). The documented position of each boundary has been used further to determine absolute varve thicknesses.

Couplets of two layers are termed 'warming varve' by spanning from the coarse bottom to the cumulate top part of each layer (Figure 6.10 A). Hence, they include the period of initialing warming (CO-BOT -> CO-TOP during spring-summer) followed by a potential lake cooling (CO-TOP -> cumulate during fall-winter). The second approach named 'cooling varve' uses couplets that are equal to initial lake cooling (cumulate during fall-winter) followed by a potential warming of the water body during spring-summer. Relative varves were calculated directly as differences (Δ V_i) between the documented location during sample preparation of each sub-sample type (Figure 6.10 A):

- CO-TOP(N+1) - CO-TOP(N)
- CO-BOT(N+1) - CO-BOT(N).

and are plotted against T_x data in Figure 6.11. Note that the calculations of Δ V_i

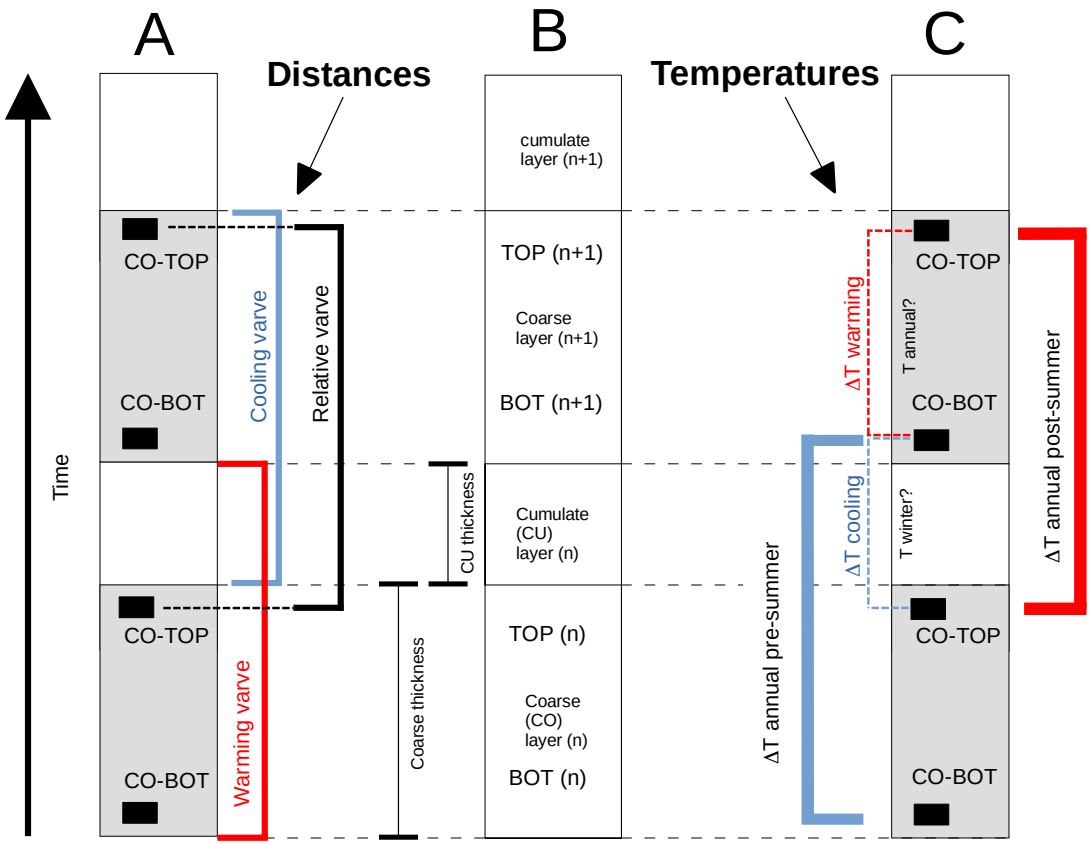

Figure 6.10 (A) Sketch of tested varve definitions used in this study. Note that both warming and cooling varve distances enclose a complete layer. (B) Terminology for both halite types in core 176-2 along one growth cycle (n -> n+1). (C) Calculation of relative temperature differences of a data set for both layer n and n+1, respectively. Black bars symbolise the location of sub-samples.

were carried out independently of the initial sampling at a later step of this work.

6.7.2 Definition of temperature couplets

The large data set obtained from 13 halite layers with 26 sub-samples gives the unique opportunity to test any existing correlations between the relative 'distances' of adjacent sub-samples and their proper 'palaeotemperatures'. For that, T_x data of all studied sub-samples were used to determine certain numerical differences $\Delta T\ i$ (Figure 6.10 C):

- ΔT annual pre-summer
- ΔT annual post-summer
- ΔT cooling
- ΔT warming

The differences between T_x of both, CO-BOT(n+1) and CO-BOT(n) (pre) could be used to describe the evolution of annual temperature deficits prior to lake warming during spring-summer along the core section. On the opposite, the difference between T_x of both, CO-TOP(n+1) and CO-TOP(n) (post) may be used to identify lake temperature deficits during the post-summer period. The lake cooling during winter may be inferred from the difference between CO-TOP(n) and CO-BOT(n+1), and a potential lake warming upon summer season from CO-TOP(n) and CO-BOT(n) (and for n+1, etc.) (Figure 6.10 C).
Although other proxy data are lacking in the Levantine region for MIS 7, the mean of each T_x of CO-TOP(n, n+1) and CO-BOT(n, n+1) might be useful to compare along the core section. Therefore, the mean annual temperature writes:

$$T_{annual} = \frac{T_x(CO-BOT) + T_x(CO-TOP)}{2} \tag{6.4}$$

The mean winter temperature is obtained by calculating the mean of CO-TOP(n) and CO-BOT(n+1), respectively.

6.7.3 Results

6.7.4 Absolute varve thicknesses

Data of all measured varves along the core section are listed in Table 6.7. Cooling varves show slightly varying values within I_{low} from CO13-TOP to CO8-TOP between 4.0 cm and 7.2 cm with a mean thickness of 5.32 cm. After a local maximum of 7.2 cm (CO8-TOP), the data show a drop to 5.4 cm, 2.6 cm, and 3.4 cm, respectively, with a mean of 3.8 cm from CO7-TOP to CO5-TOP. The upper part yields values of 2.9 cm and 3.8 cm (CO4-TOP and CO3-TOP, respectively). The last value obtained from CO2-TOP and CO1-TOP is the maximum value (7.7 cm) of all measured distances. The plotted curve against cumulate layer thicknesses correlates weakly due to the maximum at 7.2 cm (Figure 6.7 C).
Warming varves show only small variations compared to cooling varves (Figure 6.7 A). The lowermost interval of the core section yields three constant thicknesses (varves 11 to 9). An almost perfect correlation occurs during varves 8 to 6, subsequently the warming varves are in anti-phase to the cooling varves (varves 5-3), while the uppermost part of the core section is characterised by a parallel increase (Figure 6.7 A). Furthermore, the warming varve thickness correlates well ($R^2 = 0.92$) with the thickness of cumulate layers (Figure 6.7 B, C).

6.7.4.1 Relative varve thickness

Four sub-intervals of I_{low} (CO13 to CO8) yield constant values of $\Delta V_{top} = 4.5$ cm (Figure 6.11 C). The transition towards I_{cen} shows remarkably increases of relative thicknesses to 6.2 cm and 7.3 cm (CO9-TOP to CO8-TOP, and CO8-TOP to CO7-TOP, respectively). Subsequently, a declining trend follows with values of 5.0 cm, 2.5 cm, 3.5 cm, and 2.8 cm , with the two latter values being part of I_{upp}. From CO3-TOP to CO2-TOP, ΔV_{top} increases by 1.0 cm, while the last sub-interval (CO2-TOP to CO1-TOP) is marked by a sharp increase to $\Delta V_{top} =$ 8.4 cm. As a main result, ΔV_{top} is in phase with T_x values of CO-TOP sub-samples along the whole core section (Figure 6.11 D).
The calculated relative thicknesses between CO-BOT sub-sample locations (ΔV_{bot}) show a different evolution along core section 176-2. ΔV_{bot} varies stronger in its amplitude with alternating drops and rises on two-year cycles from CO13-BOT until CO8-BOT with 3.0 cm $< \Delta V_{bot} <$ 6.5 cm (Figure 6.11 A). A clear increase in ΔV_{bot} with a total maximum (8.0 cm) along the core section occurs towards CO7-BOT, followed by an overall sharp drop with mainly declining ΔV_{bot} values of 5.5 cm, 3.0 cm, and 2.5 cm until CO3-BOT. The two uppermost sub-intervals yield slightly raised thicknesses of 4.3 cm and 3.9 cm. The main finding here is that both obtained curves of ΔV_{bot} and CO-BOT T_x are first in anti-phase until

halite layer CO7, and secondly in phase until layer CO1 (Figure 6.11 B).

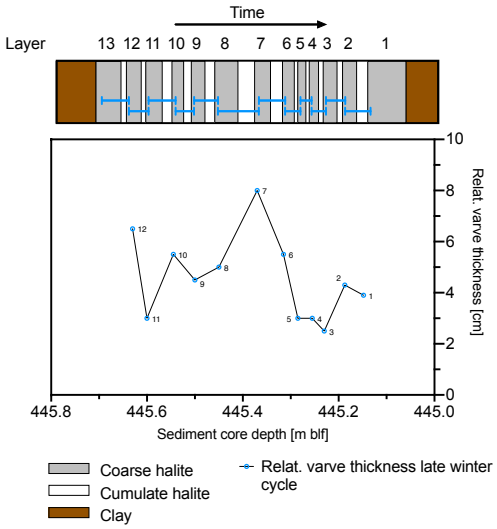

(a) Relative varve thicknesses measured from CO-BOT(n) to CO-BOT(n+1).

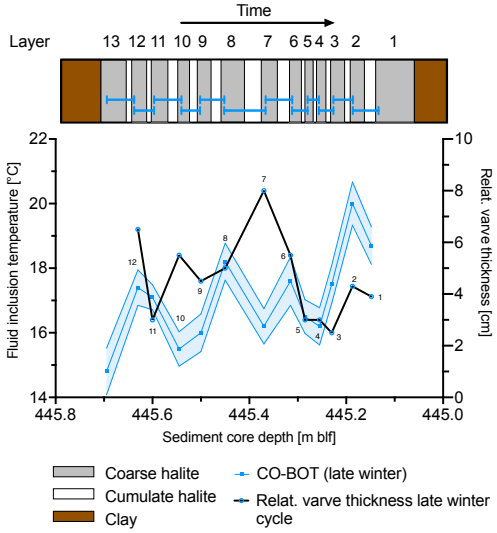

(b) T_x bottom data plotted with curve from (a).

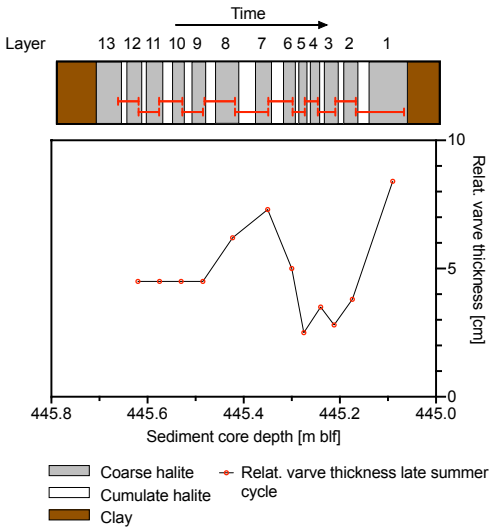

(c) Relative varve thicknesses measured from CO-TOP(n) to CO-TOP(n+1).

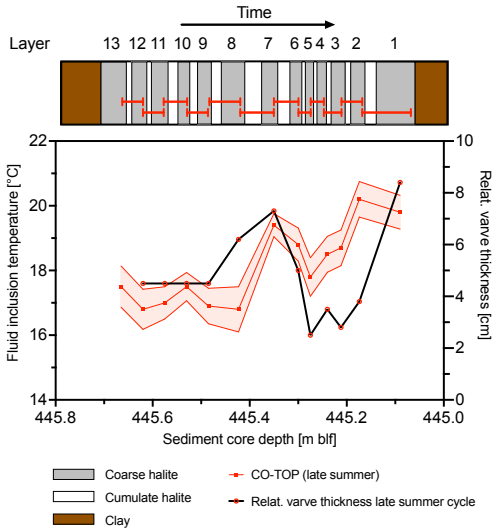

(d) T_x from coarse top data plotted with curve from (c).

Figure 6.11 Combined results of core section 176-2. Standard error indicated by blue (b) and red (d) bands surrounding the mean T_x values.

6.7.5 Data tables

Table 6.2 Pressure-corrected T_f data of core section core 5017-1-A-176-2.

Sample name	Section depth [cm]	5017-1 depth [m blf]	T_x mean [°C]	N
CO1-TOP	6	445.09	22.7	31
CO1-BOT	11.8	445.148	21.6	25
CO2-TOP	14.4	445.174	23.1	28
CO2-BOT	15.7	445.187	22.9	14
CO3-TOP	18.2	445.212	21.6	22
CO3-BOT	20	445.23	20.4	26
CO4-TOP	21	445.24	21.4	29
CO4-BOT	22.5	445.255	19.1	16
CO5-TOP	24.5	445.275	20.7	22
CO5-BOT	25.5	445.285	19.4	21
CO6-TOP	27	445.3	21.7	22
CO6-BOT	28.5	445.315	20.5	
CO7-TOP	32	445.35	22.3	20
CO7-BOT	34	445.37	19.1	21
CO8-TOP	39.3	445.423	19.7	15
CO8-BOT	42	445.45	21.1	19
CO9-TOP	45.5	445.485	19.8	24
CO9-BOT	47	445.5	18.9	17
CO10-TOP	50	445.53	20.4	17
CO10-BOT	51.5	445.545	18.4	14
CO11-TOP	54.5	445.575	19.9	25
CO11-BOT	57	445.6	20.0	13
CO12-TOP	59	445.62	19.7	19
CO12-BOT	60	445.63	20.3	16
CO13-TOP	63.5	445.665	20.4	18
CO13-BOT	66.5	445.695	17.7	15

Table 6.4 Measured lowermost sub-intervals (BOT) in coarse halite layers in core 5017-1-A-176-2.

Sample name	**Section** depth [cm]	**5017-1** depth [m blf]	T_x mean [°C]	**N**	**SD** [°C]	**SE** [°C]	**CI** 95% [°C]	**-z*** [°C]	**+z*** [°C]
CO1-BOT	11.8	445.148	18.7	25	2.9	0.6	1.14	17.6	19.8
CO2-BOT	15.7	445.187	20	14	2.5	0.7	1.31	18.7	21.3
CO3-BOT	20	445.23	17.5	26	3	0.6	1.15	16.3	18.7
CO4-BOT	22.5	445.255	16.2	16	2.3	0.6	1.13	15.1	17.3
CO5-BOT	25.5	445.285	16.5	21	2.4	0.5	1.03	15.5	17.5
CO6-BOT	28.5	445.315	17.6	16	3	0.7	1.47	16.1	19.1
CO7-BOT	34	445.37	16.2	21	2.5	0.5	1.07	15.1	17.3
CO8-BOT	42	445.45	18.2	19	2.5	0.6	1.12	17.1	19.3
CO9-BOT	47	445.5	16	17	2.4	0.6	1.14	14.9	17.1
CO10-BOT	51.5	445.545	15.5	14	2	0.6	1.05	14.5	16.5
CO11-BOT	57	445.6	17.1	13	1.4	0.4	0.76	16.3	17.9
CO12-BOT	60	445.63	17.4	16	2.2	0.5	1.08	16.3	18.5
CO13-BOT	66.5	445.695	14.8	15	2.8	0.7	1.42	13.4	16.2
Total	**54.7**	**0.547**	**17.1**	**233**	**2.5**	**0.6**	**1.14**	**15.9**	**18.2**

Table 6.5 Splitted part of the first 26 cm in core section 176-2 with uppermost sub-intervals (TOP) in coarse halite layers.

Sample name	Section depth [cm]	5017-1 depth [m blf]	T_x mean [°C]	N	SD [°C]	SE [°C]	CI 95% [°C]	-z* [°C]	+z* [°C]
CO1-TOP	6	445.09	19.8	31	2.9	0.5	1.02	18.8	20.8
CO2-TOP	14.4	445.174	20.2	28	2.9	0.5	1.07	19.1	21.3
CO3-TOP	18.2	445.212	18.7	22	2.6	0.6	1.09	17.6	19.8
CO4-TOP	21	445.24	18.5	29	3	0.6	1.09	17.4	19.6
CO5-TOP	24.5	445.275	17.8	22	2.8	0.6	1.17	16.6	19.0
CO6-TOP	27	445.3	18.8	22	2.4	0.5	1.00	17.8	19.8
CO7-TOP	32	445.35	19.4	20	1.6	0.4	0.70	18.7	20.1
Total	**26**	**0.26**	**19.0**	**174**	**2.6**	**0.5**	**1.02**	**18.0**	**20.0**

Table 6.3 Measured uppermost sub-intervals (TOP) in coarse halite layers in core 5017-1-A-176-2.

Sample name	Section depth [cm]	5017-1 depth [m blf]	T_x mean [°C]	N[a]	SD[b] [°C]	SE[c] [°C]	CI[d] 95% [°C]	-z*[e] [°C]	+z*[f] [°C]
CO1-TOP	6	445.09	19.8	31	2.9	0.5	1.02	18.8	20.8
CO2-TOP	14.4	445.174	20.2	28	2.9	0.5	1.07	19.1	21.3
CO3-TOP	18.2	445.212	18.7	22	2.6	0.6	1.09	17.6	19.8
CO4-TOP	21	445.24	18.5	29	3	0.6	1.09	17.4	19.6
CO5-TOP	24.5	445.275	17.8	22	2.8	0.6	1.17	16.6	19.0
CO6-TOP	27	445.3	18.8	22	2.4	0.5	1.00	17.8	19.8
CO7-TOP	32	445.35	19.4	20	1.6	0.4	0.70	18.7	20.1
CO8-TOP	39.3	445.423	16.8	15	2.7	0.7	1.37	15.4	18.2
CO9-TOP	45.5	445.485	16.9	24	2.7	0.6	1.08	15.8	18.0
CO10-TOP	50	445.53	17.5	17	1.8	0.4	0.86	16.6	18.4
CO11-TOP	54.5	445.575	17	25	2.5	0.5	0.98	16.0	18.0
CO12-TOP	59	445.62	16.8	19	2.7	0.6	1.21	15.6	18.0
CO13-TOP	63.5	445.665	17.5	18	2.6	0.6	1.20	16.3	18.7
Total	57.5[g]	0.575[g]	18.1[h]	292	2.6[h]	0.5[h]	1.07[h]	17.1[h]	19.2[h]

[a] number of measured fluid inclusions per sample and in total
[b] standard deviation of a sample population
[c] standard error of the mean
[d] confidence interval
[e] T_x mean - CI 95%
[f] T_x mean + CI 95%
[g] length of sampling interval in core section
[h] mean

Table 6.6 Splitted part of the lowest 24 cm in core section 176-2 with uppermost sub-intervals (TOP) in coarse halite layers.

Sample name	Section depth [cm]	5017-1 depth [m blf]	T_x mean [°C]	N	SD [°C]	SE [°C]	CI 95% [°C]	-z* [°C]	+z* [°C]
CO8-TOP	39.3	445.423	16.8	15	2.7	0.7	1.37	15.4	18.2
CO9-TOP	45.5	445.485	16.9	24	2.7	0.6	1.08	15.8	18.0
CO10-TOP	50	445.53	17.5	17	1.8	0.4	0.86	16.6	18.4
CO11-TOP	54.5	445.575	17	25	2.5	0.5	0.98	16.0	18.0
CO12-TOP	59	445.62	16.8	19	2.7	0.6	1.21	15.6	18.0
CO13-TOP	63.5	445.665	17.5	18	2.6	0.6	1.20	16.3	18.7
Total	**24.2**	**0.242**	**17.1**	**118**	**2.5**	**0.6**	**1.12**	**16.0**	**18.2**

Table 6.7 Compilation of measured varve thicknesses and calculated seasonal temperatures as defined in Figure 6.10 for core section 176-2.

Layer number	Relative CO-TOP [cm]	Relative CO-BOT [cm]	Coarse layer [cm]	Cumulate layer [cm]	Cooling varve [cm]	Warming varve [cm]	Δ T cooling [°C]	Δ T warming [°C]
13	4.5	N.A.	3.3	3.0	5.2	6.3	0.1	2.7
12	4.5	3.9	2.2	1.5	4.2	3.7	-0.3	-0.6
11	4.5	4.3	2.7	2.3	5.3	5.0	1.5	-0.1
10	4.5	2.5	3.0	2.0	4.0	5.0	1.5	2.0
9	6.2	3.0	2.0	3.0	6.0	5.0	-1.3	0.9
8	7.3	3.0	3.0	4.3	7.2	7.3	0.6	-1.4
7	5.0	5.5	2.9	2.8	5.4	5.7	1.8	3.2
6	2.5	8.0	2.6	0.6	2.6	3.2	2.3	1.2
5	3.5	5.0	2.0	1.0	3.4	3.0	1.6	1.3
4	2.8	4.5	2.4	0.9	2.9	3.3	1.0	2.3
3	3.8	5.5	2.0	1.1	3.8	3.1	-1.3	1.2
2	8.4	3.0	2.7	1.7	7.7	4.4	1.5	0.2
1	N.A.	6.5	6.0	N.A.	N.A.	6.0	N.A.	1.1
Mean	4.8	4.6	2.83	2.0	4.8	4.7	0.8	1.1

Bibliography

Arnon, A., Selker, J. S., and Lensky, N. G. (2016). Thermohaline stratification and double diffusion diapycnal fluxes in the hypersaline Dead Sea. *Limnology and Oceanography*, *61*, 1214–1231. https://doi.org/10.1002/lno.10285

Ben Dor, Y., Neugebauer, I., Enzel, Y., Schwab, M. J., Tjallingii, R., Erel, Y., and Brauer, A. (2019). Varves of the Dead Sea sedimentary record. *Quaternary Science Reviews*, *215*, 173–184. https://doi.org/10.1016/j.quascirev.2019.04.011

Berger, A. L. (1978). Long-Term Variations of Daily Insolation and Quaternary Climatic Changes. *Journal of the Atmospheric Sciences*, *35*(12), 2362–2367. https://doi.org/10.1175/1520-0469(1978)035<2362:ltvodi>2.0.co;2

Brall, N. S., Gardien, V., Ariztegui, D., Sorrel, P., Guillerm, E., and Caupin, F. (2022). Reconstructing lake bottom water temperatures and their seasonal variability in the Dead Sea Basin during MIS 5e. *The Depositional Record*. https://doi.org/10.1002/dep2.185

Candy, I., and Schreve, D. (2007). Land-sea correlation of Middle Pleistocene temperate sub-stages using high-precision uranium-series dating of tufa deposits from southern England. *Quaternary Science Reviews*, *26*(9-10), 1223–1235. https://doi.org/10.1016/j.quascirev.2007.01.012

Desprat, S., Goñi, M. F. S., Turon, J.-L., Duprat, J., Malaizé, B., and Peypouquet, J.-P. (2006). Climatic variability of Marine Isotope Stage 7: direct land–sea–ice correlation from a multiproxy analysis of a north-western Iberian margin deep-sea core. *Quaternary Science Reviews*, *25*(9-10), 1010–1026. https://doi.org/10.1016/j.quascirev.2006.01.001

Gertman, I., and Hecht, A. (2002). *The Dead Sea hydrography from 1992 to 2000*. www.elsevier.com/locate/jmarsys

Gertman, I., Kress, N., Katsenelson, B., Zavialov, P., and Shirshov, P. P. (2010). *Final Report. Equations of state for the Dead Sea and Aral Sea: Searching for common approaches*.

Goldstein, S. L., Kiro, Y., Torfstein, A., Kitagawa, H., Tierney, J., and Stein, M. (2020). Revised chronology of the ICDP Dead Sea deep drill core relates drier-wetter-drier climate cycles to insolation over the past 220 kyr. *Quaternary Science Reviews*, *244*. https://doi.org/10.1016/j.quascirev.2020.106460

Guillerm, E. (2019). *Turning halite fluid inclusions into accurate paleothermometers with Brillouin spectroscopy: development of a new method and application to the Last Interglacial in the Dead Sea.*

Guillerm, E., Gardien, V., Ariztegui, D., and Caupin, F. (2020). Restoring Halite Fluid Inclusions as an Accurate Palaeothermometer: Brillouin Thermometry Versus Microthermometry. *Geostandards and Geoanalytical Research*, *44*, 243–264. https://doi.org/10.1111/ggr.12312

Hershkovitz, I., Weber, G. W., Quam, R., Duval, M., Grün, R., Kinsley, L., Ayalon, A., Bar-Matthews, M., Valladas, H., Mercier, N., Arsuaga, J. L., Martinón-Torres, M., de Castro, J. M. B., Fornai, C., Martín-Francés, L., Sarig, R., May, H., Krenn, V. A., Slon, V., ... Weinstein-Evron, M. (2018). The earliest modern humans outside Africa. *Science*, *359*(6374), 456–459. https://doi.org/10.1126/science.aap8369

IPCC. (2022). *Climate Change 2022: Impacts, Adaptation, and Vulnerability. Contribution of Working Group II to the Sixth Assessment Report of the Intergovernmental Panel on Climate Change* (H.-O. Pörtner and D.C. Roberts and M. Tignor and E.S. Poloczanska and K. Mintenbeck and A. Alegría and M. Craig and S. Langsdorf, S. Löschke and V. Möller and A. Okem and B. Rama, Ed.) [In Press.]. Cambridge University Press.

Jouzel, J., Waelbroeck, C., Malaize, B., Bender, M., Petit, J. R., Stievenard, M., Barkov, N. I., Barnola, J. M., King, T., Kotlyakov, V. M., Lipenkov, V., Lorius, C., Raynaud, D., Ritz, C., and Sowers, T. (1996). Climatic interpretation of the recently extended Vostok ice records. *Climate Dynamics*, *12*(8), 513–521. https://doi.org/10.1007/bf00207935

Kiro, Y., Goldstein, S. L., Garcia-Veigas, J., Levy, E., Kushnir, Y., Stein, M., and Lazar, B. (2017). Relationships between lake-level changes and water and salt budgets in the Dead Sea during extreme aridities in the Eastern Mediterranean. *Earth and Planetary Science Letters*, *464*, 211–226. https://doi.org/10.1016/j.epsl.2017.01.043

Kiro, Y., Goldstein, S. L., Lazar, B., and Stein, M. (2016). Environmental implications of salt facies in the Dead Sea. *Geological Society of America Bulletin*, *128*, 824–841. https://doi.org/10.1130/b31357.1

Kishcha, P., Starobinets, B., Lechinsky, Y., and Alpert, P. (2021). Absence of Surface Water Temperature Trends in Lake Kinneret despite Present Atmospheric Warming: Comparisons with Dead Sea Trends. *Remote Sensing*, *13*(17), 3461. https://doi.org/10.3390/rs13173461

Kwiecien, O., Braun, T., Brunello, C. F., Faulkner, P., Hausmann, N., Helle, G., Hoggarth, J. A., Ionita, M., Jazwa, C. S., Kelmelis, S., Marwan, N., Nava-

Fernandez, C., Nehme, C., Opel, T., Oster, J. L., Perşoiu, A., Petrie, C., Prufer, K., Saarni, S. M., ... Breitenbach, S. F. (2022). What we talk about when we talk about seasonality – A transdisciplinary review. *Earth-Science Reviews*, *225*, 103843. https://doi.org/10.1016/j.earscirev.2021.103843

Lelieveld, J., Hadjinicolaou, P., Kostopoulou, E., Chenoweth, J., Maayar, M. E., Giannakopoulos, C., Hannides, C., Lange, M. A., Tanarhte, M., Tyrlis, E., and Xoplaki, E. (2012). Climate change and impacts in the Eastern Mediterranean and the Middle East. *Climatic Change*, *114*(3-4), 667–687. https://doi.org/10.1007/s10584-012-0418-4

Lelieveld, J., Proestos, Y., Hadjinicolaou, P., Tanarhte, M., Tyrlis, E., and Zittis, G. (2016). Strongly increasing heat extremes in the Middle East and North Africa (MENA) in the 21st century. *Climatic Change*, *137*(1-2), 245–260. https://doi.org/10.1007/s10584-016-1665-6

Lisiecki, L. E., and Raymo, M. E. (2005). A pliocene-pleistocene stack of 57 globally distributed benthic 18o records. *Paleoceanography*, *20*(1). https://doi.org/10.1029/2004pa001071

Malaizé, B., Paillard, D., Jouzel, J., and Raynaud, D. (1999). The Dole effect over the last two glacial-interglacial cycles. *Journal of Geophysical Research: Atmospheres*, *104*(D12), 14199–14208. https://doi.org/10.1029/1999jd900116

Martinson, D. G., Pisias, N. G., Hays, J. D., Imbrie, J., Moore, T. C., and Shackleton, N. J. (1987). Age Dating and the Orbital Theory of the Ice Ages: Development of a High-Resolution 0 to 300, 000-Year Chronostratigraphy. *Quaternary Research*, *27*(1), 1–29. https://doi.org/10.1016/0033-5894(87)90046-9

Matthews, A., Affek, H., Ayalon, A., Vonhof, H., and Bar-Matthews, M. (2021). Eastern Mediterranean climate change deduced from the Soreq Cave fluid inclusion stable isotopes and carbonate clumped isotopes record of the last 160 ka. *Quaternary Science Reviews*, *272*, 107223. https://doi.org/10.1016/j.quascirev.2021.107223

Neugebauer, I., Brauer, A., Schwab, M. J., Waldmann, N. D., Enzel, Y., Kitagawa, H., Torfstein, A., Frank, U., Dulski, P., Agnon, A., Ariztegui, D., Ben-Avraham, Z., Goldstein, S. L., and Stein, M. (2014). Lithology of the long sediment record recovered by the ICDP Dead Sea Deep Drilling Project (DSDDP). *Quaternary Science Reviews*, *102*, 149–165. https://doi.org/10.1016/j.quascirev.2014.08.013

Orland, I. J., Burstyn, Y., Bar-Matthews, M., Kozdon, R., Ayalon, A., Matthews, A., and Valley, J. W. (2014). Seasonal climate signals (1990–2008) in a modern Soreq Cave stalagmite as revealed by high-resolution geochemical analysis.

Chemical Geology, *363*, 322–333. https://doi.org/10.1016/j.chemgeo.2013.11.011

Penaud, A., Eynaud, F., Turon, J., Zaragosi, S., Marret, F., and Bourillet, J. (2008). Interglacial variability (MIS 5 and MIS 7) and dinoflagellate cyst assemblages in the Bay of Biscay (North Atlantic). *Marine Micropaleontology*, *68*(1-2), 136–155. https://doi.org/10.1016/j.marmicro.2008.01.007

Petit, J. R., Jouzel, J., Raynaud, D., Barkov, N. I., Barnola, J.-M., Basile, I., Bender, M., Chappellaz, J., Davis, M., Delaygue, G., Delmotte, M., Kotlyakov, V. M., Legrand, M., Lipenkov, V. Y., Lorius, C., Pépin, L., Ritz, C., Saltzman, E., and Stievenard, M. (1999). Climate and atmospheric history of the past 420,000 years from the Vostok ice core, Antarctica. *Nature*, *399*(6735), 429–436. https://doi.org/10.1038/20859

Sirota, I., Enzel, Y., and Lensky, N. G. (2017). Temperature seasonality control on modern halite layers in the Dead Sea: In situ observations. *Bulletin*, *129*, 1181–1194.

Slon, V., Sarig, R., Hershkovitz, I., Khalaily, H., and Milevski, I. (2014). The Plastered Skulls from the Pre-Pottery Neolithic B Site of Yiftahel (Israel) – A Computed Tomography-Based Analysis (D. Frayer, Ed.). *PLoS ONE*, *9*(2), e89242. https://doi.org/10.1371/journal.pone.0089242

Sowers, T., Bender, M., Labeyrie, L., Martinson, D., Jouzel, J., Raynaud, D., Pichon, J. J., and Korotkevich, Y. S. (1993). A 135,000-year Vostok-Specmap Common temporal framework. *Paleoceanography*, *8*(6), 737–766. https://doi.org/10.1029/93pa02328

Stein, M., Ben-Avraham, Z., Goldstein, S., Agnon, A., Ariztegui, D., Brauer, A., Haug, G., Ito, E., and Yasuda, Y. (2011). Deep Drilling at the Dead Sea. *Scientific Drilling*. https://doi.org/10.2204/iodp.sd.11.04.2011

Torfstein, A., Goldstein, S. L., Kushnir, Y., Enzel, Y., Haug, G., and Stein, M. (2015). Dead Sea drawdown and monsoonal impacts in the Levant during the last interglacial. *Earth and Planetary Science Letters*, *412*, 235–244. https://doi.org/10.1016/j.epsl.2014.12.013

Tzedakis, P. C., Roucoux, K. H., de Abreu, L., and Shackleton, N. J. (2004). The Duration of Forest Stages in Southern Europe and Interglacial Climate Variability. *Science*, *306*(5705), 2231–2235. https://doi.org/10.1126/science.1102398

Tzedakis, P., McManus, J., Hooghiemstra, H., Oppo, D., and Wijmstra, T. (2003). Comparison of changes in vegetation in northeast Greece with records of climate variability on orbital and suborbital frequencies over the last 450 000 years.

Earth and Planetary Science Letters, *212*(1-2), 197–212. https://doi.org/10.1016/s0012-821x(03)00233-4

Wang, J., Guan, Y., Wu, L., Guan, X., Cai, W., Huang, J., Dong, W., and Zhang, B. (2021). Changing Lengths of the Four Seasons by Global Warming. *Geophysical Research Letters*, *48*(6). https://doi.org/10.1029/2020gl091753

Watanabe, O., Jouzel, J., Johnsen, S., Parrenin, F., Shoji, H., and Yoshida, N. (2003). Homogeneous climate variability across East Antarctica over the past three glacial cycles. *Nature*, *422*(6931), 509–512. https://doi.org/10.1038/nature01525

Chapter 7

Entrapment temperatures of gypsum

7.1 Introduction

The PhD thesis was initially planned to conduct experiments using Brillouin spectroscopy on lacustrine gypsum samples from Lake Petén Itzá (Guatemala) and the Aral Sea (Kazakhstan, Uzbekistan; see chapter 2.1). Both locations are sensitive to climate variations on shorter time scales, which can be seen in their sediment records with a response of the dominating mineralogies to colder/drier (gypsum, salts) or warmer/wetter (carbonates, clay) climates (e.g., Sorrel et al., 2006; Oberhänsli et al., 2011; D. Hodell et al., 2006; D. A. Hodell et al., 2008; Hillesheim et al., 2005). This rock-climate relation offers a great potential to study abundant gypsum intervals.
The experimental part of applying BS on such samples has started with initial essays on modern gypsum crystals from a salt works in Trapani (Sicily; provided by M. Natalicchio). Such material proved to form in equilibrium with the saline parent brine during gypsum growth with the entrapment of fluid inclusions in growth bands along the host crystal direction of growth (Natalicchio et al., 2014. Although such growth bands with triangular shapes with flat bases of FIs were observed, the material did not allow to perform BS measurements, because:

- the FIs were mostly destroyed during sampling preparation (not liquid)
- the few liquid FIs analyzed did not provide clear Brillouin spectra
- the cavitation into biphasic FIs was not successful in most cases

Therefore, the material was discarded to set a "gypsum standard" for BS, and laboratory-grown gypsum has been further used throughout the experimental work during the PhD thesis.
Furthermore, it has been noted, after more than one year of experimental work during this thesis, that such lacustrine gypsum samples are not suitable for the BS approach, for several reasons:

- crystals often have lenticular shapes (difficult to prepare samples)
- crystal sizes are usually less than 500 µm
- low abundance of trapped FIs
- gypsum transforms rapidly into hemi-hydrate phase upon warming
- low amount of cavitated FIs (necessary for T_x measurements)
- <10 T_x points were measured in two years, ranging between 0-60 °C

7.2 Cavitation of gypsum fluid inclusions

The presence of a vapor in a liquid inclusion is the essential second step during experimental BS analysis, as in this case for gypsum. In general, a heating cycle is preferred to cavitate a vapor because it works without the use of liquid nitrogen, and is thus more economic. For gypsum, however, the previously proposed short-term heating to 130 °C for halite samples (Guillerm, 2019) can not be applied due to a fast thermal response of the mineral to elevated temperatures (T) which is associated with a loss of the molecular water, and a transformation to the hemi-hydrate phase bassanite (Figure 7.1).

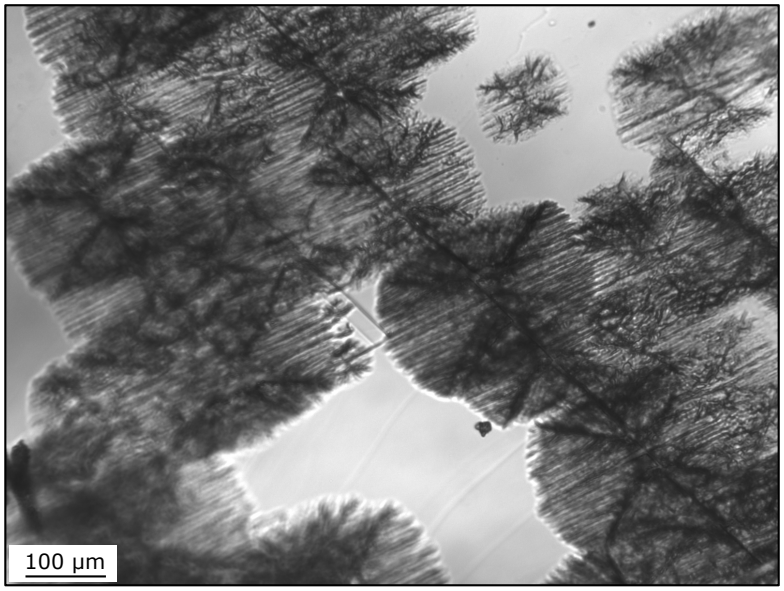

Figure 7.1 Gypsum-transformation to the hemi-hydrate phase after heating to 130 °C for ca 60 seconds.

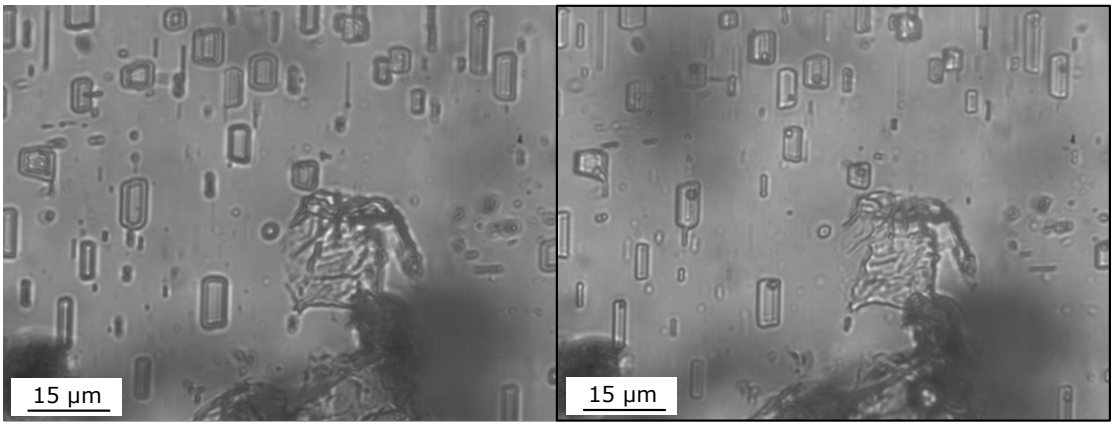

Figure 7.2 Cavitation of secondary FIs in a gypsum sample from Piedmont Basin, Italy, of Messinian age. Left: monophasic FIs before cooling. Right: biphasic FIs after three cooling cycles.

Therefore, cooling cycles enclosing negative T were used to force the cavitation of a vapor. Several cooling cycles to very low T (minimum T = -110 °C, average T ca -90 °C) at varying cooling rates (fast = 20 °C/min; slow = 5 °C/min) were necessary for lab-grown gypsum material, and often only a small portion of studied FIs during this thesis cavitated a vapor (see examples in Figure 7.3). However, both primary and secondary FIs in natural gypsum samples showed larger amounts of cavitated FIs, although not every FI cavitates reliably. Lab-grown gypsum material showed to a respond much slower to cooling than natural gypsum samples (Figure 7.2).

To summarise, several cooling-heating cycles are often needed to trigger a transformation from liquid to liquid+vapor in natural gypsum samples. The recommended procedure is to cool the sample at intermediate rates (e.g., 10 °C/min) to -60 °C for ca 2-3 minutes, followed by heating to ca 30 °C at the same rate. If needed, the cycle might be repeated until the remaining FIs cavitated, which had been previously measured in monophasic state and further selected for BS analysis.

7.3 Lab-grown gypsum

Initial experiments to derive temperature data from gypsum fluid inclusions were all based on lab-grown gypsum at the beginning. Various shapes of gypsum crystals were observed, but the low abundance of trapped fluid inclusions was a common characteristic in all samples. The few entrapment temperatures (n = 8) that could be generated for samples of known temperatures of 21 °C yield T_x values between 18.6-22.4 °C with one outlier of 46 °C (Table 7.1). Thus, the offset to the expected T_x temperatures varies between -0.43 to 2.36 °C. Another T_x values of 16.3 °C was measured in a sample with a known crystal growth temperature of 25 °C, thus with an offset of 8.7 °C.

Since each T_x value depends on the slope of both isochores and LVE curves,

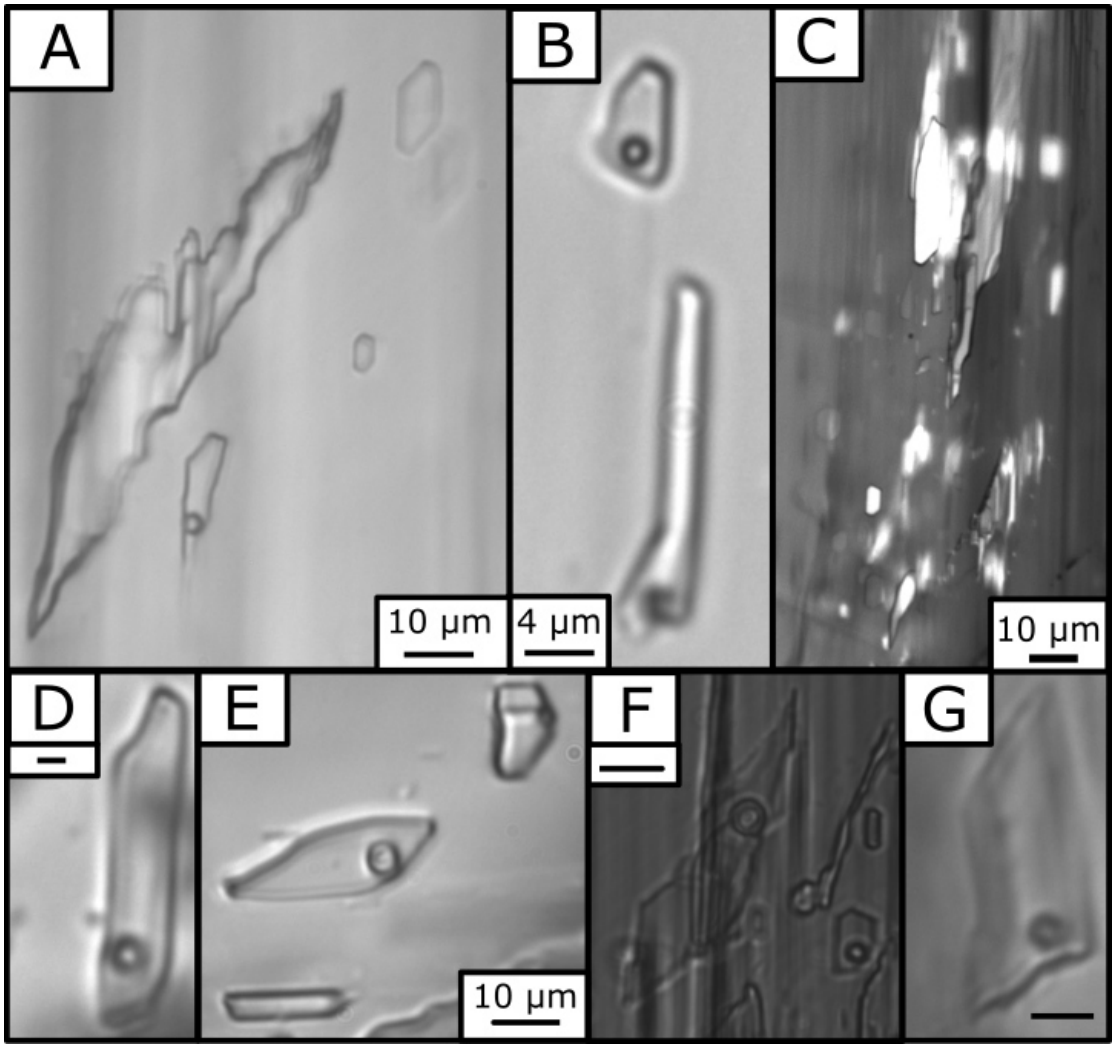

Figure 7.3 Lab-grown gypsum with trapped FIs. Black bubble mark the biphasic phase of FIs. A, B, D-G) are examples to show the various shapes observed during the experiments. C) White areas are indicative for gaseous inclusions without any liquid. Scale bars are equally to 2 µm in D), 13 µm in F, and 6 µm in G), respectively.

the choice of linear or nonlinear regression models for the data points requires manual handling. Hence, the T_x point, calculated as the intersection of both curves, can vary with each choice. Trapped fluid inclusions of a mixed enhanced saline solution (NaCl + $CaSO_4$) required a second order polynomial fit as always chosen for biphasic FIs (Figure 7.4 D, F, G). All FIs data points are elevated in terms of their sound velocity (>1780 to 1910 m/s; Figure 7.4 D-H), which is higher than the sound velocity of the parent solution of one sample ("SGH25 BULK/REP") and the NaCl saturation point ("NaCl sat.") (see Figure 8.6. On the other hand, three samples of a pure $CaSO_4$ solution yield all sound velocity values <1500 m/s and thus fall into the same interval as the capillaries of both, their parent solution from which they precipitated, and pure water (see Figure 8.6). Further, a constant linear fit was possible in each case (Figure 7.4 A-C).

Table 7.1 Overview on measured temperatures of lab-grown gypsum samples compared with the known growth temperatures.

Type	Sample name	FI name	T_x [°C]	Growth temperature [°C]	Offset [°C]
Lab-grown	SG032020-210602	1	22.0	21	-1.02
Lab-grown	SG032020-210602	9	22.4	21	-1.35
Lab-grown	SG032020-210602	11	18.6	21	2.36
Lab-grown	SGH21_22-191217	1	21.4	21	-0.43
Lab-grown	SGH21_22-191217	2	46.0	21	-25.01
Lab-grown	SGH21-400-191119	1	22.0	21	-0.99
Lab-grown	SGH21-400-191119	2	20.0	21	1.04
Lab-grown	SGH25-2_01-FI02	2	16.3	25	8.69

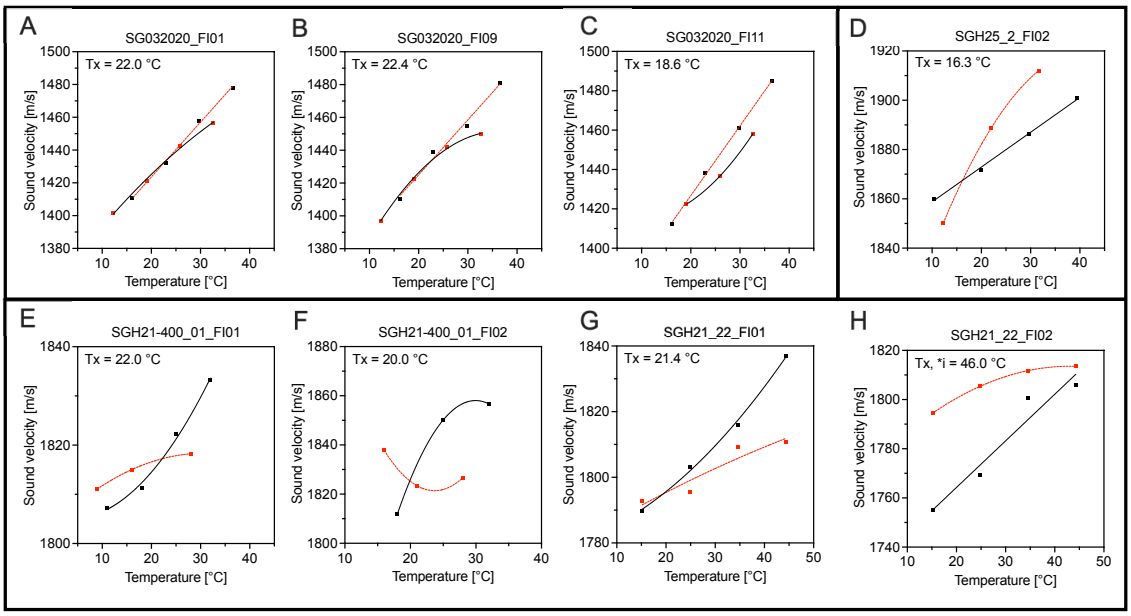

Figure 7.4 Lab-grown gypsum data from fluid inclusions from three evaporation experiments. A-C: Dissolved $CaSO_4$ in pure H_2O and evaporated at 21 °C. D: Dissolved NaCl and $CaSO_4$ in pure H_2O and evaporated at 25 °C in a water bath. E-H: Same parent solution as in D, but evaporated at 21 °C. Fitted lines represent monophasic isochores (black solid) and biphasic LVE (red dashed).

7.4 Natural gypsum

A total of 32 T_x data could be obtained by using natural gypsum samples for BS. Unlike for the challenging experimental work using lab-grown gypsum, fluid inclusions trapped in natural samples were generally easier to use because of higher probabilities in cavitating vapor bubbles during cooling-heating cycles (see section thermal cycles). Furthermore, a sufficient amount of FIs inside any sub-sample has always been found. In some cases, secondary FI types were used for T_x measurements (e.g., samples from Santa Elisabetta; Eraclea Minoa; Aral Sea). For such cases, fitted isochores / LVE points are mainly crossing with gently sloped LVE curves, resulting to reasonable T_x values (Figure 7.5).

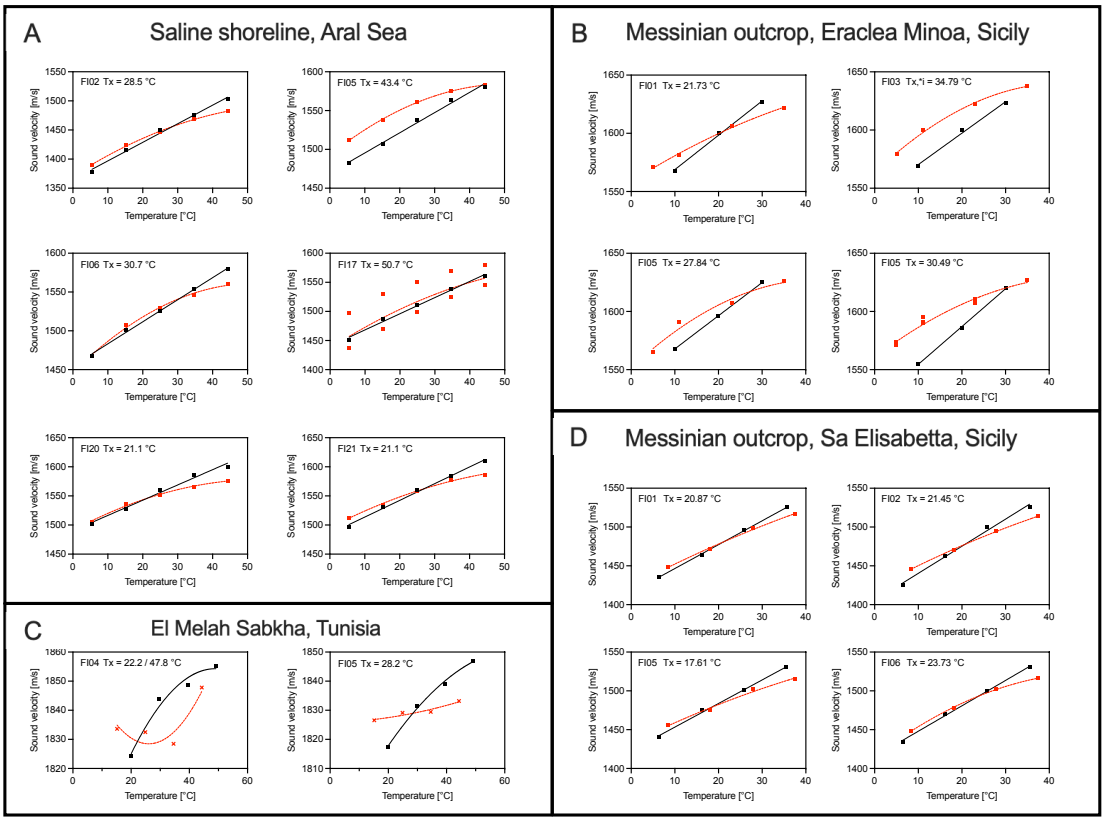

Figure 7.5 Exemplary fits of fluid inclusion data of natural gypsum samples from Table C.1. Fitted lines of monophasic FIs (isochores, black solid) and biphasic FIs (LVE, red dashed) define the T_x intersection. See Appendix A for additional fits of other samples listed in Table C.1.

7.5 Discussion

Studies dealing with the determination of formation temperatures of natural/lab-grown halite have already shown that Brillouin spectroscopy is a suitable technique with an uncertainty of ca 1.5 °C (see chapter 5; Guillerm et al., 2020). However, no studies have been performed on gypsum yet, which is after $CaCO_3$ the second mineral that precipitates from an evaporating brine or an ideal seawater solution (Holser, 1979). Hence, gypsum forms usually in surface brines supersaturated with respect to calcium sulfate and close to ambient pressure, which makes this mineral favorable for palaeotemperature-related studies.
However, there are some properties of gypsum formed in natural environments that are limiting its usage for such studies, because

- gypsum has a low temperature-stability field (<42 °C) that enables dissolution-reprecipitation with time
- a Mohs' hardness of 2 can trigger the deformation of both the host crystal and the trapped fluid inclusions,

- the high crystal water content (up to 20%) makes it favorable for dehydration-rehydration processes
- fluid inclusions can derive from several post-entrapment generations,
- former primary FIs trapped along the growth bands are vulnerable for solidification with time,
- FIs in gypsum often fail to cavitate a vapor or need multiple cooling-heating cycles.

Furthermore, the low solubility of $CaSO_4 \cdot 2\,H_2O$ has affected the crystal sizes of lab-grown samples, which caused low entrapment abundances and/or only tiny FIs that were trapped. Another point that was observed is the formation of larger water assemblages within the flat gypsum crystals which did not show the classical behaviour of FIs. Upon cooling-heating, these water assemblages changed their location, shape, and volume by incorporating adjacent FIs. Therefore, the number of T_x values (= 8) obtained from lab-grown gypsum samples was quite small and needed two years of lab work. For comparison, within one day of lab work it is normally possible to obtain 20 T_x values from a single lab-grown NaCl crystal. The most important negative point regarding the lab work is the low abundance of cavitated gypsum FIs after the measurement of isochoric data point had been done. To conclude one can state that cavitation occurs more often in natural gypsum than in lab-grown gypsum, and more often in secondary than in primary FIs.
Besides the above mentioned points, an additional limiting aspect by using gypsum FIs for Brillouin analysis is that the acquired Δf_B spectra often can not be fitted despite a sufficient amount of counts ($\geq$300), if the inner flanks of the Δf_B spectra are too narrow to the Brillouin reference peak. In this case, the analysis program can not read out the Δf_B peak, causing high chi^2 values with $w < 1000$ m/s or >2500 m/s. One solution might be to deconvolute the FI spectra or locate its peak value, which could require a manual adjustment for each sample.
Second, lab-grown gypsum data showed often abnormal fitted curves of isochores and/or SLVE (Figure 7.4 B, C, F), or even elevated SLVE data points, leading to strongly deviated entrapment temperatures, e.g., 16.3 °C instead of 25 °C, or 46 °C instead of 21 °C (Figure 7.4 D, H).
Nevertheless, natural gypsum samples that are much larger with higher abundances of trapped FIs seem to be suitable to determine T_x values (Figure 7.5). The main contrast to lab-grown gypsum data is the linear fitting of isochores with relatively flat SLVE curves as it has been observed for the accurate BS application on natural halite samples from the Dead Sea (Guillerm, 2019). It is likely that crystal

thicknesses play a role in acquiring well-fitted curves of FIs because the latter is directly related to the depth of FIs relative to the crystal surface.
A last point to be improved in the future when using BS on gypsum samples would be establish a gypsum-reference sample to correct for the instrumental drift during an experimental day in the laboratory. This is simply due to the fact that no suitable gypsum-reference crystal could be produced so far which would be big enough to work with on a daily basis. This aspect should be taken into account when applying BS on gypsum samples, because the usage of a NaCl-reference sample can cause problems during data analysis due to an increased frequency shift in saturated NaCl (ca 9 GHz vs. 6-7 GHz in low-saline gypsum). It is further recommended to use large-sized selenite samples from modern salt works, combined with *in situ* measurement of the physical-chemical properties of the parent brine.

7.6 Summary

For the first time, the calcium sulfate mineral gypsum has been studied using Brillouin spectroscopy (BS) to determine entrapment temperatures of fluid inclusions. The experiments revealed a challenging data acquisition in lab-grown material which is needed initially to test a new methods to known standard conditions. The general amount of trapped fluid inclusions in gypsum crystals was low which prohibited a complete study to setup the basis for accurate measurements of geological records.
Nevertheless, material has been used from natural subsurface locations, and trapped fluid inclusions provided a slightly larger data set to get first insights into BS analysis on this evaporitic mineral. However, the data are mainly derived from secondary FIs, which questions if the mineral is suitable to determine the pristine formation temperatures of gypsum samples. Given the potential danger of post-depositional sampling alterations in gypsum and its relatively low Moh's hardness of 2, one might however argue to avoid using gypsum for studies that aim to reconstruct palaeoenvironmental conditions at the time of crystal formation.
Nevertheless, the results rather suggest that BS could be used as a tool to study secondary FIs (e.g., the evolution of sealed cracks, the distribution of temperatures along FIAs).
More research is needed to fully answer this question, and future studies dealing with this matter should use largely grown samples obtained from locations of known growth temperatures. Further, the origin of trapped fluid inclusions should be determined to rule out post-entrapment alterations. A general recommendation is to focus on triangular-shaped FIs aligned on growth bands within a crystal which indicates pristine signals.

Bibliography

Guillerm, E. (2019). *Turning halite fluid inclusions into accurate paleothermometers with Brillouin spectroscopy: development of a new method and application to the Last Interglacial in the Dead Sea.*

Guillerm, E., Gardien, V., Ariztegui, D., and Caupin, F. (2020). Restoring Halite Fluid Inclusions as an Accurate Palaeothermometer: Brillouin Thermometry Versus Microthermometry. *Geostandards and Geoanalytical Research*, *44*, 243–264. https://doi.org/10.1111/ggr.12312

Hillesheim, M. B., Hodell, D. A., Leyden, B. W., Brenner, M., Curtis, J. H., Anselmetti, F. S., Ariztegui, D., Buck, D. G., Guilderson, T. P., Rosenmeier, M. F., and Schnurrenberger, D. W. (2005). Climate change in lowland Central America during the late deglacial and early Holocene. *Journal of Quaternary Science*, *20*(4), 363–376. https://doi.org/10.1002/jqs.924

Hodell, D., Anselmetti, F., Brenner, M., Ariztegui, D., and Party, P. S. (2006). The Lake Petén Itzá Scientifi c Drilling Project. *Scientific Drilling*, *3*, 25–29. https://doi.org/10.5194/sd-3-25-2006

Hodell, D. A., Anselmetti, F. S., Ariztegui, D., Brenner, M., Curtis, J. H., Gilli, A., Grzesik, D. A., Guilderson, T. J., Müller, A. D., and Bush, M. B. (2008). An 85-ka record of climate change in lowland Central America. *Quaternary Science Reviews*, *27*(11-12), 1152–1165. https://doi.org/10.1016/j.quascirev.2008.02.008

Holser, W. T. (1979). Mineralogy of evaporites. *Marine Minerals* (pp. 211–294). De Gruyter. https://doi.org/10.1515/9781501508646-012

Natalicchio, M., Dela Pierre, F., Lugli, S., Lowenstein, T. K., Feiner, S. J., Ferrando, S., Manzi, V., Roveri, M., and Clari, P. (2014). Did Late Miocene (Messinian) gypsum precipitate from evaporated marine brines? Insights from the Piedmont Basin (Italy). *Geology*, *42*(3), 179–182.

Oberhänsli, H., Novotná, K., Píšková, A., Chabrillat, S., Nourgaliev, D. K., Kurbaniyazov, A. K., and Grygar, T. M. (2011). Variability in precipitation, temperature and river runoff in W Central Asia during the past ~2000yrs. *Global and Planetary Change*, *76*(1-2), 95–104. https://doi.org/10.1016/j.gloplacha.2010.12.008

Sorrel, P., Popescu, S.-M., Head, M., Suc, J., Klotz, S., and Oberhänsli, H. (2006). Hydrographic development of the Aral Sea during the last 2000 years based on a quantitative analysis of dinoflagellate cysts. *Palaeogeography, Palaeoclimatology, Palaeoecology*, *234*(2-4), 304–327. https://doi.org/10.1016/j.palaeo.2005.10.012

Chapter 8

Towards a new proxy for palaeosalinity: Sound velocity of saline aqueous solutions and fluid inclusions in gypsum

8.1 Introduction

It has been known for several decades that the speed of sound in aqueous solutions depends on variations in salt concentration, temperature and pressure (Chen et al., 1978; Kleis and Sanchez, 1990). Therefore, Brillouin spectroscopy might be a potential tool to reveal relative variations in palaeosalinity from fluid inclusions along the direction of growth and/or deposition in geological samples such as evaporites. For this reason, the scientific goal of this chapter was to conduct first experiments on saline aqueous solutions and to compare the measured sound velocities with the calculated ones, and second to apply this approach on a natural gypsum sample from the sabkha El Melah, Tunisia. The selenite-type sample was selected due to its high abundance of growth bands with primary fluid inclusions along 6 cm, opening the opportunity to test if sound velocities vary significantly from the youngest to the oldest part of the host crystal.
The experimental part (saline aqueous solutions) aims also to define a standard as a function of salinity from low- to high-saline water samples, while the practical part (gypsum sample) is intended to estimate the palaeosalinity by taking into account the final ice melting points of fluid inclusions too. In addition, both primary and secondary FIs were measured in the natural gypsum sample to compare several FIAs, and to detect differences in sound velocities that might be related to variations in salinity upon crystal growth.

8.2 Saline aqueous solutions

8.2.1 Pure water

On a total temperature range of 60 °C (5-65 °C), the measured w_{H_2O} data vary between 1393 to 1510 m/s (Δ117 m/s; Table 8.1). At 25 °C, w_{H_2O} = 1457 m/s, thus, 40 m/s less than the literature value of 1497 m/s. Pure w_{H_2O} data are generally speaking $\geq$ 2.3% lower than literature values on the 5-65 °C temperature range (Table 8.1; Figure 8.1). This error, expressed in % from the final calculated value, rises with increasing temperatures to 2.76%. For ambient moderate temperatures (15-35 °C), the error does not increase significantly during a 20 °C shift (0.1%), thus it is lower than the instrumental error of 0.15% (3 m/s). Such a shift has been expected due to the refraction of light at interfaces as mentioned in 4.1. Hence, a capillary correction factor (c) needs to be adapted for all capillary samples which is expressed by the difference to literature data and further related to the fraction of measured:calculated values.
The obtained w data for H_2O are close to those from the literature with a maximum error of 1.2 % at 5 °C (Table 8.1). The fitted data are best described by a third

Table 8.1 Measured[1] and calculated[2] sound velocity data of pure H_2O between 5-65 °C. [2] after Chen and Millero, 1986. The offset is shown as the difference of [2] and [1], correction factor as the ratio of $^{[1]}:_{[2]}$, and the error represents the deviation of [1] to [2].

T [°C]	$w^{[1]}$ [m/s]	$w^{[2]}$ [m/s]	Offset [m/s]	Correction factor	Error %
5	1444	1426	18	1.012	1.2
15	1480	1466	14	1.010	1.0
25	1509	1497	12	1.008	0.8
35	1532	1520	12	1.008	0.8
45	1548	1536	12	1.008	0.8
55	1558	1547	11	1.007	0.7
65	1564	1553	11	1.007	0.7

order polynomial fit (Figure 8.1):

$$\begin{aligned} w(H_2O_{calc.}) &= 1399 + 5.248x - 5.798 * 10^{-2}x^2 + 2.128 * 10^{-4} + x^3 \\ &\qquad (R^2 = 1) \\ w(H_2O_{meas.}) &= 1369 + 4.679x - 4.623 * 10^{-2}x^2 + 1.192 * 10^{-4}x^3 \\ &\qquad (R^2 = 0.9999) \end{aligned} \tag{8.1}$$

The observed difference between measured and calculated w values further helps to treat data of saline samples with caution during the interpretation. Therefore, data obtained from salty aqueous solutions have been corrected by 1/1.008, while natural water samples are reported as raw output values of the analysis program because the refractive index of individual samples could not be determined.

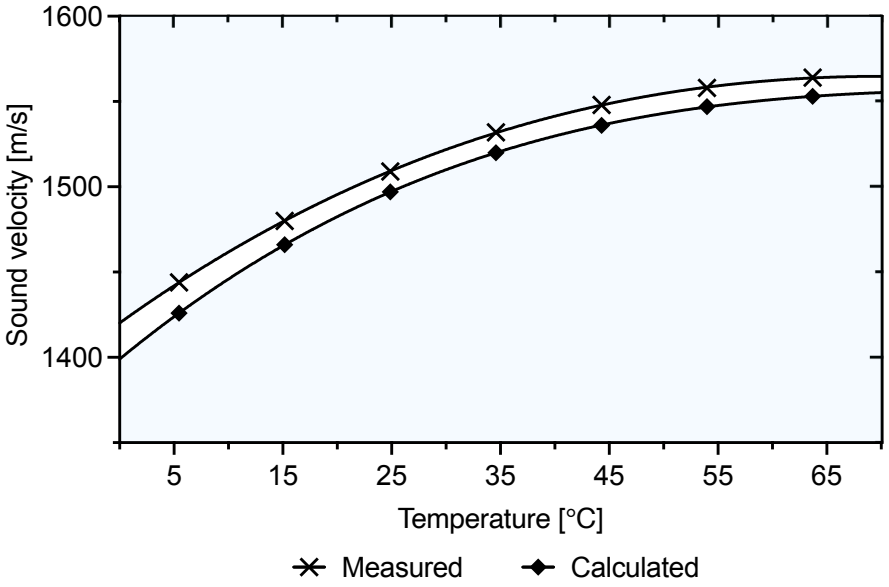

Figure 8.1 Calculated and measured sound velocity data for pure water.

8.2.2 Salty capillary solutions

The sound velocity in NaCl-bearing capillary solutions was measured at the same range as for H_2O. All data points plot within a w range of 1400-1800 m/s. Lowest w values are observed in solutions of low-saline samples with NaCl concentrations of 0.5, 2.5, 5 wt.% NaCl, whereby the fitted curve of 0.5 wt.% NaCl is slightly elevated compared to pure H_2O (Figure 8.2). Compared to those low-saline samples, w values reach a relative maximum (1560 m/s) in the sample of 5 wt.% NaCl (Figure 8.3). The intermediary saline sample (10 wt.% NaCl) ranges between 1538<w<1610

Table 8.2 Measured sound velocity values using BS at increasing NaCl concentrations at 25 °C, compared with literature w data (Chen and Millero, 1986). Sample concentrations of dissolved NaCl indicated by salinity S and molality m.

S	m	$w^{[A]}_{calc.}$ after 4.6	$w^{[B]}_{meas.}$ capillaries	offset $[A]-[B]$	c $[B]:[A]$	Error c
[wt.% NaCl]	[mol/kg]	[m/s]	[m/s]	[m/s]		±0.2%
0.5	0.086	1502	1502	0	1.000	0
2.5	0.4388	1524	1525	-1	1.001	-0.1
5	0.901	1551	1549	2	0.999	0.1
10	1.901	1606	1609	-3	1.002	-0.2
20	4.278	1721	1708	13	0.992	0.8
26.4	6.167	1795	1774	21	0.988	1.2

m/s. The high-saline capillary solution (20 wt.% NaCl) falsl between 1687<w<1710 m/s, and the saturated NaCl sample finally yields a nearly constant interval of 1783<w<1791 m/s (Figure 8.3).

Following this, a decreasing trend of w ranges coincides with increasing NaCl

concentration. As a second finding, significantly w windows can be defined by comparing the NaCl fitted curves:

(1) <1600 m/s for low-saline samples,

(2) <1700 m/s for intermediary saline samples, and

(3) >1700 m/s for high-saline samples (Figure 8.2).

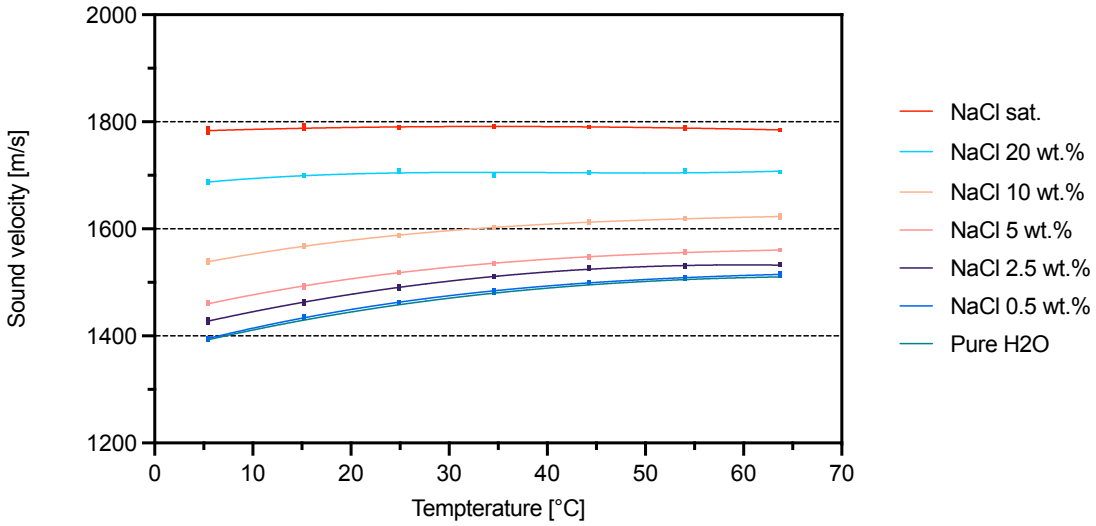

Figure 8.2 Sound velocity data as a function of NaCl concentrations in prepared sample solutions, showing a distinct w window between 1400-1800 m/s.

Moreover, the results of NaCl solutions reveal that one "working temperature" (e.g., 25 °C) is sufficient to characterise the approximate salinity regime of liquid samples as illustrated by Figures 8.2 and 8.3.

Data of NaCl solutions needed to be adjusted for the refractive index n of pure water, that of NaCl solutions, and finally to be corrected for the capillary effect by multiplying the adjusted values with 1 over the average capillary factor obtained from pure water:

$$w_{adj.} = \frac{w_{raw} * n_{NaCl(T,msat(T))}}{n_{NaCl(T,m)}} \tag{8.2}$$

with w_{raw} the measured values by BS, $n_{NaCl(T,msat(T))}$ the refractive index of saturated NaCl at any temperature, and $n_{NaCl(T,m)}$ the refractive index of NaCl at both any temperature and molality, respectively. It follows:

$$w_{corrected} = w_{adj.} * \frac{1}{1.008} \tag{8.3}$$

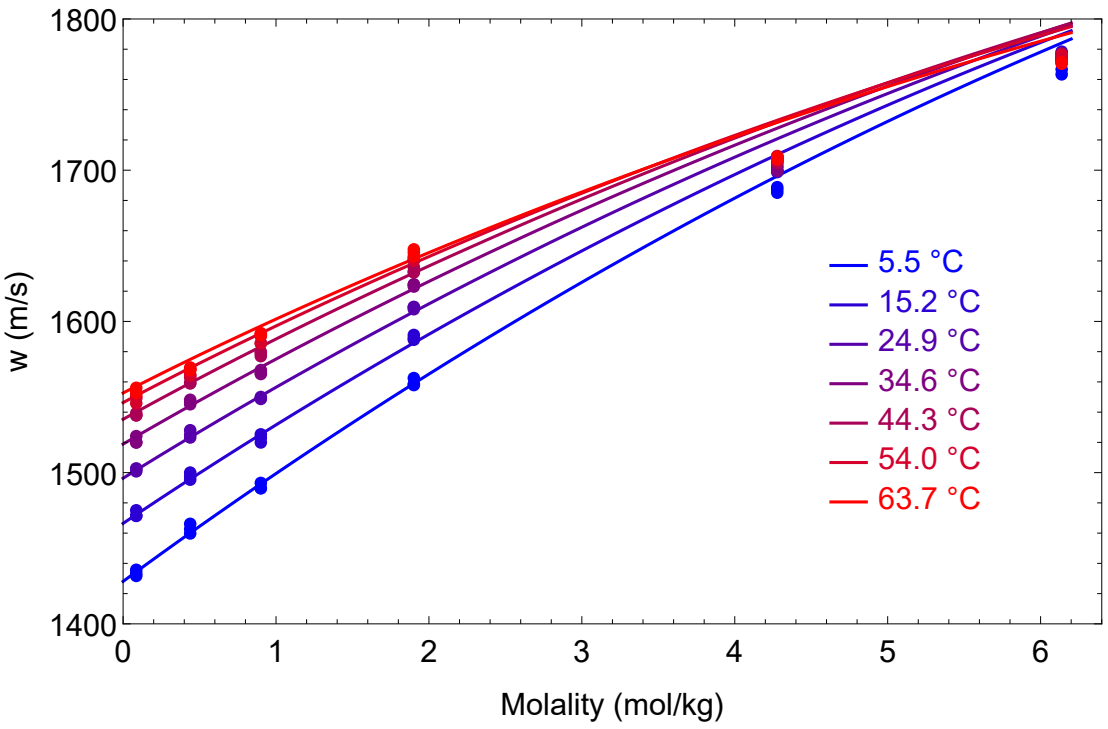

Figure 8.3 Temperature distribution of w values decreases with increasing NaCl concentration.

The sound velocity depends on the salinity of any liquid often with linear relationship (Chen and Millero, 1977; Brewer et al., 2015). The derived BS data for low-saline ranges (0-5 wt.% NaCl) show a parallel pattern of increasing w as a function of T and S, which is in good agreement with modelled fits by Allen et al. (2017) who used an extended approach of the standard UNESCO equation (IOC, 2010).

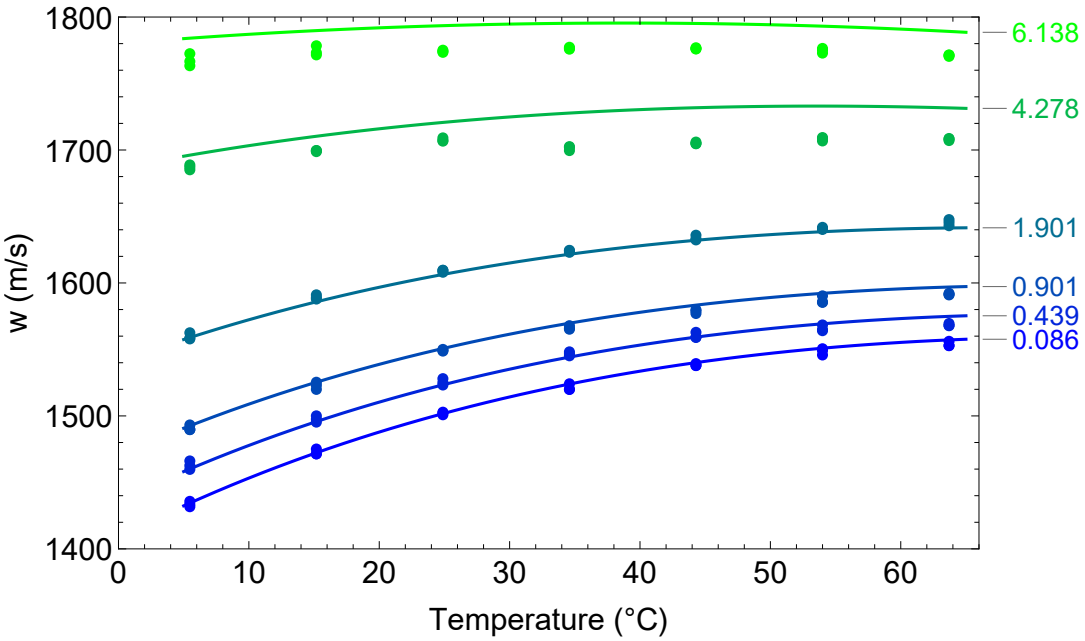

Figure 8.4 Corrected NaCl capillary data with fits from the literature. Molality in mol/kg shown by added numbers right of the plot.

8.2.3 Water samples from saline environments

The results reported in this section are reported as raw w values only. Distributions of capillary w data of waters, brines, and other solutions measured by BS are presented in Figure 8.6. Three major w intervals as a function of dissolved ions and/or the sampling locations are derived from the data set: Solutions of pure H_2O, pure $CaSO_4$ ("CaSO4 sat", "SG032020"), 0.01 m sodic-sulphatic ("NaCl-CaSO4 0.01 m"), and of Mediterranean seawater from a shoreline NW of Sicily ("MS Sicily") yield w values >1400 and <1600 m/s. Secondly, an interval between 1600-1800 m/s defines intermediary solutions with, e.g., mixed $NaCl, CaSO_4$ compounds ("SGH25 BULK", "SGH25 REP"). The aforementioned solutions are followed by elevated w values of two water samples collected from the Aral Sea surface ("AS surface") and from the bottom at ca 30 m depth ("AS bottom"). The border to more than 1800 m/s is marked by a saturated NaCl sample ("NaCl sat."). The third interval defines a range between 1800-2000 m/s. It contains data sets of four water samples that were collected from high-saline environments, in ascending order of w values: sabkha El Melah (Tunisia), shoreline near to Ein Gedi, the Dead Sea, and two ponds with groundwater outflow at the western shoreline of the Aral Sea ("AS11", "AS13"). The sample AS11 (or "Aral11") not only has the highest w values, but is also the only one of all measured samples to have a fitted sound velocity curve that decreases strongly with increasing temperature (Figure 8.5). All other samples always increase towards a certain local maximum, followed by w values that rather form a plateau than a negative slope like Aral11 (Figure 8.5,).

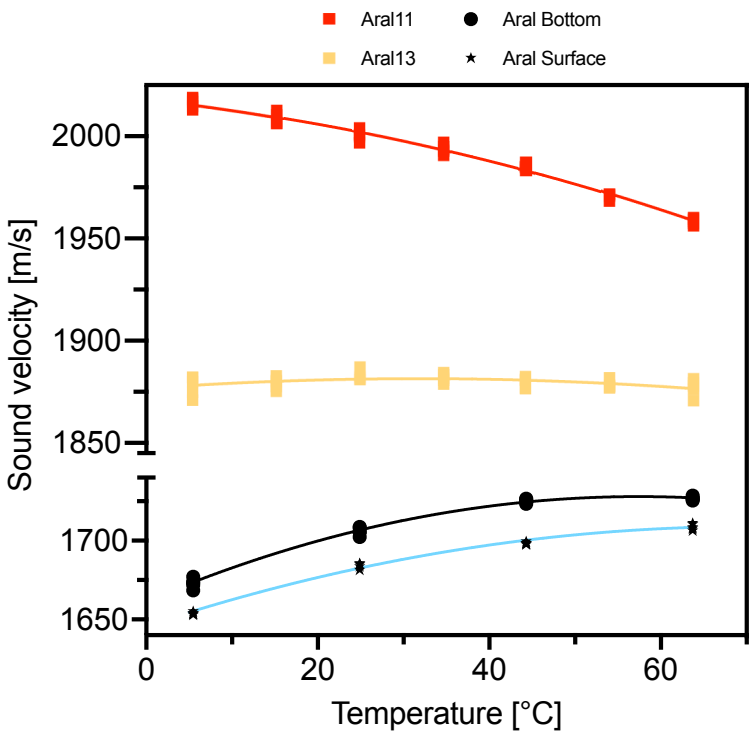

Figure 8.5 Comparison of sound velocity data of water samples from the Aral Sea. Groundwater pounds (Aral11, Aral13) vs. bottom waters and surface waters.

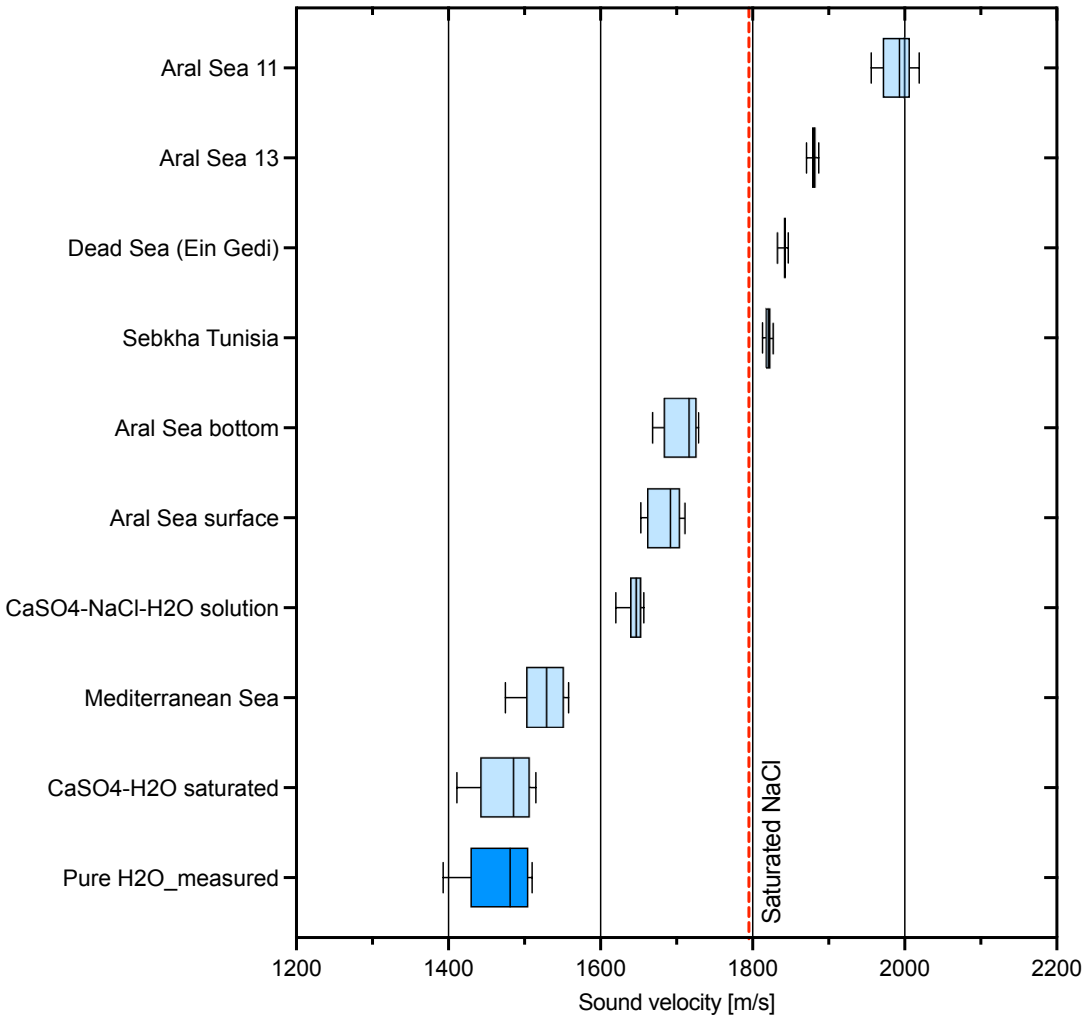

Figure 8.6 Sound velocity data of water samples from different geographical locations and experimental solutions, measured between 5-75 °C. Certain thresholds of w values define low, intermediate, and high saline areas. Note that four samples from known saline brines fall above the NaCl saturation line.

8.3 Sound velocity from FIs in natural gypsum

8.3.1 Introduction

A selenite-type gypsum samples has been collected from a saline sabkha, Tunisia, and further split into three sub-samples (labelled as "05", "07", and "09", respectively). The studied host crystal shows a typical growth direction with a V-shaped structure, consisting of cloudy, clear, and intermediate intervals, as it had been reported for Messinian twinned selenite (Figure 8.7; Natalicchio et al., 2014; Costanzo et al., 2019). Following this, the lower sub-sample "07" marks the relatively oldest part with respect to sub-samples "09" (central part) and "05" (upper/youngest part).

This section of the thesis aims to compare sound velocity data sets taken from these three intervals, and to test if the sound velocity varies significantly along the growth direction of the selenite host crystal. Following one of the classical approaches of evaporating brines (e.g., Warren, 2016), the hypothesis is that a brine becomes more saline the more water evaporates, leading to more saline entrapped fluid inclusions in a crystal over a longer temporal distance. On the contrary, a brine could have been diluted over time by rainfall, groundwater inflow, or marine flooding, which would lower the brine's salinity. Therefore, this study is limited to the first application of the BS method to gypsum only, in order to provide the fundamental knowledge for further projects. Since the growth duration of the studied sample is unknown and other methods could not have been applied (e.g., δ^{34}S, δ^{18}O, δD isotopic composition; elemental concentrations), the interpretation of the obtained data set remains tentative.

8.3.2 Results

A total of 284 fluid inclusions were measured at constantly 25 °C, and final data range from 1468 to 1975 m/s. By grouping the data set according to each sub-sample, a strong contrast is observed in the statistics for mean, median, standard deviation (SD), standard error (SE), minimum (min), and maximum (max) values (Table 8.3). Sub-sample "05" has a mean of 1644 ±79 (SD) m/s (n = 185) versus 1837 ±54 m/s (SD) of sub-sample "07" (N = 98). The minimum value of "05" ("07") is 1468 m/s (1739 m/s), the maximum is about 1877 m/s (1975 m/s).

Further ordering by both FI type (primary, secondary, mono- or biphasic) and thermodynamic phase (primary biphasic) of each grouped data set shows mean offsets of 184 m/s for **primary monophasic** (n = 107 and 49 for "05" and "07", respectively), 227 m/s for **secondary monophasic** (n = 39 and 13 for "05" and "07", respectively), and 141 m/s for **primary biphasic** fluid inclusions (n = 39

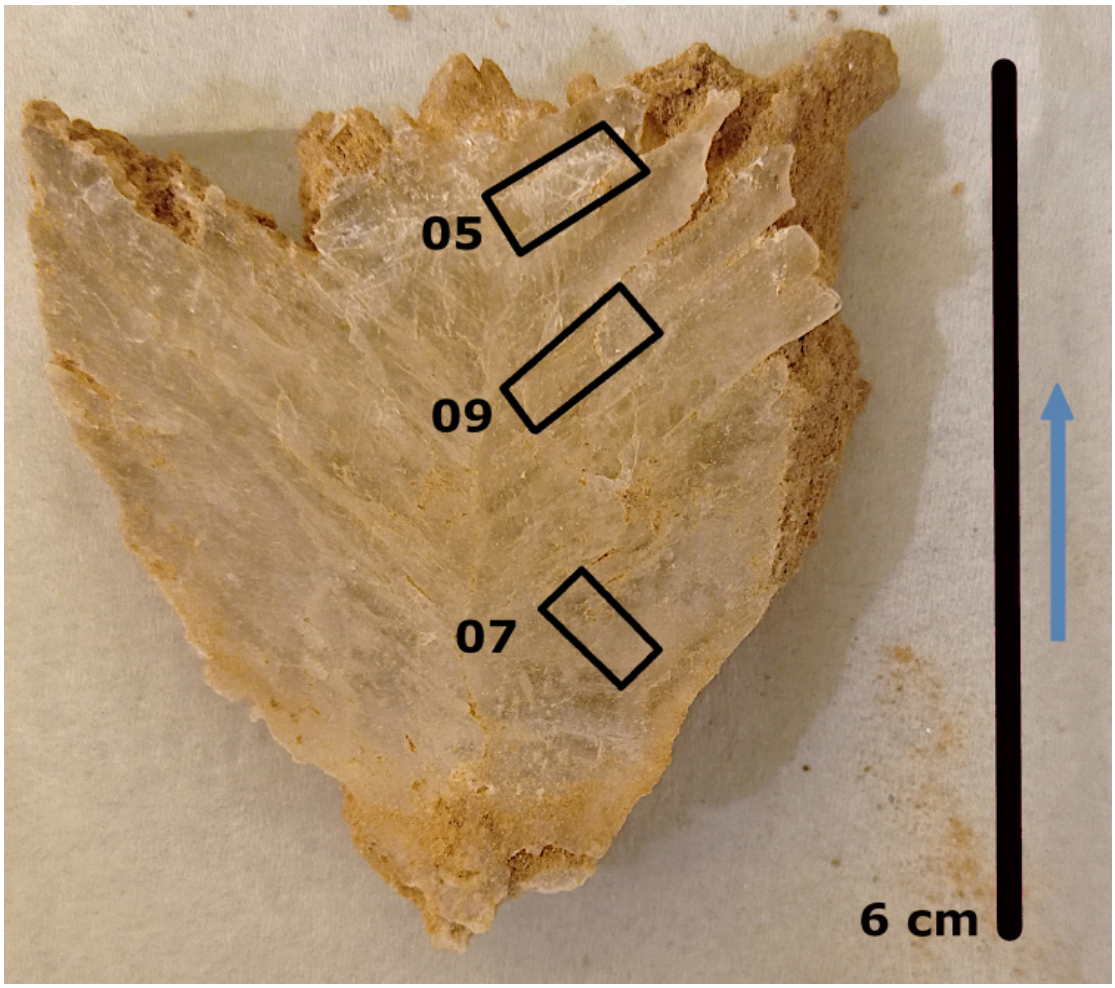

Figure 8.7 Selenite gypsum sample MG1 from the El Melah sabkha. Numbers mark approximate location of sub-samples. Blue arrow indicates the direction of growth.

and 36 for "05" and "07", respectively). While the statistical errors are similar for both phases and FI types, they are **twice as high** as in **biphasic FIs** in sample "05" than in "07".

The apparent data variations of both sub-samples are shown in Figure 8.8. **Lowest** sound velocity values are observed in both **primary** (Figure 8.8C, D) and **secondary monophasic FIs** (Figure 8.8E, F) in sample "05". The highest goodness of fits is described by R^2 close to 1 which is only found for **secondary monophasic** FIs in both samples (0.9952 and 0.9882 for "05" and "07", respectively).

To introduce to the next sections 8.4 and 8.5, and due to the fact that not all FIs could have been observed for their final melting points, only selected biphasic fluid inclusions are presented in Figure 8.9. In addition, a third sub-sample (labelled "09") was collected in the central part of the host gypsum sample for biphasic sound velocity measurements (n = 21). The descriptive statistics for all samples used for salinity reconstructions (see section 4.5) are listed in Table 8.4. As shown in

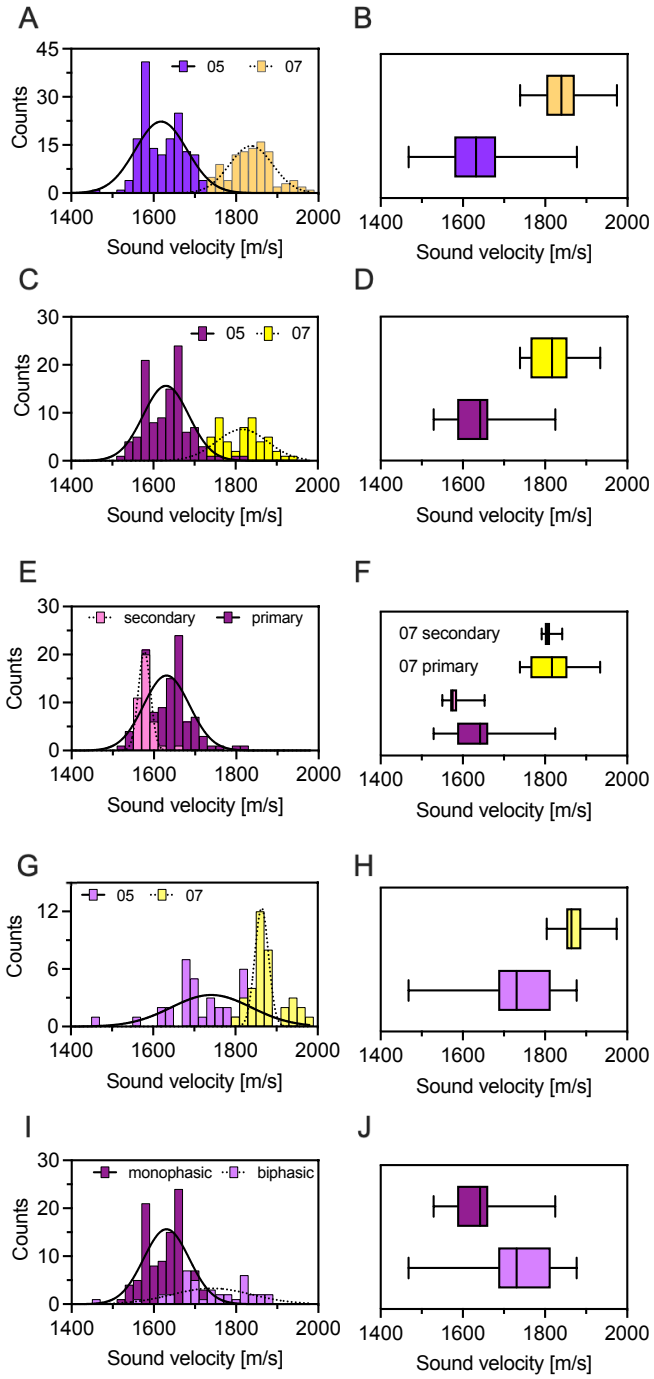

Figure 8.8 Data distribution of two sub-samples (05, 07) from natural gypsum, Tunisia. All shown data were measured at 25 °C. A, B: Monophasic and biphasic FI data points without differentiation. C, D: Only primary monophasic FIs. E: Monophasic primary (dark) and secondary (bright) FI data from sample 05. F: Additional data of sample 07 with monophasic primary (yellow) and secondary (black) FIs. G, H: Biphasic data from sample 05 and 07. I, J: Monophasic and biphasic data from primary FIs of sample 05. Chosen bin width for all histograms is 20 m/s.

Table 8.3 Statistics of mono- and biphasic FIs of crystal 05 and 07 from gypsum sample MG1 (Tunisia).

Crystal	05+07	05				07			
	Total	All data	Mono. prim.	Mono. secon.	Bi.	All data	Mono. prim.	Mono. secon.	Bi.
n	284	185	107	39	39	98	49	13	36
Mean	1711	1644	1633	1580	1735	1837	1817	1807	1876
Median	1689	1632	1642	1575	1731	1839	1817	1805	1864
SD	117	79	55	18	91	54	52	13	43
SE	7	6	5	3	15	5	7	3	7
Min	1468	1468	1529	1550	1468	1739	1739	1792	1804
Max	1975	1877	1825	1653	1877	1975	1934	1842	1975

Figure 8.8 H, the data distribution is broader in sample "05" which is observed also in selected FIs (Figure 8.9). The mean of sample "09" is slightly lower than that of "05" and "07" while its range is the lowest of all sub-samples (Table 8.4). Moreover, a step-wise decrease in minimum sound velocity values coincides with the growth direction of the host gypsum sample with sub-sample "05" being the youngest part, "09" the intermediate part, and "07" the oldest part with respect to the location inside the whole sample. The minimum value of "05" (1550 m/s) equals the calculated capillary value of 5 wt.% NaCl, whereas "09" (1630 m/s) is close to the capillary value of >10 wt.% NaCl, and "07" (1754 m/s) already well above 20 wt.% NaCl (see Table 8.2).

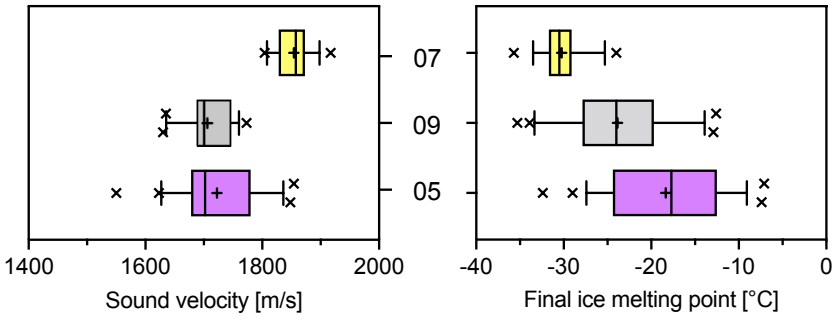

Figure 8.9 Data of three crystals from gypsum sample MG1. Left panel: only sound velocity data of fluid inclusions that were also used for freezing experiments. Right panel: Data of freezing experiments with final ice melting points. Whiskers showing the 10-90 percentiles, vertical black line the median, black cross in boxes show the mean values.

8.4 Final ice melting points

Final ice melting points (T_{ice}) mark the temperature point when the last ice crystal of a frozen fluid inclusion melts in the presence of a vapor bubble. To get rough estimates if the chosen fluid inclusions fall into the NaCl-H2O system, the eutectic points were documented in most cases and are listed in Appendix B (Tables D.1, D.3, D.2). The mean of all documented T_{ice} values only varies in sub-sample "07" (-63 °C) while those of "05" and "09" are equal (-54.7 °C). The eutectic points are relatively low compared to that of NaCl-H2O (-21.3 °C), pointing to it being a system of more than two components, however, the significance of such partly erroneous observations should also be taken with a degree of caution (see discussion).

Upon further slow heating, a vapor occurred in most cases around -45 to -40 °C, while FIs with small (<10 µm) sizes needed two or more cooling-heating cycles to nucleate a vapor. Lowest T_{ice} values were observed in sub-sample "07" (-35.7 °C). In general, the obtained overall data set covers a temperature range between -7.1 to -35.7 °C (Table 8.4). Both mean T_{ice} and the maximum negative T_{ice} values for each sub-sampled data set show a trend towards less negative values along the direction of growth of the host crystal (Figure 8.9, Table 8.4). The combined T_{ice} vs. sound velocity plot indicates that both crystals "09" and "07" from the intermediate-oldest parts fall into distinct intervals (1600-1800 m/s and 1800-1900 m/s, respectively), as previously seen for (non-)saline capillary solutions (Figure 8.10 D). A relatively narrow T_{ice} range is observed only for crystal "07" (Figure 8.10 D). On the contrary, T_{ice} data of crystals "05" and "09" form a broader interval between -7.1 to -32.4 °C, and -12.6 to -35.3 °C, respectively. The enlarged interval might be likely due to internal growth band distances from up to 1 mm. Any observed data outliers were checked using the microscopic images of each distinct biphasic FI phase to identify high ratios of vapor:liquid in small FIs. A vapor bubble filling the entire FI space affects the Brillouin spectra due to the interference of the laser light with the vapor phase.

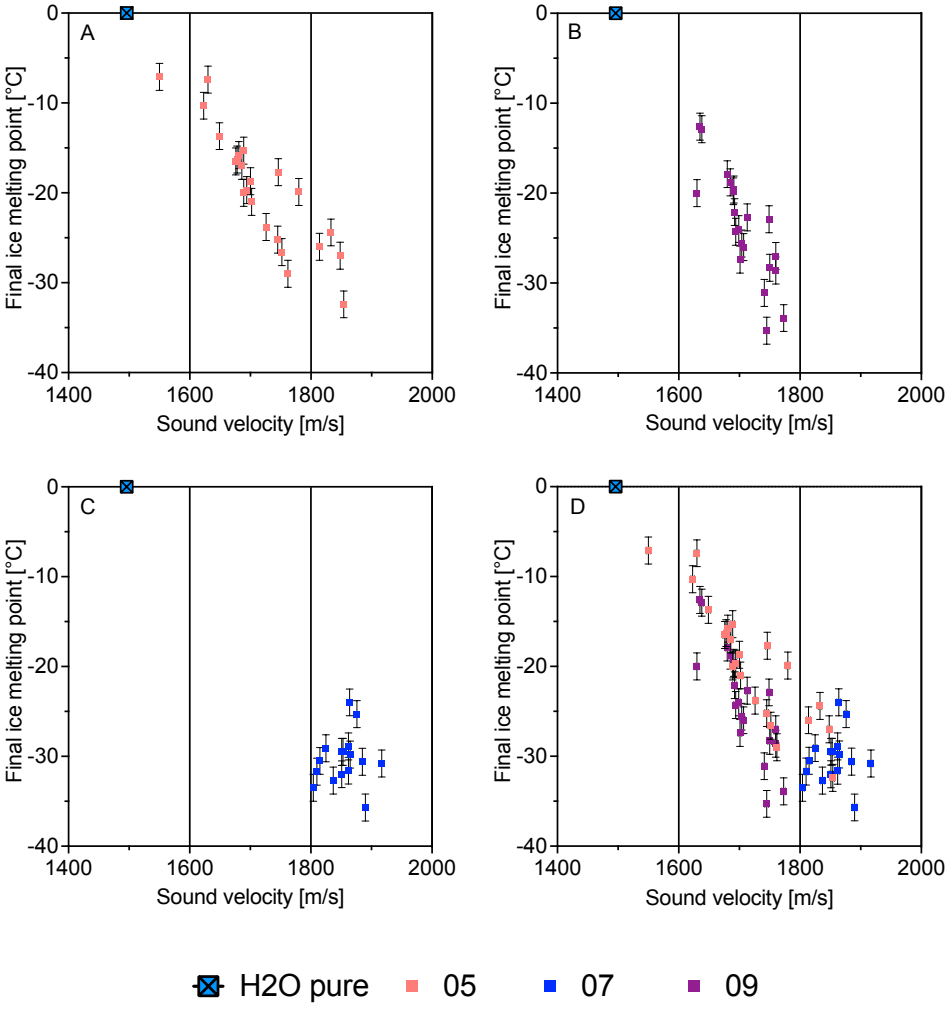

Figure 8.10 Observed final ice melting points as a function of measured sound velocity data of biphasic FIs in sample MG1. A: Crystal 05, B: crystal 09, C: crystal 07, D: all data grouped by their respective colors from A-C. Pure water indicated at y = 0 with w = 1496 m/s by squared box.

Table 8.4 Statistics with sound velocity and final ice melting points of gypsum MG1 sub-samples (Tunisia)

	Sub-sample		
	05	09	07
mean w_{LVE} [m/s]	1722	1707	1848
n	23	20	17
SD w_{LVE} [m/s]	77	41.4	38.0
range w_{LVE} [m/s]	304	143	163
min w_{LVE} [m/s]	1550	1630	1754
max w_{LVE} [m/s]	1854	1773	1917
T_{ice} mean [°C]	-19.6	-23.9	-30.2
n	23	21	18
T_{ice} SD [°C]	6.6	6.0	2.7
T_{ice} range [°C]	25.3	22.7	11.7
min T_{ice} [°C]	-32.4	-35.3	-35.7
max T_{ice} [°C]	-7.1	-12.6	-24.0

8.5 Derived salinity

Despite the very low eutectic temperatures that indicate a rather multi-component ionic system, the observed T_{ice} values were inserted into equation 4.7 that is valid only for NaCl-bearing FIs until saturation (Bodnar, 1993). The resulting salinity values are inverse to those of T_{ice}, simply due to the quadratic function being used to convert T_{ice} into weight % NaCl equivalent salinity (Figure 8.11 D). The plotted values can be described best by a forth order polynomial fit including pure water as initial theoretical starting point before any water loss of the parent brine (R^2=0.8248). However, it is worth noting that the fitted curve starts at highest salinity, representing the oldest part of the host crystal above the NaCl saturation point of 26 wt.% (blue points in Figure 8.11 C-D). Towards the intermediate-youngest part, the salinity decreases to approximately 10 wt.% NaCl eq.

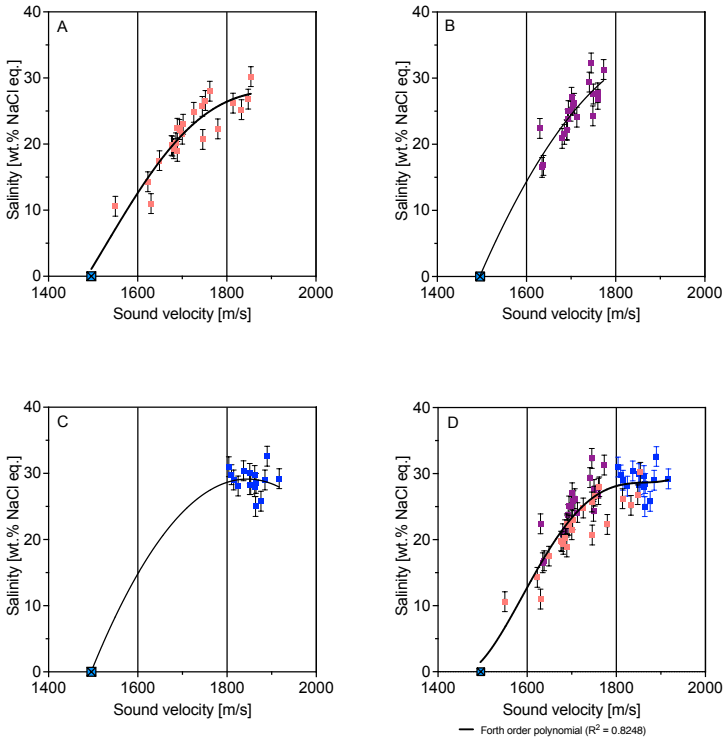

Figure 8.11 Calculated salinity from ice melting points in biphasic gypsum FIs vs. measured sound velocity. Plots presented for sub-samples 05 (A), 09 (B), 07 (C), and a complete plot with data from A-C.

A crucial point of determining the bulk salinity of fluid inclusions is the identification of the correct chemical system (Goldstein and Reynolds, 1994). A problem is that the true chemical composition of fluid inclusions (FIs) or a selected fluid inclusion assemblage (FIA) remains unknown at higher salinities without additional analytical methods. In the case of the Messinian Salinity

Crisis - a period of massive deposition of evaporites (mainly salt and gypsum) in the Mediterranean Sea - two major studies have suggested that selenite gypsum types might have rather formed in low-saline, freshwater-dominated environments (Natalicchio et al., 2014), or in usual marine environments (Bigi et al., 2022). The latter study revealed that FIs might be likely affected by a crack-and-seal mechanism which could directly alter the composition of the trapped brine. Further, the authors hypothesized that this process could affect as well the geochemistry of the crystallization water, making gypsum-rich FIs not very suitable for palaeosalinity studies (Bigi et al., 2022). However, the same authors also proposed an extended temperature excursion (220 °C from -100 to +120 °C) to cavitate vapor bubbles which are necessary for both Brillouin spectroscopy and the classical microthermometry method. The experimental work performed during this thesis to cavitate vapor bubbles in gypsum samples did not cover such a temperature range, which might explain the low abundance of biphasic FIs in both lab-grown and natural gypsum samples during temperature and salinity experiments (see section 7.2). It should be tested in future studies dealing with gypsum samples in combination with both BS and microthermometry, e.g., to measure final ice melting points.

In this preliminary study, only the determination of first melting temperatures ("eutectic temperatures"; T_e) of FIs can help to classify the aqueous system (Bodnar, 1993). Here, nearly all observed eutectic temperatures fall below that one of the NaCl–H_2O system (-21.2 °C). However, as described in Goldstein and Reynolds (1994), the identification of the true system ≠ NaCl is often ambitious and problematic if daughter minerals appear.

Therefore, the obtained T_{ice} data were used only for simplification because the aim of this work is not to reconstruct the absolute ("true") salinity of single FIs, but rather to test if relative salinity variations occur along the growth direction of the gypsum host crystal. By comparing the data set with other experimental data obtained during the PhD thesis, the apparent maximum sound velocity data are observed in sub-sample "07" (oldest part). On the contrary, lowest sound velocity data are found in (1) two data sets derived from secondary FIs from Messinian sampling locations, which reflect likely infiltrating freshwater through time, and (2) in a lab-grown gypsum sample (pure water FIs) (Figure 8.12). Therefore, it can be argued that sub-sample "07" originated in a highly saline brine that was later slightly diluted but still above the gypsum saturation point. This is underlined by both sub-samples "09" and "05" which yield sound velocity values below the NaCl saturation line (red dotted curve in Figure 8.12).

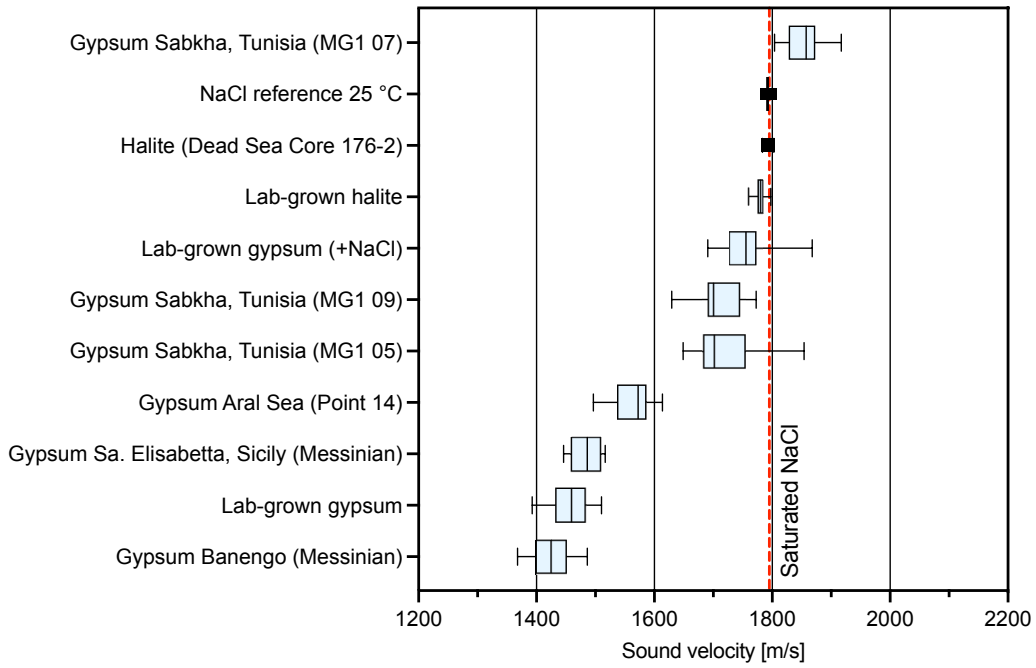

Figure 8.12 Overview on sound velocity data of halite and gypsum FIs. Note that data from Messinian samples and Aral Sea are derived from secondary FIs. NaCl reference and lab-grown halite produced at controlled conditions (24-25 °C). Dead Sea core 176-2 = MIS 7c (ca 215 ka).

The final comparison with the theoretical "pure" NaCl curve shows a deviation in both salinity and sound velocity values, which might be explained by the non-binary system of the fluid inclusions of the natural gypsum sample. The results need to be re-evaluated by future studies including additional methods to account for the brine composition. Furthermore, a larger data set should be produced by measuring ≥ 50 biphasic FIs in each crystal, being aligned along the same growth bands. In addition, the more complex brine composition should be modeled to compare both, the measured and the theoretical salinity of gypsum FIs.
Nevertheless, the results give hope to use gypsum from outcrops, bore cores, or arid sabkha environments, to estimate the palaeosalinity of a well-dated sample. It is recommended to setup a bunch of laboratory-controlled standard samples at varying salinity, which then could be used to compare natural samples after analysis with Brillouin spectroscopy. The advantage of this method is the fast acquisition of large data sets, since only biphasic FIs need to be measured at one constant temperature (e.g., 25 °C). This reduces the lab costs because it avoids the usage of liquid nitrogen resources.

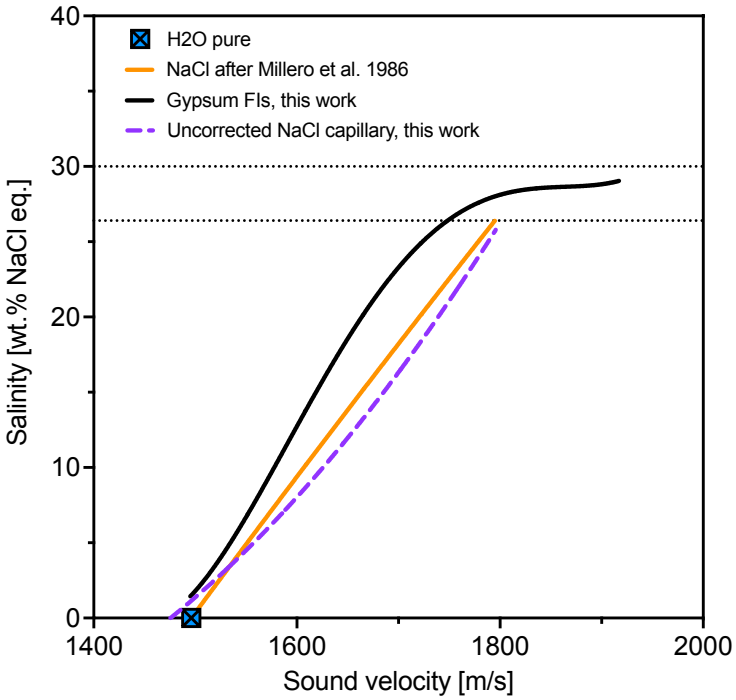

Figure 8.13 Final plot of salinity vs. sound velocity data from biphasic gypsum samples

8.6 Summary

The determination of ice melting points T_{ice} in biphasic fluid inclusions is a good proxy for salinity estimates, however, the lab work is relatively lengthy when studying a large amount of FIs. To test a new approach for salinity estimates in both solutions and solids, experiments were performed first on natural high-saline water samples. The produced data showed significantly higher sound velocity values than water samples from the Mediterranean Sea, or synthetically-produced low-saline solutions. The results show that this approach helps to estimate roughly the relative salinity of aqueous samples in a very short time.

Second, sound velocity data of gypsum FIs from an arid sabkha location are indicative of relatively salinity variations during crystal growth in a parent brine supersaturated with respect to $CaSO_4$. Furthermore, sound velocity data were combined with the detection of T_{ice} in the same samples. A link was found between low T_{ice} and elevated sound velocity values, which supports that the salinity of the parent brine could have been highly saline at the start of gypsum crystal formation. Furthermore, the results suggest a complex parent brine due to very low T_{ice} data. Thus, salinity estimates derived from ice melting points and Brillouin spectroscopy should be combined with other analytical methods to identify the fluid's composition which is indispensable in terms of palaeoclimate interpretations of any sample. If another method is unavailable, it is recommended to measure the

sound velocity of numerous biphasic FIs at constant temperature, and to compare the data with both, a standard sample and calculated values using a model. If unavailable, a calibration line of various final ice melting points might help to translate the sound velocity data into relative salinity estimates. Subsequently, BS might be used only on other FIs at 25 °C to quickly get the salinity variations in a crystal. However, the sampling distances should be chosen rather largely (ca 4-6 cm) to detect salinity variations high enough for palaeoclimate interpretations of the parent brine. Hence, the outcome of this chapter provides evidence that Brillouin spectroscopy is a prospective tool to increase the throughput of salinity estimates in geological records.

Bibliography

Allen, J., Keen, P., Gardiner, J., Quartley, M., and Quartley, C. (2017). A new salinity equation for sound speed instruments. *Limnology and oceanography: Methods*, *15*(9), 810–820.

Bigi, D., Lugli, S., Manzi, V., and Roveri, M. (2022). Are fluid inclusions in gypsum reliable paleoenvironmental indicators? An assessment of the evidence from the Messinian evaporites. *Geology*.

Bodnar, R. J. (1993). Revised equation and table for determining the freezing point depression of H2O-NaCl solutions. *Geochimica et Cosmochimica acta*, *57*, 683–684.

Brewer, P. G., Peltzer, E. T., Ryan, J., Kirkwood, W. J., and Hofmann, A. F. (2015). Ocean chemistry and the speed of sound in seawater. *Marine Chemistry*, *177*, 591–606.

Chen, C.-T., Chen, L.-S., and Millero, F. J. (1978). Speed of sound in NaCl, MgCl2, Na2SO4, and MgSO4 aqueous solutions as functions of concentration, temperature, and pressure. *The Journal of the Acoustical Society of America*, *63*(6), 1795–1800. https://doi.org/10.1121/1.381917

Chen, C.-T., and Millero, F. J. (1977). Speed of sound in seawater at high pressures. *The Journal of the Acoustical Society of America*, *62*(5), 1129–1135.

Chen, C.-T., and Millero, F. J. (1986). Thermodynamic properties for natural waters covering only the limnological range 1. *Limnology and Oceanography*, *31*(3), 657–662.

Costanzo, A., Cipriani, M., Feely, M., Cianflone, G., and Dominici, R. (2019). Messinian twinned selenite from the Catanzaro Trough, Calabria, Southern Italy: field, petrographic and fluid inclusion perspectives. *Carbonates and Evaporites*, *34*(3), 743–756. https://doi.org/10.1007/s13146-019-00516-0

Goldstein, R. H., and Reynolds, T. J. (1994). Systematics of fluid inclusions in diagenetic minerals.

IOC. (2010). The Practical Salinity Scale 1978 and the International Equation of State of Seawater 1980. *Unesco Technical Papers in Marine Science 36*, 196. https://unesdoc.unesco.org/ark:/48223/pf0000188170

Kleis, S., and Sanchez, L. (1990). Dependence of speed of sound on salinity and temperature in concentrated nacl solutions. *Solar Energy*, *45*(4), 201–206.

Natalicchio, M., Dela Pierre, F., Lugli, S., Lowenstein, T. K., Feiner, S. J., Ferrando, S., Manzi, V., Roveri, M., and Clari, P. (2014). Did Late Miocene (Messinian) gypsum precipitate from evaporated marine brines? Insights from the Piedmont Basin (Italy). *Geology*, *42*(3), 179–182.

Warren, J. K. (2016). *Evaporites*. Springer International Publishing. https://doi.org/10.1007/978-3-319-13512-0

Chapter 9

Final conclusions

This work addressed experimental trials on climate archives from arid to semi-arid climate regions in order to anchor the application of a new climate proxy in the scientific community. Fluid inclusions (FIs) in evaporitic samples (halite, gypsum) from different study sites were used to extend a recently developed palaeothermometer for subsurface materials (Brillouin spectroscopy). The study sites included Pleistocene-Holocene lake sediments (Dead Sea basin (DSB), Aral Sea region), Holocene sabkha sediments (El Melah, Tunisia), and outcrops dating back to the Messinian Salinity Crisis in the Mediterranean (Piedmont basin, Sicily).

A 445 m long sedimentary core from the DSB showed depositional features of varved halite units formed under increasingly warmer global climate conditions. Such interglacial periods are coherent with less negative isotopic excursions on global scales (Marine Isotope Stages, MIS). Modern halite deposits respond to seasonal changes by precipitating fine cumulate (winter) or coarse (summer) halite crystals in the whole water column (fine) or solely on the deep lake floor (coarse). Thus, the modern Dead Sea served as an analogue for interglacial periods with halite deposition.

In this work, a new approach to study varved halite section has been applied to decipher palaeo-seasonal temperatures during two interglacial periods (MIS 5e, MIS 7c). By preparing sub-samples at lowermost and uppermost parts within individual halite layers, differences in palaeotemperatures were studies along the direction of growth. Thus, palaeo-seasonal periods of a single year are reflected by sub-sampling locations in coarse layers during late winter (lowermost parts) and late summer (uppermost parts).

The study shows a cyclic increase in palaeotemperatures of coarse halite along the growth direction in three consecutive varves (= three years) at the beginning of MIS 5e. In contrast, data from fine-grained cumulate halite layers reflect consistently lower temperatures. The inferred summer-winter seasonality was about twice as large as today. However, the number of samples is too small to draw conclusions about long-term trends in Lake Samra. Therefore, a salt interval of another interglacial (MIS 7c) was selected to reconstruct for the first time the complete temperature development of the deep lake layers over a period of 13 years. From the lithology of the drill core, it can first be concluded that the salt layers surrounded by clay layers were deposited in holomictic periods. Data from coarse-grained layers show that summer temperatures initially remained unchanged for 5-6 years after the start of the annual mixing process, whereas winter temperatures varied. A stable annual seasonality with clear temperature differences of about 2 °C between summers (warm) and winters (colder) set in after about 6 years. Furthermore, a

relatively high temperature increase of up to 5 ± 0.9 °C was observed over more than one decade. Overall, the mean winter temperature increase was 3.9 °C and 2.3 °C in summers. The results are in general agreement with a short-term global warm phase, which has already been proven by other proxy methods. In relation to the current warm phase and rising global temperatures, especially in the Middle East, the results show that the region and the Dead Sea are very sensitive to external regional or global warm phases. In the future, further studies should be carried out on interglacial salt layers in drill core 5017-A to create a uniform data set for comparing deep water temperatures.

The application of Brillouin spectroscopy was further tested on laboratory-grown gypsum samples by comparing measured entrapment temperatures with known growth temperatures. The work proved challenging due to an insufficient amount of trapped FIs in gypsum crystals. However, a few temperatures could be obtained and showed the potential for future research on gypsum samples containing a larger amount of FIs. Nevertheless, it was shown that natural gypsum samples could be suitable for palaeoclimatic purposes, although the data obtained might correspond to secondary FIs.
However, an encouraging point that inspires us to continue the methodological development on gypsum is that, data from biphasic FIs in natural gypsum indicate a positive correlation between sound velocity and increasing salinity. Thus, sound velocity can be used as a salinity proxy in evaporites what is also supported by data from capillary solution experiments with increasing NaCl concentrations (0 - 26.4 wt. % NaCl). Thus, sound velocity measurements of biphasic FIs in natural gypsum samples might be a promising tool for future palaeosalinity reconstructions.

Overall, the results obtained in this thesis proved that the approach to combine evaporites with the Brillouin spectroscopy method gives hope to investigate more well-dated geological records at varying temporal scales. This tool is not limited to other proxy methods, and therefore powerful palaeoclimatic reconstructions can be performed on salt records in any geographical area. Such high-resolution studies on halite intervals will be helpful to gain a better understanding on seasonal processes in lakes for an area of interest. Here, it is recommended to use preferable halite instead of gypsum because practical work done in this PhD project has shown that large data sets can be obtained within a short time.

List of publications

1. Brall, N.S., Gardien, V., Ariztegui, D., Sorrel, P., Guillerm, E. and Caupin, F. (2022). Reconstructing lake bottom water temperatures and their seasonal variability in the Dead Sea Basin during MIS5e. The Depositional Record, 48(10), pp.592-597, https://doi.org/10.1002/dep2.185.

Appendices

Appendix A

Protocol for Brillouin Spectroscopy analysis

Brillouin spectroscopy

1. To start the microscope, turn on two controls which are situated on the top of the blue shelf at the wall: First, turn on the microscope control (responsible for the XY-stage) which is indicated by number 1. Then turn on control 2. If you have to restart the microscope, turn off first control 2, afterwards control 1.

Note: if you want to work either with transmitted or reflected light, you have to press the corresponding bottom at the back of control 2 on top of the blue shelf. 2. Linkam stage: turn on the two control boxes left to the microscope, indicated by 1 and 2.

4. Switch on both, the screen and the camera.

5. Brillouin box: press both "power on" buttons in front of the interferometer controls right above the black Brillouin box. At the backside, turn the "detector" bottom to ON.

6. Softwares:

(a) Use "SPOT" to connect the camera. Make sure to stay in manual mode and to have the option "auto-adjust exposure" switched-off. There are different profiles to choose with different options. Usually, acquisition time for halte = 125 ms, gypsum = 86 ms, liquids = 40 ms.

(b) Open "Linksys32" to manage the temperature conditions inside the linkam box ("File", "Connect", confirmation of successful connection "OK"). Values to type in (for example): Rate: 20 °C/min, Limit: 25 °C (for NeoHal reference measurements), Hold: 500 mins, LNP: 0, and click at the top-left "manual LNP mode". Note: you need always to check that LNP is set to ZERO when you work with temperatures 22 °C. If you forget this and, e.g., the profile is stopped, the

N2 flux is not interrupted. Hence, the Linkam box will be freezed quickly, which may destroy the sample!

(c) Open "Ghost" for the laser spectrum setup. You have to set ALWAYS the "Edit comments" once you start during a day. Values to type in: Mirror spacing: 3 mm Beam power: 54 mW Channel number: 256 or 512 or 1024 [typically we use 256] Scan amplitude: 200 nm.

Tipp: place all three software windows to the left screen in order to have an overview while working with the microscope! Make sure that you have put the same channel number at the interferometer control as set in "edit comments", and be aware that the filter configuration for the reference light beam (behind the black Brillouin box) has likely to be changed in order to get an appropriate baseline.

7. Leave the laserside to find the laser control at the top of the construction. Turn the key (on the left-bottom corner) to the right, wait until the current reaches ca. 19.20 A and go slowly with the big black knob to "4.00 W" and press (just once) "Shutter". A "klicking" sound occurs, the display shows "laser signal seeking". The usual current is between 22.20 to 22.45 A, a slight increase during the day is normal. Usually, the shutter should be turned off at the end of the day, in order to avoid any unforeseen accidents. The laser control display indicates the status of the shutter (closed / open). Further, it tells you as well any instrumental errors with a certain number and name. In case of any errors, think first before you act. Look into the laser manual (situated in the small shelf box to the very right) or call for help.

8. Now that the laser is running, USE THE SPECIAL GOGGLES BEFORE ENTERING THE BRILLOUIN LAB!

9. Brillouin alignment: Before you start this part, make sure to stay in "align mode" in front of the black Brillouin box. Click on "Observe signal" in the "Ghost" software. The baseline occurs with two negative peaks corresponding to each FPI. Write down the baseline number. At the interferometer control, the knobs X2, Y2, X1, Y1 belong to each FPI and need to be used to for the alignment. Turn the knobs slowly and separately while observing the signal peak. After you reached the sharpest peak, repeat it for the other FPI. Use ΔZ to superimpose both peaks, and Z to set this single new peak to 0 GHz. Leave the "align mode" with turning the knob from "align" to "tandem". It takes ca. 15 seconds to change the position. Observe the signal intensity on the screen: (a) If the signal is higher than your initial baseline, only use slowly ΔZ to increase the intensity. (b) If the signal is low, you may use ΔZ very carefully to increase the signal. If this does not help,

use carefully singlewise X2, Y2, X1, Y1.

Note that the position of Z might change quickly, so that you have to reset the peak again to 0 GHz. Afterwards press "stabilization on" at the interferometer control. Wait several seconds (or minutes) for the signal to be computed and stabilized until it reaches ca. 4x times the signal intensity of the initial baseline.

10. Further, check the shape of the reference laser signal: This is very important before starting the experiment because the laser could not stay in monomode but in multimode. This has a direct influence on all measurements and might be responsible for a full laser signal shutdown while analysing samples. Hence, the reference laser signal has to be sharp and symmetric, without having any bulbs or plateaus. In case of laser multimode, stop stabilization ("stabilization off"), go back to align mode ("align"), close the shutter, turn the big black knob at the laser control to 0.01 W, turn the key to the left, and wait for 5-10 minutes. Restart the laser afterwards and check again the signal shape.

11. Loading the sample: when you use single crystals, make always sure that a glass plate is already covering the silver block in the Linkam stage! Otherwise the sample can fall into the hole, which will result in much additional work to clean the whole instrument. When you use a capillary already stucked with wax on a glass plate, use an air siphoning tool: first, remove the big whitish tube from the Linkam and replace it, then use 1 LNP an push the small hole at the air siphoning tool for aspiration, remove the finger to make it fall.

12. Measuring a ΔfB signal in a liquid: after having set the laser spot on your sample, switch from "shutter" to "window mode" at the interferometer control (first!) and set carefully the pinhole at the entrance to the black Brillouin box to "300". Pause the camera. While still observing, turn off the microscope light (reduce the voltage manually to 0 V, then click "reflected light off"). Wear your GOGGLES before you turn the shutter. In reflected light mode, you need to turn a silver wheel right next to the microscope light exit to unblock the light. Otherwise you will have no laser signal. In order to get the highest signal, check and compare the spectrum at several depths while turning the big knob at the microscope control. If you use a capillary, it might be necessary to go deeper manually. Stop observing and click "start acquisition" to detect the spectrum.

13. Filename structure for Mathematica analysis package: Sample name_number of crystal_FI number_number of FI measurement_L_ (liquid) or _LV (liquid-vapor) _FI size_FI depth_objective_pinhole_number of scans_time_temperature.DAT

14. General important rules/recommendations: (a) Always start with the lowest magnification 2.5x in order to avoid any damages at the objectives and the glas window. (b) Wear gloves and goggles. (c) Open the white lid (couvercle) slowly and with caution, without touching the window in the middle. If necessary, clean the Linkam box afterwards. (d) Always use plastic tools to load the sample material. (e) Make sure in which joystick mode (fast or slow) you are before moving the XY-stage. (f) To move the objectives, always use your hands (meaning, not only one finger!) by using the turret, NEVER touch the objectives! (g) The Linkam box has to be centered relatively to the objectives to avoid any crashes with the 100x objective when displaced! (h) You can save five positions with the option "save position" when holding the respective button for some seconds. (i) At temperatures 90 °C remove the big whitish tube (N2 flow line) to avoid melting of the small black plastic tube.

Appendix B

Ruling out thermal effects due to the laser beam

B.1 Method

One way to speed up measurements is to increase the laser intensity on the sample. In order to check that this is not the case, experiments were performed to compare the values of speed of sound for selected FIs in synthetical NaCl samples with known entrapment temperatures.
As a first step to change the laser intensity, the first Brillouin filter must be turned to > 2. A power meter (Brand, type) before the microscope filter measures the incoming laser intensity. The relation between laser intensities on a sample and the used scan amplitude is expressed by equation B.1:

$$\frac{IF_{new}}{S_A} = IF_{m,b} \tag{B.1}$$

with IF_{new} the desired laser intensity on the sample in mW, S_A the scan amplitude (for 37.57 GHz = 0.3757) and IF_m the laser intensity to be measured by using a power meter.
For example, if the laser intensity on the sample needs to be increased to 101 mW, B.1 yields the intensity IF_m, b to be measured:

$$\frac{101mW}{0.3757} = 269mW \tag{B.2}$$

Additionally, $IF_{m,b}$ is expressed by two different laser intensities on a sample and the measured intensity before the sample is expressed by B.3:

$$\frac{IF_{m,b} * IF_{new}}{IF_{old}} = IF_{m,b} \tag{B.3}$$

with IF_{old} the prevalent used laser intensity on a sample, and $IF_{m,a}$ the currently

measured intensity by using IF_{old} (all in mW). For instance, if approximately doubling the intensity of a current setting with 54 mW on a sample and measured 144 mW, B.3 yields:

$$\frac{144mW * 101mW}{54mW} = 269mW \tag{B.4}$$

This means that a value of around 269 mW must be reached on a powermeter to increase the intensity on a sample to 101 mW. A proportional ratio of 3.6 was calculated by B.5:

$$\frac{a}{b} = ratio \tag{B.5}$$

with a the higher (new) intensity after the filter and b the lower (older) intensity after the filter in mW. To keep a standard baseline of ca. 300 counts, we used B.6:

$$\frac{b}{a} * b_i = baseline \tag{B.6}$$

with b_i the intensity on the sample in mW. For an increase in laser intensity, Following equation B.6, the new (reduced) intensities on a sample are:

$$\frac{75mW}{270mW} * 101mW = 28mW \tag{B.7}$$

and

$$\frac{144mW}{270mW} * 101mW = 54mW \tag{B.8}$$

As a result, no significant increase in speed of sound values was observed. T_x data showed similar values within the instrumental error for one FI, by using both 54 mW and 101 mW for its isochores and LVE measurements. Based on these findings, an induced heating of the sample by increased laser intensity can be ruled out.

B.2 Results experiment A

Initially, a cubic-shaped halite fluid inclusion (FI01Hal24; length = 18 µm, width = 15 µm, depth = 36 µm) was selected from a controlled growth experiment (Hal24 with T_f = 24.5 ± 1 °C) for Brillouin analysis. Isochores of FI01Hal24 were measured at 4 descending temperature steps (29, 21, 13, 5 °C) at 101 mW. Then, the setting was changed to 28 mW and isochores were measured at same

descending temperature steps. After a thermal cycle to cavitate a vapor bubble in FI01 by heating the sample to +130 °C at 30 °C/min, the biphasic FI01 was measured at 101 mW and 28 mW without changing the temperature steps. For a better comparison of each laser intensity, a reference sample (NeoHal) (mean sound velocity = 1789 m/s at 54 mW and 25 °C) was measured at each laser intensity, before and after acquiring the Brillouin spectra of FI01Hal24 (n = 5 for each run; total n = 20 per laser intensity). This allowed to detect possible deviations in acquired reference sound velocity values from the expected mean value for each laser intensity (Figure B.1). It is important to note that sound velocity values are rather relative than absolute due to an instrumental drift during a day of experiments. Thus, each batch of reference sound velocity data at laser intensity X should be compared to the overall mean value of NeoHal (n > 1000) when the data had been acquired during a longer period or at several days. The number of scans is linear related to the acquisition time of each Brillouin spectra to reach 300 counts, with 1 scan = 0.64 s. Further, the number of scans is not dependent on the instrumental drift unlike sound velocity measurements but only on both, the optical alignment and the laser stability. Accordingly, the number of scans vary largely between 28 mW and 101 mW, with a mean of 38 scans per 300 counts and a mean of 11 scans per 300 counts, respectively (Figure B.1). Hence, the laser intensity at 101 mW is 3.4 times faster than at 28 mW, with mean sound velocity values of 1784 ± 1.5 m/s (n = 20) and 1785 ± 1.1 m/s (n = 20), respectively (Figure B.1). The resulting plot shows that both curves of isochores and SLVE for FI01Hal24 at 101 mW are slightly lower than at 28 mW (Figure B.2), leading to a lower T_x value of 23.2 °C at 101 mW compared to 24.5 °C at 28 mW. Since both values are within the instrumental error of 3 °C and within the uncertainty of 1 °C for the formation temperature of the host crystal, further experiments at three laser intensities were conducted for 3 FIs that are entrapped in another crystal from sample Hal24 (see Experiment B).

B.3 Results experiment B

To refine if a higher laser intensity would still yield accurate data, T_x measurements were performed on three FIs entrapped in a crystal from batch Hal24. Isochores of FIs 01, 02, 03 were measured in one run at each intensity I (101, 54, 28 mW) with measurements of the reference FI (NeoHal) before and after each run. After a thermal cycle to cavitate vapor bubbles and transform monophasic into biphasic FIs, sound velocity data were acquired for SLVE curves in each FI at I. Data of the biphasic reference FI (NeoHal) were grouped for each intensity and plotted by sound velocity as a function of number of scans (Figure B.3). The number

of scans (and thus the acquisition time) to reach 300 counts are lowest at 101 mW and increase with lowering the intensity to 54 and 28 mW, respectively. The fitted curve for 3 monophasic FIs at 4 temperatures (29, 21, 13, 5 °C) shows no difference in sound velocity values at varying intensity, with a typical range of < 15 m/s (Figure B.4). In contrast, fitted SLVE curves vary stronger between 54 and 101 mW and show larger differences between both SLVE curves with increasing temperature (Figure B.5). Although the number of FIs (n < 4) is too low to determine the most accurate entrapment temperature, one can still compare the mean T_x values between varying laser intensity. The lowest intensity at 28 mW yields a mean T_x of 21.8 ± 1.1 °C, the intermediate intensity at 54 mW gives 24.3 ± 0.4 °C and the highest intensity has a mean T_x value of 24.4 ± 1.8 °C (Table B.1).

Table B.1 Experiment B: Comparison T_x data of halite FIs at different laser intensities.

Laser intensity [mW]	FI01	FI02	FI03	FI04	Mean T_x [°C]	SD [°C]
28	22.5	20.5	22.4		21.8	1.1
54	24.8	24	24	24.5	24.3	0.4
101	23.1	27	24.3	23.2	24.4	1.8

Results for NaCl T_x measurements. The T_x data for sample Hal24 reveal a mean value of 24 ± 1.6 °C (n = 24), which is in good agreement with the known formation temperature of the host NaCl crystal of 24.5 ± 1 °C. Further, 13 T_x values are within the error range of 1 °C during NaCl crystallization (23.5 < T_x < 25.5 °C).

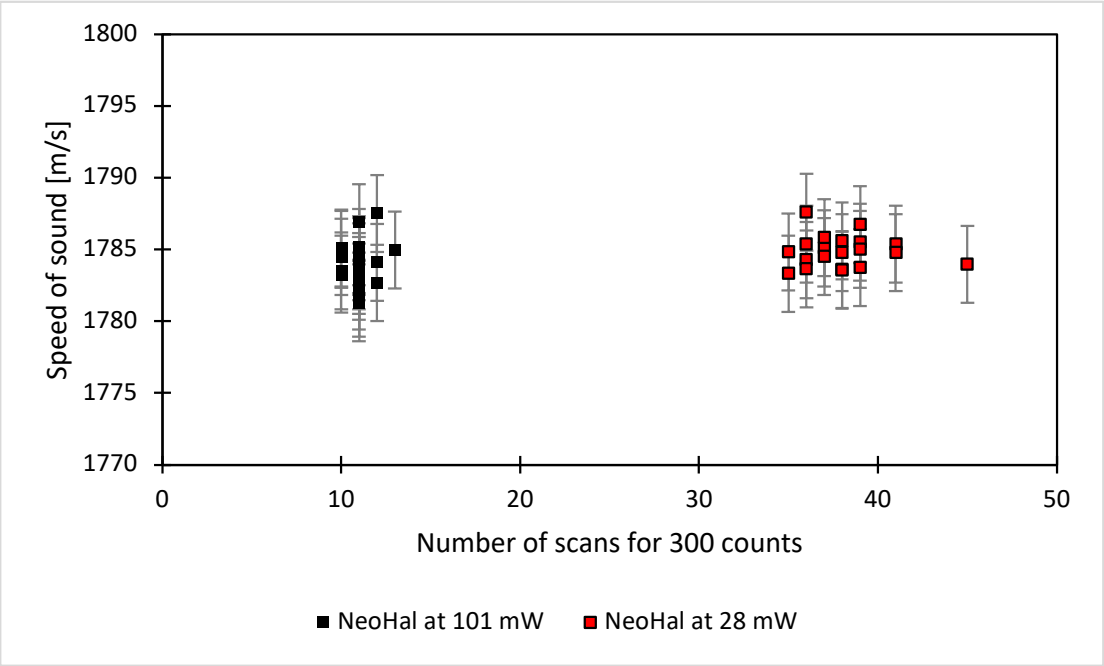

Figure B.1

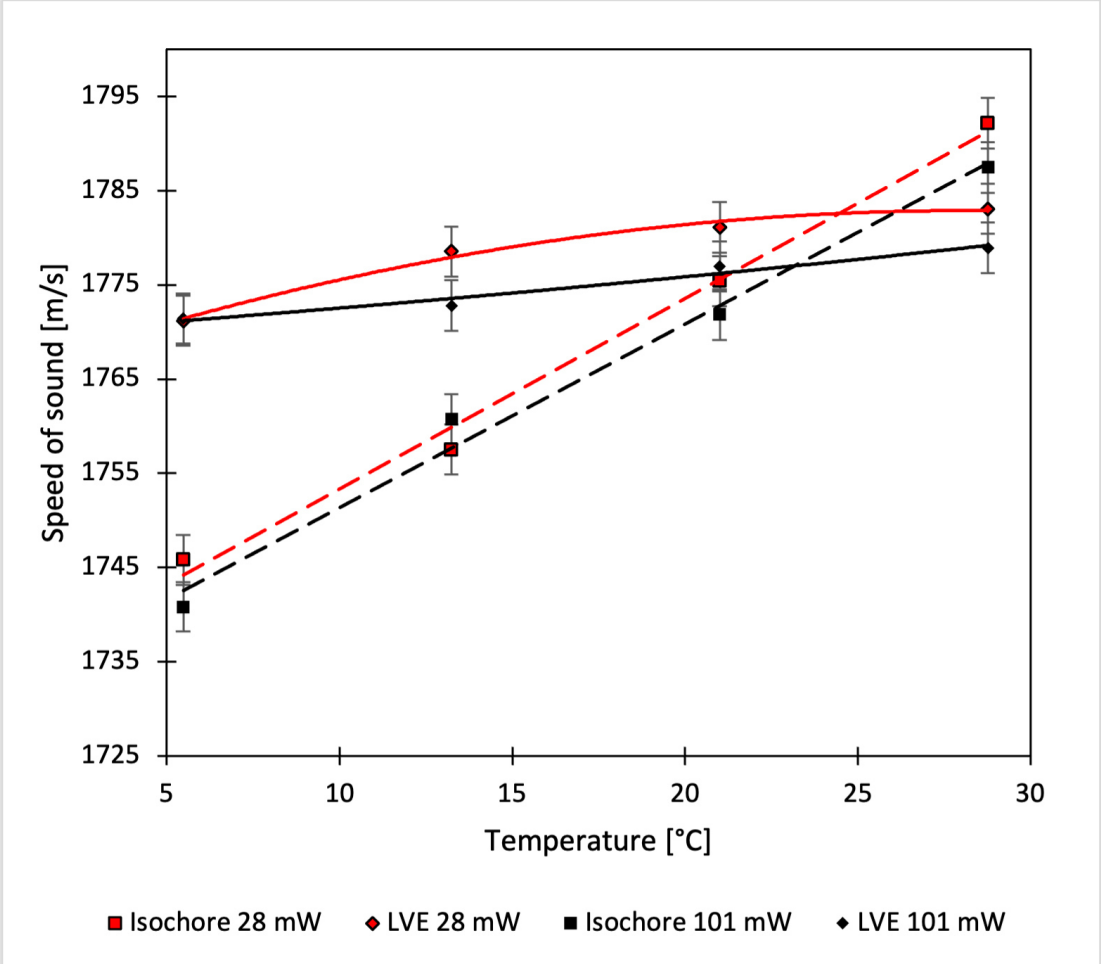

Figure B.2

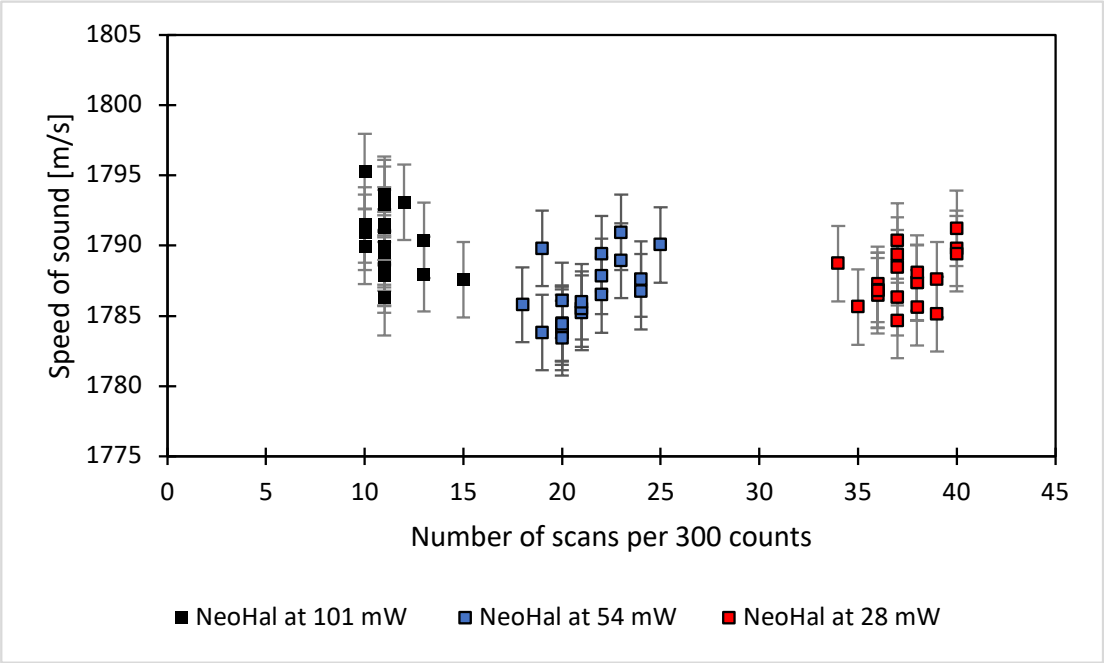

Figure B.3

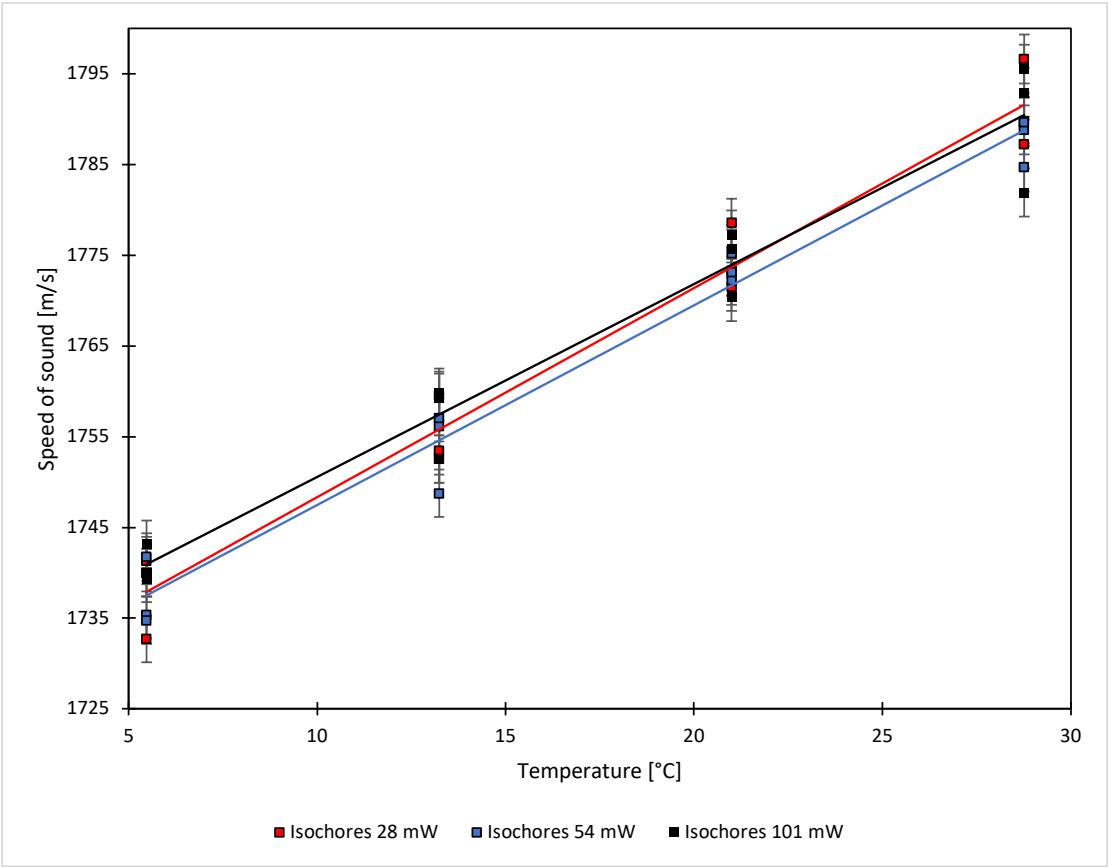

Figure B.4

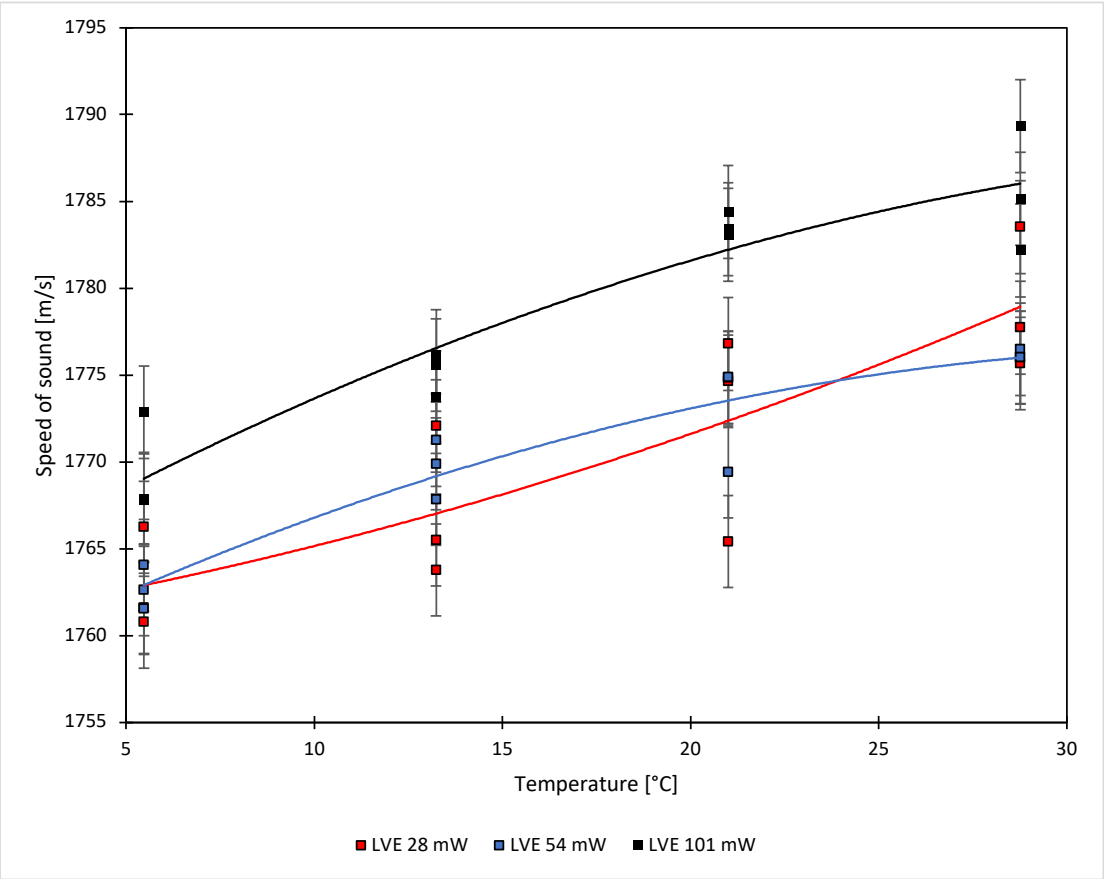
1795
1790
1785
1780
1775
1770
1765
1760
1755
Speed of sound [m/s]
5
10
15
20
25
30
Temperature [°C]
LVE 28 mW
LVE 54 mW
LVE 101 mW

Figure B.5

Appendix C

Entrapment temperatures from natural gypsum samples

Table C.1 Overview on T_x data acquired in natural gypsum samples

Age (Location)	Sample name	FI name	Tx [°C]
Messinian (Eraclea Minoa, Sicily)	EM-TOP	8	12.3 / 37.4
"	EM-MID	5	30.5
"	EM-BOT	1	21.7
"	EM-BOT	2	34.8
"	EM-BOT	3	27.8
Messinian (Santa Elisabetta, Sicily)	SE_cyano	1	20.9
"	SE_cyano	2	21.5
"	SE_cyano	5	17.6
"	SE_cyano	6	23.7
Holocene (Aral Sea shore)	AS14-210719	5	43.4
"	AS14-210719	17	50.7
"	AS14-210719	21	21.1
"	AS14-210719	6	30.7
"	AS14-210719	2	28.4
"	AS14-210719	20	21.1
Messinian (Piedmont, Banengo, Italy)	BAN_200716	3	51.9
"	BAN_200716	5	29.2
"	BAN_200716	13	36.6
"	BAN_200716	14	35.5
"	BAN_200716	20	36.5
Holocene (Sabkha El Melah, Tunisia)	MG1_01-201215	7	21.6
"	MG1_05-210720	1	54.7
"	MG1_05-210720	2	44.8
"	MG1_05-210720	3	48.1
"	MG1_05-210720	4	41.3
"	MG1_05-210720	5	75.2
"	MG1_07-210428	6	30.0
"	MG1_07-210428	44	59.7
"	MG1_07-210428	47	48.6
"	MG1_07-210428	51	47.4
"	MG1_07-210428	56	17.7
"	MG1_07-210428	66	46.4
"	MG1_07-210428	71	13.7
"	MG1_07-210428	73	47.2
"	MG1_08-210429	1	33.9
"	MG1_10-210721	15	37.8

Appendix D

MG1 fluid inclusion data tables

Table D.1 Sub-sample 05: Fluid inclusion data from microthermometry and Brillouin Spectroscopy with calculated salinity values after Bodnar (1993).

	FI	T eu [°C]	T ice [°C]	w biphasic [m/s]	Salinity [wt. % NaCl eq.]
	2	-58	-19.9	1780	22.3
	7	-56	-13.7	1649	17.5
	9	-49	-16.3	1678	19.7
	15	-49.8	-15.8	1681	19.3
	18	-52	-17	1686	20.2
	20		-21	1702	23.0
	21	-54.8	-16.5	1676	19.8
	22		-29	1762	28.0
	28	-58	-18.7	1700	21.5
	31		-23.8	1726	24.8
	34		-27	1848	26.8
	50		-32.4	1854	30.2
	52	-55.4	-17.7	1746	20.7
	54		-25.2	1745	25.7
	55		-26	1814	26.2
	104		-20	1689	22.4
	150	-54.8	-26.6	1752	26.6
	151		-24.4	1833	25.2
	152		-10.3	1623	14.3
	153		-15.3	1689	18.9
	154		-7.4	1630	11.0
	155		-7.1	1550	10.6
	1051		-19.7	1694	22.2
Total	23	-54.7	-18.3	1722	20.6

Table D.2 Sub-sample 09: Fluid inclusion data from microthermometry and Brillouin Spectroscopy with calculated salinity values after Bodnar (1993).

	FI	T eu [°C]	T ice [°C]	w biphasic [m/s]	Salinity [wt. % NaCl eq.]
	4	-51	-31.1	1741	29.4
	15	-54.7	-17.9	1680	20.9
	18	-50	-22.9	1749	24.3
	20	-52.7	-22.1	1692	23.8
	21	-49	-19.6	1691	22.1
	22	-69	-35.3	1745	32.3
	25	-58.5	-24.3	1694	25.1
	30	_	-24	1699	25.0
	33	-53.1	-19.8	1690	22.2
	35	-57	-27.4	1701	27.1
	37	_	-25.6	1704	25.9
	43	_	-12.6	1635	16.5
	44	-51.4	-12.9	1638	16.8
	45	_	-20	1630	22.4
	46	-54.7	-18.8	1685	21.5
	48	-51	-26	1707	26.2
	49	-57	-28.3	1750	27.6
	50	-57.7	-22.7	1713	24.1
	52	-54.2	-27	1760	26.8
	53	_	-33.9	1773	31.3
Total	20	-54.7	-23.9	1707	24.7

Table D.3 Sub-sample 07: Fluid inclusion data from microthermometry and Brillouin Spectroscopy with calculated salinity values after Bodnar (1993).

	FI	T eu [°C]	T ice [°C]	w biphasic [m/s]	Salinity [wt. % NaCl eq.]
	6		-25.3	1876	25.8
	20	-54.2	-29.5	1853	28.3
	31	-51.2	-32.7	1837	30.4
	32	-55.2	-24	1864	25.0
	44	-61	-31.7	1810	29.8
	47		-33.5	1804	31.0
	48		-31.5		29.6
	52	-70	-27.3		27.0
	53	-57	-32	1851	30.0
	61	-64	-30.8	1917	29.2
	62	-73	-30.6	1885	29.0
	65	-66	-29.8	1865	28.5
	66		-31.6	1862	29.7
	67	-72	-29.5	1851	28.3
	68	-61	-28.9	1862	28.0
	69		-35.7	1890	32.6
	71	-70	-30.5	1815	29.0
	73		-29.1	1825	28.1
Total	17	-63.4	-30.2	1848	28.8

Bibliography

Affek, H. P., Bar-Matthews, M., Ayalon, A., Matthews, A., and Eiler, J. M. (2008). Glacial/interglacial temperature variations in Soreq cave speleothems as recorded by 'clumped isotope' thermometry. *Geochimica et Cosmochimica Acta*, *72*(22), 5351–5360. https://doi.org/10.1016/j.gca.2008.06.031

Agassiz, L. (1840). Glaciers, and the evidence of their having once existed in Scotland, Ireland, and England. *Proceedings of The Geological Society of London*, *3*(72), 327–332.

Allen, J., Keen, P., Gardiner, J., Quartley, M., and Quartley, C. (2017). A new salinity equation for sound speed instruments. *Limnology and oceanography: Methods*, *15*(9), 810–820.

Al-Youssef, M. (2014). Gypsum Crystals Formation and Habits, Umm Said Sabkha, Qatar. *Sabkha ecosystems* (pp. 23–54). Springer.

Anati, D. A., and Stiller, M. (1991). The post-1979 thermohaline structure of the Dead Sea and the role of double-diffusive mixing. *Limnology and Oceanography*, *36*, 342–353. https://doi.org/10.4319/lo.1991.36.2.0342

Anati, D. A., Stiller, M., Shasha, S., and Gat, J. R. (1987). Changes in the thermohaline structure of the Dead Sea: 1979-1984. *Earth and Planetary Science Letters*, *84*, 109–121.

Ariztegui, D., Anselmetti, F. S., Robbiani, J. M., Bernasconi, S. M., Brati, E., Gilli, A., and Lehmann, M. F. (2010). Natural and human-induced environmental change in southern Albania for the last 300 years - Constraints from the Lake Butrint sedimentary record. *Global and Planetary Change*, *71*, 183–192. https://doi.org/10.1016/j.gloplacha.2009.11.016

Arnon, A., Selker, J. S., and Lensky, N. G. (2016). Thermohaline stratification and double diffusion diapycnal fluxes in the hypersaline Dead Sea. *Limnology and Oceanography*, *61*, 1214–1231. https://doi.org/10.1002/lno.10285

Aronson, J. R., Emslie, A. G., Miseo, E. V., Smith, E. M., and Strong, P. F. (1983). Optical constants of monoclinic anisotropic crystals: Gypsum. *Applied Optics*, *22*(24), 4093. https://doi.org/10.1364/ao.22.004093

Arrhenius, S. (1896). On the influence of carbonic acid in the air upon the temperature of the ground. *The London, Edinburgh, and Dublin Philosophical*

Magazine and Journal of Science, *41*(251), 237–276. https://doi.org/10.1080/14786449608620846

Aston, F. (1920). The mass-spectra of chemical elements. *The London, Edinburgh, and Dublin Philosophical Magazine and Journal of Science*, *39*(233), 611–625. https://doi.org/10.1080/14786440508636074

Baldini, J. U., Lechleitner, F. A., Breitenbach, S. F., van Hunen, J., Baldini, L. M., Wynn, P. M., Jamieson, R. A., Ridley, H. E., Baker, A. J., Walczak, I. W., and Fohlmeister, J. (2021). Detecting and quantifying palaeoseasonality in stalagmites using geochemical and modelling approaches. *Quaternary Science Reviews*, *254*. https://doi.org/10.1016/j.quascirev.2020.106784

Ball, M., and Norwood, L. (1969). Studies in the system calcium sulphate–water. part i. kinetics of dehydration of calcium sulphate dihydrate. *Journal of the Chemical Society A: Inorganic, Physical, Theoretical*, 1633–1637.

Bar-Matthews, M., Ayalon, A., Gilmour, M., Matthews, A., and Hawkesworth, C. J. (2003). *Sea-land oxygen isotopic relationships from planktonic foraminifera and speleothems in the Eastern Mediterranean region and their implication for paleorainfall during interglacial intervals*.

Bar-Matthews, M., Ayalon, A., and Kaufman, A. (2000). *Timing and hydrological conditions of sapropel events in the eastern mediterranean, as evident from speleothems, soreq cave, israel*. www.elsevier.comrlocaterchemgeo

Barnes, H. (1954). Some tables for the ionic composition of sea water. *Journal of experimental biology*, *31*(4), 582–588.

Barnola, J.-M., Raynaud, D., Korotkevich, Y. S., and Lorius, C. (1987). Vostok ice core provides 160,000-year record of atmospheric CO2. *Nature*, *329*(6138), 408–414.

Ben Ameur, M., Masmoudi, S., Omar, H., Ouameni, I., Medhioub, M., and Yaich, C. (2022). Middle to late Holocene sedimentary filling history of the Sebkha el Melah in the south-eastern Tunisia. *Sedimentology*. https://doi.org/10.1111/sed.12995

Ben Dor, Y., Neugebauer, I., Enzel, Y., Schwab, M. J., Tjallingii, R., Erel, Y., and Brauer, A. (2019). Varves of the Dead Sea sedimentary record. *Quaternary Science Reviews*, *215*, 173–184. https://doi.org/10.1016/j.quascirev.2019.04.011

Benison, K. C., and Goldstein, R. H. (1999). Permian paleoclimate data from fluid inclusions in halite. *Chemical Geology*, *154*(1-4), 113–132.

Berger, A. L. (1978). Long-Term Variations of Daily Insolation and Quaternary Climatic Changes. *Journal of the Atmospheric Sciences*, *35*(12), 2362–2367. https://doi.org/10.1175/1520-0469(1978)035<2362:ltvodi>2.0.co;2

Beurlen, H., da Silva, M. R., and de Castro, C. (2001). Fluid inclusion microthermometry in Be-Ta-(Li-Sn)-bearing pegmatites from the Borborema Province, northeast Brazil. *Chemical Geology*, *173*(1-3), 107–123.

Bigi, D., Lugli, S., Manzi, V., and Roveri, M. (2022). Are fluid inclusions in gypsum reliable paleoenvironmental indicators? An assessment of the evidence from the Messinian evaporites. *Geology*.

Blättler, C. L., Claire, M. W., Prave, A. R., Kirsimäe, K., Higgins, J. A., Medvedev, P. V., Romashkin, A. E., Rychanchik, D. V., Zerkle, A. L., Paiste, K., Kreitsmann, T., Millar, I. L., Hayles, J. A., Bao, H., Turchyn, A. V., Warke, M. R., and Lepland, A. (2018). Two-billion-year-old evaporites capture Earth's great oxidation. *Science*, *360*(6386), 320–323. https://doi.org/10.1126/science.aar2687

Bodnar, R. J. (1993). Revised equation and table for determining the freezing point depression of H2O-NaCl solutions. *Geochimica et Cosmochimica acta*, *57*, 683–684.

Boon, J. P., and Yip, S. (1991). *Molecular hydrodynamics*. Courier Corporation.

Bradshaw, A., and Schleicher, K. (1980). Electrical conductivity of seawater. *IEEE Journal of Oceanic Engineering*, *5*(1), 50–62.

Brall, N. S., Gardien, V., Ariztegui, D., Sorrel, P., Guillerm, E., and Caupin, F. (2022). Reconstructing lake bottom water temperatures and their seasonal variability in the Dead Sea Basin during MIS 5e. *The Depositional Record*. https://doi.org/10.1002/dep2.185

Brauer, A., Allen, J. R. M., Mingram, J., Dulski, P., Wulf, S., and Huntley, B. (2007). *Evidence for last interglacial chronology and environmental change from Southern Europe*. www.pnas.orgcgidoi10.1073pnas.0603321104

Brauer, A., and Dulski, P. (2009). *The potential of varves in high-resolution paleolimnological studies*.

Brewer, P. G., Peltzer, E. T., Ryan, J., Kirkwood, W. J., and Hofmann, A. F. (2015). Ocean chemistry and the speed of sound in seawater. *Marine Chemistry*, *177*, 591–606.

Brewster, D. (1823). On the existence of two new fluids in the cavities of minerals which are immiscible and possess remarkable physical properties. *Transactions of the Royal Society of Edinburgh*, *10*, 94–107.

Brocas, W. M., Felis, T., Gierz, P., Lohmann, G., Werner, M., Obert, J. C., Scholz, D., Kölling, M., and Scheffers, S. R. (2018). Last Interglacial Hydroclimate Seasonality Reconstructed From Tropical Atlantic Corals. *Paleoceanography and Paleoclimatology*, *33*, 198–213. https://doi.org/10.1002/2017PA003216

Buckland, W. (1824). *Reliquiae diluvianae; or, observations on the organic remains contained in caves, fissures and diluvial gravel, and on other geological phenomena, attesting the action of an universal deluge*. John Murray; Albemarle-Street.

Burke, E. A. (2001). Raman microspectrometry of fluid inclusions. *Lithos*, *55*(1-4), 139–158.

Callendar, G. S. (1938). The artificial production of carbon dioxide and its influence on temperature. *Quarterly Journal of the Royal Meteorological Society*, *64*(275), 223–240.

Candy, I., and Schreve, D. (2007). Land-sea correlation of Middle Pleistocene temperate sub-stages using high-precision uranium-series dating of tufa deposits from southern England. *Quaternary Science Reviews*, *26*(9-10), 1223–1235. https://doi.org/10.1016/j.quascirev.2007.01.012

Chen, C.-T., Chen, L.-S., and Millero, F. J. (1978). Speed of sound in NaCl, MgCl2, Na2SO4, and MgSO4 aqueous solutions as functions of concentration, temperature, and pressure. *The Journal of the Acoustical Society of America*, *63*(6), 1795–1800. https://doi.org/10.1121/1.381917

Chen, C.-T., and Millero, F. J. (1977). Speed of sound in seawater at high pressures. *The Journal of the Acoustical Society of America*, *62*(5), 1129–1135.

Chen, C., and Litt, T. (2018). Dead Sea pollen provides new insights into the paleoenvironment of the southern Levant during MIS 6–5. *Quaternary Science Reviews*, *188*, 15–27. https://doi.org/10.1016/j.quascirev.2018.03.029

Chen, C.-T., and Millero, F. J. (1986). Thermodynamic properties for natural waters covering only the limnological range 1. *Limnology and Oceanography*, *31*(3), 657–662.

Chu, G., Liu, J., Schettler, G., Li, J., Sun, Q., Gu, Z., Lu, H., Liu, Q., and Liu, T. (2005). Sediment fluxes and varve formation in Sihailongwan, a maar lake from northeastern China. *Journal of Paleolimnology*, *34*, 311–324. https://doi.org/10.1007/s10933-005-4694-0

Clemens, S. C., and Prell, W. L. (2003). A 350,000 year summer-monsoon multi-proxy stack from the Owen Ridge, Northern Arabian Sea. *Marine Geology*, *201*, 35–51. https://doi.org/10.1016/S0025-3227(03)00207-X

Costanzo, A., Cipriani, M., Feely, M., Cianflone, G., and Dominici, R. (2019). Messinian twinned selenite from the Catanzaro Trough, Calabria, Southern Italy: field, petrographic and fluid inclusion perspectives. *Carbonates and Evaporites*, *34*(3), 743–756. https://doi.org/10.1007/s13146-019-00516-0

Cox, A., Doell, R., and Dalrymple, G. (1964). Reversals of the Earth's Magnetic Field. *Science*, *144*(3626), 1537–1543. https://doi.org/10.1126/science.144.3626.1537

Cox, R., Culkin, F., and Riley, J. (1967). The electrical conductivity/chlorinity relationship in natural sea water. *Deep Sea Research and Oceanographic Abstracts*, *14*(2), 203–220.

Culkin, F., and Smed, J. (1979). History of standard seawater. *Oceanologica Acta*, *2*(3), 355–364.

Dauphinee, T., Ancsin, J., Klein, H., and Phillips, M. (1980). The electrical conductivity of weight diluted and concentrated standard seawater as a function of salinity and temperature. *IEEE Journal of Oceanic Engineering*, *5*(1), 28–41.

Davaud, E. J., Jedoui, Y., and Strasser, A. (1996). Holocene peritidal and evaporitic sedimentation in Southern Tunisia. *17th Regional African European Meeting of Sedimentology: field trips guide book*, 1–13.

De Korte, A., and Brouwers, H. (2010). Calculation of thermal conductivity of gypsum plasterboards at ambient and elevated temperature. *Fire and Materials: An International Journal*, *34*(2), 55–75.

De La Vega, E., Chalk, T. B., Wilson, P. A., Bysani, R. P., and Foster, G. L. (2020). Atmospheric CO2 during the Mid-Piacenzian Warm Period and the M2 glaciation. *Scientific reports*, *10*(1), 1–8.

Debure, M., Lassin, A., Marty, N. C., Claret, F., Virgone, A., Calassou, S., and Gaucher, E. C. (2019). Thermodynamic evidence of giant salt deposit formation by serpentinization: An alternative mechanism to solar evaporation. *Scientific reports*, *9*(1), 1–11.

Decima, A., and Wezel, F. (1971). Osservazioni sulle evaporiti messiniane della Sicilia centro-meridionale. *Rivista Mineraria Siciliana*, *130–134*, 172–187.

Del Grosso, V., and Mader, C. (1972). Speed of sound in pure water. *the Journal of the Acoustical Society of America*, *52*(5B), 1442–1446.

Denton, G. H., Alley, R. B., Comer, G. C., and Broecker, W. S. (2005). The role of seasonality in abrupt climate change. *Quaternary Science Reviews*, *24*, 1159–1182. https://doi.org/10.1016/j.quascirev.2004.12.002

Desprat, S., Goñi, M. F. S., Turon, J.-L., Duprat, J., Malaizé, B., and Peypouquet, J.-P. (2006). Climatic variability of Marine Isotope Stage 7: direct land–sea–ice correlation from a multiproxy analysis of a north-western Iberian margin deep-sea core. *Quaternary Science Reviews*, *25*(9-10), 1010–1026. https://doi.org/10.1016/j.quascirev.2006.01.001

Devkota, K. P., Devkota, M., Rezaei, M., and Oosterbaan, R. (2022). Managing salinity for sustainable agricultural production in salt-affected soils of irrigated drylands. *Agricultural Systems*, *198*, 103390.

Dittmar, W. et al. (1884). Report on researches into the composition of ocean-water collected by HMS Challenger during the years 1873-76. *Physics and Chemistry*, *1*, 1–251.

Dolomieu, D. G. (1792). Sur de l'huile de pétrole dans le cristal de roche and les fluides élastiques tirés du quartz (Lettre à Monsieur Delamétherie). *Journal de Physique*, *40*, 318–319.

Drebushchak, V., Drebushchak, T., Ogienko, A., and Yunoshev, A. (2019). Crystallization of sodium chloride dihydrate (hydrohalite). *Journal of Crystal Growth*, *517*, 17–23. https://doi.org/10.1016/j.jcrysgro.2019.04.009

Eiler, J. M. (2007). "Clumped-isotope" geochemistry—The study of naturally-occurring, multiply-substituted isotopologues. *Earth and Planetary Science Letters*, *262*(3-4), 309–327. https://doi.org/10.1016/j.epsl.2007.08.020

Eiler, J. M. (2011). Paleoclimate reconstruction using carbonate clumped isotope thermometry. *Quaternary Science Reviews*, *30*(25-26), 3575–3588. https://doi.org/10.1016/j.quascirev.2011.09.001

Emiliani, C. (1955). Pleistocene Temperatures. *The Journal of Geology*, *63*(6), 538–578. https://doi.org/10.1086/626295

Emiliani, C. (1970). Pleistocene Paleotemperatures. *Science*, *168*(3933), 822–825. https://doi.org/10.1126/science.168.3933.822

Emiliani, C., and Edwards, G. (1953). Tertiary Ocean Bottom Temperatures. *Nature*, *171*(4359), 887–888. https://doi.org/10.1038/171887c0

Emiliani, C. (1961). Cenozoic climatic changes as indicated by the stratigraphy and chronology of deep sea cores of Globigerina ooze facies. *Annals of the New York Academy of Sciences*, *95*(1), 521–536. https://doi.org/10.1111/j.1749-6632.1961.tb50057.x

Epstein, S., Buchsbaum, R., Lowenstam, H., and Urey, H. C. (1951). Carbonate-water isotopic temperature scale. *Geological Society of America Bulletin*, *62*(4), 417. https://doi.org/10.1130/0016-7606(1951)62[417:cits]2.0.co;2

Epstein, S., Buchsbaum, R., Lowenstam, H. A., and Urey, H. C. (1953). Revised carbonate-water isotopic temperature scale. *Geological Society of America Bulletin*, *64*(11), 1315. https://doi.org/10.1130/0016-7606(1953)64[1315:rcits]2.0.co;2

Fall, A., and Bodnar, R. J. (2018). How Precisely Can the Temperature of a Fluid Event be Constrained Using Fluid Inclusions? *Economic Geology*, *113*(8), 1817–1843. https://doi.org/10.5382/econgeo.2018.4614

Felis, T., Lohmann, G., Kuhnert, H., Lorenz, S. J., Scholz, D., Pätzold, J., Al-Rousan, S. A., and Al-Moghrabi, S. M. (2004). Increased seasonality in Middle

East temperatures during the last interglacial period. *Nature*, *429*, 164–168. https://doi.org/10.1038/nature02493

Flint, R. F. (1968). The Idea of an Ice Age: Studies on Glaciers. Preceded by the Discourse of Neuchâtel. Louis Agassiz. Translated from the French and edited by Albert V. Carozzi. Hafner, New York, 1967. lxxii 213 pp., illus. 27.50. *Science*, *159*(3814), 520–520. https://doi.org/10.1126/science.159.3814.520.a

Fofonoff, N. (1985). Physical properties of seawater: A new salinity scale and equation of state for seawater. *Journal of Geophysical Research: Oceans*, *90*(C2), 3332–3342.

Fontes, J. C., and Perthuisot, J. (1973). Climatic recorder for past 50,000 yr in Tunisia. *Nature-Physical Science*, *244*(135), 74–75.

Forch, C., Knudsen, M., and Sørensen, S. (1902). Berichte uber die Konstantenbestimmungen zur Aufstellung der Hydrographischen Tabellen. *Kongekie Danske Videnskabernes Selskabs Skrifter, 61 Raekke naturvidensk. og mathem*, *1*, 1–151.

Forchhammer, G. (1865). Iv. on the composition of sea-water in the different parts of the ocean. *Philosophical Transactions of the Royal Society of London*, (155), 203–262.

Francus, P., von Suchodoletz, H., Dietze, M., Donner, R. V., Bouchard, F., Roy, A. J., Fagot, M., Verschuren, D., and Kröpelin, S. (2013). Varved sediments of Lake Yoa (Ounianga Kebir, Chad) reveal progressive drying of the Sahara during the last 6100 years. *Sedimentology*, *60*, 911–934. https://doi.org/10.1111/j.1365-3091.2012.01370.x

Friedrich, J., and Oberhänsli, H. (2004). Hydrochemical properties of the Aral Sea water in summer 2002. *Journal of Marine Systems*, *47*(1-4), 77–88.

Frumkin, A., Magaritz, M., Carmi, I., and Zak, I. (1991). The Holocene climatic record of the salt caves of Mount Sedom Israel. *The Holocene*, *1*(3), 191–200.

Gertman, I., and Hecht, A. (2002). *The Dead Sea hydrography from 1992 to 2000.* www.elsevier.com/locate/jmarsys

Gertman, I., Kress, N., Katsenelson, B., Zavialov, P., and Shirshov, P. P. (2010). *Final Report. Equations of state for the Dead Sea and Aral Sea: Searching for common approaches.*

Ghazleh, S. A., and Kempe, S. (2021). Discovery of high-level terraces of Last Glacial Lake Lisan (Dead Sea) and Eastern Mediterranean paleoclimatic implications. *Quaternary International*, *604*, 38–50.

Giauque, W. F., and Johnston, H. L. (1929a). An isotope of oxygen, mass 17, in the Earth atmosphere. *Journal of the American Chemical Society*, *51*(12), 3528–3534. https://doi.org/10.1021/ja01387a004

Giauque, W. F., and Johnston, H. L. (1929b). An Isotope of Oxygen, Mass 18. *Nature*, *123*(3096), 318–318. https://doi.org/10.1038/123318c0

Godwin, H. (1962). Half-life of Radiocarbon. *Nature*, *195*(4845), 984–984. https://doi.org/10.1038/195984a0

Goldstein, R. H. (2001). Fluid inclusions in sedimentary and diagenetic systems. *Lithos*, *55*(1-4), 159–193.

Goldstein, R. H., and Reynolds, T. J. (1994). Systematics of fluid inclusions in diagenetic minerals.

Goldstein, S. L., Kiro, Y., Torfstein, A., Kitagawa, H., Tierney, J., and Stein, M. (2020). Revised chronology of the ICDP Dead Sea deep drill core relates drier-wetter-drier climate cycles to insolation over the past 220 kyr. *Quaternary Science Reviews*, *244*. https://doi.org/10.1016/j.quascirev.2020.106460

Gornitz, V., Lebedeff, S., and Hansen, J. (1982). Global sea level trend in the past century. *Science*, *215*(4540), 1611–1614.

Griffiths, M. L., Drysdale, R. N., Vonhof, H. B., Gagan, M. K., Zhao, J.-x., Ayliffe, L. K., Hantoro, W. S., Hellstrom, J. C., Cartwright, I., Frisia, S., et al. (2010). Younger Dryas–Holocene temperature and rainfall history of southern Indonesia from δ18O in speleothem calcite and fluid inclusions. *Earth and Planetary Science Letters*, *295*(1-2), 30–36.

Grimmer, J. O., Pironon, J., Teinturier, S., and Mutterer, J. (2003). Recognition and differentiation of gas condensates and other oil types using microthermometry of petroleum inclusions. *Journal of Geochemical Exploration*, *78*, 367–371.

Guillerm, E. (2019). *Turning halite fluid inclusions into accurate paleothermometers with Brillouin spectroscopy: development of a new method and application to the Last Interglacial in the Dead Sea.*

Guillerm, E., Gardien, V., Ariztegui, D., and Caupin, F. (2020). Restoring Halite Fluid Inclusions as an Accurate Palaeothermometer: Brillouin Thermometry Versus Microthermometry. *Geostandards and Geoanalytical Research*, *44*, 243–264. https://doi.org/10.1111/ggr.12312

Hansen, J., Johnson, D., Lacis, A., Lebedeff, S., Lee, P., Rind, D., and Russell, G. (1981). Climate impact of increasing atmospheric carbon dioxide. *Science*, *213*(4511), 957–966.

Hardie, L. A. (1991). On the significance of evaporites. *Annual Review of Earth and Planetary Sciences*, *19*(1), 131–168. https://doi.org/10.1146/annurev.ea.19.050191.001023

Hardie, L. A., and Lowenstein, T. K. (2004). Did the Mediterranean Sea dry out during the Miocene? A reassessment of the evaporite evidence from DSDP Legs 13 and 42A cores. *Journal of Sedimentary Research*, *74*(4), 453–461.

Haynes, W. M., Lide, D. R., and Bruno, T. J. (2017). *Crc handbook of chemistry and physics. 97th edition*. Boca Raton, Florida: CRC Press/Taylor and Francis.

Hays, J. D., Imbrie, J., and Shackleton, N. J. (1976). Variations in the Earth's Orbit: Pacemaker of the Ice Ages. *Science*, *194*(4270), 1121–1132. https://doi.org/10.1126/science.194.4270.1121

Hays, J. D., and Opdyke, N. D. (1967). Antarctic Radiolaria, Magnetic Reversals, and Climatic Change. *Science*, *158*(3804), 1001–1011. https://doi.org/10.1126/science.158.3804.1001

He, K., Nie, A., Yuan, Y., Ghodsi, S. M., Song, B., Firlar, E., Lu, J., Lu, Y.-p., Shokuhfar, T., Megaridis, C. M., et al. (2018). In situ transmission electron microscopy explores a new nanoscale pathway for direct gypsum formation in aqueous solution. *ACS Applied Nano Materials*, *1*(10), 5430–5440.

Herdendorf, C. E. (1990). Distribution of the world's large lakes. *Large lakes* (pp. 3–38). Springer.

Hershkovitz, I., Weber, G. W., Quam, R., Duval, M., Grün, R., Kinsley, L., Ayalon, A., Bar-Matthews, M., Valladas, H., Mercier, N., Arsuaga, J. L., Martinón-Torres, M., de Castro, J. M. B., Fornai, C., Martín-Francés, L., Sarig, R., May, H., Krenn, V. A., Slon, V., ... Weinstein-Evron, M. (2018). The earliest modern humans outside Africa. *Science*, *359*(6374), 456–459. https://doi.org/10.1126/science.aap8369

Hilgen, F., Krijgsman, W., Langereis, C., Lourens, L., Santarelli, A., and Zachariasse, W. (1995). Extending the astronomical (polarity) time scale into the Miocene. *Earth and Planetary Science Letters*, *136*(3-4), 495–510.

Hilgen, F., Lourens, L., Berger, A., and Loutre, M.-F. (1993). Evaluation of the astronomically calibrated time scale for the late Pliocene and earliest Pleistocene. *Paleoceanography*, *8*(5), 549–565.

Hillesheim, M. B., Hodell, D. A., Leyden, B. W., Brenner, M., Curtis, J. H., Anselmetti, F. S., Ariztegui, D., Buck, D. G., Guilderson, T. P., Rosenmeier, M. F., and Schnurrenberger, D. W. (2005). Climate change in lowland Central America during the late deglacial and early Holocene. *Journal of Quaternary Science*, *20*(4), 363–376. https://doi.org/10.1002/jqs.924

Hodell, D., Anselmetti, F., Brenner, M., Ariztegui, D., and Party, P. S. (2006). The Lake Petén Itzá Scientifi c Drilling Project. *Scientific Drilling*, *3*, 25–29. https://doi.org/10.5194/sd-3-25-2006

Hodell, D. A., Anselmetti, F. S., Ariztegui, D., Brenner, M., Curtis, J. H., Gilli, A., Grzesik, D. A., Guilderson, T. J., Müller, A. D., and Bush, M. B. (2008). An 85-ka record of climate change in lowland Central America. *Quaternary Science*

Reviews, *27*(11-12), 1152–1165. https://doi.org/10.1016/j.quascirev.2008.02.008

Holser, W. T. (1979). Mineralogy of evaporites. *Marine Minerals* (pp. 211–294). De Gruyter. https://doi.org/10.1515/9781501508646-012

Hsu, K., Cita, M., and Ryan, W. (1973). The origin of the Mediterranean evaporites: Initial Reports of Deep Sea Drilling Project, v. 13.

Huguet, C., Kim, J. H., Damsté, J. S., and Schouten, S. (2006). Reconstruction of sea surface temperature variations in the Arabian Sea over the last 23 kyr using organic proxies (TEX86 and U 37K′). *Paleoceanography*, *21*(3). https://doi.org/10.1029/2005PA001215

Hutton, J. (1795). Theory of the Earth.

Hutton, J. (1788). Theory of the Earth, or an Investigation of the Laws observable in the Composition, Dissolution, and Restoration of Land upon the Globe. *Transactions of the Royal Society of Edinburgh*, *1*(2), 209–304. https://doi.org/10.1017/s0080456800029227

Intergovernmental Oceanographic Commission. (2010). *The Practical Salinity Scale 1978 and the International Equation of State of Seawater 1980.* https://unesdoc.unesco.org/ark:/48223/pf0000188170

International Labour Organization. (n.d.). International Chemical Safety Cards ICSC [Accessed: 2022-01-15]. http://www.ilo.org/dyn/icsc/showcard.home

IOC. (2010). The Practical Salinity Scale 1978 and the International Equation of State of Seawater 1980. *Unesco Technical Papers in Marine Science 36*, 196. https://unesdoc.unesco.org/ark:/48223/pf0000188170

IPCC. (2022). *Climate Change 2022: Impacts, Adaptation, and Vulnerability. Contribution of Working Group II to the Sixth Assessment Report of the Intergovernmental Panel on Climate Change* (H.-O. Pörtner and D.C. Roberts and M. Tignor and E.S. Poloczanska and K. Mintenbeck and A. Alegría and M. Craig and S. Langsdorf, S. Löschke and V. Möller and A. Okem and B. Rama, Ed.) [In Press.]. Cambridge University Press.

Jacobsen, J., and Knudsen, M. (1940). Urnormal 1937 or primary standard sea water 1937. publ. sci. *Ass. Océanogr. phy*, (7).

Jones, P. D., and Mann, M. E. (2004). Climate over past millennia. *Reviews of Geophysics*, *42*(2).

Jouzel, J., Waelbroeck, C., Malaize, B., Bender, M., Petit, J. R., Stievenard, M., Barkov, N. I., Barnola, J. M., King, T., Kotlyakov, V. M., Lipenkov, V., Lorius, C., Raynaud, D., Ritz, C., and Sowers, T. (1996). Climatic interpretation of the recently extended Vostok ice records. *Climate Dynamics*, *12*(8), 513–521. https://doi.org/10.1007/bf00207935

Kah, L. C., Lyons, T. W., and Chesley, J. T. (2001). Geochemistry of a 1.2 Ga carbonate-evaporite succession, northern Baffin and Bylot Islands: implications for Mesoproterozoic marine evolution. *Precambrian Research*, *111*(1-4), 203–234. https://doi.org/10.1016/s0301-9268(01)00161-9

Kele, S., Breitenbach, S. F., Capezzuoli, E., Meckler, A. N., Ziegler, M., Millan, I. M., Kluge, T., Deák, J., Hanselmann, K., John, C. M., Yan, H., Liu, Z., and Bernasconi, S. M. (2015). Temperature dependence of oxygen- and clumped isotope fractionation in carbonates: A study of travertines and tufas in the 6–95°C temperature range. *Geochimica et Cosmochimica Acta*, *168*, 172–192. https://doi.org/10.1016/j.gca.2015.06.032

Kelson, J. R., Huntington, K. W., Breecker, D. O., Burgener, L. K., Gallagher, T. M., Hoke, G. D., and Petersen, S. V. (2020). A proxy for all seasons? A synthesis of clumped isotope data from Holocene soil carbonates. *Quaternary Science Reviews*, *234*, 106259. https://doi.org/10.1016/j.quascirev.2020.106259

Kimura, H., and Kai, J. (1984). Phase change stability of CaCl2x6H2O. *Solar Energy*, *33*(6), 557–563. https://doi.org/10.1016/0038-092x(84)90011-2

Kiro, Y., Goldstein, S. L., Garcia-Veigas, J., Levy, E., Kushnir, Y., Stein, M., and Lazar, B. (2017). Relationships between lake-level changes and water and salt budgets in the Dead Sea during extreme aridities in the Eastern Mediterranean. *Earth and Planetary Science Letters*, *464*, 211–226. https://doi.org/10.1016/j.epsl.2017.01.043

Kiro, Y., Goldstein, S. L., Lazar, B., and Stein, M. (2016). Environmental implications of salt facies in the Dead Sea. *Geological Society of America Bulletin*, *128*, 824–841. https://doi.org/10.1130/b31357.1

Kishcha, P., Starobinets, B., Lechinsky, Y., and Alpert, P. (2021). Absence of Surface Water Temperature Trends in Lake Kinneret despite Present Atmospheric Warming: Comparisons with Dead Sea Trends. *Remote Sensing*, *13*(17), 3461. https://doi.org/10.3390/rs13173461

Kleis, S., and Sanchez, L. (1990). Dependence of speed of sound on salinity and temperature in concentrated nacl solutions. *Solar Energy*, *45*(4), 201–206.

Kleis, S., and Sanchez, L. (1991). Dependence of sound velocity on salinity and temperature in saline solutions. *Solar Energy*, *46*(6), 371–375. https://doi.org/10.1016/0038-092x(91)90052-x

Knudsen, M. (1901). *Hydrographische Tabellen*. G.E.C. Gad.

Knudsen, M. (1903). On the standard-water used in the hydrographical research until July 1903. *ICES Journal of Marine Science*, *1*(2), 3–9.

Kouzmanov, K., Bailly, L., Ramboz, C., Rouer, O., and Beny, J.-M. (2002). Morphology, origin and infrared microthermometry of fluid inclusions in pyrite from

the Radka epithermal copper deposit, Srednogorie zone, Bulgaria. *Mineralium deposita*, *37*(6), 599–613.

Krijgsman, W., Hilgen, F., Raffi, I., Sierro, F., and Wilson, D. (1999). Chronology, causes and progression of the Messinian salinity crisis. *Nature*, *400*(6745), 652–655.

Kutzbach, J. E., Chen, G., Cheng, H., Edwards, R. L., and Liu, Z. (2014). Potential role of winter rainfall in explaining increased moisture in the Mediterranean and Middle East during periods of maximum orbitally-forced insolation seasonality. *Climate Dynamics*, *42*, 1079–1095. https://doi.org/10.1007/s00382-013-1692-1

Kutzbach, J. E., Guan, J., He, F., Cohen, A. S., Orland, I. J., and Chen, G. (2020). African climate response to orbital and glacial forcing in 140,000-y simulation with implications for early modern human environments. *PNAS*, *117*. https://doi.org/10.1073/pnas.1917673117/-/DCSupplemental

Kwiecien, O., Braun, T., Brunello, C. F., Faulkner, P., Hausmann, N., Helle, G., Hoggarth, J. A., Ionita, M., Jazwa, C. S., Kelmelis, S., Marwan, N., Nava-Fernandez, C., Nehme, C., Opel, T., Oster, J. L., Perşoiu, A., Petrie, C., Prufer, K., Saarni, S. M., ... Breitenbach, S. F. (2022). What we talk about when we talk about seasonality – A transdisciplinary review. *Earth-Science Reviews*, *225*, 103843. https://doi.org/10.1016/j.earscirev.2021.103843

Labuhn, I., Tell, F., Grafenstein, U. V., Hammarlund, D., Kuhnert, H., and Minster, B. (2021). A modern snapshot of the isotopic composition of lacustrine biogenic carbonates: Records of seasonal water temperature variability. https://doi.org/10.5194/egusphere-egu21-13178

Lazar, B., Sivan, O., Yechieli, Y., Levy, E., Antler, G., Gavrieli, I., and Stein, M. (2014). Long-term freshening of the Dead Sea brine revealed by porewater Cl- and $\delta^{1}8O$ in ICDP Dead Sea deep-drill. *Earth and Planetary Science Letters*, *400*, 94–101.

Lelieveld, J., Hadjinicolaou, P., Kostopoulou, E., Chenoweth, J., Maayar, M. E., Giannakopoulos, C., Hannides, C., Lange, M. A., Tanarhte, M., Tyrlis, E., and Xoplaki, E. (2012). Climate change and impacts in the Eastern Mediterranean and the Middle East. *Climatic Change*, *114*(3-4), 667–687. https://doi.org/10.1007/s10584-012-0418-4

Lelieveld, J., Proestos, Y., Hadjinicolaou, P., Tanarhte, M., Tyrlis, E., and Zittis, G. (2016). Strongly increasing heat extremes in the Middle East and North Africa (MENA) in the 21st century. *Climatic Change*, *137*(1-2), 245–260. https://doi.org/10.1007/s10584-016-1665-6

Létolle, R., and Chesterikoff, A. (1999). Salinity of surface waters in the Aral sea region. *International Journal of Salt Lake Research*, *8*(4), 293–306. https://doi.org/10.1007/bf02442116

Libby, W. F., Anderson, E. C., and Arnold, J. R. (1949). Age Determination by Radiocarbon Content: World-Wide Assay of Natural Radiocarbon. *Science*, *109*(2827), 227–228. https://doi.org/10.1126/science.109.2827.227

Lindsay, J. F. (1987). Upper Proterozoic evaporites in the Amadeus basin, central Australia, and their role in basin tectonics. *Geological Society of America Bulletin*, *99*(6), 852. https://doi.org/10.1130/0016-7606(1987)99<852:upeita>2.0.co;2

Lisiecki, L. E., and Raymo, M. E. (2005). A pliocene-pleistocene stack of 57 globally distributed benthic 18o records. *Paleoceanography*, *20*(1). https://doi.org/10.1029/2004pa001071

Liu, J., and An, Z. (2020). Leaf wax n-alkane carbon isotope values vary among major terrestrial plant groups: Different responses to precipitation amount and temperature, and implications for paleoenvironmental reconstruction. *Earth-Science Reviews*, *202*. https://doi.org/10.1016/j.earscirev.2020.103081

Lowenstein, T. K., Li, J., Brown, C., Roberts, S. M., Ku, T.-L., Luo, S., and Yang, W. (1999). 200 ky paleoclimate record from Death Valley salt core. *Geology*, *27*(1), 3–6.

Lowenstein, T. K., Weldeghebriel, M. F., Sirota, I., Eyal, H., Mor, Z., and Lensky, N. G. (2021). Criteria for the recognition of clastic halite: The modern Dead Sea shoreline. *Sedimentology*, *68*(6), 2253–2269.

Lyell, C. (1837). *Principles of Geology: Being an Inquiry how Far the Former Changes of the Earth's Surface are Referable to Causes Now in Operation*. J. Kay, jun. and brother. https://books.google.de/books?id=4BlDAAAAIAAJ

Lyell, C., and Deshayes, G. P. (1830). *Principles of geology: Being an attempt to explain the former changes of the earth's surface, by reference to causes now in operation* (Vol. 1). J. Murray.

Malaizé, B., Paillard, D., Jouzel, J., and Raynaud, D. (1999). The Dole effect over the last two glacial-interglacial cycles. *Journal of Geophysical Research: Atmospheres*, *104*(D12), 14199–14208. https://doi.org/10.1029/1999jd900116

Manzi, V., Gennari, R., Hilgen, F., Krijgsman, W., Lugli, S., Roveri, M., and Sierro, F. J. (2013). Age refinement of the Messinian salinity crisis onset in the Mediterranean. *Terra Nova*, *25*(4), 315–322.

Manzi, V., Gennari, R., Lugli, S., Roveri, M., Scafetta, N., and Schreiber, B. C. (2012). High-frequency cyclicity in the Mediterranean Messinian evaporites:

evidence for solar–lunar climate forcing. *Journal of Sedimentary Research*, *82*(12), 991–1005.

Martinson, D. G., Pisias, N. G., Hays, J. D., Imbrie, J., Moore, T. C., and Shackleton, N. J. (1987). Age Dating and the Orbital Theory of the Ice Ages: Development of a High-Resolution 0 to 300, 000-Year Chronostratigraphy. *Quaternary Research*, *27*(1), 1–29. https://doi.org/10.1016/0033-5894(87)90046-9

Martrat, B., Grimalt, J. O., Lopez-Martinez, C., Cacho, I., Sierro, F. J., Flores, J. A., Zahn, R., Canals, M., Curtis, J. H., and Hodell, D. A. (2004). Abrupt temperature changes in the Western Mediterranean over the past 250,000 years. *Science*, *306*, 1762–1765. https://doi.org/10.1126/science.1101706

Matthews, A., Affek, H., Ayalon, A., Vonhof, H., and Bar-Matthews, M. (2021). Eastern Mediterranean climate change deduced from the Soreq Cave fluid inclusion stable isotopes and carbonate clumped isotopes record of the last 160 ka. *Quaternary Science Reviews*, *272*, 107223. https://doi.org/10.1016/j.quascirev.2021.107223

McCrea, J. M. (1950). On the Isotopic Chemistry of Carbonates and a Paleotemperature Scale. *The Journal of Chemical Physics*, *18*(6), 849–857. https://doi.org/10.1063/1.1747785

Mekki-Azouzi, M. E., Tripathi, C. S. P., Pallares, G., Gardien, V., and Caupin, F. (2015). Brillouin spectroscopy of fluid inclusions proposed as a paleothermometer for subsurface rocks. *Scientific Reports*, *5*. https://doi.org/10.1038/srep13168

Milankovitch, M. (1930). Mathematische Klimalehre und astronomische Theorie der Klimaschwankungen. In W. Köppen and R. Geiger (Eds.), *Handbuch der Klimatologie. Band 1: Allgemeine Klimalehre.* Borntraeger, Berlin 1930.

Millero, F. J., Feistel, R., Wright, D. G., and McDougall, T. J. (2008). The composition of Standard Seawater and the definition of the Reference-Composition Salinity Scale. *Deep Sea Research Part I: Oceanographic Research Papers*, *55*(1), 50–72.

Milner, A. M., Collier, R. E., Roucoux, K. H., Müller, U. C., Pross, J., Kalaitzidis, S., Christanis, K., and Tzedakis, P. C. (2012). Enhanced seasonality of precipitation in the Mediterranean during the early part of the Last Interglacial. *Geology*, *40*, 919–922. https://doi.org/10.1130/G33204.1

Mitchell, M. W., Lundeen, J. S., and Steinberg, A. M. (2004). Super-resolving phase measurements with a multiphoton entangled state. *Nature*, *429*, 161–164. https://doi.org/10.1038/nature02493

Natalicchio, M., Dela Pierre, F., Lugli, S., Lowenstein, T. K., Feiner, S. J., Ferrando, S., Manzi, V., Roveri, M., and Clari, P. (2014). Did Late Miocene (Messinian) gypsum precipitate from evaporated marine brines? Insights from the Piedmont Basin (Italy). *Geology*, *42*(3), 179–182.

Natalicchio, M., Pellegrino, L., Clari, P., Pastero, L., and Pierre, F. D. (2021). Gypsum lithofacies and stratigraphic architecture of a Messinian marginal basin (Piedmont Basin, NW Italy). *Sedimentary Geology*, *425*, 106009.

Neev, D., and Emery, K. O. (1967). The Dead Sea: depositional processes and environments of evaporites. *Geol. Surv. Israel Bull.*, *41*, p. 167.

Nelson, K. H., and Thompson, T. G. (1954). Concentration of brines and deposition of salts from sea water under frigid conditions. *American Journal of Science*, *254*, 227–238.

Neugebauer, I., Brauer, A., Schwab, M. J., Waldmann, N. D., Enzel, Y., Kitagawa, H., Torfstein, A., Frank, U., Dulski, P., Agnon, A., Ariztegui, D., Ben-Avraham, Z., Goldstein, S. L., and Stein, M. (2014). Lithology of the long sediment record recovered by the ICDP Dead Sea Deep Drilling Project (DSDDP). *Quaternary Science Reviews*, *102*, 149–165. https://doi.org/10.1016/j.quascirev.2014.08.013

Norton, C. F., and Grant, W. D. (1988). Survival of halobacteria within fluid inclusions in salt crystals. *Microbiology*, *134*(5), 1365–1373.

Oberhänsli, H., Novotná, K., Píšková, A., Chabrillat, S., Nourgaliev, D. K., Kurbaniyazov, A. K., and Grygar, T. M. (2011). Variability in precipitation, temperature and river runoff in W Central Asia during the past ~2000yrs. *Global and Planetary Change*, *76*(1-2), 95–104. https://doi.org/10.1016/j.gloplacha.2010.12.008

Ojala, A. E., Kosonen, E., Weckström, J., Korkonen, S., and Korhola, A. (2013). Seasonal formation of clastic-biogenic varves: The potential for palaeoenvironmental interpretations. *GFF*, *135*, 237–247. https://doi.org/10.1080/11035897.2013.801925

Orland, I. J., Burstyn, Y., Bar-Matthews, M., Kozdon, R., Ayalon, A., Matthews, A., and Valley, J. W. (2014). Seasonal climate signals (1990–2008) in a modern Soreq Cave stalagmite as revealed by high-resolution geochemical analysis. *Chemical Geology*, *363*, 322–333. https://doi.org/10.1016/j.chemgeo.2013.11.011

Palchan, D., Neugebauer, I., Amitai, Y., Waldmann, N. D., Schwab, M. J., Dulski, P., Brauer, A., Stein, M., Y., E., and Enzel, Y. (2017). North Atlantic controlled depositional cycles in MIS 5e layered sediments from the deep Dead Sea basin. *Quaternary Research*, *87*, 168–179.

Pallares, G., Azouzi, M. E. M., González, M. A., Aragones, J. L., Abascal, J. L., Valeriani, C., and Caupin, F. (2014). Anomalies in bulk supercooled water at negative pressure. *Proceedings of the National Academy of Sciences*, *111*(22), 7936–7941.

Penaud, A., Eynaud, F., Turon, J., Zaragosi, S., Marret, F., and Bourillet, J. (2008). Interglacial variability (MIS 5 and MIS 7) and dinoflagellate cyst assemblages in the Bay of Biscay (North Atlantic). *Marine Micropaleontology*, *68*(1-2), 136–155. https://doi.org/10.1016/j.marmicro.2008.01.007

Perthuisot, J.-P. (1975). *La Sebkha el Melah de Zarzis: genèse et évolution d'un bassin salin paralique [Tunisie]: annexe: les gisement néolithiques des abords de la Sebkha el Melah*. Laboratoire de géologie de l'Ecole normale supérieure.

Perthuisot, J.-P., Castanier, S., and Maurin, A. (1990). La huntite (CaMg 3 (CO 3) 4) de la Sebkha el Melah (Zarzis, Tunisie); un exemple de microbiodiagenese carbonatogene. *Bulletin de la Société géologique de France*, *6*(4), 657–666.

Petit, J. R., Jouzel, J., Raynaud, D., Barkov, N. I., Barnola, J.-M., Basile, I., Bender, M., Chappellaz, J., Davis, M., Delaygue, G., Delmotte, M., Kotlyakov, V. M., Legrand, M., Lipenkov, V. Y., Lorius, C., Pépin, L., Ritz, C., Saltzman, E., and Stievenard, M. (1999). Climate and atmospheric history of the past 420,000 years from the Vostok ice core, Antarctica. *Nature*, *399*(6735), 429–436. https://doi.org/10.1038/20859

Pinho, S. P., and Macedo, E. A. (1996). Representation of salt solubility in mixed solvents: A comparison of thermodynamic models. *Fluid Phase Equilibria*, *116*(1-2), 209–216.

Poisson, A. (1980). Conductivity/salinity/temperature relationship of diluted and concentrated standard seawater. *IEEE Journal of Oceanic Engineering*, *5*(1), 41–50.

Posnjak, E. (1938). The system caso4-h20. *Am. J. Sci.*, *35A*, 247–272.

Riechelmann, D. F., Riechelmann, S., Wassenburg, J. A., Fohlmeister, J., Schöne, B. R., Jochum, K. P., Richter, D. K., and Scholz, D. (2020). High-Resolution Proxy Records From Two Simultaneously Grown Stalagmites From Zoolithen-cave (Southeastern Germany) and their Potential for Palaeoclimate Reconstruction. *Geochemistry, Geophysics, Geosystems*, *21*. https://doi.org/10.1029/2019GC008755

Rigaudier, T., Gardien, V., Martineau, F., Reverdy, G., and Lécuyer, C. (2012). Hydrogen and Oxygen Isotope Reference Materials for the Analysis of Water Inclusions in Halite. *Geostandards and Geoanalytical Research*, *36*(1), 51–59. https://doi.org/10.1111/j.1751-908x.2011.00139.x

Rigaudier, T., Lécuyer, C., Gardien, V., Suc, J.-P., and Martineau, F. (2011). The record of temperature, wind velocity and air humidity in the δD and δ18O of water inclusions in synthetic and Messinian halites. *Geochimica et Cosmochimica Acta*, *75*(16), 4637–4652. https://doi.org/10.1016/j.gca.2011.05.034

Roedder, E. (1963). Studies of fluid inclusions;[Part] 2, Freezing data and their interpretation. *Economic geology*, *58*(2), 167–211.

Roedder, E. (1972). *Composition of Fluid Inclusions: Reviews of World Literature*. US Government Printing Office.

Roedder, E. (1984). Volume 12: Fluid inclusions. *Reviews in mineralogy*, *12*.

Roedder, E., and Bodnar, R. J. (1980). Geologic Pressure Determinations from Fluid Inclusion Studies. *Annual Review of Earth and Planetary Sciences*, *8*(1), 263–301. https://doi.org/10.1146/annurev.ea.08.050180.001403

Roedder, E. (1962). Studies of fluid inclusions; Part 1, Low temperature application of a dual-purpose freezing and heating stage. *Economic Geology*, *57*(7), 1045–1061.

Roedder, E. (1967). Metastable Superheated Ice in Liquid-Water Inclusions under High Negative Pressure. *Science*, *155*(3768), 1413–1417. https://doi.org/10.1126/science.155.3768.1413

Rouchy, J. M., and Caruso, A. (2006). The Messinian salinity crisis in the Mediterranean basin: a reassessment of the data and an integrated scenario. *Sedimentary Geology*, *188*, 35–67.

Roveri, M., and Manzi, V. (2006). The Messinian salinity crisis: looking for a new paradigm? *Palaeogeography, Palaeoclimatology, Palaeoecology*, *238*(1-4), 386–398.

Roveri, M., Manzi, V., Bergamasco, A., Falcieri, F., Gennari, R., Lugli, S., and Schreiber, B. (2014). Dense shelf water cascading and Messinian canyons: a new scenario for the Mediterranean salinity crisis. *American Journal of Science*, *314*(3), 751–784.

Roveri, M., Flecker, R., Krijgsman, W., Lofi, J., Lugli, S., Manzi, V., Sierro, F. J., Bertini, A., Camerlenghi, A., De Lange, G., et al. (2014). The Messinian Salinity Crisis: past and future of a great challenge for marine sciences. *Marine Geology*, *352*, 25–58.

Roveri, M., Lugli, S., Manzi, V., and Schreiber, B. C. (2008). The Messinian Sicilian stratigraphy revisited: new insights for the Messinian salinity crisis. *Terra Nova*, *20*(6), 483–488.

Samson, I., Anderson, A., and Marshall, D. D. (2003). *Fluid inclusions: Analysis and interpretation* (Vol. 32). Mineralogical Association of Canada.

Sanahuja, J., Dormieux, L., Meille, S., Hellmich, C., and Fritsch, A. (2010). Micromechanical explanation of elasticity and strength of gypsum: From elongated anisotropic crystals to isotropic porous polycrystals. *Journal of engineering mechanics*, *136*(2), 239–253.

Schmid, T., Jungnickel, R., and Dariz, P. (2020). Insights into the CaSO4–H2O System: A Raman-Spectroscopic Study. *Minerals*, *10*(2), 115. https://doi.org/10.3390/min10020115

Schubel, K. A., and Lowenstein, T. K. (1997). Criteria for the recognition of shallow-perennial-saline-lake halites based on recent sediments from the Qaidam Basin, western China. *Journal of Sedimentary Research*, *67*(1), 74–87.

Shackleton, N. J. (1969). The last interglacial in the marine and terrestrial records. *Proceedings of the Royal Society of London. Series B. Biological Sciences*, *174*(1034), 135–154. https://doi.org/10.1098/rspb.1969.0085

Shi, J., Cook, E. R., Lu, H., Li, J., Wright, W. E., and Li, S. (2010). Tree-ring based winter temperature reconstruction for the lower reaches of the yangtze river in southeast China. *Climate Research*, *41*, 169–175. https://doi.org/10.3354/cr00851

Sirota, I., Arnon, A., and Lensky, N. G. (2016). Seasonal variations of halite saturation in the Dead Sea. *Water Resources Research*, *52*, 7151–7162.

Sirota, I., Enzel, Y., and Lensky, N. G. (2017). Temperature seasonality control on modern halite layers in the Dead Sea: In situ observations. *Bulletin*, *129*, 1181–1194.

Sirota, I., Enzel, Y., Mor, Z., Moshe, L. B., Eyal, H., Lowenstein, T. K., and Lensky, N. G. (2021). Sedimentology and stratigraphy of a modern halite sequence formed under Dead Sea level fall. *Sedimentology*, *68*, 1069–1090. https://doi.org/10.1111/sed.12814

Slon, V., Sarig, R., Hershkovitz, I., Khalaily, H., and Milevski, I. (2014). The Plastered Skulls from the Pre-Pottery Neolithic B Site of Yiftahel (Israel) – A Computed Tomography-Based Analysis (D. Frayer, Ed.). *PLoS ONE*, *9*(2), e89242. https://doi.org/10.1371/journal.pone.0089242

Smit, J., Brun, J. P., Fort, X., Cloetingh, S., and Ben-Avraham, Z. (2008). Salt tectonics in pull-apart basins with application to the Dead Sea Basin. *Tectonophysics*, *449*, 1–16. https://doi.org/10.1016/j.tecto.2007.12.004

Sofer, Z. (1978). Isotopic composition of hydration water in gypsum. *Geochimica et Cosmochimica Acta*, *42*(8), 1141–1149.

Sorby, H. C. (1858). On the Microscopical, Structure of Crystals, indicating the Origin of Minerals and Rocks. *Quarterly Journal of the Geological Society*, *14*(1-2), 453–500. https://doi.org/10.1144/gsl.jgs.1858.014.01-02.44

Sorrel, P. (2006). *The Aral Sea: a palaeoclimate archive*. University of Potsdam, Germany.

Sorrel, P., Popescu, S.-M., Head, M., Suc, J., Klotz, S., and Oberhänsli, H. (2006). Hydrographic development of the Aral Sea during the last 2000 years based on a quantitative analysis of dinoflagellate cysts. *Palaeogeography, Palaeoclimatology, Palaeoecology*, *234*(2-4), 304–327. https://doi.org/10.1016/j.palaeo.2005.10.012

Sorrel, P., Popescu, S.-M., Klotz, S., Suc, J.-P., and Oberhänsli, H. (2007). Climate variability in the Aral Sea basin (Central Asia) during the late Holocene based on vegetation changes. *Quaternary Research*, *67*(3), 357–370. https://doi.org/10.1016/j.yqres.2006.11.006

Sowers, T., Bender, M., Labeyrie, L., Martinson, D., Jouzel, J., Raynaud, D., Pichon, J. J., and Korotkevich, Y. S. (1993). A 135,000-year Vostok-Specmap Common temporal framework. *Paleoceanography*, *8*(6), 737–766. https://doi.org/10.1029/93pa02328

Spear, N., Holland, H., Garcia-Veígas, J., Lowenstein, T., Giegengack, R., and Peters, H. (2014). Analyses of fluid inclusions in Neoproterozoic marine halite provide oldest measurement of seawater chemistry. *Geology*, *42*(2), 103–106. https://doi.org/10.1130/g34913.1

Stein, M. (2003). The limnological history of late Pleistocene-Holocene water bodies in the Dead Sea basin.

Stein, M. (2014). The evolution of Neogene-Quaternary water-bodies in the Dead Sea rift valley. *Dead Sea Transform fault system: reviews* (pp. 279–316). Springer.

Stein, M. (2001). *The sedimentary and geochemical record of Neogene-Quaternary water bodies in the Dead Sea Basin-inferences for the regional paleoclimatic history*.

Stein, M., Ben-Avraham, Z., Goldstein, S., Agnon, A., Ariztegui, D., Brauer, A., Haug, G., Ito, E., and Yasuda, Y. (2011). Deep Drilling at the Dead Sea. *Scientific Drilling*. https://doi.org/10.2204/iodp.sd.11.04.2011

Stein, M., Torfstein, A., Gavrieli, I., and Yechieli, Y. (2010). Abrupt aridities and salt deposition in the post-glacial Dead Sea and their North Atlantic connection. *Quaternary Science Reviews*, *29*(3-4), 567–575.

Steinhorn, I. (1983). In situ salt precipitation at the Dead Sea. *Limnology and oceanography*, *28*, 580–583.

Steinhorn, I. (1985). The disappearance of the long term meromictic stratification of the Dead Sea. *Limnology and Oceanography*, *30*, 451–472. https://doi.org/10.4319/lo.1985.30.3.0451

Sterner, S., and Bodnar, R. (1984). Synthetic fluid inclusions in natural quartz I. Compositional types synthesized and applications to experimental geochemistry. *Geochimica et Cosmochimica Acta*, *48*(12), 2659–2668. https://doi.org/10.1016/0016-7037(84)90314-4

Thomas, C., and Ariztegui, D. (2019). Fluid inclusions from the deep Dead Sea sediment provide new insights on Holocene extreme microbial life. *Quaternary Science Reviews*, *212*, 18–27.

Thomson, J. (1912). Further experiments on positive rays. *The London, Edinburgh, and Dublin Philosophical Magazine and Journal of Science*, *24*(140), 209–253. https://doi.org/10.1080/14786440808637325

Torfstein, A. (2019). Climate cycles in the southern Levant and their global climatic connections. *Quaternary Science Reviews*, *221*. https://doi.org/10.1016/j.quascirev.2019.105881

Torfstein, A., Goldstein, S. L., Kushnir, Y., Enzel, Y., Haug, G., and Stein, M. (2015). Dead Sea drawdown and monsoonal impacts in the Levant during the last interglacial. *Earth and Planetary Science Letters*, *412*, 235–244. https://doi.org/10.1016/j.epsl.2014.12.013

Torfstein, A., Goldstein, S. L., Stein, M., and Enzel, Y. (2013). Impacts of abrupt climate changes in the Levant from Last Glacial Dead Sea levels. *Quaternary Science Reviews*, *69*, 1–7. https://doi.org/10.1016/j.quascirev.2013.02.015

Trachsel, M., Kamenik, C., Grosjean, M., McCarroll, D., Moberg, A., Brázdil, R., Büntgen, U., Dobrovolný, P., Esper, J., Frank, D. C., Friedrich, M., Glaser, R., Larocque-Tobler, I., Nicolussi, K., and Riemann, D. (2012). Multi-archive summer temperature reconstruction for the European Alps, AD 1053-1996. *Quaternary Science Reviews*, *46*, 66–79. https://doi.org/10.1016/j.quascirev.2012.04.021

Tyler, R. H., Boyer, T. P., Minami, T., Zweng, M. M., and Reagan, J. R. (2017). Electrical conductivity of the global ocean. *Earth, Planets and Space*, *69*(1), 1–10.

Tzedakis, P. C., Raynaud, D., McManus, J. F., Berger, A., Brovkin, V., and Kiefer, T. (2009). Interglacial diversity. *Nature Geoscience*, *2*, 751–755. https://doi.org/10.1038/ngeo660

Tzedakis, P. C., Roucoux, K. H., de Abreu, L., and Shackleton, N. J. (2004). The Duration of Forest Stages in Southern Europe and Interglacial Climate Variability. *Science*, *306*(5705), 2231–2235. https://doi.org/10.1126/science.1102398

Tzedakis, P., McManus, J., Hooghiemstra, H., Oppo, D., and Wijmstra, T. (2003). Comparison of changes in vegetation in northeast Greece with records of climate

variability on orbital and suborbital frequencies over the last 450 000 years. *Earth and Planetary Science Letters*, *212*(1-2), 197–212. https://doi.org/10.1016/s0012-821x(03)00233-4

Urey, H. C. (1947). The thermodynamic properties of isotopic substances. *Journal of the Chemical Society (Resumed)*, 562. https://doi.org/10.1039/jr9470000562

Urey, H. C., Lowenstam, H. A., Epstein, S., and McKinney, C. R. (1951). Measurement of paleotemperatures and temperatures of the upper Cretaceous of England, Denmark, and the Southeastern United States. *Geological Society of America Bulletin*, *62*(4), 399. https://doi.org/10.1130/0016-7606(1951)62[399:mopato]2.0.co;2

Urey, H. C. (1948). Oxygen Isotopes in Nature and in the Laboratory. *Science*, *108*(2810), 489–496. https://doi.org/10.1126/science.108.2810.489

Urey, H. C., and Teal, G. K. (1935). The Hydrogen Isotope of Atomic Weight Two. *Reviews of Modern Physics*, *7*(1), 34–94. https://doi.org/10.1103/revmodphys.7.34

Van Couvering, J. A., Castradori, D., Cita, M. B., Hilgen, F. J., and Rio, D. (2000). The base of the Zanclean Stage and of the Pliocene Series. *Episodes*, *23*(3), 179–187.

Van Driessche, A., Benning, L. G., Rodriguez-Blanco, J., Ossorio, M., Bots, P., and García-Ruiz, J. (2012). The role and implications of bassanite as a stable precursor phase to gypsum precipitation. *Science*, *336*(6077), 69–72.

Van Driessche, A., Stawski, T., and Kellermeier, M. (2019). Calcium sulfate precipitation pathways in natural and engineered environments. *Chemical Geology*, *530*, 119274.

van't Hoff, J. (1912). Untersuchungen über die bildungsverhältnisse der ozeanischen salzablagerungen.

Waldmann, N., Stein, M., Ariztegui, D., and Starinsky, A. (2009). Stratigraphy, depositional environments and level reconstruction of the last interglacial Lake Samra in the Dead Sea basin. *Quaternary Research*, *72*, 1–15. https://doi.org/10.1016/j.yqres.2009.03.005

Wang, J., Guan, Y., Wu, L., Guan, X., Cai, W., Huang, J., Dong, W., and Zhang, B. (2021). Changing Lengths of the Four Seasons by Global Warming. *Geophysical Research Letters*, *48*(6). https://doi.org/10.1029/2020gl091753

Wang, M., Zong, Y., Zheng, Z., Man, M., Hu, J., and Tian, L. (2018). Utility of brGDGTs as temperature and precipitation proxies in subtropical China. *Scientific Reports*, *8*. https://doi.org/10.1038/s41598-017-17964-0

Wang, S.-F., Hsu, Y.-F., Pu, J.-C., Sung, J. C., and Hwa, L. (2004). Determination of acoustic wave velocities and elastic properties for diamond and other hard

materials. *Materials Chemistry and Physics*, *85*(2-3), 432–437. https://doi.org/10.1016/j.matchemphys.2004.02.003

Warren, J. K. (2016). *Evaporites*. Springer International Publishing. https://doi.org/10.1007/978-3-319-13512-0

Watanabe, O., Jouzel, J., Johnsen, S., Parrenin, F., Shoji, H., and Yoshida, N. (2003). Homogeneous climate variability across East Antarctica over the past three glacial cycles. *Nature*, *422*(6931), 509–512. https://doi.org/10.1038/nature01525

Werner, M., Mikolajewicz, U., Heimann, M., and Hoffmann, G. (2000). Borehole versus isotope temperatures on Greenland: Seasonality does matter. *Geophysical Research Letters*, *27*, 723–726. https://doi.org/10.1029/1999GL006075

Wilkinson, J. (2001). Fluid inclusions in hydrothermal ore deposits. *Lithos*, *55*(1-4), 229–272.

Wirth, S. B., Gilli, A., Simonneau, A., Ariztegui, D., Vannière, B., Glur, L., Chapron, E., Magny, M., and Anselmetti, F. S. (2013). A 2000 year long seasonal record of floods in the southern European Alps. *Geophysical Research Letters*, *40*, 4025–4029. https://doi.org/10.1002/grl.50741

Wooster, W. (1936). On the Crystal Structure of Gypsum, $CaSO_4 \cdot 2\,H_2O$. *Zeitschrift für Kristallographie-crystalline materials*, *94*(1-6), 375–396.

Wooster, W., Lee, A., and Dietrich, G. (1969). Redefinition of salinity. *Z. Geophys*, *35*, 611–613.

Yang, X., Wang, N., He, J., Hua, T., Qie, Y., et al. (2020). Changes in area and water volume of the Aral Sea in the arid Central Asia over the period of 1960–2018 and their causes. *Catena*, *191*, 104566.

Yechieli, Y., Gavrieli, I., Berkowitz, B., and Ronen, D. (1998). Will the Dead Sea die? *Geology*, *26*(8), 755–758.

Zavialov, P., Ni, A., Kudyshkin, T., Kurbaniyazov, A., and Dikarev, S. (2009). Five years of field hydrographic research in the Large Aral Sea (2002–2006). *Journal of Marine Systems*, *76*(3), 263–271.

Zaw, K., Hunns, S., Large, R., Gemmell, J., Ryan, C., and Mernagh, T. (2003). Microthermometry and chemical composition of fluid inclusions from the Mt Chalmers volcanic-hosted massive sulfide deposits, central Queensland, Australia: implications for ore genesis. *Chemical Geology*, *194*(1-3), 225–244.